

# Closed-loop Circulation Control for wind gust alleviation

Shaoze Li

Submitted in accordance with the requirements for the degree of  
Doctor of Philosophy

The University of Leeds  
School of Mechanical Engineering

June, 2023

The candidate confirms that the work submitted is his own, except where work which has formed part of jointly authored publications has been included. The contribution of the candidate and the other authors to this work has been explicitly indicated below. The candidate confirms that appropriate credit has been given within the thesis where reference has been made to the work of others.

The preliminary study of a 2D circulation controlled aerofoil described in Chapter 5 was published in the AIAA Journal of Aircraft with the title "The dynamic response of circulation control for step and sinusoidal inputs" on 24 April 2023. (<https://doi.org/10.2514/1.C037042>)

The results of the dynamic performance of circulation control presented in chapter 7 were presented by the candidate at the RAeS Applied Aerodynamics Conference, hosted by the Royal Aeronautical Society, at No. 4 Hamilton Place, UK and virtually, on 14th September 2022. The presentation title was "Dynamic Performance of Circulation Control for gust alleviation".

*This copy has been supplied on the understanding that it is copyright material and that no quotation from the thesis may be published without proper acknowledgement.*

# Acknowledgements

First and foremost, I would like to thank my three supervisors for their tremendous support, Dr Andrew Shires, Dr Jongrae Kim and Professor Harvey Thompson. They have monitored my progress and offered valuable advice and guidance throughout.

A special thank you goes out to Professor Yunsong Gu, who supported wind tunnel equipment for my research.

My acknowledgements would not be complete without thanking my parents for their tremendous support and encouragement.

My gratitude is also extended to the China Scholarship Council and the University of Leeds for the funding opportunity.

# Abstract

An investigation into the dynamic performance of the circulation control wing (CCW) was undertaken. This research aimed to explore the possibility of using circulation control (CC) as means of gust suppression for Unmanned Aerial Vehicles (UAV). Computational Fluid Dynamics (CFD) was used to investigate the actuation speed of CC.

Firstly a two-dimensional (2D) CC aerofoil was analysed through CFD simulations and validated by existing experimental results from the literature, and a good agreement was observed. The actuation speed of the CC aerofoil was compared with a mechanical flap (aileron), it was found that the actuation speed of CC was 5 times faster than typical mechanical actuators under cruise conditions. A joint simulation that combines CFD and feedback control algorithm was undertaken to demonstrate the automatic actuation of CC jet under wind gust conditions. Results showed that the gust loading was sufficiently eliminated, and a constant lift was observed.

Secondly, a datum UAV aircraft was used to analyse the application of CC for gust alleviation in three-dimensional (3D) coupled with longitudinal flight dynamics. The aerodynamic performance of the aircraft was obtained by CFD simulations. The flap (aileron) of the aircraft was modified to a CC slot and compared with its initial mechanical control surface. Additionally, step responses of CC under various flow conditions are compared. It is observed that the responses are very similar for different flow conditions and very close to the Küssner function.

Finally, a control algorithm was designed using a Linear-quadratic regulator (LQR) controller. The model of the aircraft was obtained and flight dynamic simulations were undertaken to verify the effectiveness of CC in an unsteady atmosphere. Results showed that 96% of the vertical acceleration due to wind gusts were suppressed.

# Contents

<b>1</b>	<b>Introduction</b>	<b>1</b>
1.1	Aims and Objectives . . . . .	3
1.2	Contributions . . . . .	4
1.3	Thesis Structure . . . . .	5
<b>2</b>	<b>Theory</b>	<b>8</b>
2.1	Flow characteristics . . . . .	8
2.1.1	Steady / unsteady flow . . . . .	9
2.1.2	Turbulent / Laminar flow . . . . .	9
2.1.3	Viscous / inviscid flow . . . . .	10
2.1.4	Rotational / irrotational flow . . . . .	11
2.1.5	Compressible / incompressible flow . . . . .	12
2.2	Aerodynamic forces . . . . .	13
2.2.1	Lift generation . . . . .	14
2.2.2	Circulation . . . . .	15
2.2.3	Drag . . . . .	17
2.2.4	Pitching moment . . . . .	17
2.3	Boundary layer . . . . .	18
2.3.1	Boundary layer transition . . . . .	20
2.3.2	Boundary layer separation . . . . .	21
2.3.3	Effect of Reynolds number . . . . .	23
2.4	Wall Jet Flow and Coanda Effect . . . . .	24
2.5	Development of the Flight Dynamics Model . . . . .	31
2.5.1	Aerodynamic Stability and Control Derivatives . . . . .	31
2.5.2	Linearised Equations of Motion for Small Perturbations . . . . .	35
2.5.3	Concise Longitudinal Aerodynamic Stability Derivatives . . . . .	37
2.6	The Control Algorithm . . . . .	38
2.6.1	PID controller . . . . .	39
2.6.2	LQR controller . . . . .	40
2.7	Summary . . . . .	42

---

<b>3 Literature Review</b>	<b>43</b>
3.1 Atmospheric Disturbances . . . . .	44
3.2 Lift Control . . . . .	47
3.3 Flow Control . . . . .	50
3.3.1 Passive Flow Control . . . . .	51
3.3.2 Active Flow Control . . . . .	52
3.3.3 Circulation Control . . . . .	54
3.3.4 Closed-Loop Flow Control . . . . .	63
3.4 Actuators and Sensors for Flow Control . . . . .	65
3.4.1 Actuators . . . . .	66
3.4.2 Excitation Parameters . . . . .	69
3.4.3 Sensors . . . . .	72
3.5 Applications of Flow Control on Modern Aircraft . . . . .	73
3.5.1 Application on Unmanned Aerial Vehicles . . . . .	74
3.5.2 Application on Civil Transport Aircraft . . . . .	75
3.6 Gust Alleviation Based on Conventional Control Surfaces . . . . .	80
3.6.1 Direct Lift control (DLC) . . . . .	80
3.6.2 Load Alleviation and Ride Smoothing . . . . .	82
3.7 Gust Alleviation Based on CC . . . . .	84
3.8 Summary . . . . .	87
<b>4 Methodology</b>	<b>89</b>
4.1 Gas Properties and Assumptions . . . . .	92
4.2 CFD methods . . . . .	93
4.2.1 Navier-Stokes Equations . . . . .	94
4.2.2 Discretisation . . . . .	97
4.2.3 Pressure-Velocity Coupling . . . . .	102
4.2.4 Turbulence Model . . . . .	106
4.2.5 Boundary Conditions . . . . .	115
4.2.6 Mesh Generation . . . . .	118
4.2.7 Numerical Errors . . . . .	121
4.3 Summary . . . . .	123
<b>5 The Preliminary Study of a 2D CC Aerofoil</b>	<b>124</b>
5.1 Validation . . . . .	124

---

5.1.1	The General Aviation Circulation Control (GACC) aerofoil . . . . .	124
5.1.2	Mesh and Boundary Conditions . . . . .	126
5.1.3	Validation Result for steady and unsteady simulations . . . . .	129
5.2	Study of the CC dynamic response . . . . .	141
5.2.1	Time step sensitivity study . . . . .	141
5.2.2	Comparison of the response of CC and mechanical ailerons . . . . .	142
5.3	Circulation control algorithm design & CFD verification . . . . .	151
5.4	Summary . . . . .	154
<b>6</b>	<b>Steady State Study of the Datum Aircraft</b>	<b>156</b>
6.1	CFD Validation of the Datum Aircraft with Mechanical Flap . . . . .	160
6.2	Re-design of the trailing edge for CC . . . . .	167
6.3	Hybrid Meshing of the Aircraft with CC Wing . . . . .	170
6.3.1	Unstructured Tetra Meshing . . . . .	171
6.3.2	Structured Meshing . . . . .	171
6.3.3	Hybrid Meshing . . . . .	172
6.4	3D Effect of the Trailing Edge Coanda Surface . . . . .	175
6.4.1	Flow Field at the Nozzle Exit . . . . .	176
6.4.2	The Flow Field Without the Edge Vortex . . . . .	177
6.4.3	Trailing Edge Thickness . . . . .	182
6.5	Spanwise Velocity Distribution . . . . .	186
6.6	Spanwise Effect of the CC Flap . . . . .	187
6.7	Simulation Results of the CC Half Wing-body Model. . . . .	194
6.7.1	Steady State CFD Results of the 3D Wing-body Model . . . . .	194
6.7.2	Comparisons Between 3D Wing and 2D Aerofoil . . . . .	196
6.7.3	Comparison of the CCW and the Mechanical Flap . . . . .	203
6.8	Summary . . . . .	205
<b>7</b>	<b>The Dynamic Performance of CC</b>	<b>206</b>
7.1	2D Step Response of the CC Flap . . . . .	206
7.2	Flow Field in Different Phase . . . . .	208
7.3	Factors of the Dynamic Response of CC . . . . .	215
7.3.1	Mesh Density . . . . .	215
7.3.2	Freestream Velocity Effect . . . . .	215
7.3.3	Nozzle Pressure Effect . . . . .	216

---

7.3.4	Trailing Edge Shape . . . . .	220
7.4	Transfer Function Modelling of the CC for dynamic analysis . . . . .	230
7.5	Summary . . . . .	233
<b>8</b>	<b>Application of the CC on Gust Alleviation</b>	<b>235</b>
8.1	LQR Controller Design . . . . .	235
8.2	Statistical Modelling of the Wind Gust . . . . .	238
8.3	Gust Alleviation Results using Closed-loop LQR Control . . . . .	241
8.4	Summary . . . . .	243
<b>9</b>	<b>Conclusions and Future Work</b>	<b>245</b>
9.1	The Dynamic Performance of CC . . . . .	246
9.2	Assessment of the bandwidth for gust alleviation relative to conventional actuators . . . . .	247
9.3	Coupled Simulation of CFD and Closed-Loop Control . . . . .	247
9.4	The Applications of CC on Gust Alleviation . . . . .	248
9.5	Future Work . . . . .	249

# List of Figures

2.1 The forces acting on an aircraft (Barnard & Philpott 2010). . . . .	13
2.2 The flow pattern over an aerofoil(Anderson & Bowden 2005) . . . . .	14
2.3 The streamlines around a curved thin plate. . . . .	15
2.4 The circulation of an enclosed area in the flow field(Anderson & Bowden 2005). . . . .	16
2.5 The flow past around an asymmetrical aerofoil, (a) Irrotational flow, (b)Actual flow.(Shires 2016) . . . . .	16
2.6 The development of boundary layer on a flat plate (Anderson Jr 2016). . . . .	19
2.7 The velocity profile with the linear region and log-law region (Nishino et al. 2010). . . . .	20
2.8 Flow development in adverse pressure gradient. (Shires 2016) . . . . .	22
2.9 The pressure distribution on the upper surface of an aerofoil at high AoA (An- derson & Bowden 2005) . . . . .	22
2.10 Lift and drag variation with Reynolds number in unblown condition (ENGLAR et al. 2009) . . . . .	23
2.11 (a) A Coanda jet stay attached to the curved surface, (b) Streamlines around a Coanda jet ( $y_2 = 1/2U_{max}$ ) (Neuendorf & Wygnanski 1999) . . . . .	25
2.12 The variation of stagnation point and separation bubble created by the Coanda jet, (a) $C_\mu = 0.005$ , (b) $C_\mu = 0.015$ . . . . .	27
2.13 The jet around a Coanda surface. . . . .	28
2.14 The pressure distribution around a Coanda surface at $C_\mu = 0.1$ (NOVAK et al. 1987). . . . .	30
2.15 The definition of the axes. . . . .	31
3.1 The road map of technologies involved in this research. . . . .	43
3.2 The flow structure of a maturation thunderstorm. (Allen 2013) . . . . .	44
3.3 The microburst under a thunderstorm. (Allen 2013) . . . . .	45
3.4 Wind speed profiles of different types of atmospheric disturbances. . . . .	46
3.5 Typical control surfaces on modern transport aircraft. . . . .	48
3.6 The flaperon of a Boeing 787 aircraft (Wagner & Norris 2009). . . . .	48

3.7	Schematic of different types of trailing edge high-lift devices, a: split flap, b: single slotted flap, c: double-slotted flap. (Kundu 2010) . . . . .	49
3.8	Experimental data of high-lift devices at $Re_c = 4.4 \times 10^6$ (Dovey 2003). . . . .	49
3.9	Outboard cross-section of 737NG (McLean et al. 1999). . . . .	50
3.10	The tendency of high-lift systems (Reckzeh 2003). . . . .	51
3.11	Schematic of passive flow control. . . . .	51
3.12	Passive flow control devices: (a)Vortex generators to enhance low speed performance, (b)Nacelle Vortex Generator, (c)Forebody strakes (Cobleigh 1994). . . . .	52
3.13	Summary of the active flow control implementations (Jones & Joslin 2006, King 2010, Joslin & Miller 2009). . . . .	53
3.14	The CC blowing flap. (Jones et al. 2013) . . . . .	54
3.15	The Quiet Short-Haul Research Aircraft (QSRA) (Huff 2013). . . . .	55
3.16	The application of CC on heavy vehicles, 4 aft blowing slots and one leading edge blowing slot are displayed (Englar 2000b). . . . .	56
3.17	The sketch of the CC020-010EJ aerofoil (ENGLAR et al. 2009, Englar 1975a) . . . . .	59
3.18	The CC wind tunnel model (ENGLAR et al. 2009). . . . .	59
3.19	The sketch of the NCCR 1510-7607N aerofoil (Jones & Joslin 2005). . . . .	60
3.20	Examples of trailing edge surface for CC. (a) Circular (b) Logarithmic spiral (Slomski, Marino, Ebert & Abramson 2006) (c) Multipoint optimisation (Forster et al. 2016) (d) Dual radius (Golden & Marshall 2010) (e) Retractable (Englar 1975b) . . . . .	61
3.21	The location of the separation point versus $C_\mu$ with different nozzle height, h: nozzle height, R: radius of trailing edge as displayed in Figure 3.17 on page 59 (Englar 1975b). . . . .	62
3.22	Actuator and sensor arrangement of the adaptive closed-loop separation control model (Becker et al. 2007). . . . .	64
3.23	Stemme S10-VT with two pods for carrying pressurized air and the actuation slots on the flap (King et al. 2013). . . . .	65
3.24	A type classification of flow control actuators. (Cattafesta III & Sheplak 2011). . . . .	66
3.25	Principle of operation of a dimple. (Dearing et al. 2007). . . . .	68
3.26	Stages of the SparkJet operation cycle (Grossman et al. 2003). . . . .	69
3.27	The effect of modulating envelope shape on Integral parameters vs. non-dimensional excitation frequency (F+). (a)Normal force coefficient ( $\Delta C_n$ ), (b)Waveform (Margalit et al. 2002). . . . .	70

3.28 Schematic of a rotary valve. (Cattafesta III & Sheplak 2011). . . . .	70
3.29 Conceptual diagram for rotating cap actuator (Choi et al. 2006). . . . .	71
3.30 Wing-adaptation and boundary layer control devices (Stanewsky 2001). . . . .	73
3.31 The Demon UAV (Buonanno 2009). . . . .	74
3.32 Photographs of the hybrid model with actuators on the apex, midspan and trailing edge (Williams & Seidel 2016). . . . .	75
3.33 The micro geometric spoiler and counter-flow fluidic spoiler (Harley 2011). . . . .	75
3.34 2D CFD simulation and schlieren contours for 60° flap configuration for varying blowing conditions (Jones et al. 2013). . . . .	77
3.35 The DLR-F15 wing model and actuation system (Ciobaca & Wild 2013). . . . .	78
3.36 The B757 tail model and sweeping jet actuator (Whalen et al. 2015). . . . .	79
3.37 The schematic of direct lift control. . . . .	80
3.38 The lift build up after a step change in $C_{\mu}$ , compared with the Wagner's function (Friedman et al. 2016). . . . .	86
3.39 The gust response with adaptive blowing compared with no blowing (Li & Qin 2020). . . . .	87
4.1 Hierarchy of models for flow over an aircraft. . . . .	90
4.2 The discretization process (F. Moukalled 2016). . . . .	97
4.3 Two adjacent cells to illustrate the quantities at the cell centroid and at the faces (Ansys 2018). . . . .	98
4.4 The solving sequence of governing equations (ANSYS 2010). . . . .	103
4.5 Transient SIMPLE algorithm for a 2D domain. $p$ is the pressure, $u$ and $v$ are velocity components, $\phi$ denotes additional scalars such as turbulent quantities and energy scalars. The $p^*, u^*, v^*$ are guessed terms, $p', u', v'$ are correction terms (Versteeg & Malalasekera 2007, Ansys 2018). . . . .	105
4.6 Mean velocity profiles of a curved wall jet with external flow, $C_{\mu} = 0.03$ , $d$ : normal distance to the wall, $\mathbf{u}_{\text{parallel}}$ : tangential velocity component (Swanson & Rumsey 2009). . . . .	108
4.7 The schematic of the boundary settings. (a) wall, (b) inlet, (c) far field. The right figure shows a close-view of the nozzle. . . . .	117
4.8 The topology of structured mesh. (a) C-shape, (b) H-shape, (c) O-shape. . . . .	119
4.9 The cells of unstructured mesh. (a) prism, (b) tetrahedral, (c) hexahedral, (d) pyramid. . . . .	119
4.10 T-Rex meshing of a multi-element aerofoil (Pointwise n.d.). . . . .	120
4.11 Non-orthogonal (left) and skewed (right) cells (Ansys 2018). . . . .	122

5.1	(a)The geometry of the GACC aerofoil. (b)Comparison with the original GAW-1 aerofoil (blue curve) . . . . .	125
5.2	Boundary conditions and dimensions of the nozzle ( m ), for GACC aerofoil. . .	127
5.3	Sensitivity study for far field distance of 10, 25, 100 chord length, at $C_\mu = 0.017$ , $M = 0.1$ . . . . .	128
5.4	The variation of lift coefficient over increasing mesh scale with SIMPLE method and S-A turbulence model, GACC aerofoil, $M=0.1$ , $AoA=0$ , $C_\mu = 0.025$ . . . .	129
5.5	The mesh of the GACC geometry with 149,001 cells. . . . .	129
5.6	Comparison between $k - \omega$ SST model, S-A model and experimental data. (2D GACC aerofoil in CFD compared with a 2D wing section model in the wind tunnel, $C_\mu = 0.017$ and $0.025$ , $M=0.1$ , $Re=4.6 \times 10^5$ ) . . . . .	131
5.7	Comparison of the residuals between SIMPLE, SIMPLEC and PISO methods. (GACC aerofoil, $C_\mu = 0.025$ , $M=0.1$ , $Re=4.6 \times 10^5$ ) . . . . .	133
5.8	Comparison of the time-history $C_L$ using SIMPLE, SIMPLEC and PISO methods. (GACC aerofoil, $C_\mu = 0.025$ , $M=0.1$ , $Re=4.6 \times 10^5$ ) . . . . .	134
5.9	$C_L$ vs. $C_\mu$ of the GACC aerofoil at $M = 0.1$ , unsteady S-A model, $AoA = 0$ , time step = 0.0001s. Compared with experimental data. . . . .	135
5.10	The surface distribution of pressure at $C_\mu = 0.06$ , $M = 0.1$ , compared with experimental data, for the GACC aerofoil. . . . .	136
5.11	$C_L$ vs. AOA of the GACC aerofoil in different blowing momentum coefficients at $M = 0.1$ . Compared with experimental data. . . . .	136
5.12	The velocity profiles on the trailing edge of the GACC aerofoil at $C_\mu = 0.015$ , $M=0.1$ . Left, nozzle exit. Right, separation point on the round trailing edge. . .	137
5.13	The computational mesh for unsteady validation of NACA0012 aerofoil, left: the computational domain with a uniform density from the aerofoil to the far field, right: the mesh distribution near the wall. . . . .	139
5.14	The vertical velocity field ( m/s ) showing the gust front marching from the left side of the domain, NACA0012 aerofoil. . . . .	140
5.15	Unsteady validation results of the NACA0012 aerofoil encountered a sharp edge gust, left: $M_\infty = 0.1$ , right: $M_\infty = 0.2$ . . . . .	141
5.16	Simulated lift coefficient response with different time steps, GACC aerofoil, $M = 0.1$ , $C_\mu = 0.025$ . . . . .	142
5.17	The experimental rig for a fast-actuation flap, with NACA0021 aerofoil (Phillips & Wygnanski 2013). . . . .	143

5.18	Lift response to a step input for GACC aerofoil and mechanical flap. . . . .	144
5.19	Comparison of the GACC actuation and typical plain flaps of the lift response to a step input over physical time. . . . .	145
5.20	Comparison of the lift response of GACC aerofoil to a step input and the Küssner and Wagner function. . . . .	147
5.21	Response of lift to a sinusoidal input. . . . .	148
5.22	Comparison of amplitude and phase response with different nozzle pressure range and velocity. . . . .	149
5.23	Lift response to axial gust, GACC aerofoil, $P_{tJ}=10\text{kPa}$ , $M = 0.1$ , $\Delta U_g = \pm 3.4\text{m/s}$ , $\Delta V_g = 6.8\text{m/s}$ . . . . .	150
5.24	The schematic of the system: (a) for controller tuning, (b) for CFD in the loop testing. . . . .	150
5.25	System identification for the lift response at $M=0.1$ , $P_{tJ} = 10 \text{ kPa}$ , GACC aerofoil.	152
5.26	Gust suppression performance of the tuned PID controller with identified plant model, simulated without CFD. . . . .	152
5.27	The time-history variation of the variables under 1-cosine vertical gust at $M0.1$ , simulated with CFD, GACC aerofoil with blowing. . . . .	154
6.1	The geometry of the 33% scale Zivko Edge 540T aircraft with a NACA0013 aerofoil and a modified CC trailing edge. . . . .	157
6.2	The dimensions of the 33% scale Zivko Edge 540T aircraft (mm). . . . .	159
6.3	Unstructured tetra mesh for the half-wing-body, 33% scale Zivko Edge 540T with flap. . . . .	160
6.4	The mesh details near the trailing edge and far field for the half-wing-body, 33% scale Zivko Edge 540T with flap. (a) the surface meshes on the flap, (b) the volume mesh in the gap region, (c) the top view of the wing-body junction region, (d) the volume mesh near trailing edge, (e) the far field and symmetry plane. . . . .	161
6.5	Lift coefficient of different mesh densities, for the 33% scale Zivko Edge 540T aircraft with mechanical flap at $M = 0.1$ . . . . .	163
6.6	Contour of $y^+$ value for the tapered NACA0013 wing at $M = 0.1$ , $\text{AoA} = 0$ . . .	163
6.7	Validation of the present CFD results with wind tunnel data for the 9% thickness wing-body model(Ol et al. 2013) at $\text{Re}=140,000$ , top: $C_L$ and $C_D$ vs. $\text{AoA}$ for clean wing, bottom: $C_L$ and $C_D$ vs. flap deflection at $\text{AoA}=0$ . . . . .	165

6.8	Lift, drag and pitch moment coefficients of the 3D wing-body model in various AoA (33% scale Zivko Edge 540T aircraft with NACA0013 aerofoil, $M = 0.1$ ).	166
6.9	Lift, drag and pitch moment coefficients of the 3D wing-body model in various flap deflection angle (33% scale Zivko Edge 540T aircraft with NACA0013 aerofoil, $M = 0.1$ ).	167
6.10	Trailing edge configurations by modifying the NACA0013 aerofoil. h: Nozzle height, r: TE radius, c: Chord length.	169
6.11	Lift coefficient of the 4 configurations of the modified NACA0013 aerofoil under different $C_{\mu}$ . AoA=0, $M=0.1$ .	170
6.12	Drag coefficient of the 4 configurations of the modified NACA0013 aerofoil under different $C_{\mu}$ . AoA=0, $M=0.1$ .	171
6.13	Structured mesh for the 33% scale Zivko Edge 540T wing-body model with CC trailing edge.	172
6.14	Hybrid mesh for the 33% scale Zivko Edge 540T wing-body model with CC trailing edge.	173
6.15	Mesh independent study for the 33% scale Zivko Edge 540T wing-body model with hybrid mesh at $C_{\mu} = 0.01$ , $M = 0.1$	174
6.16	The streamline view of the vortex patterns at $M = 0.1$ , $C_{\mu}=0.01$ , for the 33% scale Zivko Edge 540T wing-body model.	176
6.17	The vector field of the vortex patterns at $M = 0.1$ , $C_{\mu}=0.01$ , for the 33% scale Zivko Edge 540T wing-body model.	177
6.18	The vortex patterns of the modified wing and the original wing-body case at $M = 0.1$ , nozzle pressure 7500Pa, $C_{\mu}=0.01$ , 33% scale Zivko Edge 540T model. (a): modified wing geometry, (b): original wing-body geometry, (c): streamlines of the modified wing, (d): streamlines of the original wing-body case, (e): pressure distribution of the trailing edge of the modified wing, (f): pressure distribution of the original wing-body case.)	179
6.19	The jet sheet for a wing section model with a modified TE NACA0013 aerofoil, nozzle pressure 7500Pa, $M = 0.1$ .	181

6.20 Streamlines and trailing edge pressure distribution of the thicker trailing edge ( $h/r=0.05$ , $r/c=0.01$ ) and the original thinner trailing edge ( $h/r=0.1$ , $r/c=0.005$ ) at $M = 0.1$ , nozzle pressure 7500Pa, $C_{\mu}=0.01$ , 33% scale Zivko Edge 540T model. (a): streamlines of the thicker trailing edge, (b): streamlines of the original thinner trailing edge, (c): pressure distribution on the trailing edge showing a straight separation line (d): pressure distribution showing an unstable separation line.) . . . . .	183
6.21 The side view of the research model and the wavy vortices conducted in a water tunnel, the slot is at the bottom of figure (b), flow direction is upward, $Re_h = 63$ (Dunaevich & Greenblatt 2020). . . . .	184
6.22 The stability map of slot height based Gortler number $G'$ in terms of wavenumber $\alpha$ (Dunaevich & Greenblatt 2020) . . . . .	185
6.23 The axial(X) and spanwise (Y) velocity distribution from the wing root to the wing tip (Nozzle pressure = 7500Pa, 33% scale Zivko Edge 540T wing-body model). . . . .	187
6.24 The local nozzle height and $C_{\mu}$ from the wing root to the wing tip (Nozzle pressure = 7500Pa, 33% scale Zivko Edge 540T wing-body model). . . . .	187
6.25 The geometries of the half-span cases, 33% scale Zivko Edge 540T wing-body model. a) original nozzle, b) inner half-span nozzle, c) outer half-span nozzle. . . . .	188
6.26 Lift coefficient of various blowing momentum coefficient with full-span nozzle, inner half and outer half at $M = 0.1$ , 33% scale Zivko Edge 540T wing-body model. . . . .	189
6.27 The mass flow rate and power consumption under various lift coefficients with full-span nozzle and inner half nozzle at $M = 0.1$ , 33% scale Zivko Edge 540T wing-body model. . . . .	189
6.28 The streamlines and pressure distribution of the upper surface at $M = 0.1$ , 33% scale Zivko Edge 540T wing-body model, (a) (c) (e): half span, (b) (d) (f): full-span. . . . .	191
6.29 The streamlines and pressure distribution of the lower surface at $M = 0.1$ , 33% scale Zivko Edge 540T wing-body model, (a) (c) (e): half span, (b) (d) (f): full-span. . . . .	192
6.30 The lift coefficients of the 33% scale Zivko Edge 540T wing-body model in various AoA, $M = 0.1$ . . . . .	194

6.31	The drag coefficients and nozzle thrust of the 33% scale Zivko Edge 540T wing-body model in various AoA, $M = 0.1$ . . . . .	195
6.32	The pitch moment coefficients of the 33% scale Zivko Edge 540T wing-body model in various AoA, $M = 0.1$ . . . . .	195
6.33	The lift coefficient of the 2D NACA0013 aerofoil and 3D tapered wing without blowing at $M = 0.1$ . . . . .	197
6.34	The lift coefficient of the 2D NACA0013 aerofoil and 3D tapered wing with blowing at $M = 0.1$ . . . . .	198
6.35	Comparison of the 2D NACA0013 aerofoil (b, d) and mid-span slice of the 3D tapered wing (a, c) at $C_\mu = 0.01$ , AoA=0. . . . .	200
6.36	Comparison of the 2D NACA0013 aerofoil (b, d) and mid-span slice of the 3D tapered wing (a, c) at $C_\mu = 0.02$ , AoA=0. . . . .	201
6.37	x-y plane at $C_\mu = 0.012$ , AoA=0 for the 3D tapered wing. . . . .	202
6.38	The $C_L$ of the 3D tapered wing with modified CC trailing edge and the original mechanical flap of the 33% scale Zivko Edge 540T at $M = 0.1$ , AoA=0°, $C_\mu = 0 - 0.02$ . . . . .	203
6.39	The drag polar of the 3D tapered wing with modified CC trailing edge and the original mechanical flap of the 33% scale Zivko Edge 540T at $M = 0.1$ , AoA=0°, $C_\mu = 0 - 0.02$ . . . . .	204
6.40	The $C_M$ of the 3D tapered wing with modified CC trailing edge and the original mechanical flap of the 33% scale Zivko Edge 540T at $M = 0.1$ , AoA=0°, $C_\mu = 0 - 0.02$ . . . . .	204
7.1	Step response of $C_L$ when $P_{tJ}$ increased by 10kPa, for the modified TE NACA0013 with various time step settings from $10^{-3}$ s ( $7.4 \times 10^{-2}c/U_\infty$ ) to $5 \times 10^{-6}$ s ( $3.7 \times 10^{-4}c/U_\infty$ ) at AoA=0, $M = 0.1$ and 10 inner iterations per time step. .	207
7.2	Step response of $C_L$ and jet velocity on the nozzle exit when $P_{tJ}$ increased by 10kPa, for the modified TE NACA0013 , plenum pressure rises from 0Pa to 10kPa at T=0s. . . . .	208
7.3	Phases of the flow field and streamlines at different stages when $P_{tJ}$ increased by 10kPa, for the modified TE NACA0013, $M = 0.1$ , AoA = 0. . . . .	209
7.4	The pressure distribution of different phases when $P_{tJ}$ increased by 10kPa, for the modified TE NACA0013, $M = 0.1$ , AoA = 0 ( Legend: time in seconds ). .	210
7.5	The schematic of the jet stream variation on different phases, when $P_{tJ}$ increased by 10kPa, for the modified TE NACA0013,. . . . .	211

7.6	Step response of $C_L$ and jet velocity on the nozzle exit, when $P_{tJ}$ drops from 10kPa to 0Pa at $T=0s$ , for the modified TE NACA0013. . . . .	212
7.7	Phases of the flow field and streamlines at different stages when $P_{tJ}$ drops from 10kPa to 0Pa at $T=0s$ , for the modified TE NACA0013. . . . .	213
7.8	The pressure distribution of different phases when $P_{tJ}$ drops from 10kPa to 0Pa at $T=0s$ , for the modified TE NACA0013 ( Legend: time in seconds ). . . . .	214
7.9	Lift response with different mesh, when $P_{tJ}$ rises from 0Pa to 10kPa at $T=0s$ , for the modified TE NACA0013. . . . .	216
7.10	Steady state $C_L$ vs. nozzle pressure with different Mach number for the modified TE NACA0013. . . . .	217
7.11	The step response for a $C_L$ increment of 0.3 under different Mach number. $M = 0.1$ ( $Re = 1.04 \times 10^6$ ), $M = 0.2$ ( $Re = 2.07 \times 10^6$ ), $M = 0.3$ ( $Re = 3.11 \times 10^6$ ), for the modified TE NACA0013. . . . .	217
7.12	The $C_L$ versus nozzle pressure at $M = 0.1$ , $AoA=0^\circ$ , for the modified TE NACA0013, the data labels show exact values on the x-axis. . . . .	218
7.13	Step response of the $C_L$ in different $P_{tJ}$ , for the modified TE NACA0013 at $M = 0.1$ , $AoA=0^\circ$ . . . . .	219
7.14	The flow field of different TE configurations at $T=0.003s$ , when $P_{tJ}$ rises from 0Pa to 10kPa, at $T=0s$ , $M = 0.1$ , $AoA=0^\circ$ . . . . .	221
7.15	The flow field of different configurations at $T=0.005s$ , when $P_{tJ}$ rises from 0Pa to 10kPa, at $T=0s$ , $M = 0.1$ , $AoA=0^\circ$ . . . . .	222
7.16	The flow field of different configurations at $T=0.01s$ , when $P_{tJ}$ rises from 0Pa to 10kPa, at $T=0s$ , $M = 0.1$ , $AoA=0^\circ$ . . . . .	223
7.17	The flow field of different configurations at $T=0.05s$ , when $P_{tJ}$ rises from 0Pa to 10kPa, at $T=0s$ , $M = 0.1$ , $AoA=0^\circ$ . . . . .	224
7.18	The flow field of different configurations at $T=0.1s$ , when $P_{tJ}$ rises from 0Pa to 10kPa, at $T=0s$ , $M = 0.1$ , $AoA=0^\circ$ . . . . .	225
7.19	The time history $C_L$ of different TE configurations, when $P_{tJ}$ rises from 0Pa to 10kPa, at $t=0$ , $M = 0.1$ , $AoA=0^\circ$ . . . . .	226
7.20	Comparison of the Küssner problem and the CC in potential flow. . . . .	228
7.21	Steady state $C_L, C_D, C_M$ on various $AoA$ for the modified TE NACA0013, at $M = 0.1$ . . . . .	230
7.22	The step response under various $AoA$ , for the modified TE NACA0013, at $M = 0.1$ . . . . .	231

7.23	The step response identified by the second-order model (solid line: CFD results, dash line: second-order model). . . . .	232
7.24	The bode diagram under various AoA identified by the second-order model for the modified TE NACA0013 aerofoil. . . . .	233
8.1	The control architecture for the gust alleviation system based on a CC actuator.	235
8.2	The aircraft response to continuous vertical turbulence. . . . .	241
8.3	The controller input and the normal acceleration of the aircraft. . . . .	242

# List of Tables

1.1	Summary of the simulation cases. . . . .	7
3.1	Summary of the simulation meshes for CC aerofoil . . . . .	61
3.2	Comparison of sensors for gust detection . . . . .	72
3.3	Gust alleviation systems in operational aircraft(Regan & Jutte 2012) . . . . .	83
4.1	Computational expense of different turbulence modelling methods. . . . .	109
5.1	The plenum chamber conditions for various blowing momentum coefficients ( Reference pressure: 101325Pa, T=288K, $\gamma=1.4$ , R=287 ). . . . .	130
5.2	The computational effort of different solvers for 10,000 steps. . . . .	132
6.1	Aircraft parameters . . . . .	158
6.2	Mesh independent study of the 33% scale Zivko Edge 540T aircraft with mechanical flap at $M = 0.1$ . . . . .	162
6.3	Comparison of the literature reference data and the CFD results (33% scale Zivko Edge 540T aircraft with NACA0013 aerofoil, $M = 0.1$ ) . . . . .	167
6.4	Circulation control trailing edge parameters, r: TE radius, h: Nozzle height, c: Chord length (33% scale Zivko Edge 540T aircraft with NACA0013 aerofoil and modified circular trailing edge). . . . .	168
6.5	The $C_{\mu}$ of the 2D modified NACA0013 aerofoil and 3D tapered wing under various pressure settings. . . . .	186
6.6	Parameters for the simulation of flight dynamics . . . . .	196
7.1	Comparison of stabilisation time of different aerofoils. . . . .	227
7.2	Identified model of different AoA . . . . .	232

# Nomenclature

## Roman alphabet

$h$	height
$U, u$	total and perturbation axial velocity component
$X$	axial force
$\dot{m}$	mass flow rate, kg/s
$a$	The speed of sound
$a_z$	vertical acceleration
$C_\mu$	jet momentum coefficient
$C_i$	coefficient of $i$
$c_p$	specific heat capacity at constant pressure
$c_v$	specific heat capacity at constant volume
$D$	drag
$d$	gust length, s
$e$	internal energy, error output for PID
$f$	body force
$G'$	slot height based Gortler number
$G(s)$	transfer function
$h$	enthalpy, height
$H_\infty$	a robust control method
$I_y$	pitch inertia
$k$	thermal conductivity / turbulent kinetic energy

---

$k_p, k_i, k_d$	PID gains
$k_T$	induced drag coefficient
$L$	lift, gust scale length
$l$	reference length
$M$	Mach number, pitching moment
$P$	pressure, Pa
$P_{shaft}$	pump power
$q$	pitch rate
$R^-$	Riemann invariant
$Re$	Reynolds number
$S$	reference area, source term
$s$	nondimensional time $s = t * U/c$ or $2t * U/c$
$T$	temperature, K
$t$	time
$TI$	turbulent intensity
$u$	control input
$u, v, w$	velocity components in x, y, z direction
$U, W$	axial and normal velocity, m/s
$V$	flight velocity, m/s
$W, w$	total and perturbation vertical velocity component
$w_g$	vertical velocity component of gust
$x_{cg}$	centre of gravity
$x_{cr}$	critical position for boundary layer transition
$y$	control output

$y^+$  dimensionless wall distance

$Z$  vertical force

$b$  span, m

$c$  chord, m

$h$  jet slot height, m

$q$  dynamic pressure, Pa

$R$  gas constant

$r$  radius

$w$  slot width, m

### **Greek alphabet**

$\alpha$  angle of attack, wavenumber

$\Delta$  the difference of a variable over a time period

$\delta$  control deflection angle, positive downwards, rad

$\eta_{pump}$  pump efficiency

$\Gamma$  circulation, diffusion coefficient

$\gamma$  heat capacity ratio

$\lambda$  wavelength

$\Psi$  dissipation term

$\mu$  gas dynamic viscosity

$\mu_t$  turbulent viscosity

$\nabla$  vector differential operator

$\nu_t$  turbulent kinematic viscosity

$\Omega$  spatial frequency of gust

$\omega$  specific rate of dissipation of kinetic energy, frequency, rad/s

$\phi$	a scalar quantity
$\rho$	density of the fluid
$\sigma$	turbulent Prandtl number, gust intensity
$\tau_w$	wall shear stress
$\tau$	thrust force
$\tau_a$	Flap effectiveness
$\tau_{ij}$	stress on $j$ direction applied to the plane perpendicular to $i$ direction
$\theta$	perturbed pitch angle
$\varepsilon$	turbulent dissipation rate, downwash angle at the tailplane
$\xi$	vorticity

**Subscripts**

$\eta$	deflection angle of elevator
$\infty$	Freestream condition
$D$	drag
$dlc$	deflection angle of CC
$e$	equilibrium state, elevator
$f$	flap, cell face
$g$	gust variable
$J$	Jet variable
$M$	pitching moment of aerofoil or wing
$m$	pitching moment of aircraft
$ss$	quasi steady state value
$T$	tailplane derivatives
$t$	Total condition

$u, w, \dot{w}, q$  partial derivatives with respect to variable

$w$  variable at the wall

0 Initial condition

### Superscripts

◦ dimensional quantity

' fluctuation or correction term

+ dimensionless term

· differentiation with respect to time

$\bar{i}$  mean value of  $i$

### Abbreviations

AoA Angle of Attack

ATTAS Advanced Technologies Testing Aircraft System

CC Circulation Control

CFD Computational Fluid Dynamics

CFL Courant Friedrichs Lewy condition

DNS Direct Numerical Simulation

GACC General Aviation Circulation Control

LARS Load Alleviation and Ride Smoothing

LES Large Eddy Simulation

LIDAR Light Detection and Ranging system

LQR Linear Quadratic Regulator

LSE Linear Stochastic Estimation

MAC Mean Aerodynamic Chord

NPR nozzle pressure ratio

PID	Proportional Integral Derivative
POD	Proper Orthogonal Decomposition
PRBS	Pseudo Random Binary Signal
PRT	Powered Resonance Tube
PSD	Power Spatial Density
RANS	Reynolds Averaged Navier Stokes
S-A	Spalart Allmaras
SIMPLE	Semi Implicit Method for Pressure Linked Equations
STOL	Short Take Off and Landing
UAV	Unmanned Aerial Vehicle
VGJ	Vortex Generator Jet
ZNMF	Zero Net Mass FLux

# Chapter 1:

## Introduction

Civilian Unmanned Aerial Vehicles (UAVs) have been widely used in missions such as transportation, photography, civil security, search and rescue. To expand the range of operations and applications, improved stability is required, particularly to allow operations in challenging weather conditions. Civilian UAVs have a significantly smaller weight and inertia than manned transport aircraft and usually fly at lower altitudes where turbulence is greater. Additionally, when conducting operations in mountainous terrain (such as search and rescue missions), the aircraft may encounter terrain-induced weather features such as Katabatic wind or turbulence. Consequently, UAVs are more likely to experience unsteady wind conditions than manned transport aircraft, and will experience higher accelerations and less stability which may cause damage and failure of components or the aircraft. Therefore there is a need to increase the gust/turbulence resilience of the UAV to improve stability and expand its mission profile.

The bandwidth and authority of control surfaces is the main limiting factor for the performance of gust alleviation systems (Khalil & Fezans 2021). Although conventional mechanical control surfaces can effectively change lift in response to a vertical gust (i.e. using ailerons, elevators, spoilers etc.), they have a relatively slow actuation speed and fluidic response, and therefore a greater lead time in the control loop is required in order to be effective (Fezans et al. 2019). This can be realised through aerodynamic sensors or dedicated laser based sensors (Cates et al. 2013) located ahead of the wing, near the front of the fuselage, to preview gust information in sufficient time to be reactive. UAVs are typically much smaller than manned transport aircraft (this research has assumed a baseline UAV with a 2.56m wing span and 13.2kg take off weight), and consequently, the available preview time is much less. Their simpler design and packaging constraints also limit where sensors can be located. Therefore changing lift in response to a gust using mechanical devices is less effective without this preview information. Despite this, most of the current literature for small UAVs is focused on the use of conventional ailerons and elevators (Smith et al. 2016, Yang et al. 2012, Lungu 2020, Yeo et al. 2019), and since their performance has physical limits of bandwidth and authority, the literature focuses on algorithm development for improved dynamic response. Therefore

---

the present research considers how the reaction speed (i.e. actuation and fluidic response) can be improved using active flow control instead of mechanical devices, and specifically the use of Circulation Control (CC).

Active flow control already has a wide range of aerospace applications for the purpose of lift augmentation and/or drag reduction (Jones & Joslin 2006), and CC is one such method that has been thoroughly investigated by researchers (McGowan et al. 2004, Golden & Marshall 2010, Buonanno 2009, Buonanno & Cook 2006, Savvaris et al. 2013, Yang et al. 2008, ENGLAR et al. 2009, Cagle 2002, Swanson et al. 2005b, Rogers & Donnelly 2004, Paschal et al. 2012). A typical CC wing (CCW) has a circular trailing edge and a blowing slot tangential to the circular surface. The slot or nozzle produces a high-speed jet sheet that stays attached to the circular surface for a distance, due to the Coanda effect, before finally separating from this surface. Since CC can significantly increase lift, it has therefore been used as means of lift augmentation for short-take-off and landing. CC has also been investigated as a means to provide quasi-steady flight controls (Savvaris et al. 2013, Englar 1979). Most significantly, the DEMON flapless UAV has performed test flights using a CC wing and Fluidic Thrust Vectoring as manouver effectors (Wilde et al. 2008, Crowther et al. 2009), and more recently, C Rosen et al. tested a demonstrator UAV with CC actuators with research focusing on the controller design (Rosen et al. 2017). Consequently, although the characteristics of CC have been extensively investigated, with some applications focused on using CC for the primary flight controls, all these studies have considered quasi-steady flight conditions. The research described in the present study aims to characterise the dynamic performance of CC so that actuation speeds can be determined and compared with those of conventional mechanical control surfaces. These dynamic characteristics will subsequently be used in this research to design a suitable flight control algorithm that will be evaluated in both 2D and 3D applications.

For gust alleviation, a high bandwidth and fast response actuator is essential. In low speed flight ( $M \approx 0.1$ ), the frequency of atmospheric gusts is typically  $< 10^1$  Hz according to the Dryden gust model (Stevens et al. 2015). However, the Dryden model is a statistical model for a standard atmosphere, and gusts can be more severe near terrain. The gust frequency near the short-period mode of an aircraft has a relatively stronger influence which is approximately in the range of  $10^0$  to  $10^1$  Hz (Nelson et al. 1998, Cook 2012, Regan & Jutte 2012). Mechanical control surfaces are capable of attenuating the short-period mode frequency region. The attenuation performance, for example, the reduction of normal acceleration due to vertical gust, is directly related to the deflection rate of the actuator, which will deteriorate as the hinge moment increases (with forward airspeed, for example) (Hahn & König 1992). In the process

of deflecting a conventional mechanical control surface at high rotational speed, the surrounding air is accelerated vertically, which generates an additional force in the opposite direction to this airflow. This force temporarily changes the overall lift but does not increase the net circulation around the aerofoil, and is termed non-circulatory lift (Taha & Rezaei 2019). The non-circulatory lift will increase the hinge moment and is one of the factors that limit the maximum deflection rate of a control surface. Other factors include the inertia of the actuators and mechanical linkages. Also, as the flight speed increases, the maximum deflection rate reduces further due to higher aerodynamic loading on the control surface. This characteristic exists in most of the mechanical actuators such as hydraulic and electric actuators. However, CC does not have these limitations. It can rapidly change the aft stagnation point by controlling the nozzle pressure, eliminating the need for actuators, levers, gears and hinges. Pneumatic valves are used to adjust the blowing coefficient, which can easily reach a high bandwidth since the valve cores have a very small inertia (SMC n.d.). Furthermore, CC does not create non-circulatory lift and so the actuation speed is not limited by its effect on the hinge moment. CC directly influences the surrounding flow pattern and hence the dynamic response mainly depends on the reaction speed of the fluid, which is in theory much faster than a mechanical system. This will be investigated in the present research.

The dynamic modelling for conventional actuators has been widely investigated (Küssner 1936, Jones 1940, Raveh 2007, Medina et al. 2017, Zaide & Raveh 2006, KARAKAŞ 2020, Ghoreyshi et al. 2018). However, there is little quantitative research on the actuation speed of CC, neither in the time domain nor in the frequency domain. In order to compare the gust alleviation performance between CC and mechanical control surface, this research investigates the response of CC with step and sinusoidal inputs in various frequencies. In addition, the gust alleviation system requires a feedback loop to compensate for the unsteady loading, including sensors to detect the presence and profile of a vertical wind gust, and a control algorithm to regulate the actuator according to the instantaneous gust velocity. Existing research in terms of gust alleviation algorithms is generally based on mechanical control surfaces (Zaide & Raveh 2006, Regan & Jutte 2012, Fezans et al. 2019, Khalil & Fezans 2021). By combining the existing algorithms with a CC actuator, a closed-loop system will be developed in this research in order to demonstrate the effective reduction in gust loading.

## 1.1 Aims and Objectives

The aim of this research is to develop an improved understanding of the dynamic characteristics of CC and therefore to consider its feasibility as a means of improving the stability and

resilience of a UAV when encountering vertical wind gusts.

This aim is achieved by the following objectives:

1. Validation of a Computational Fluid Dynamics (CFD) methodology for predicting the steady and unsteady behaviour of CC with sufficient accuracy.
2. In 2D, investigate the time domain and frequency domain lift responses of CC and compare with a mechanical control surface to quantify potential improvements in the reaction time of CC.
3. Design a control algorithm based on the dynamic response of CC, and subsequently integrate this control algorithm within an unsteady 2D CFD simulation (as a user defined function), to demonstrate the feasibility of using CC for gust alleviation.
4. In 3D, design and evaluate a circulation controlled trailing-edge for a small datum aircraft, similar in size to a UAV, using steady CFD.
5. Investigate the dynamic behaviour of the CC aerofoil on the datum aircraft over a range of flow conditions (blowing coefficients, angles of attack, gust magnitude), using unsteady CFD.
6. Develop a control algorithm for the aircraft using CC to provide longitudinal stability when encountering continuous vertical gusts, and compare the gust alleviation performance with conventional control surfaces.

## 1.2 Contributions

The principal novel contributions of this research are:

1. The investigation of time and frequency domain characteristics of the CC lift response to step and sinusoidal changes in nozzle pressure (Objective 2 and 5). These results will allow improved controller design for flight manoeuvre and longitudinal stability using CC.
2. The feasibility of using CC as a vertical gust alleviation actuator for UAVs was established for the first time. The study has demonstrated that CC gives a significant improvement in actuation speed compared with conventional mechanical actuators, thereby giving a better bandwidth and control authority for gust alleviation (Objective 6).

3. A novel coupled system has been designed and implemented by integrating a closed-loop feedback controller within a high-fidelity unsteady CFD simulation to maintain steady lift when a vertical gust is encountered (Objective 3). A coupled simulation showed that the system could significantly reduce gust loading by automatically adjusting the plenum pressure according to the instantaneous results from the CFD solver.

### 1.3 Thesis Structure

The thesis contains the following chapters:

- **Chapter 2 Theory:** This chapter introduces the key fundamental aerodynamic theories relevant to the research, including the properties of fluids, an introduction to aerodynamic forces, boundary, wall jet flows (i.e. Coanda effect), aerodynamic derivatives and control theory.
- **Chapter 3 Literature Review:** This chapter presents previous research relevant to the present study, and outlines the key ideas and theories of CC.
- **Chapter 4 Methodology:** This chapter reviews the potential methodologies available and justifies the methods used in the current work, including the meshing techniques, CFD solver and turbulence models.
- **Chapter 5 Preliminary study of a 2D CC aerofoil:** This chapter describes how objectives 1 to 3 are satisfied. Before investigating complex 3D aircraft models and flight dynamics, it is more convenient to consider 2D aerofoil performance to evaluate the modelling approaches, particularly since there is a greater amount of existing data available for comparison.

Initially, a steady CFD study of a 2D CC aerofoil was made and compared with existing wind tunnel data to evaluate the methodology (Objective 1).

Secondly, the unsteady response of this aerofoil was evaluated for a sharp edge vertical gust and compared with literature using an analytical solution based on the Küssner function derived for a flat plate. The dynamic characteristics of CC were then investigated considering a sinusoidal plenum pressure using unsteady CFD simulations to determine the frequency response. The dynamic characteristics were then compared with existing experimental data for a conventional mechanical flap, in terms of the speed of actuation and fluidic response (Objective 2).

Finally, the dynamic response information was used to design a closed-loop feedback controller, which was coupled with CFD (as a user defined function), and successfully demonstrated its effectiveness at maintaining a constant lift in vertical wind gusts (Objective 3). The dynamics and control of an aircraft with CC, considering both lift and pitching moment, are discussed in the following chapters.

- **Chapter 6 Steady State Study of the Datum Aircraft:** This chapter describes how objective 4 was satisfied, by expanding the application of CC to the wing of a 3D datum aerobatic aircraft. A design for a modified CC trailing edge is described, and a series of steady 3D CFD simulations to analyse the flow field around the wing and obtain the aerodynamic derivatives for further simulations in Chapter 8.
- **Chapter 7 The Dynamic Performance of CC :** This chapter describes how objective 5 was satisfied, considering the effects of a wider range of parameters such as blowing coefficient, Mach number, and geometry on the dynamic response with comparisons with existing literature. The results are used to identify a model for the effector for further simulation with longitudinal motion.
- **Chapter 8 Application of the CC on Gust Alleviation:** This chapter describes how objective 6 was satisfied. Using the steady aerodynamic derivatives described in Chapter 6 and the unsteady results in Chapter 7, the aircraft flight performance is simulated and a controller is implemented to alleviate the unsteady loading due to vertical gusts.
- **Chapter 9 Conclusions and Future Work:**The final chapter presents concluding remarks and discusses the industrial and academic relevance of the research outputs.

In this research, both 2D and 3D simulations were used. Although every effort has been made to ensure a consistent approach, it is computationally expensive to use 3D simulation for dynamic performance due to the large number of iterations. Consequently, most of the transient CFD studies were conducted in 2D, as summarised in Table 1.1.

This research is based on unsteady simulations for both 2D and 3D geometries, and the final conclusion, including the dynamic characteristics and the relevant control algorithm, is primarily based on lift variation versus non-dimensional time. The concluded results are highly dependent on the accuracy of the simulation and therefore steady and unsteady validation is necessary. The initial validation is using the 2D generic aerofoils since they have extensive experimental, simulation, and analytical databases. Firstly, steady state validation using a 2D CC aerofoil compared with wind tunnel data has been conducted. This verifies the solver

Table 1.1: Summary of the simulation cases.

Simulation	Geometry	Dimension	Steady/unsteady	Valiation
Section 5.1 on page 124 Initial validation	GACC aerofoil	2D	steady+unsteady	✓
Section 5.2 on page 141: Dynamic response	GACC aerofoil	2D	unsteady	
Section 5.3 on page 151: Gust alleviation	GACC aerofoil	2D	unsteady	
Section 6.1 on page 160: Aircraft validation	wing, flap, fuselage	3D	steady	✓
Section 6.7.1 on page 194: Aircraft with CC	wing, CC, fuselage	3D	steady	
Chapter 7 on page 206: Dynamic response	NACA0013 with CC	2D	unsteady	
Chapter 8 on page 235: Aircraft motion, gust alleviation	Aircraft with CC	3D	unsteady	

settings and turbulence models. Subsequently, as unsteady validation databases are relatively rear, by the time of writing, in the existing literature, only 2D unsteady cases are available for validation. An aerofoil is therefore validated by an analytical time-domain result. This verifies the time step settings, solver settings and the implicit scheme. The subsequent results including the Dynamic response and Gust alleviation of the GACC aerofoil are based on the 2D steady and unsteady validations. The CC gust alleviation method is then expanded to 3D aircraft, where a 3D steady state validation using wind tunnel data has been conducted. The unsteady validation in 3D is not provided due to the lack of a usable database. The subsequent simulation results are all based on the validated 3D geometry and solver.

# Chapter 2:

## Theory

This chapter introduces the fundamental aerodynamic theories, flight dynamics and control theories relevant to this research. Firstly some basic flow properties are discussed. Based on these properties, the physics of primary aerodynamic forces is explained. Subsequently, some distinct flow structures are introduced, such as the boundary layer and the Coanda effect. Then the formulations for flight dynamics are provided. The formulations are used in Chapter 8 to establish a simulation of aircraft. Finally, the control algorithms used for closed-loop gust alleviation are introduced. The purpose of this chapter is to give an overview of the fundamental knowledge necessary for this research.

### 2.1 Flow characteristics

The real flows in aerospace engineering have complex flow structures and a variety of physical properties interacting with each other. To study the flow characteristics of aerodynamic bodies, it is not always necessary or practical to precisely model every detail of the flow. By making some assumptions and neglecting less significant properties, a complex flow field can be simplified. For example, a flow around an aerofoil can be treated as two regions, a thin layer adjacent to the solid wall and an external region. The flow adjacent to a wall is affected by the shear forces due to friction between the air and the solid surface, which forms the so-called boundary layer. However, such effects can be largely neglected in the external region away from the wall. Using different flow models in each region can reduce the complexity when analysing aerodynamics. This section introduces several assumptions and characteristics for typical types of flow.

Before introducing the flow characteristics, two similarity parameters need to be introduced, the Reynolds number ( $Re$ ) and Mach number ( $M$ ). These parameters govern the properties of different types of flow. The Reynolds number  $Re = \rho_{\infty} V_{\infty} c / \mu_{\infty}$  gives the ratio of inertia force to viscous force, where  $\rho_{\infty}$  is the freestream density,  $V_{\infty}$  is the freestream velocity,  $c$  is a reference length, which is taken to be the chord length for an aerofoil, and  $\mu_{\infty}$  is the freestream viscosity coefficient. For a high Reynolds number, the inertia forces dominate, where the turbulent flow is expected to occur. On the contrary, if viscous forces are dominant,

the flow turns to be laminar. Reynolds number has a strong influence on the flow, such as the boundary layer properties and flow separation characteristics, and is discussed in detail in Section 2.3.3 on page 23. Whereas the Mach number  $M = V_\infty/a_\infty$  is the ratio of velocity to the speed of sound, where  $a_\infty$  denotes the freestream speed of sound. Mach number governs the compressibility effects of the flow, which influences aerodynamic forces and gas physics. Most civil transport aircraft cruise at transonic speeds ( $0.6 < M < 0.9$ ) at which the flow can be considered compressible and shock waves can be created, which are characterised by an abrupt change in pressure, temperature, and density, which creates a significant wave drag component. However, civil UAVs normally fly at subsonic conditions ( $M < 0.3$ ) so the subsequent chapters only consider an incompressible flow. However, flow in the CC nozzle and jet is at a higher Mach number, and is discussed in section 4.2.3 on page 102.

The majority of flows in aerospace engineering can be categorised by the following characteristics, steady or unsteady, turbulent or laminar, viscous or inviscid, rotational or irrotational, and compressible or incompressible. The purpose of this section is to describe and contrast these types.

### **2.1.1 Steady / unsteady flow**

A steady flow is a flow field where all the variables, such as velocity, pressure, temperature and density, are invariant with time. In contrast, the variables at any point in an unsteady flow are changing with time. This research considers both steady and quasi-unsteady flow. In Chapters 5 and 6, the validation of CFD simulations for CC was conducted to match the steady experimental conditions and consequently the variables are assumed to remain constant over time. Wind gusts generally exhibit continuous and random velocity distributions in all directions. However, the aerodynamic and structural response of aircraft is often assessed for a discrete single function such as “one minus cosine” velocity distribution, and in a 2D plane, since the vertical gust loading is the most significant for structural design. Consequently, this research considers discrete longitudinal gust profiles and as such, the quasi-unsteady flow (Ghoreyshi et al. 2018). Examples can be found in Section 5.2 on page 141 and Chapter 7 on page 206.

### **2.1.2 Turbulent / Laminar flow**

Turbulent flow is a flow state in which fluid elements have a chaotic and irregular motion (Blazek 2005b). In contrast, the fluid elements in a laminar flow move smoothly along the streamlines. The transported quantities (e.g. mass and momentum) in a turbulent flow fluctuate in time and space. However, aerodynamic analysis of forces and flow structures can often be

restricted to the mean flow where the fluctuation details in a turbulent flow are insignificant. The approach of using time-averaged flow simulations that require the use of a semi-empirical model to represent the turbulent fluctuations is introduced in Section 4.2.4 on page 109.

Turbulence can be treated as a combination of a mean component and a fluctuating component. A parameter used to quantitatively describe turbulence is turbulent intensity ( $TI$ ), which is defined as the ratio of the root-mean-square of the velocity fluctuations to the mean velocity.

$$TI = \frac{\sqrt{u'(t)^2}}{\bar{u}} \quad (2.1)$$

where,  $u'(t)$  is the velocity fluctuation and  $\bar{u}$  is the mean velocity. The velocity fluctuation is defined as the instantaneous velocity  $u(t)$  without the mean component,

$$u'(t) = u(t) - \bar{u} \quad (2.2)$$

### 2.1.3 Viscous / inviscid flow

The real flows have a transport phenomenon that flow molecules can transfer the mass, momentum and energy to other regions of the flow field. This transport effect causes mass diffusion, friction, and thermal conduction. Such flows are viscous flows. By contrast, a flow without any mass diffusion, friction and thermal conduction is referred to as an inviscid flow. The flows with high Reynolds number can generally be assumed as inviscid flow, except for a thin layer that forms adjacent to a solid wall and into the wake, where viscosity has a dominant effect. These layers are defined as boundary and free-shear layers respectively. Reynolds number has a significant effect on the growth and stability of these layers. The mechanism of boundary-layer separation, where the boundary layer is no longer attached to the wall, is discussed in Section 2.3.2 on page 21. Inviscid theory can predict valid pressure distributions and lift for an aerofoil at low AoA (Angle of attack, the angle between the chord line and the incoming flow) reasonably well. However, the inviscid theory is unable to predict drag accurately as skin friction is one of the main sources of drag and is created due to the presence of viscosity. In the presented research, the CCW using jet blowing involves strong viscous effects, and the lift of the wing is greatly affected by the separation point of the jet flow, which is dominated by viscosity. Consequently, it is necessary for this research to include viscous effects.

### 2.1.4 Rotational / irrotational flow

In a rotational flow, the angular velocity of fluid elements is finite. In contrast, fluid elements would have zero angular velocity at every point in an irrotational flow. In an irrotational flow, there exists a scalar function of the spatial coordinates called the velocity potential, that the velocity of any point in the flow is simply the gradient of the velocity potential. The concept of an irrotational flow is therefore useful in potential flow theory that allows a complex flow field to be simulated by combining elementary flow patterns. In comparison, rotational flows, such as those found in turbulent and viscous regions, are more complex to simulate but necessary for most practical problems. The flow is highly rotational within the boundary layer where the viscous effect exists. The velocity gradient in the boundary layer and turbulence (at a high Reynolds number) exert rotational moments on a fluid element therefore producing rotational flow. In summary, viscous flows are always rotational, whereas inviscid flows can be either irrotational or rotational. If there is no viscosity, the irrotational flow will remain irrotational, and rotational will remain rotational (Anderson Jr 2016).

The rotational / irrotational flow are defined by vorticity  $\xi$ , which is given by (Anderson Jr 2016)

$$\xi = \left( \frac{\partial w}{\partial y} - \frac{\partial v}{\partial z} \right) \mathbf{i} + \left( \frac{\partial u}{\partial z} - \frac{\partial w}{\partial x} \right) \mathbf{j} + \left( \frac{\partial v}{\partial x} - \frac{\partial u}{\partial y} \right) \mathbf{k} = \nabla \times \mathbf{V} \quad (2.3)$$

where  $u, v, w$  are the velocity components in  $x, y, z$  direction. Also,  $\xi$  can be expressed by the curl of velocity  $\nabla \times \mathbf{V}$ , where  $\mathbf{V} = u\mathbf{i} + v\mathbf{j} + w\mathbf{k}$ , and  $\nabla = \mathbf{i}\frac{\partial}{\partial x} + \mathbf{j}\frac{\partial}{\partial y} + \mathbf{k}\frac{\partial}{\partial z}$ . For a rotational flow,  $\xi \neq 0$  at any point in the flow. On the contrary, if  $\xi = 0$  at any point, the flow is irrotational. In the present research, the flow domain is treated as rotational to capture the viscous flows in the boundary layer, Coanda jet and tip vortices. Vorticity is also used to analyse the unsteady vortices found in the flow field of the 3D CCW shown in Figure 6.16 on page 176.

If the flow is irrotational, inviscid, incompressible, and the aerofoil is thin, the flow is simplified so that analytical methods are available. In the 1920s and 1930s, researchers have developed the classical theory of unsteady aerodynamics (Wagner 1924, Küssner 1936, von Karman & Sears 1938, Gülçat 2010). The main concept is using a vortex sheet to represent the aerofoil and the wake ( assuming the wake is flat ). Wagner has solved the lift response to a step change of AoA (Wagner 1924). Based on the same theory, Theodorsen solved the frequency response problem for an aerofoil in sinusoidal oscillation (Theodorsen & Mutchler 1935). Theodorsen also introduced a classification of lift: the circulatory and non-circulatory components. The former is due to circulation and the latter is caused by the acceleration of the surrounding fluid when the aerofoil is rotating. The non-circulatory component acts

as a resistance force to the aerofoil; it also contributes to the hinge moment of a plain flap when it suddenly deflects (Medina et al. 2017). In 1936, Küssner developed the theory for a sharp-edge gust encounter problem (Küssner 1936). In 1938, their theories were improved by von Karman and Sears (von Karman & Sears 1938), who provided a more general method to calculate the transient lift. Their theories are widely used for analysing the flight mechanics and controller design (Gülçat 2010), whereas unsteady CFD simulations usually use analytical results for validation and obtain good agreement (Zaide & Raveh 2006, Raveh 2007, Zhou et al. 2017, Ghoreyshi et al. 2018, Li & Qin 2020). Currently, no analytical method based on potential flow is available for unsteady CC, although McGowan et al. (McGowan et al. 2004) have provided a Thin-Airfoil Thin-Jet Theory, it is only for steady state. The strong shear layers, separation and the curved wake, are additional difficulties for analytical studies (Friedman et al. 2007).

### **2.1.5 Compressible / incompressible flow**

In a compressible flow, the density of the fluid is a variable, whereas in a flow where the density is constant is incompressible. In nature, all the flows are to some extent compressible. Nevertheless, there are still a number of flows where compressibility is insignificant. For example, aerodynamic flows at a low Mach number are usually considered incompressible. When  $M < 0.32$ , the air density deviates by less than 5 % (Anderson Jr 2016), thus can be treated as incompressible with acceptable accuracy. Conversely, density changes by more than 5% when  $M > 0.32$ , and compressibility increasingly needs to be considered. Generally, the flow problems when  $M < 0.3$  are assumed as incompressible flow. Most of the flow simulations in this research are incompressible, except in the region of the jet flow for CC, where the local velocity can exceed Mach 0.3 at high plenum pressures.

The vast majority of real flows in nature are unsteady, viscous, compressible and rotational, whilst turbulence exists everywhere in nature. A truly inviscid, incompressible and irrotational flow doesn't exist in the real world. The purpose of defining these idealized flows is to reduce the mathematical complexity and enable a flow to be simulated. With appropriate assumptions, using idealized flow models can give valid flow patterns and resultant lift forces. However, the flow problems considered in this research include complex physics with high velocity jets, boundary layers, and separations that are highly dependent on viscous and rotational effects, whilst the dynamic response of the flow is also of significant interest. Consequently, most of the problems in this research used unsteady, viscous, incompressible and rotational flow theories. In the simulation of the flow problems, the flow is assumed to be

fully turbulent if Reynolds-averaged Navier–Stokes ( RANS ) model is used, this is discussed in detail in Chapter 4 on page 89.

## 2.2 Aerodynamic forces

This section explains the primary forces and moments that allow an aircraft to fly. The background of this research is to study a UAV in cruise, which is mainly straight and level flight and investigating the effect of vertical gust. This means most of the motion is in the vertical plane thus only longitudinal motion is investigated here. Figure 2.1 shows the forces acting on the aircraft for straight and level flight. The aircraft is in an equilibrium state where the lift equals weight, and the thrust equals drag. Lift is an aerodynamic force perpendicular to the flight path, primarily generated by the wing and acts upward. While drag is generated by surface friction of any parts exposed to the flow and pressure distribution over the surface. Weight is the total load of the aircraft itself and acts downward due to gravity. Thrust is the forward force produced by the engine and overcomes drag. However, the lift and weight, thrust and drag generally do not act through the same point, so a pitching moment is created. The pitching moment is balanced by the horizontal stabilizer, which provides longitudinal stability and control.

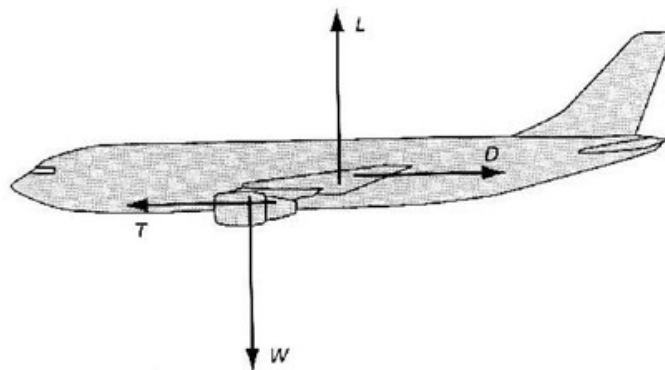


Figure 2.1: The forces acting on an aircraft (Barnard & Philpott 2010).

The forces and moment exerted on an aerodynamic body are the integration result of pressure and shear stress applied on its surface. The derivation of these forces and moments is based on some fundamental principles.

1. Conservation of mass - Mass cannot be created nor destroyed.
2. Newton's second law - The force on an object equals the mass multiplied by the acceleration.

3. Conservation of energy - Energy cannot be created nor destroyed; it can only change form.

From these fundamental principles, the generation of primary forces and moments acting on the aircraft is explained here.

### 2.2.1 Lift generation

Lift is the component of a resultant aerodynamic force perpendicular to the direction of freestream flow. The aerodynamic force can be determined by integrating the surface pressure and shear stress distribution around the aerofoil. Figure 2.2 shows a schematic of the flow pattern over an aerofoil. On the upper surface of the aerofoil, due to the pressure difference between the ambient pressure and the pressure at the wall, the flow follows the curvature of the surface, as long as the viscosity does not induce separation (the flow separation is described in the next section). The shape of the aerofoil turns the flow downward, and according to Newton's second law, this vertical acceleration of the flow imparts a vertical lift force (i.e. upwards) acting on the aerofoil.

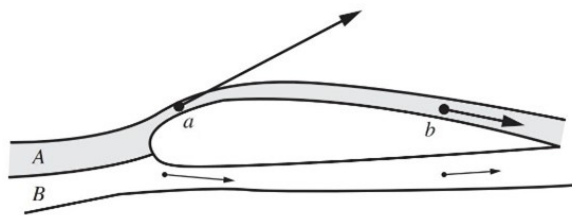


Figure 2.2: The flow pattern over an aerofoil (Anderson & Bowden 2005)

The max deviation of the mean camber line ( the locus of the halfway point between the upper surface and the lower surface ) and the chord line ( the straight line connecting the leading edge and trailing edge ) is called the camber of the aerofoil. The relation between camber and lift can be explained by Figure 2.3 , which shows a cambered thin plate at zero AoA. A positive camber results in a positive lift coefficient because a cambered aerofoil increases the ability of turning air downward, and results in curved streamlines around the aerofoil and increased circulation and lift, causes a lower pressure on the upper surface (Babinsky 2003). The low pressure over the upper surface and the higher pressure at the lower surface result in a vertical force normal to the free stream flow direction, which is the lift. Similarly, a hinged flap that is deflected downward increases the camber of the aerofoil, as well as the AoA of the equivalent chord line ( the virtual line that connects the leading edge and the trailing edge of the deflected flap ). As a result, the lift is increased (Anderson & Bowden 2005).

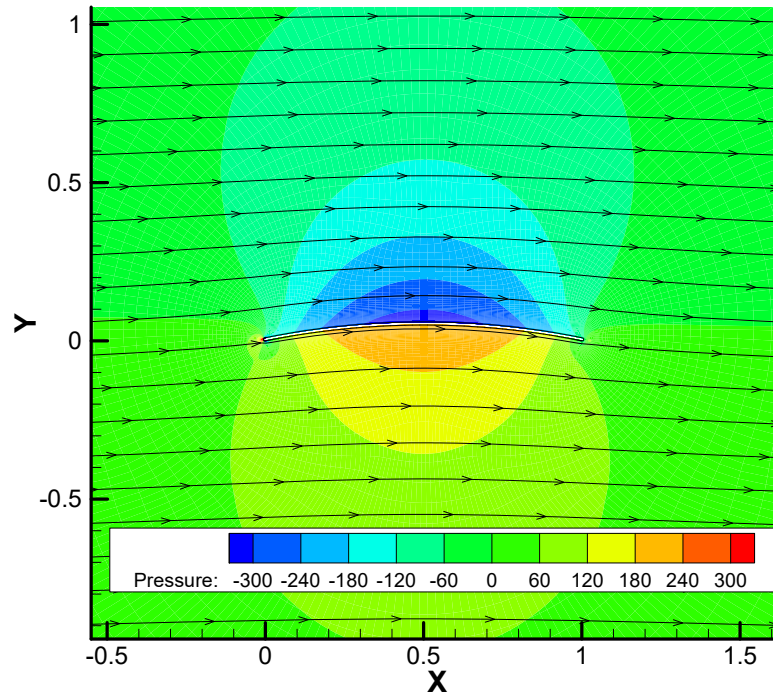


Figure 2.3: The streamlines around a curved thin plate.

In conclusion, the shape of the aerofoil, including its camber and AoA, results in a deflection and acceleration of the incoming flow that results in a non-uniform pressure distribution around the aerofoil. The pressure over the upper surface is lower than that on the lower surface. Consequently, the net imbalance of the pressure distribution around the aerofoil provides a means of quantifying the lift force generated (Anderson & Bowden 2005).

### 2.2.2 Circulation

A widely used variable to analyse the lift is circulation, introduced by Frederick Lanchester (CRAeS 2014), Wilhelm Kutta, and Nikolai Joukowski (Anderson & Bowden 2005). The circulation along a closed curve  $C$  is given by Equation 2.4,

$$\Gamma = - \oint_C \mathbf{V} \cdot d\mathbf{s} \quad (2.4)$$

where  $\mathbf{V}$  is the local velocity on the closed curve,  $d\mathbf{s}$  is the line segment. The circulation  $\Gamma$  refers to the line integral along this closed curve, displayed in Figure 2.4 . If the curve encloses an aerofoil, the circulation can be used to calculate lift, according to the Kutta-Joukowski theorem, given by Equation 2.5.

$$L' = \rho_{\infty} V_{\infty} \Gamma \quad (2.5)$$

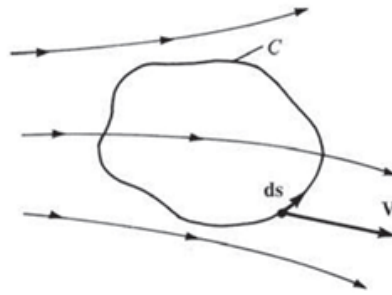


Figure 2.4: The circulation of an enclosed area in the flow field(Anderson & Bowden 2005).

where  $L'$  is the lift per unit span,  $\rho_\infty$  is the free stream air density and  $V_\infty$  is the free stream velocity.

Considering the circulation around the aerofoil, with the same geometry, the same AoA and the same freestream velocity, there are infinite flow solutions, corresponding to various circulation values. In irrotational flow, the circulation around an aerofoil is zero which, for a non-symmetrical aerofoil, results in the rear stagnation point not being at the trailing edge (i.e. the Kutta condition is not satisfied), as shown in Figure 2.5. While in an actual (rotational and incompressible) flow, the circulation around an aerofoil is such that the flow smoothly leaves a sharp trailing edge, which is the Kutta condition. Therefore this condition gives a particular solution for the circulation of the flow at a given AoA. It also gives the corresponding pressure distribution around the aerofoil, and lift produced by integrating this pressure distribution.

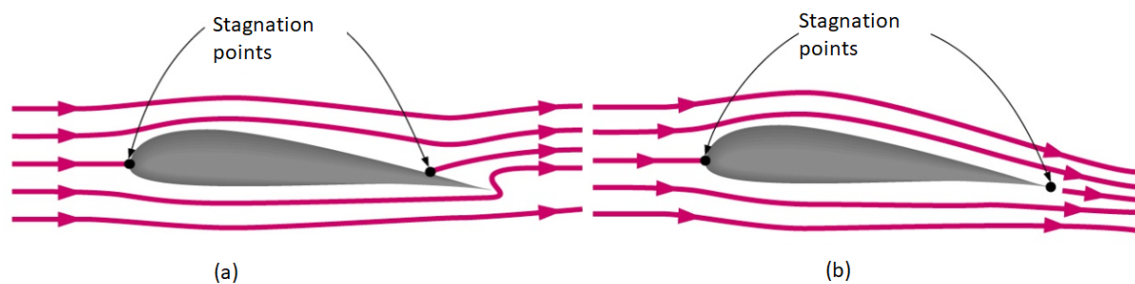


Figure 2.5: The flow past around an asymmetrical aerofoil, (a) Irrotational flow, (b)Actual flow.(Shires 2016)

The viscosity of a flow is one of the reasons that an aerofoil generates lift. In fact, in real flow, the friction between flow and surface ensures that the flow leaves the trailing edge smoothly to satisfy the Kutta condition (Anderson & Bowden 2005). Moreover, inviscid flow is not suitable for the present research of CC, since viscosity has a great influence on the separation position of the Coanda jet. Furthermore, the trailing edge of a CC aerofoil is not sharp, and the rear stagnation point is at the separation point of the jet. Hence a RANS solver

that assumes viscous and rotational flow is used.

### 2.2.3 Drag

Drag is defined as the component of a resultant aerodynamic force parallel to the direction of freestream flow. For a 2D aerofoil, there are two types of drag. The skin-friction drag due to the shear stress acting on the solid boundary, and the pressure drag due to the pressure variation created by the presence of the aerofoil and its boundary layer. The sum of skin-friction drag and pressure drag yields the profile drag of an aerofoil. While for a 3D finite wing, the induced drag is generated due to the downwash effect caused by the tip vortex.

Similar to a conventional aerofoil, the drag of a CC aerofoil also consists of pressure drag and friction drag. The difference is, there is a separation zone on the rear of the trailing edge, induced by the jet separation. Additionally, the jet produces low pressure acting on the circular trailing edge, and such low pressure results in an additional drag force compared with a conventional aerofoil. The separation zone and jet properties are shown in Figure 2.13 on page 28.

Considering the drag of a complete aircraft, the drag components are more complicated. The total drag is usually higher than the sum of the drag from each component due to the interaction between different flows. For example, the junction region between the wing and fuselage where vortices can form, creates additional drag. The extra drag is defined as interference drag. Meanwhile, except for the wing, a real aircraft has other parts exposed in the airflow that create parasitic drag. Parasitic drag is usually used to describe the drag caused by components that do not directly contribute to lift generation. Examples include undercarriage, engine nacelles, and excrescence on the aircraft, such as small gaps or steps on the surface. Typically the total drag of an aircraft can be synthesised by adding these components (i.e. profile, induced, parasitic) for each part of the aircraft, in addition to interference drag. In this study, a 3D aircraft with wing and fuselage was investigated in Chapter 6 on page 156. The profile drag, induced drag and interference drag of the wing-body junction are considered.

### 2.2.4 Pitching moment

The aerodynamic moment acting on an aerofoil can be used to analyse the flight mechanics of an aircraft. The moment acting on the pitch axis is defined as the pitching moment, it is balanced by the horizontal stabilizer and affects the longitudinal stability of the aircraft. The ailerons, flaps and flow control devices on an aerofoil strongly affect the pitching moment.

A pitching moment about an arbitrary point can be obtained by integrating the pressure

and shear stress distribution. The moments that tend to increase AoA are positive, and those that tend to reduce AoA are negative. As ailerons, flaps and flow control devices are usually located at the trailing edge of the aerofoil, they typically produce a negative pitching moment on the aerofoil when increasing lift. The deployment of these devices also has a great influence on the horizontal stabilizer as they tend to increase the downwash effect over the tail.

The distributed loading on an aerofoil is equivalent to a resultant force acting on a specified point, about which the aerodynamic moment is zero. This point is the centre of pressure. The location of the centre of pressure varies with different AoA and velocity. A more convenient method to analyse the pitching moment is to use the aerodynamic centre, it is the point on an aerofoil where the pitching moment is independent of AoA. The aerodynamic centre is approximately located at the quarter-chord of a thin symmetric aerofoil. For other asymmetric aerofoils, the aerodynamic centre is also very close to the quarter-chord.

By convention, the lift, drag and moment are usually used as non-dimensional coefficients. These coefficients are calculated as the force / moment divided by dynamic pressure and reference area, defined by the following equations:

Dynamic pressure:

$$q_{\infty} = \frac{1}{2} \rho_{\infty} V_{\infty}^2 \quad (2.6)$$

Lift coefficient:

$$C_L = \frac{L}{q_{\infty} S} \quad (2.7)$$

Drag coefficient:

$$C_D = \frac{D}{q_{\infty} S} \quad (2.8)$$

Moment coefficient:

$$C_M = \frac{M}{q_{\infty} S l} \quad (2.9)$$

where  $\rho$  is the density,  $V$  is the freestream velocity,  $q$  is the dynamics pressure,  $S$  is the reference area,  $l$  is the reference length which is the aerofoil chord,  $L/D/M$  denotes the lift, drag force and pitch moment,  $\infty$  denotes the freestream condition.

## 2.3 Boundary layer

Consider a flow over a flat plate, the boundary layer is a thin layer of flow adjacent to the wall and affected by friction. The flow at the bottom of the boundary layer has a zero velocity according to the no-slip condition, as shown in Figure 2.6 . In the direction normal to the surface, the velocity gradually increases from the interface to the external undisturbed flow, at which point it equals the freestream velocity.

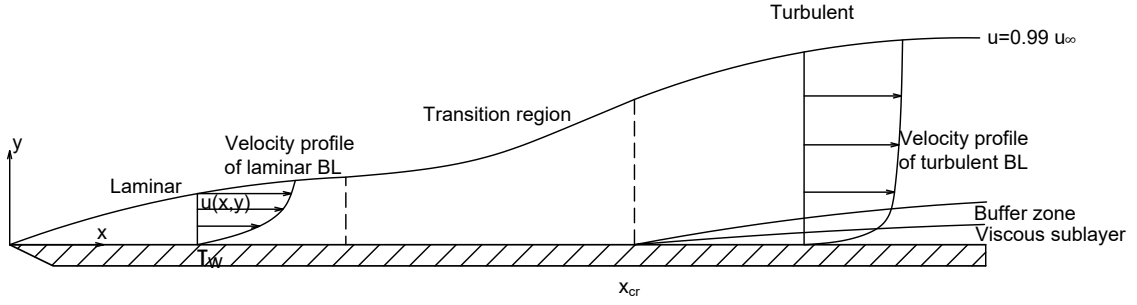


Figure 2.6: The development of boundary layer on a flat plate (Anderson Jr 2016).

The velocity gradient at the wall ( $y = 0$ ) is generally high and produces a shear stress on the wall given by:

$$\tau_w = \mu \left( \frac{\partial u}{\partial y} \right)_{y=0} \quad (2.10)$$

where  $\tau_w$  is the wall shear stress,  $\mu$  is the dynamic viscosity of air,  $\frac{\partial u}{\partial y}$  is the velocity gradient at the wall. The thickness of the boundary layer is defined as the distance to the wall where the local velocity ( $u$ ) equals 99% of the free stream velocity ( $u_\infty$ ). Figure 2.6 shows the development of a boundary layer on a flat plate. Note the shape of the boundary layer, including the buffer zone and viscous sublayer, is exaggerated and does not reflect the real shape.

The thickness of the boundary layer is a function of Reynolds number, distance from the leading edge and other factors. To solve the velocity profile for various conditions, it is useful to define a dimensionless distance normal to the wall, which scales with the thickness of the boundary layer. The following equations give the dimensionless wall distance  $y^+$  and the dimensionless velocity  $u^+$ .

$$y^+ = \frac{\rho y u_\tau}{\mu} \quad (2.11)$$

$$u^+ = \frac{u}{u_\tau} \quad (2.12)$$

where  $u_\tau = \sqrt{\tau_w / \rho}$  is the friction velocity,  $u$  is the local velocity,  $y$  is the distance normal to the wall,  $\mu$  is the dynamic viscosity of air.

The relation between  $y^+$  and  $u^+$  gives a relatively consistent shape of the fully developed boundary layer, this shape is approximately independent of flow parameters such as Reynolds number, density, boundary layer thickness etc. Figure 2.7 shows an example from an LES (Large-eddy simulations) result of the velocity profile from four different locations on a CC aerofoil. The near wall region ( $y^+ < 5$ ) of the profile, known as the viscous sublayer is approximately a linear distribution, where the turbulent fluctuations are damped and the shear stress in this region is approximately constant. While the outer region ( $y^+ > 30$ ) can be fitted by a

logarithmic curve, known as the log-law region. In the region that  $5 < y^+ < 30$ , the profile gradually transitions from the viscous sublayer to the log-law region, and is known as the buffer layer. The velocity profile in the viscous sublayer is generally similar at different locations, but profiles in the buffer layer and the log-law region vary with different locations.

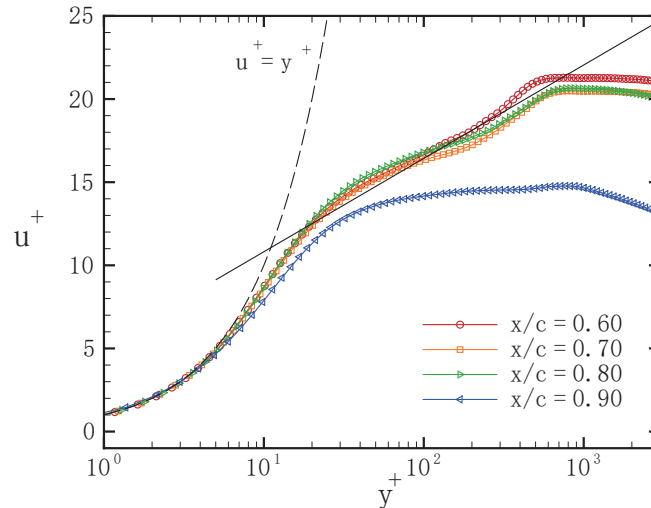


Figure 2.7: The velocity profile with the linear region and log-law region (Nishino et al. 2010).

The properties of the boundary layer profile strongly affect its growth and stability as well as the skin friction at the wall. Therefore selecting a suitable turbulence model is essential to ensure that these layers are correctly modelled for the types of flows considered in this research. Also, it is essential to ensure that the mesh is sufficient to resolve this profile and that the  $y^+$  of the first layer near the wall is small enough so that the velocity gradients can be resolved correctly at the wall. This is discussed further in Section 4.2.5 on page 115.

### 2.3.1 Boundary layer transition

When a flow initially attaches to a solid body, and a boundary layer begins to grow, it is initially a laminar flow. As the Reynolds number increases along the flow direction, the boundary layer can become unstable and develop into a transitional region where small disturbances begin to grow. Finally, the boundary layer grows to a fully turbulent flow at the critical position  $x_{cr}$  ( Figure 2.6 ). The thickness of the boundary layer grows from its attachment point and thickens more rapidly in the turbulent region as the turbulent boundary layer has a strong mixing effect. Several factors influence the transition from laminar flow to turbulent flow, including surface roughness, freestream turbulence level and adverse pressure gradient. For example, in some wind tunnel tests, transition strips are placed on the surface of a wing to induce transition at a desired point to mimic the transition position expected at full-scale flight

conditions and a higher Reynolds number.

The shape of the velocity profile of a laminar boundary layer is different from the turbulent boundary layer, as shown in Figure 2.6 on page 19. The wall velocity gradient of a turbulent profile is larger than for a laminar profile. This is because the turbulence flow has a strong mixing effect, and high energy flow in the outer part of the boundary layer is mixed with the low energy flow near the surface, increasing the energy in the boundary layer. As a result, the turbulent boundary layer is more resistant to separation. Meanwhile, the skin friction is higher than the laminar boundary layer because the velocity gradient of the turbulent boundary layer adjacent to the wall is greater.

### 2.3.2 Boundary layer separation

Boundary layer separation is a phenomenon that occurs when an attached boundary layer separates from a surface, creating a detached shear layer that typically bounds a region of recirculating flow downstream of the separation point. Its occurrence is strongly related to local pressure gradients. A favourable pressure gradient, where the pressure decreases in the flow direction, will accelerate the primary flow and boundary layer. Even though the near-wall flow is retarded by friction, it can still maintain a positive velocity due to the pressure distribution, thus the boundary layer is stable. In contrast, an adverse pressure gradient, where the pressure increases in the flow direction, will tend to retard the boundary layer flow and eventually contribute to its separation. Due to the friction, the flow within the boundary layer is already slower and has less momentum than the external flow, and it is further decelerated by the adverse pressure gradient. Finally, the velocity gradient at the wall is reduced to zero at which point it separates. Figure 2.8 shows the development of the velocity profile in an adverse pressure gradient ( $p_1 < p_2 < p_3$ ). The flow at  $S_1$  is a regular attached velocity profile where the pressure gradient is zero. At  $S_2$  and  $S_3$ , the adverse pressure gradient gradually increases, the near-wall flow slows down to rest at  $S_2$  (marking the onset of separation) and reversed flow occurs at the wall at  $S_3$ . At  $S_2$ , the normal velocity gradient is zero, thus the wall shear stress ( $\tau_w$ ) is also zero, which is considered as the separation point. However, for a turbulent boundary layer, the flow fluctuates at the separation region, and its location is not necessarily fixed. The separation point is defined as the location where the mean wall shear stress ( $\overline{\tau_w}$ ) is zero.

At high AoA, the flow around an aerofoil is greatly deflected downward, creating a strong suction peak on the upper surface near the leading edge that leads to a severe adverse pressure gradient over the rear portion of the aerofoil. If this pressure recovery is too high, it will

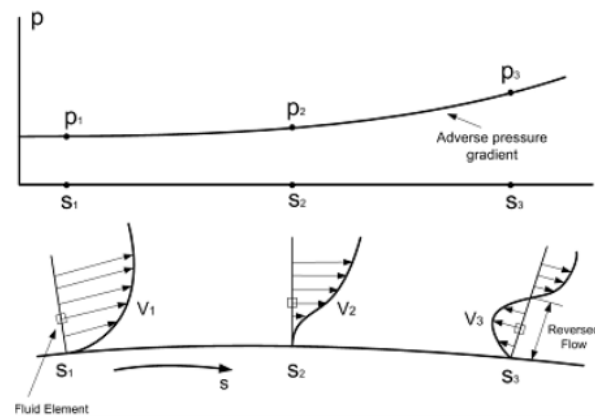


Figure 2.8: Flow development in adverse pressure gradient. (Shires 2016)

eventually lead to boundary layer separation, as shown in Figure 2.9

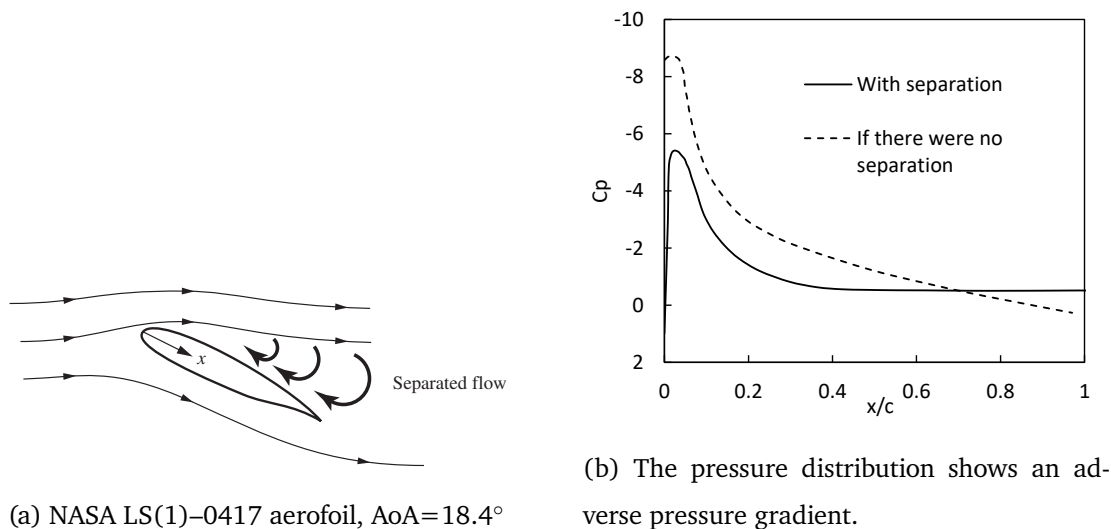


Figure 2.9: The pressure distribution on the upper surface of an aerofoil at high AoA (Anderson & Bowden 2005)

The separated flow over the top surface of the aerofoil is actually equivalent to a much thicker aerodynamic shape, and the flow pattern over the aerofoil is dramatically changed. Due to the separation, the suction near the leading edge is weaker than for the attached flow, which coupled with the higher pressure associated with the low momentum flow in the separated region, results in a reduction in lift. It can be seen in Figure 2.9, the surface pressure coefficient of the separated flow is approaching zero between  $0.4 > x/c > 1.0$ , and it remains constant after the separation point. Also considering the resultant force in the axial axis, a lower suction acting near the leading edge (towards the left) creates less thrust and therefore a higher pressure drag. In the separation region, the wall shear stress is relatively small compared with the attached flow since the velocity gradient at the wall ( $du/dy$ ) approaches zero and

thus creates less friction drag. Although an aerofoil with a separated flow has less friction drag, the pressure drag is dramatically increased due to the increased momentum losses in the wake. Consequently, the overall drag of a separated flow is larger than an attached flow.

### 2.3.3 Effect of Reynolds number

The boundary layer properties and therefore separation location are very dependent on the local Reynolds number. A CC aerofoil generally requires a relatively thick semi-cylinder trailing edge shape, which is likely to promote flow separation without blowing. An example of such aerofoil has been studied by Englar et al. under various Reynolds number conditions. Figure 2.10 shows the effect of chord Reynolds number on the lift and drag coefficients of a CC aerofoil with no blowing, zero AoA. The non-linear behaviour of lift and drag is observed at a lower Reynolds number. Whilst at  $Re > 0.57 \times 10^6$ , the  $C_L$  remains linear, and  $C_D$  remains constant. The  $C_D$  has a significant drop in drag at a higher Reynolds number. This can be explained by the flow separation of a bluff body with round corners. Since the boundary layer is developed to turbulent flow at a higher Reynolds number ( $Re > 10^5$ ), a turbulent boundary layer is more resistant to separation so that the wake is smaller, producing less pressure drag.

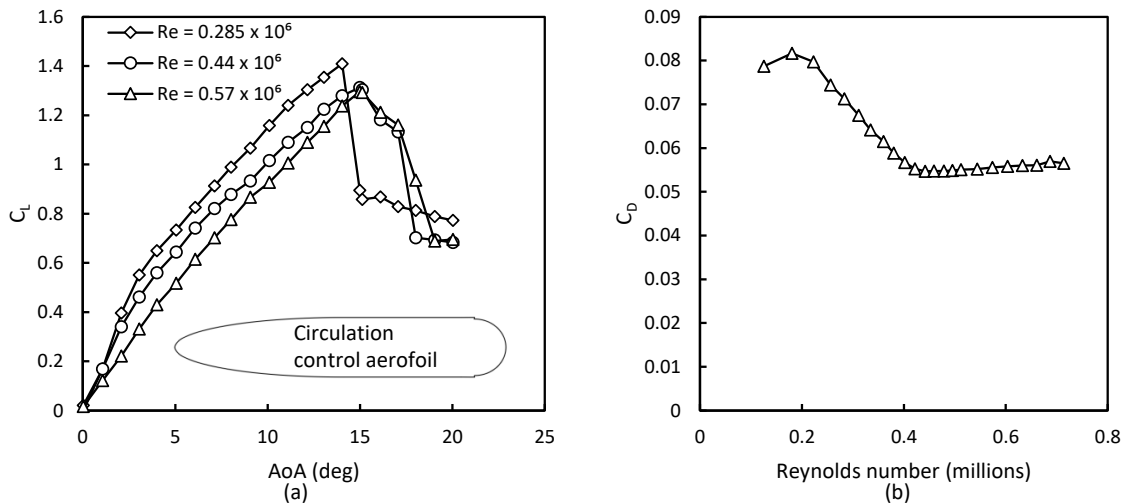


Figure 2.10: Lift and drag variation with Reynolds number in unblown condition (ENGLAR et al. 2009)

The chord Reynolds number used in this research ranges from 0.5 million to 3 million, but most results were conducted at 1 million. The nonlinearity of  $C_L$  and  $C_D$  is not expected in this range of  $Re$ . The boundary layer is expected to be mostly turbulent except at the region close to the leading edge, where a favourable pressure gradient exists. According to the study conducted by Nishino et al., at  $Re = 0.49 \times 10^6$ , the transition occurs approximately

at  $x/c=0.1$  on the upper side of the aerofoil (Nishino et al. 2010). Whereas on the lower side, the transitional region remains up to  $x/c=0.4$  before developing to fully turbulent flow. The boundary layer properties in various Reynolds numbers have a great influence on the selection of turbulent models, this is discussed in Chapter 4 on page 89.

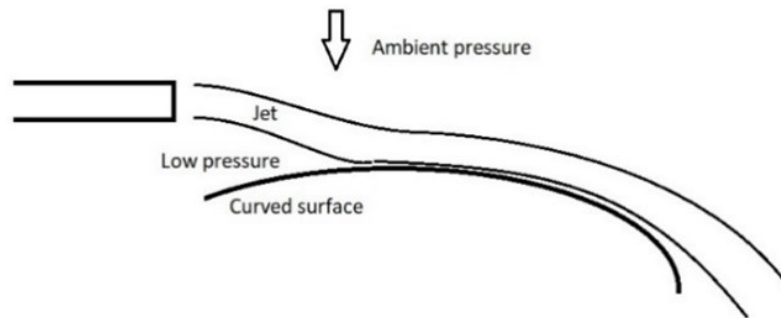
## 2.4 Wall Jet Flow and Coanda Effect

The Coanda effect is named after a Romanian inventor Henri Coanda (Wille & Fernholz 1965, Reba 1966, Trancossi 2011). It occurs when a jet of fluid flows over an adjacent curved surface or a flat plate, and it is observed to bend to follow the surface shape of the curved solid boundary, as shown in Figure 2.11(a). Meanwhile, the jet entrains the surrounding fluid into the stream. In the region adjacent to a surface, there is not enough fluid to supply the low-pressure region due to the presence of the wall, consequently, the pressure is lower than the ambient pressure. However, on the other side of the jet, which is open to the surrounding, there is enough fluid to supply those removed by the entrainment of the primary jet. Therefore the pressure on the open side is higher than the other side adjacent to a surface. This pressure difference is the reason that there is a deflection of the primary jet to follow the surface contour.

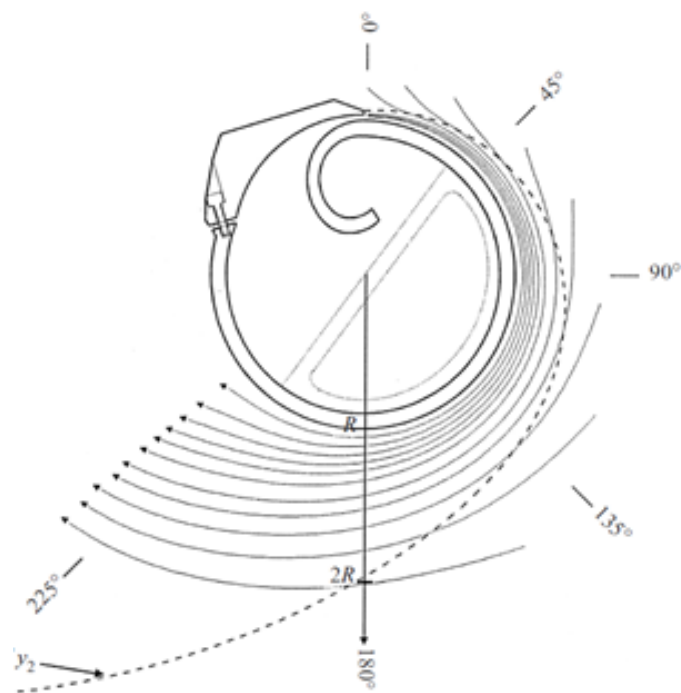
Figure 2.11(b) is an experimental rig designed by Neuendorf et al. (Neuendorf & Wygnanski 1999) to study the development of the boundary layer and shear layer on a curved wall jet flow. The figure shows a cross-section of a cylinder with a tangential jet slot on the top (marked as  $0^\circ$ ). Inside the cylinder, the compressed air is supplied to create a high-speed jet sheet discharging from the slot nozzle. The streamlines show how the Coanda jet stay attached to the circular surface, where  $y_2$  is equal to  $1/2$  of the maximum velocity magnitude in the jet  $U_{max}$ . The  $y_2$  curve shows that the Coanda jet thickens rapidly after leaving the nozzle by entraining ambient air. Only a small portion of the streamlines adjacent to the surface originally come from the nozzle, since the outer part of the jet flow is entrained from the surrounding area. The entrainment is a result of turbulent shear stress at the shear layer between the primary flow (Coanda jet) and the secondary flow (induced flow from the surrounding). This effect transfers a part of the momentum from the primary flow to the secondary flow, and decelerates the jet simultaneously. (Schlichting & Gersten 2003). Neuendorf's experimental rig reveals how rapidly the Coanda jet thickens by inducing the ambient air, and significantly influences the development of the boundary layer next to the curved wall and the shear layer on the other side of the jet. Such flow is different compared with a normal boundary layer over a flat plate, bringing challenges for CFD simulations.

The rig shown in Figure 2.11(b) can not explain the mechanism of lift enhancement due

to the Coanda effect in a CC aerofoil, this will be discussed in the following part.



(a)



(b)

Figure 2.11: (a) A Coanda jet stay attached to the curved surface, (b) Streamlines around a Coanda jet ( $y_2 = 1/2U_{max}$ ) (Neuendorf & Wygnanski 1999)

Although a jet flow passing over a curved surface is similar to the flow over an aerofoil, they are two different mechanisms. The Coanda effect includes a jet within a fluid i.e. the velocity or momentum of the jet is much higher than the surrounding fluid, consequently, the entrainment effect is present. However for the flow above an aerofoil, the velocity gradient perpendicular to the flow direction is small compared with that for a Coanda jet, thus entrainment occurs to a lesser extent.

The Coanda effect can be adopted as a form of flow control for an aerofoil or wing to increase lift. One of the CC techniques is using a tangentially blowing jet over a rounded trailing edge to alter the circulation in order to change lift. The jet can produce a significant increment of lift with relatively little energy input. This is achieved by moving the rear stagnation point and delaying separation. As a result, the flow pattern around the aerofoil is dramatically changed. Figure 2.12 shows two different stagnation locations under different blowing magnitude,  $C_\mu = 0.005$  and  $C_\mu = 0.015$  respectively (the variable  $C_\mu$  is defined in Equation 5.1 on page 125). Figure 2.12(b) has a faster blowing jet than Figure 2.12(a), thus the stagnation point is moved further downward. Consequently, the streamlines around the aerofoil in Figure 2.12(b) are curved greater than (a), resulting in a higher velocity over the upper side of the aerofoil, and therefore more circulation and lift.

Compared with a Coanda jet in stationary air (Nishino et al. 2010), the jet on a CC aerofoil has different characteristics. Firstly, the jet exiting from the nozzle will meet the external flow which is from the upstream turbulent boundary layer that has developed over the upper surface. The external flow brings turbulent disturbances to the jet hence the Coanda jet becomes turbulent flow as soon as it leaves the nozzle. While for a Coanda jet in stationary air, if the jet is laminar in the nozzle, it may remain laminar for a certain distance before finally developing to turbulent flow. Secondly, when the jet finally detaches from the surface, a separation bubble may emerge between the jet and the external flow from the lower side of the aerofoil.

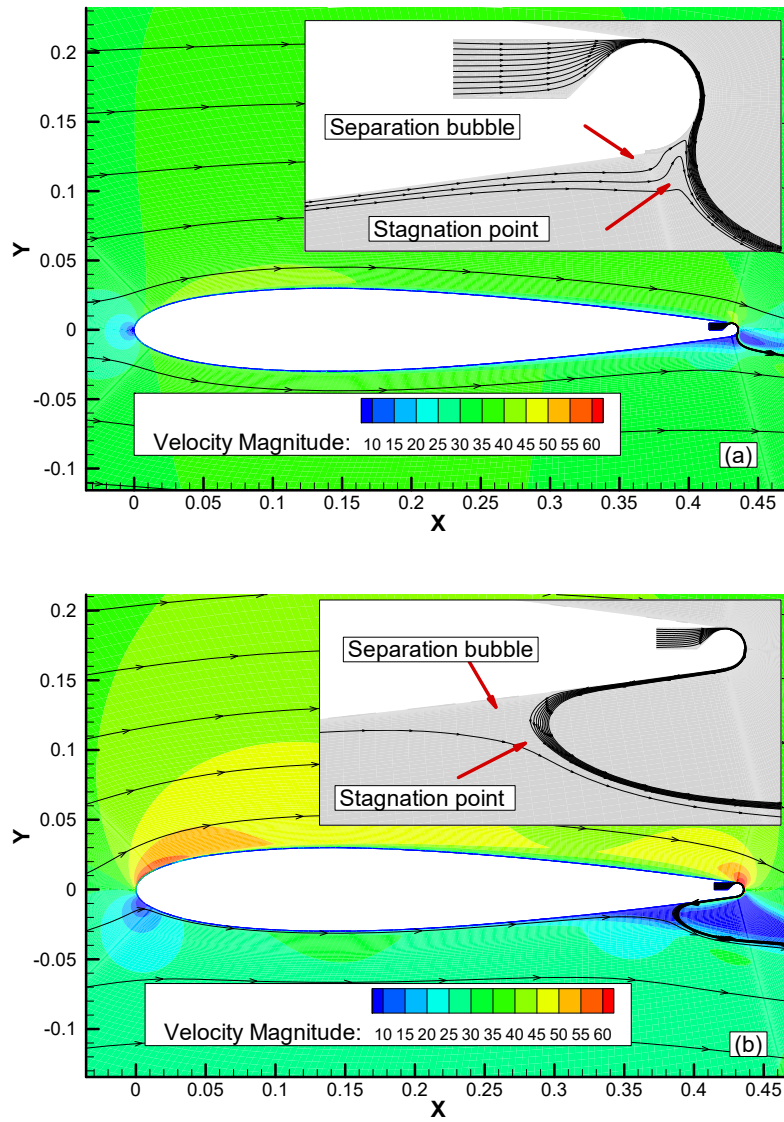


Figure 2.12: The variation of stagnation point and separation bubble created by the Coanda jet, (a)  $C_\mu = 0.005$ , (b)  $C_\mu = 0.015$ .

Figure 2.13 displays a jet sheet from the nozzle attached to a Coanda surface. The air jet is directed by the Coanda surface and also drives the flow field around the jet to further increase circulation. The behaviour of the jet around a curved surface is mainly governed by the ambient pressure applied to the jet sheet, the pressure at the curvature surface, the centrifugal force due to the curvature, the skin-friction stress due to the interaction between the jet and the surface, and the viscous shear stress.

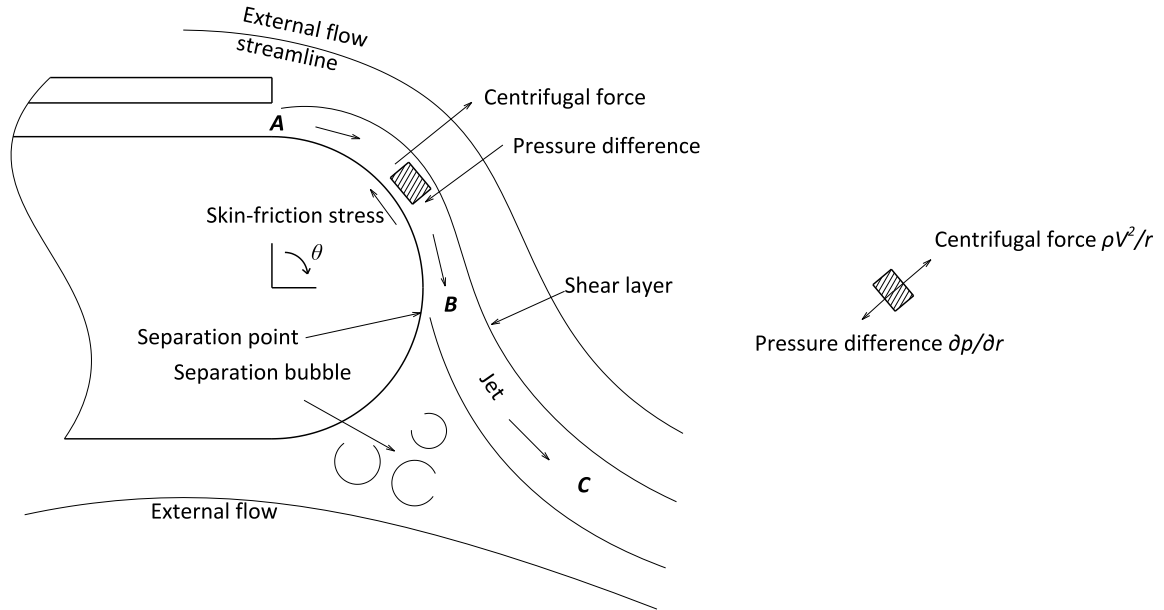


Figure 2.13: The jet around a Coanda surface.

Considering a fluid element in Figure 2.13 by the radial direction, the pressure difference applied to the element is equal to the centrifugal force which can be expressed as (Carpenter & Green 1997)

$$\frac{\partial p}{\partial r} = \rho V^2 / r \quad (2.13)$$

where  $p$  is the pressure,  $r$  is the radial distance from the centre of curvature,  $\rho$  is air density and  $V$  is the local flow velocity. According to Bernoulli's principle,

$$p + \frac{1}{2} \rho V^2 = \text{const} \quad (2.14)$$

where  $p$  is the pressure,  $\rho$  is the density,  $V$  is the velocity of the fluid. For the irrotational flow, this equation is satisfied in all streamlines (Anderson Jr 2016).

Assuming the flow is inviscid, Equation 2.13 can be derived as

$$p_w = p_\infty - \rho V^2 b / R_c \quad (2.15)$$

where the  $p_w$  is the pressure at the wall,  $p_\infty$  is the ambient pressure,  $R_c$  is the surface radius.

Equation 2.13 expresses the pressure gradient in the radial direction that overcomes the centrifugal force so that the fluid element can follow the curvature of the circular wall (Babin-sky 2003). Equation 2.15 describes the equilibrium state that the jet attached to the circular surface. The pressure at wall  $p_w$  is lower than the ambient pressure on the other side of the jet so that the jet stay attached to the circular surface. As the tangential velocity of the jet ( $V$ ) reduces,  $p_w$  increases in the stream-wise direction, which slows down the flow within the boundary layer (Schlichting & Gersten 2003). Finally, when the tangential velocity of the flow near the wall reaches zero, the boundary layer separates.

When the jet leaves the nozzle (Figure 2.13 - Point **A**), it has a high momentum and a lower static pressure, the pressure at the curved surface is lower than the ambient pressure on the other side of the jet, this pressure difference overcomes the centrifugal force, consequently the jet stays attached to the curved surface (Trancossi 2011). As the air travels around this surface, the velocity and momentum of the jet reduce due to the viscous shear stress and mixing with low energy external flow, which also results in increasing static pressure. Eventually, the jet separates from the curved surface due to the adverse pressure gradient and the centrifugal force. Through this process, the jet itself increases circulation and also entrains the surrounding flow to further increase circulation around the aerofoil. Meanwhile, a separation bubble is formed at the position where the jet sheet separates (Figure 2.13 - Point **B**). The streamlines around the aerofoil are changed by the Coanda jet and deflected downwards, which is equivalent to an aerofoil with camber, and results in a higher circulation.

Figure 2.14 displays the pressure distribution around a Coanda surface (NOVAK et al. 1987), where the horizontal axis is the clockwise angular location around the circular surface and the nozzle exit is defined as  $\theta = 0^\circ$ . The blowing momentum coefficient is defined as  $C_\mu$ . The pressure result is obtained with a steady blowing jet at  $C_\mu = 0.1$ . The flow initially accelerates slightly due to the favourable pressure gradients, achieving a maximum velocity (i.e. a high negative pressure) around  $\theta = 40^\circ$ . The jet sheet then slows down around the Coanda surface giving an increasing adverse pressure gradient until at  $\theta = 115^\circ$ , the jet sheet becomes detached. Subsequently, the pressure becomes constant and close to the ambient pressure after the separation of the jet. The separation point of the jet and the aft stagnation point can be controlled by varying the blowing momentum coefficient. The jet sheet over a Coanda surface increases the energy in the boundary layer, changes the stagnation point and increases circulation. This technique can be used on the leading edge or trailing edge of a wing to effectively increase lift, but is more commonly applied to the trailing edge.

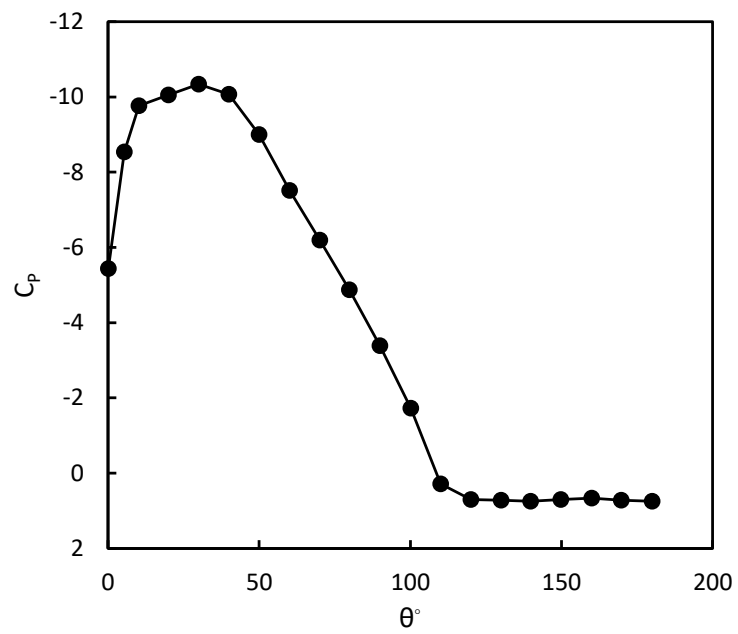


Figure 2.14: The pressure distribution around a Coanda surface at  $C_\mu = 0.1$  (NOVAK et al. 1987).

## 2.5 Development of the Flight Dynamics Model

The aerodynamic forces and moments in the previous sections are in steady state, 2D and they were acting on the aerofoil. For a 3D aircraft that consists of a wing and tailplanes, its dynamics is a result of all forces and moments acting on each aerodynamic surface. Moreover, when the aircraft is in motion, the aerodynamic forces and moments are also dependent on the transient attitude (for example, the AoA), velocity and acceleration. A dynamic model of the aircraft is required when analysing the motion and trajectory due to control inputs or disturbances. This research focuses on the longitudinal flight dynamics during a gust encounter, the following sections provide the relevant aerodynamic stability and control derivatives and the equations of motion.

### 2.5.1 Aerodynamic Stability and Control Derivatives

To analyse flight dynamics and design a controller, the flow details such as boundary layer flow are not the main focus, thus a low-order model is essential. Low-order model is obtained by linearising the CFD results and decoupling the aerodynamic forces to a series of coefficients. The modelling is based on wind axes under which the dynamic equations have the simplest form.

The definition of axes is shown in Figure 2.15.

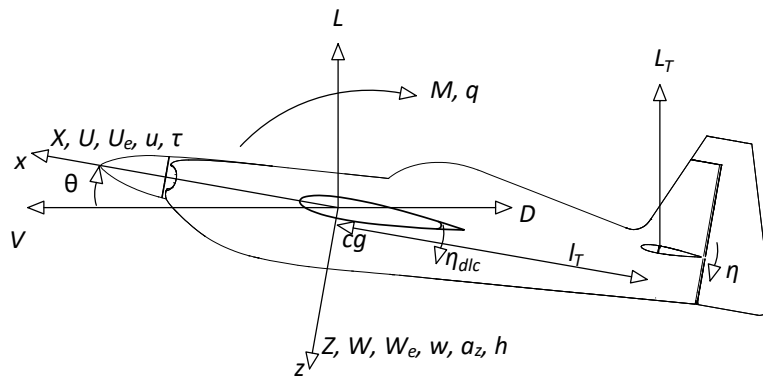


Figure 2.15: The definition of the axes.

The derivative expressions are following the approach in the reference (Cook 2012) on Page 371. Assuming the aircraft is in steady and level flight with initial velocity  $V_0$ . The components of velocity on  $x$  and  $z$  axes are  $U$  and  $W$  respectively. The perturbation of pitch attitude is  $\theta$ . As the gust velocity is small compared to the flight velocity, it is assumed that the  $\theta$  caused by the gust is small, so that in a limited time period, the aerodynamic force is

linearly related to the perturbed input quantity. The attitude and velocity components only have a small deviation from equilibrium (Stevens et al. 2015).

Based on the following assumptions, the equations of flight dynamics are linearised, according to the method in the literature (Stevens et al. (2015), Section 2.6 Linear Models and The Stability Derivatives, page 116. )

- The wing is level, with no sideslip, no rolling, and steady-state flight.
- The aircraft has a rigid body.
- The perturbation is small.
- The thrust is constant.

If the aircraft encounters a small perturbation about its trimmed condition, assuming the aerodynamic force, moment, and thrust  $\tau$  are only dependent on the disturbed variables (Cook 2012, Babister 2013). The complex forces acting on an aircraft can be reduced to derivatives which remain constant. This treatment greatly simplifies the problem by using algebraic terms to approximate differential terms (Babister 2013). As mentioned in Section 6 on page 157, the CFD results are represented by lift, drag, and moment coefficients with respect to velocity or AoA, therefore they can be used to calculate the perturbed aerodynamic force and moment. The derivatives provide a link between the aerodynamics and the flight mechanics, the values of such derivatives are given in Table 6.6, according to the CFD results in Section 6.7.1 on page 194.

The lift and drag forces can be resolved to give the following expressions of aerodynamic forces and moments.

Axial force due to perturbation

$$X = L \sin \theta - D \cos \theta + \tau = \frac{1}{2} \rho V^2 S (C_L \sin \theta - C_D \cos \theta) + \tau \quad (2.16)$$

Normal force due to perturbation

$$Z = -L \cos \theta - D \sin \theta = -\frac{1}{2} \rho V^2 S (C_L \cos \theta + C_D \sin \theta) \quad (2.17)$$

Pitching moment due to perturbation

$$M = \frac{1}{2} \rho V^2 S \bar{c} C_m \quad (2.18)$$

By differentiating Equation 2.16,2.17,2.18 with respect to  $U, W, q, \eta, dlc$ , the aerodynamic derivatives can be expressed by coefficients (Babister 2013).

Axial force due to axial velocity.

$$\dot{X}_u = \frac{\partial X}{\partial U} = -\rho V_0 S C_D - \frac{1}{2} \rho V_0^2 S \frac{\partial C_D}{\partial V} + \frac{\partial \tau}{\partial V} \quad (2.19)$$

Normal force due to axial velocity.

$$\dot{Z}_u = \frac{\partial Z}{\partial U} = -\rho V_0 S C_L - \frac{1}{2} \rho V_0^2 S \frac{\partial C_L}{\partial V} \quad (2.20)$$

Axial force due to normal velocity.

$$\dot{X}_w = \frac{\partial X}{\partial W} = \frac{1}{2} \rho V_0 S (C_L - \frac{\partial C_D}{\partial \alpha}) \quad (2.21)$$

Normal force due to normal velocity

$$\dot{Z}_w = \frac{\partial Z}{\partial W} = -\frac{1}{2} \rho V_0 S (\frac{\partial C_L}{\partial \alpha} + C_D) \quad (2.22)$$

Pitching moment due to axial velocity

$$\dot{M}_u = \frac{\partial M}{\partial U} = -\frac{1}{2} \rho V_0^2 S \bar{c} \frac{\partial C_m}{\partial V} \quad (2.23)$$

Pitching moment due to normal velocity

$$\dot{M}_w = \frac{\partial M}{\partial W} = -\frac{1}{2} \rho V_0^2 S \bar{c} \frac{\partial C_m}{\partial \alpha} \quad (2.24)$$

Axial force due to pitch rate

$$\dot{X}_q = \frac{\partial X}{\partial q} = -\frac{1}{2} \rho V_0 S_T l_T \frac{\partial C_{DT}}{\partial \alpha_T} \quad (2.25)$$

Normal force due to pitch rate

$$\dot{Z}_q = \frac{\partial Z}{\partial q} = -\frac{1}{2} \rho V_0 S_T l_T \frac{\partial C_{LT}}{\partial \alpha_T} \quad (2.26)$$

Pitching moment due to pitch rate

$$\dot{M}_q = \frac{\partial M}{\partial q} = l_T \dot{Z}_q \quad (2.27)$$

Axial force due to rate of change of normal velocity

$$\dot{X}_{\dot{w}} = \frac{\partial X}{\partial \dot{w}} = -\frac{1}{2} \rho S_T l_T \frac{\partial C_{DT}}{\partial \alpha_T} \frac{d\varepsilon}{d\alpha} \quad (2.28)$$

Normal force due to rate of change of normal velocity

$$\dot{Z}_{\dot{w}} = \frac{\partial Z}{\partial \dot{w}} = -\frac{1}{2}\rho S_T l_T \frac{\partial C_{L_T}}{\partial \alpha_T} \frac{d\varepsilon}{d\alpha} \quad (2.29)$$

Pitching moment due to rate of change of normal velocity

$$\dot{M}_{\dot{w}} = \frac{\partial M}{\partial \dot{w}} = -\frac{1}{2}\rho S_T l_T^2 \frac{\partial C_{L_T}}{\partial \alpha_T} \frac{d\varepsilon}{d\alpha} \quad (2.30)$$

Axial force due to elevator

$$\dot{X}_\eta = \frac{\partial X_T}{\partial \eta} = -\frac{1}{2}\rho V_0^2 S_T \frac{\partial C_{D_T}}{\partial \eta} \quad (2.31)$$

Normal force due to elevator

$$\dot{Z}_\eta = \frac{\partial Z_T}{\partial \eta} = -\frac{1}{2}\rho V_0^2 S_T \frac{\partial C_{L_T}}{\partial \eta} \quad (2.32)$$

Pitching moment due to elevator

$$\dot{M}_\eta = \frac{\partial M_T}{\partial \eta} = \dot{Z}_\eta l_T \quad (2.33)$$

Circulation control is equivalent to a flap on the wing, thus the derivatives are the same as flaps. From the steady state CFD study, the force and moment by the CC are obtained.

Axial force due to Direct lift control of CC

$$\dot{X}_{dlc} = \frac{\partial X_{dlc}}{\partial \eta_{dlc}} = -\frac{1}{2}\rho V_0^2 S \frac{\partial C_{D_{dlc}}}{\partial \eta_{dlc}} \quad (2.34)$$

Normal force due to Direct lift control of CC

$$\dot{Z}_{dlc} = \frac{\partial Z_{dlc}}{\partial \eta_{dlc}} = -\frac{1}{2}\rho V_0^2 S \frac{\partial C_{L_{dlc}}}{\partial \eta_{dlc}} \quad (2.35)$$

Pitching moment due to Direct lift control of CC

$$\dot{M}_{dlc} = \frac{\partial M_{dlc}}{\partial \eta_{dlc}} = -\frac{1}{2}\rho V_0^2 S \frac{\partial C_{M_{dlc}}}{\partial \eta_{dlc}} \quad (2.36)$$

The coefficients related to wing-body  $\frac{\partial C_L}{\partial \alpha}$ ,  $\frac{\partial C_D}{\partial \alpha}$  and the CC  $\frac{\partial C_{L_{dlc}}}{\partial \eta_{dlc}}$ ,  $\frac{\partial C_{D_{dlc}}}{\partial \eta_{dlc}}$ ,  $\frac{\partial C_{M_{dlc}}}{\partial \eta_{dlc}}$  are interpolated from the CFD database in previous sections. The  $C_L$ ,  $C_D$ ,  $C_m$  can be considered as unchanged for a small perturbation of  $V$ , hence  $\frac{\partial C_L}{\partial V} = 0$ ,  $\frac{\partial C_D}{\partial V} = 0$ ,  $\frac{\partial C_m}{\partial V} = 0$ . The  $\dot{X}_{\dot{w}}$ ,  $\dot{X}_q$  are also negligible in practice (Babister 2013). The coefficients related to tailplane  $C_{L_T}$  are available from reference (Babister 2013, Cook 2012).

The rate of change of pitching moment with  $\alpha$  about the centre of gravity  $cg$  is given by

$$\frac{\partial C_m}{\partial \alpha} = -aK_n \quad (2.37)$$

where  $a$  is the lift curve slope,  $K_n$  is the controls-fixed static margin.

$$K_n = h_n - h \quad (2.38)$$

$h$  is the  $cg$  position as a fraction of  $\bar{c}$ ,  $h_n$  is the control fixed neutral point as a fraction of  $\bar{c}$

$$h_n = h_0 + \bar{V}_T \frac{a_1}{a} \left( 1 - \frac{d\varepsilon}{d\alpha} \right) \quad (2.39)$$

$h_0$  is the position of aerodynamic centre  $ac$  as a fraction of  $\bar{c}$ . During a small perturbation in low Mach number,  $ac$  is fixed and assumed to be at the quarter-chord point.

$\bar{V}_T$  is the tail volume ratio given by

$$\bar{V}_T = \frac{S_T l_T}{S \bar{c}} \quad (2.40)$$

In this research, the  $cg$  is set to  $0.25\bar{c}$ , for a symmetrical aerofoil, assuming  $ac$  is also on  $0.25\bar{c}$ , we have  $h_0 = h = 0.25\bar{c}$ . The above-mentioned equations are reduced to

$$\frac{\partial C_m}{\partial \alpha} = -\bar{V}_T a_1 \left( 1 - \frac{d\varepsilon}{d\alpha} \right) \quad (2.41)$$

where  $a_1$  is the lift curve slope of the tailplane.

### 2.5.2 Linearised Equations of Motion for Small Perturbations

The CC does not intend to fully control the aircraft but only to compensate for the gust loading. To simplify the modelling, it is assumed that the deployment of CC only has a minor influence on the aircraft's attitude and flight path. Therefore the equation of small perturbations is used to model the dynamics of the aircraft. The vertical gust ( $w_g$ ), elevator input ( $\eta$ ) and CC input ( $\eta_{dlc}$ ) are regarded as control vector  $u = [\eta_{dlc} \quad \eta \quad w_g]^T$ .

Bryan has provided the derivation of equations of motion for a rigid aircraft (Bryan 1911). His treatment was based on the following laws:

Force = Mass  $\times$  Inertial Acceleration

Moment = Moment of Inertia  $\times$  Angular Acceleration

The 'Force' and 'Moment' with respect to aerodynamic effects, control surface, CC jet and gusts, can be expressed as a summation of the Taylor series and only the first term of the series is significant. (Cook 2012, Babister 2013). The equations of motion can be simplified and only consist of the disturbed variables and their derivatives, such as  $\dot{X}_u, \dot{X}_w, \dot{X}_q$ , given in the previous section.

The following equation shows the longitudinal motion of the aircraft with control inputs and vertical gust.

$$m\dot{u} - \dot{X}_u u - \dot{X}_{\dot{w}}(\dot{w} - \dot{w}_g) - \dot{X}_w(w - w_g) - \dot{X}_q q + mW_e q + mg \cos \theta_e = \dot{X}_\eta \eta + \dot{X}_{dlc} \eta_{dlc} \quad (2.42)$$

$$- \dot{Z}_u u + m\dot{w} - \dot{Z}_{\dot{w}}(\dot{w} - \dot{w}_g) - \dot{Z}_w(w - w_g) - \dot{Z}_q q - mU_e q + mg \sin \theta_e = \dot{Z}_\eta \eta + \dot{Z}_{dlc} \eta_{dlc} \quad (2.43)$$

$$- \dot{M}_u u - \dot{M}_{\dot{w}}(\dot{w} - \dot{w}_g) - \dot{M}_w(w - w_g) + I_y \dot{q} - \dot{M}_q q = \dot{M}_\eta \eta + \dot{M}_{dlc} \eta_{dlc} \quad (2.44)$$

The altitude and vertical acceleration are also important to observe the controller performance of eliminating vertical gust loading. These two factors are given by the following equation.

$$\dot{h} = -w + V_0 \theta \quad (2.45)$$

$$a_z = \dot{w} - V_0 q \quad (2.46)$$

These equations can be written as a state-space equation:

$$\begin{bmatrix} m & -\dot{X}_{\dot{w}} & 0 & 0 & 0 \\ 0 & m - \dot{Z}_{\dot{w}} & 0 & 0 & 0 \\ 0 & -\dot{M}_{\dot{w}} & I_y & 0 & 0 \\ 0 & 0 & 0 & 1 & 0 \\ 0 & 0 & 0 & 0 & 1 \end{bmatrix} \begin{bmatrix} \dot{u} \\ \dot{w} \\ \dot{q} \\ \dot{\theta} \\ \dot{h} \end{bmatrix} = \begin{bmatrix} \dot{X}_u & \dot{X}_w & \dot{X}_q - mW_e & -mg \cos \theta_e & 0 \\ \dot{Z}_u & \dot{Z}_w & \dot{Z}_q + mU_e & -mg \sin \theta_e & 0 \\ \dot{M}_u & \dot{M}_w & \dot{M}_q & 0 & 0 \\ 0 & 0 & 1 & 0 & 0 \\ 0 & -1 & 0 & V & 0 \end{bmatrix} \begin{bmatrix} u \\ w \\ q \\ \theta \\ h \end{bmatrix} \quad (2.47)$$

$$+ \begin{bmatrix} \dot{X}_{dlc} & \dot{X}_\eta \\ \dot{Z}_{dlc} & \dot{Z}_\eta \\ \dot{M}_{dlc} & \dot{M}_\eta \\ 0 & 0 \\ 0 & 0 \end{bmatrix} \begin{bmatrix} \eta_{dlc} \\ \eta \end{bmatrix} + \begin{bmatrix} -\dot{X}_w \\ -\dot{Z}_w \\ -\dot{M}_w \\ 0 \\ 0 \end{bmatrix} w_g \quad (2.48)$$

$$\mathbf{M}\dot{\mathbf{x}} = \mathbf{A}'\mathbf{x} + \mathbf{B}'\mathbf{u} + \mathbf{E}'\mathbf{w}_g \quad (2.49)$$

where the state vector and control vector are

$$\mathbf{x} = [u \ w \ q \ \theta \ h]^T \quad (2.50)$$

$$\mathbf{u} = [\eta_{dlc} \ \eta]^T \quad (2.51)$$

$$\mathbf{y} = [u \ w \ q \ \theta \ h \ a_z]^T \quad (2.52)$$

### 2.5.3 Concise Longitudinal Aerodynamic Stability Derivatives

Equation 2.49 can be transferred to a standard state space equation given by Equation 2.53 and 2.54. The following derivatives are the concise form of the state space matrix.

$$\begin{aligned}
 x_u &= \frac{\dot{X}_u}{m} + \frac{\dot{X}_{\dot{w}}\dot{Z}_u}{m(m - \dot{Z}_{\dot{w}})} & z_u &= \frac{\dot{Z}_u}{m - \dot{Z}_{\dot{w}}} & m_u &= \frac{\dot{M}_u}{I_y} + \frac{\dot{Z}_u\dot{M}_{\dot{w}}}{I_y(m - \dot{Z}_{\dot{w}})} \\
 x_w &= \frac{\dot{X}_w}{m} + \frac{\dot{X}_{\dot{w}}\dot{Z}_w}{m(m - \dot{Z}_{\dot{w}})} & z_w &= \frac{\dot{Z}_w}{m - \dot{Z}_{\dot{w}}} & m_w &= \frac{\dot{M}_w}{I_y} + \frac{\dot{Z}_w\dot{M}_{\dot{w}}}{I_y(m - \dot{Z}_{\dot{w}})} \\
 x_q &= \frac{\dot{X}_q - mW_e}{m} + \frac{(\dot{Z}_q + mU_e)\dot{X}_{\dot{w}}}{m(m - \dot{Z}_{\dot{w}})} & z_q &= \frac{\dot{Z}_q + mU_e}{m - \dot{Z}_{\dot{w}}} & m_q &= \frac{\dot{M}_q}{I_y} + \frac{(\dot{Z}_q + mU_e)\dot{M}_{\dot{w}}}{I_y(m - \dot{Z}_{\dot{w}})} \\
 x_\theta &= -g \cos \theta_e - \frac{\dot{X}_{\dot{w}}g \sin \theta_e}{m - \dot{Z}_{\dot{w}}} & z_\theta &= -\frac{mg \sin \theta_e}{m - \dot{Z}_{\dot{w}}} & m_\theta &= -\frac{\dot{M}_{\dot{w}}mg \sin \theta_e}{I_y(m - \dot{Z}_{\dot{w}})} \\
 x_\eta &= \frac{\dot{X}_\eta}{m} + \frac{\dot{X}_{\dot{w}}\dot{Z}_\eta}{m(m - \dot{Z}_{\dot{w}})} & z_\eta &= \frac{\dot{Z}_\eta}{m - \dot{Z}_{\dot{w}}} & m_\eta &= \frac{\dot{M}_\eta}{I_y} + \frac{\dot{M}_{\dot{w}}\dot{Z}_\eta}{I_y(m - \dot{Z}_{\dot{w}})} \\
 x_{dlc} &= \frac{\dot{X}_{dlc}}{m} + \frac{\dot{X}_{\dot{w}}\dot{Z}_{dlc}}{m(m - \dot{Z}_{\dot{w}})} & z_{dlc} &= \frac{\dot{Z}_{dlc}}{m - \dot{Z}_{\dot{w}}} & m_{dlc} &= \frac{\dot{M}_{dlc}}{I_y} + \frac{\dot{M}_{\dot{w}}\dot{Z}_{dlc}}{I_y(m - \dot{Z}_{\dot{w}})}
 \end{aligned}$$

$$\begin{bmatrix} \dot{u} \\ \dot{w} \\ \dot{q} \\ \dot{\theta} \\ \dot{h} \end{bmatrix} = \begin{bmatrix} x_u & x_w & x_q & x_\theta & 0 \\ z_u & z_w & z_q & z_\theta & 0 \\ m_u & m_w & m_q & m_\theta & 0 \\ 0 & 0 & 1 & 0 & 0 \\ 0 & -1 & 0 & V & 0 \end{bmatrix} \begin{bmatrix} u \\ w \\ q \\ \theta \\ h \end{bmatrix} + \begin{bmatrix} x_{dlc} & x_\eta \\ z_{dlc} & z_\eta \\ m_{dlc} & m_\eta \\ 0 & 0 \\ 0 & 0 \end{bmatrix} \begin{bmatrix} \eta_{dlc} \\ \eta \end{bmatrix} + \begin{bmatrix} -x_w \\ -z_w \\ -m_w \\ 0 \\ 0 \end{bmatrix} w_g \quad (2.53)$$

$$\begin{bmatrix} u \\ w \\ q \\ \theta \\ h \\ a_z \end{bmatrix} = \begin{bmatrix} 1 & 0 & 0 & 0 & 0 \\ 0 & 1 & 0 & 0 & 0 \\ 0 & 0 & 1 & 0 & 0 \\ 0 & 0 & 0 & 1 & 0 \\ 0 & 0 & 0 & 0 & 1 \\ z_u & z_w & z_q - V_0 & 0 & 0 \end{bmatrix} \begin{bmatrix} u \\ w \\ q \\ \theta \\ h \end{bmatrix} + \begin{bmatrix} 0 & 0 \\ 0 & 0 \\ 0 & 0 \\ 0 & 0 \\ 0 & 0 \\ z_{dlc} & z_\eta \end{bmatrix} \begin{bmatrix} \eta_{dlc} \\ \eta \end{bmatrix} + \begin{bmatrix} 0 \\ 0 \\ 0 \\ 0 \\ 0 \\ -z_w \end{bmatrix} w_g \quad (2.54)$$

$$\dot{\mathbf{x}} = \mathbf{A}\mathbf{x} + \mathbf{B}\mathbf{u} + \mathbf{E}\mathbf{w}_g \quad (2.55)$$

$$\mathbf{y} = \mathbf{C}\mathbf{x} + \mathbf{D}\mathbf{u} + \mathbf{F}\mathbf{w}_g \quad (2.56)$$

## 2.6 The Control Algorithm

The above-mentioned flight dynamic equations only describe the aircraft's response to the state variables without any control inputs. They still need control algorithms to close the system. Therefore the system can alleviate any gust disturbance automatically according to observations of states.

In this section, the word 'control' is different from the previous 'circulation control'. The CC is a physical method and involves actual devices and energy to actuate the system. While control in this section is a concept from Control Theory, and is a mathematical methodology being used to regulate physical systems. In aerospace engineering, stability augmentation, autopilot and actuation systems are all based on control algorithms. Such algorithms are developed by modelling aircraft dynamics and simulating various flight conditions. The modelling of an aircraft is conducted using aerodynamic data from CFD or wind tunnel results. These results are simplified and trends extracted as equations or aerodynamic derivatives which are easily processed by software tools, as described by the previous section. Consequently, a flight dynamics simulation can be performed and control algorithms can be designed.

The classical control theory and the modern control theory are two methods that have been widely used in the aerospace industry. The classical control theory is mainly based on the transfer function and frequency domain. Classical control is suitable for single input and single output (SISO) systems and is largely based on empirical and experimental data to fulfil the design criteria. Historically, the Proportional-Integral-Derivative (PID) controller is the most commonly used design method. The PID controller does not require a precise system model and can be adapted to a broad area of systems. In comparison, the modern control theory is fundamentally a time-domain method, it overcomes the limitation of classical control by utilising the state space to describe a system and can represent multiple inputs and outputs. For example, considering the influence of CC on the aircraft dynamics, the additional drag and moment induced by CC need to be compensated by elevators or throttle. A multiple-input and multiple-output (MIMO) control strategy is therefore needed to regulate these actuators coordinately.

Another classification of control approaches depends on the sensors used, there are two primary approaches: feedforward control and feedback control. Feedforward control uses sensors ahead of the wing to capture the gust profile before it hits the wing (Khalil & Fezans 2021, Fezans et al. 2019), such as AoA vanes on the nose and the LIDAR. The gust information is fed to the controller and generates an output signal for the aerodynamic surfaces to counteract the gust loading. This approach is open-loop and does not have any time delay as the controller already has the gust information before it impacts the aircraft. The feedback control mainly uses inertial sensors such as an accelerometer or gyroscope, after the gust creates an unsteady load on the wing, the unsteady loading information is fed back to the input of the controller, which is a closed-loop approach. Feedback control is more robust than open-loop feedforward control, and the bandwidth of inertial sensors is much wider than AoA sensors or LIDAR sensors. In comparison, due to the lack of information from the system output, the feedforward control is less tolerant to system uncertainties and disturbances. Therefore both methods can be combined when designing the control architecture (Fezans et al. 2019)(De Breuker et al. 2007). In this study, the feedback approach is used because the feedforward controller requires special sensors which may not be available in small UAVs, whereas inertial sensors are available in any UAV.

The CFD can provide a model of the CC system for controller design, the working condition in this research is fixed in low speed (  $M = 0.1$ ,  $AoA \approx 0$  ), and there is no stall so the aerodynamic forces and stability derivatives can be treated as linear functions. The aircraft is considered a rigid body. Based on these characteristics, several controllers are suitable for this application, such as the PID, Linear quadratic regulator (LQR),  $H_\infty$ . The following sections introduce the first two controllers used in this research. The  $H_\infty$  is not used but can be found in other literature for CC applications, it will be reviewed in the next chapter.

### 2.6.1 PID controller

The PID controller (Nelson et al. 1998) is a feedback controller in which the output is a combination of three terms: the proportional term, the integral term, and the derivative term in terms of the error input:

$$u(t) = k_p e(t) + k_i \int_0^t e(\tau) d\tau + k_d \frac{de}{dt} \quad (2.57)$$

where  $u$  is the output,  $e$  is the error input,  $k_p, k_i, k_d$  are the gains.

The integral term is proportional to the integration of input, to eliminate the steady-state error. The derivative term provides corrections even when the error is small, but it is sensitive

to noise. By tuning the three gains of the PID controller, the drawbacks of each individual term can be attenuated, and the desired system response can be achieved. This can be performed in the time domain or by root locus (Nelson et al. 1998) methods. The original PID controllers are only suitable for SISO systems, or for some MIMO systems where the loops are not coupled. For example, the flight controller for a UAV contains multiple loops with various inputs and outputs, the PID controller can be adopted in the actuator loop since it is not coupled with other loops (Rosén et al. 2018).

PID controller has been used in CC applications, for example, the UC2AV developed by Cameron Rosen et al. (Rosén et al. 2018), and the Jet Powered aircraft in the Innovative Control Effectors (ICE) project (Smith & Warsop 2019). These two projects adopted the PID controller as a part of the primary flight controller and used CC as effectors, the wind gusts were not considered. Some applications adopt PID for gust alleviation, but use mechanical aerodynamic surfaces (Caverly et al. 2017). However, due to the complexity of control architectures in these applications, PID controllers are only integrated as a part of the inner feedback loop. This is identical to the 2D case in the present research, an aerofoil equipped with CC is regarded as an inner loop. Although the aircraft autopilot and control augmentation systems are complex MIMO systems, the CC actuator can be simplified as a SISO system which is feasible for PID, assuming the pitch angle is constant (pitch attitude can be maintained coordinately with the elevator) during the transition of the gust field. In addition, the input information is provided by CFD simulation, so there is no noise. Consequently, the typical PID controller is used to close the feedback loop.

### **2.6.2 LQR controller**

Modern control has two fundamental tools, the state space model and the performance specifications. The state space model is a mathematical description of the system dynamics (Kalman 1963), which contains time-dependent state variables (e.g., the speed, altitude, and pitch rate of an aircraft). System states contain more information than the traditional black-box model represented by transfer functions, which do not provide information inside the system. State space model was introduced to dynamic system theory by Kalman (Kalman 1960), who has also contributed to the regulator problem of optimal control theory, known as linear quadratic regulator (LQR) control (Kalman et al. 1960). Kalman's work provides new insights into modern control and accelerates the implementation of aerospace engineering. LQR also became a widely used method for aircraft control (Stevens et al. 2015). On the other hand, performance specifications create a precise evaluation of the system performance, all the control gains can

be solved by mathematical methods to fulfil the performance criterion.

The gust alleviation based on CC is a regulator problem, which means the controller's objective is to keep the output to zero or the input reference is zero. The control gains are determined to minimise the performance index. In this research, the development of the controller does not consider any robustness or stability requirement. Such a requirement is only essential when the system is implemented in engineering development, where modelling errors and measurement noise are inevitable. While this study is based on RANS equations, the feedback variables are acquired directly from flow field results, hence the measurement noise and uncertainty are neglected.

In this research, the operational condition is in cruise flight and can be linearized. The fuel consumption, trimming condition, and flight speed are assumed to be constant during the simulation. Hence, the system is time-invariant and can be considered a Linear time-invariant (LTI) system. Assuming the aircraft is in straight and level flight when encountering wind gusts, the trajectory following problem and pilot input are not considered. In the simulation, only the force, pitch angle, velocity and position are used to provide feedback information without any feedforward loop. Therefore the LQR full state feedback controller is selected for 3D cases. LQR controller is suitable for MIMO optimal control problems. Through performance equations, the control gains of different feedback variables can be simultaneously and precisely solved to achieve an optimal control performance with the least energy consumption. The state space description and LQR performance functions are introduced in the following part.

The standard model of a dynamic system is generally defined as state-space form:

$$\dot{\mathbf{x}} = \mathbf{A}\mathbf{x} + \mathbf{B}\mathbf{u} \quad (2.58)$$

$$\mathbf{y} = \mathbf{C}\mathbf{x} \quad (2.59)$$

where  $\mathbf{x}$  is the state,  $\mathbf{u}$  is the control input,  $\mathbf{y}$  is the output.  $\mathbf{A}$ ,  $\mathbf{B}$ ,  $\mathbf{C}$  represent the matrix form of the state, input and output equations respectively.

Then the performance function is used to find the optimal feedback gain, which is defined as

$$J = \frac{1}{2} \int_0^{\infty} (\mathbf{x}^T \mathbf{Q} \mathbf{x} + \mathbf{u}^T \mathbf{R} \mathbf{u}) dt \quad (2.60)$$

where the  $\mathbf{Q}$  matrix is to penalise undesirable performance and the  $\mathbf{R}$  matrix is to penalise actuator effort. The control gains ( $\mathbf{K}$ ) can be solved by programs to achieve a minimum cost of the performance index ( $J$ ). Therefore the control law is

$$\mathbf{u} = -\mathbf{K}\mathbf{x} \quad (2.61)$$

where  $\mathbf{K}$  is the gain matrix.

According to the dynamic response of the aircraft and the wind gust model, the LQR control law can be designed to demonstrate the feasibility of gust alleviation by CC. The process of investigating and modelling a 3D aircraft and the controller design, are provided in Chapters 6, 7, and 8.

## 2.7 Summary

This chapter introduces the fundamental aerodynamic theories relevant to this research. Several basic flows have been explained, and the mechanism of how aerodynamic forces are generated and controlled is discussed. The Coanda effect is introduced, including how lift is enhanced by a curved wall jet, the entrainment effect and the jet separation. Subsequently, the formulation of flight dynamics for a datum aircraft, and theories of control algorithms are provided, they are used to build the closed-loop system for gust alleviation in Chapters 5 and 8.

The Coanda effect has been used on aircraft for decades, it has been investigated thoroughly by experimental and computational methods. The next Chapter will review existing literature for CC from the application perspective. The complex flows involved in the Coanda jet, such as convex wall jet, shear layers and separations, determine the selection of simulation approaches, this is discussed in Chapter 4 on page 89.

# Chapter 3:

## Literature Review

This chapter reviews the literature relates to fundamental knowledge and industrial applications of flow control and gust alleviation. Although this research mainly focused on the CC, which is one of several flow control approaches, a wider area has been reviewed, including other types of flow control, as they have a very similar methodology. Moreover, considering the application of CC on an aircraft involves multiple systems, the actuators and sensors of CC are also reviewed. In this research, the flight parameters are acquired by simulation; hence physical actuators and sensors are not used. However, it is still worth reviewing the actuator and sensor requirements that would be necessary, and whether these are currently available, in order to consider the feasibility of a CC system on an aircraft.

As an interdisciplinary study, several concepts are introduced in this chapter, the following chart presents a road map of the techniques involved in this study, and where the fluid dynamics and automatic control algorithms are connected to solve the research problem. The terms in black are relevant techniques that have been reviewed in this chapter, but are not used in developing the research results, whilst the terms in red are used in the following chapters.

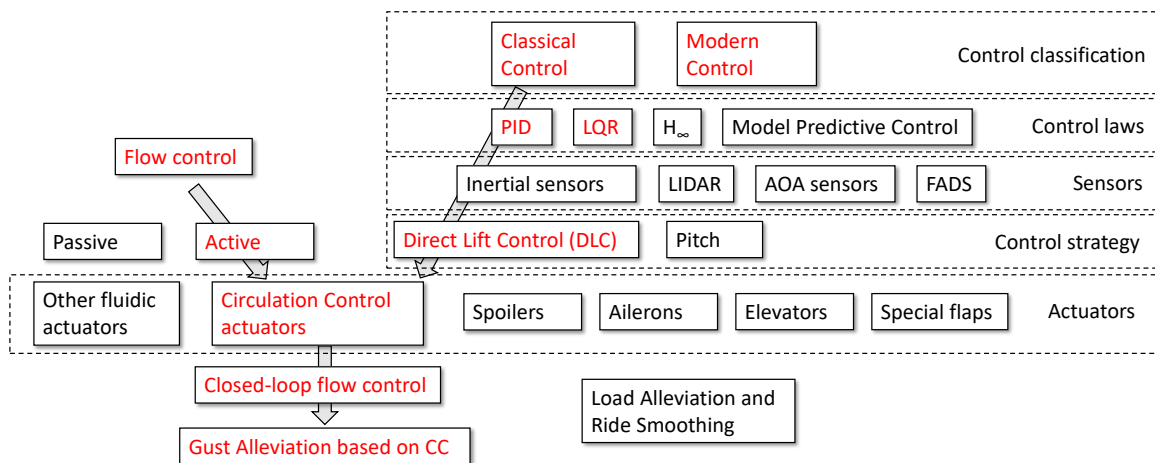


Figure 3.1: The road map of technologies involved in this research.

### 3.1 Atmospheric Disturbances

Many reasons can cause atmospheric disturbances, one is the interaction between atmospheric flow and ground objects such as irregular terrain, trees or buildings (Kaimal & Finnigan 1994). The turbulence induced by terrain is a hazard for UAVs flying at low altitudes. When the wind follows over steep hills or buildings, it is likely to create a separated region behind the object and a local reversal of the flow direction. The wake zone is highly turbulent, and would reduce flight stability if encountered.

The other source of disturbances is Meteorological Conditions such as thunderstorms and frontal surfaces; there is also clear-air turbulence that exists in regions at high altitudes and far away from clouds or mountains (Chambers 1955). There are complex vertical flows and severe turbulence associated with thunderstorms that can lead to accidents. Figure 3.2 is a schematic of the structure of a maturing thunderstorm (Allen 2013). The circulation inside the thunderstorm produces updrafts and downdrafts, creating wind shear and turbulence at the interface between these moving columns of air. At low altitudes, below the thunderstorm, a microburst or strong downdraft can develop. Figure 3.3 shows an aircraft during landing as it penetrates a microburst (Allen 2013). It initially encounters the gust front and climbs slightly due to an increase in the effective AoA, then rapidly sinks towards the ground as the downdraft is encountered, which is clearly dangerous when the aircraft is landing and already close to the ground.

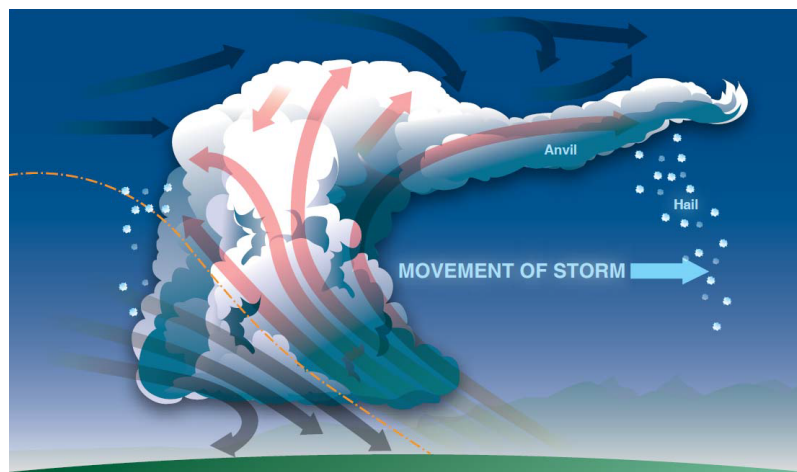


Figure 3.2: The flow structure of a maturation thunderstorm. (Allen 2013)

Among all the hazards induced by thunderstorms and frontal surfaces, wind shear is one of the most dangerous phenomena. Wind shear refers to a rapid change in wind direction or velocity (FAA November 25, 1988). Wind shear can abruptly change the airspeed or vertical

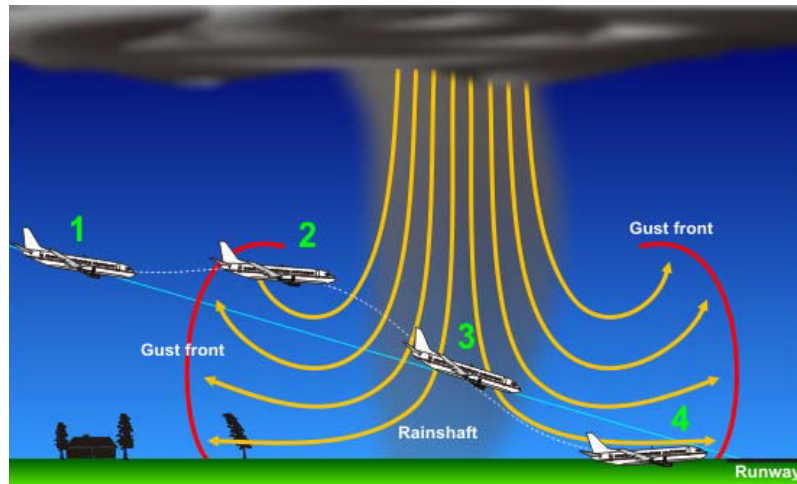


Figure 3.3: The microburst under a thunderstorm. (Allen 2013)

speed of an aircraft. It is extremely dangerous during take-off and landing when the aircraft is close to the ground. In 1985, a Lockheed L-1011 crashed when approaching the runway, after passing through a microburst-induced wind shear (NTSB AUGUST 2,1985). The accident report shows that the aircraft's attitude changed dramatically before ground contact. The AoA increased from  $6^\circ$  to  $23^\circ$  due to an atmospheric disturbance. When the aircraft was 280 feet above the ground, the descend rate was 5000 feet per minute. Within 4 seconds before crashing, the aircraft encountered an upward acceleration of 2g followed by a downdraft. Then the aircraft impacted the ground and broke apart. The wind shear was the main cause of this accident. It was also reported that from 1959 to 1983, there were 51 accidents or incidents related to wind shear (FAA November 25, 1988). Although modern transport aircraft are equipped with weather radars and wind shear warning systems, the pilot usually avoids flying into extreme weather conditions such as wind shear, as there is no effective technology that can eliminate the hazard of severe disturbance. In terms of civilian UAVs, which are not equipped with weather radars due to the limitation of payload, a method to decrease the effect of disturbance is needed. Moreover, for search and rescue UAVs, the ability to fly in extreme weather conditions is desired.

Atmospheric disturbances vary in scale, direction and frequency, so precisely modelling them is challenging but essential for academic research. For the simulation of aircraft dynamics, the disturbances are normally classified as steady wind, discrete gust, continuous turbulence and wind shear (Stevens et al. 2015). Figure 3.4 shows the profiles of different atmospheric disturbances. The steady wind defines a wind model in which the direction and velocity are not changing over time. While the discrete gust and continuous turbulence define profiles of unsteady wind. The discrete gust is a bump signal which is used to study the aircraft

dynamics when encountering a single gust. Continuous turbulence is a filtered noise signal that varies in frequency and magnitude. Whereas the wind shear profile defines a velocity gradient in a spatial field.

This research aims at applying flow control techniques to UAVs to improve flight stability in unsteady atmospheric conditions where discrete gusts and continuous turbulence are considered. The flight in the steady wind can be solved by quasi-steady simulation, which is not in the scope of this research. In terms of wind shear, there are various forms of wind shear to be considered. If the wind shear has vertical gradients, it is usually modelled by a wind profile with variation in different heights, while the wind shear with horizontal gradients can be simulated by discrete gusts. (Jones 1980). This research was focused on the longitudinal motion of the aircraft and mainly used discrete gust and continuous turbulence models, which can cover most of the atmospheric disturbances.

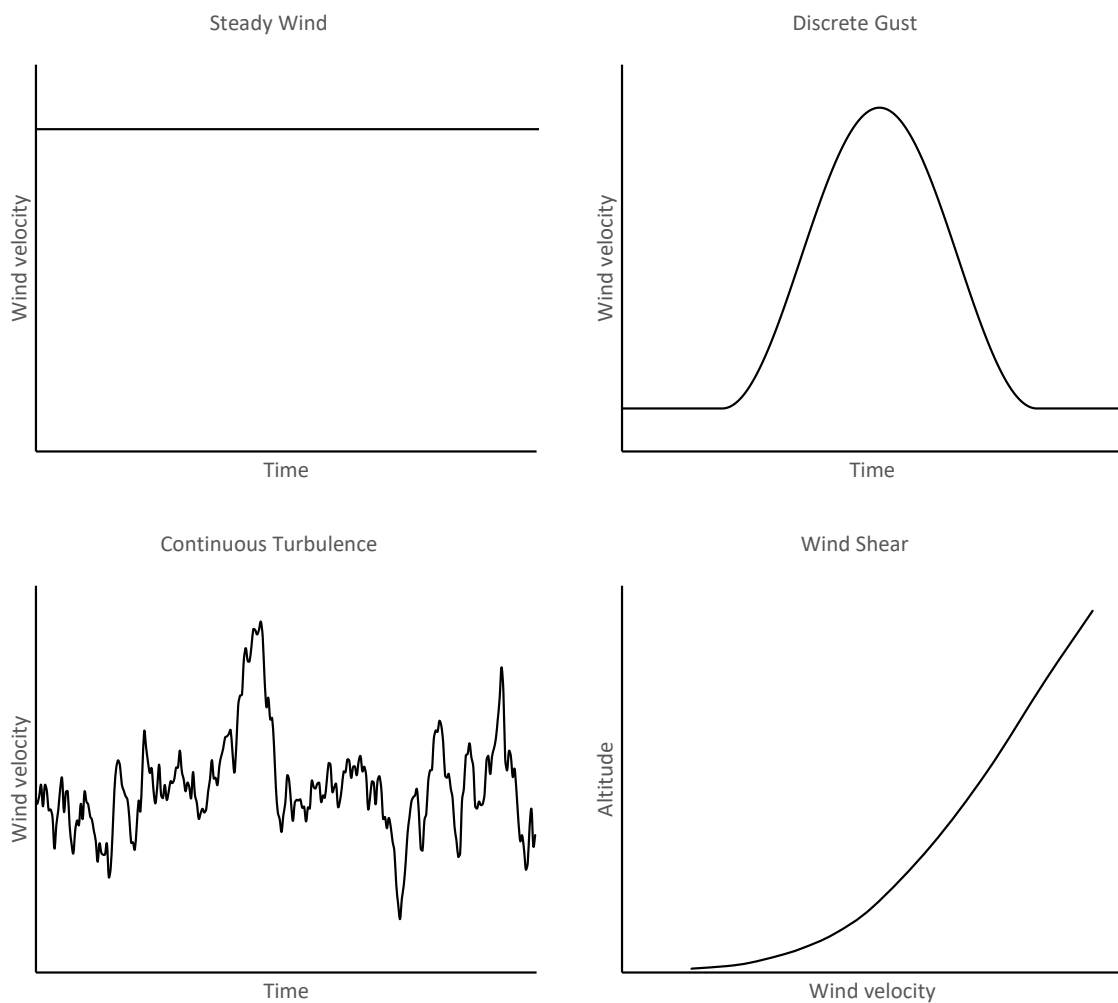


Figure 3.4: Wind speed profiles of different types of atmospheric disturbances.

The discrete gust is a simplified model for simulating the wind gust. It is usually a simple

ramp velocity profile extracted from continuous turbulence, the scale and magnitude are also derived from continuous turbulence (Cook 2012). In this research, a vertical discrete gust profile is used when simulating the 2D aerofoil encountering a gust wind (Chapter 5).

The modelling of continuous turbulence is usually given by filtering the white noise, according to the power spectral density (PSD) statistic character of the real atmosphere. Real turbulence is highly unstable and varies from time to time. To reduce the modelling complexity, it is simplified as a stationary wind field which is frozen in time but the velocity varies in different locations, which is the frozen field turbulence (Cook 2012). Currently, there are two widely used turbulence models, the von Kármán model and the Dryden model (DEFENSE 1997). The two models both define a linear velocity PSD, while the Dryden model also defines angular velocity. In the simulation of the 3D response of an aircraft in this research, the Dryden model is used to create a vertical gust profile. The equations of this model are presented in Chapter 8.

## 3.2 Lift Control

Manoeuvring flight is achieved by increasing or decreasing the lift of the wing or other aerodynamic surfaces in order to create pitching, rolling or yawing moments. This is achieved by changing the AoA, or by using hinged mechanical control surfaces and high-lift devices to increase the camber or the chord length of the wing or other aerodynamic surfaces.

In addition to flight controls for manoeuvre, modern transport aircraft use control surfaces for improving flight stability and quality. For example, a gust suppression system was introduced on the Boeing 787 to improve passenger comfort when the aircraft encounters gusts or turbulence. This can also be used to reduce the bending moment at the wing root, which can lead to weight saving. An airdata sensor detects a gust or turbulence to produce reference data for the flight controller, and then the aileron, elevator and spoilers rapidly compensate for the dynamic loading (Wagner & Norris 2009). Another example is the camber variable trailing edge found on the Boeing 787 (Nelson 2005), which optimises wing camber to compensate for the weight loss during cruise due to fuel burning. Figure 3.5 demonstrates typical control surfaces on modern transport aircraft.

On modern large transport aircraft, aerodynamic control is achieved through the coordinated operation of different control surfaces depending on the flight conditions. For example, the deployment of ailerons, flaperons and spoilers are typically coordinated for roll control at low speed, while at high speed, the flaperon alone is often sufficient to provide effective roll control (Reckzeh 2003, Nield 1995). Ailerons and flaperons also find applications for gust

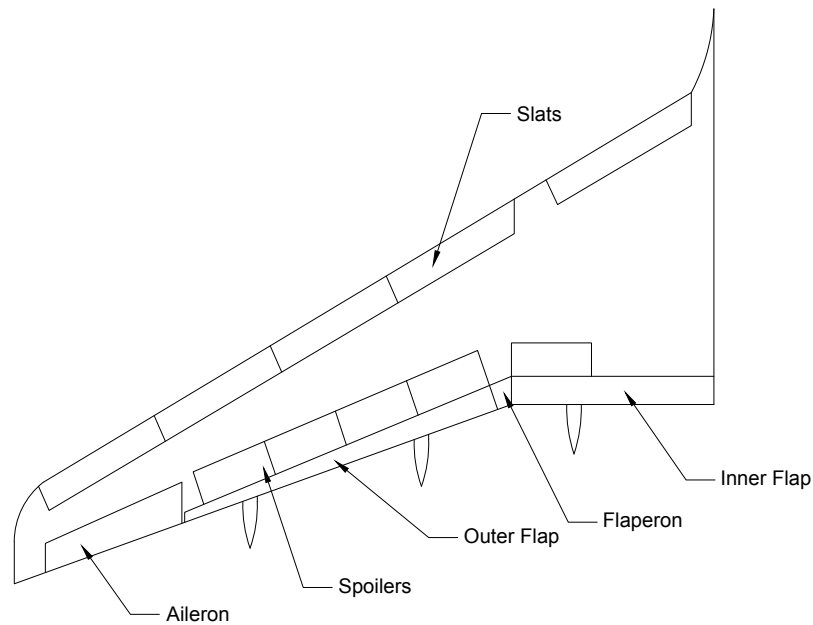


Figure 3.5: Typical control surfaces on modern transport aircraft.

alleviation. The dynamic loading can be reduced by rapidly deflecting these control surfaces (Walton et al. 2014, Kelm & Grabietz 2000). Figure 3.6 shows the flaperon of a Boeing 787 aircraft which is located between the inner flap and outer flap. (Wagner & Norris 2009)



Figure 3.6: The flaperon of a Boeing 787 aircraft (Wagner & Norris 2009).

Among all the control surfaces, the high-lift device is one of the most complex systems. Modern civil aircraft require a low drag during cruise and high lift during take-off and landing to reduce the required length of the runway. Traditional high lift devices include single hinged flaps, slotted flaps, plain leading edge flaps, Kruger flaps, split flaps and slats (Kundu 2010). The single hinged flap is very simple in shape and is commonly used in small general aviation aircraft. However, its performance is restricted by flow separation over the flap at high deflection angles, so the lift enhancement is limited. Therefore, most modern civil aircraft adopt both trailing edge slotted flaps and leading edge slats. A schematic of split flaps and slotted flaps is shown in Figure 3.7. The high-lift systems significantly increase the lift

coefficient at take-off and landing, as shown in Figure 3.8, which compares the lift increment of different types of modern high lift devices. Figure 3.9 is an example of the high lift devices used for the Boeing 737NG outboard wing (McLean et al. 1999). The cross-section shows a complex actuation mechanism with a hydraulic actuator. Although the slotted flaps produce a significant increase in lift, as shown in Figure 3.8, the additional structural weight and maintenance cost of the mechanical system cannot be overlooked.

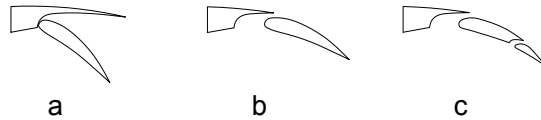


Figure 3.7: Schematic of different types of trailing edge high-lift devices, a: split flap, b: single slotted flap, c: double-slotted flap. (Kundu 2010)

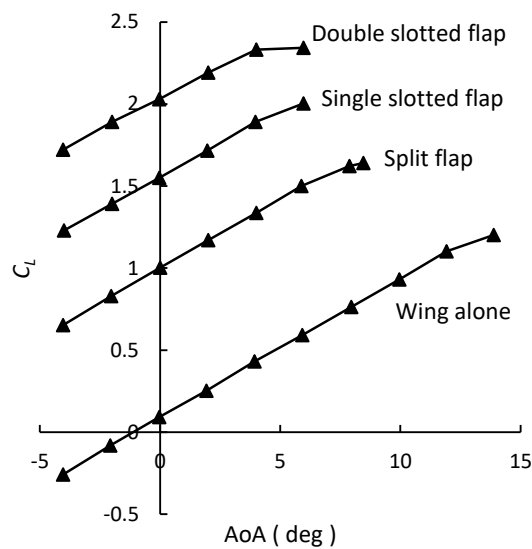


Figure 3.8: Experimental data of high-lift devices at  $Re_c = 4.4 \times 10^6$  (Dovey 2003).

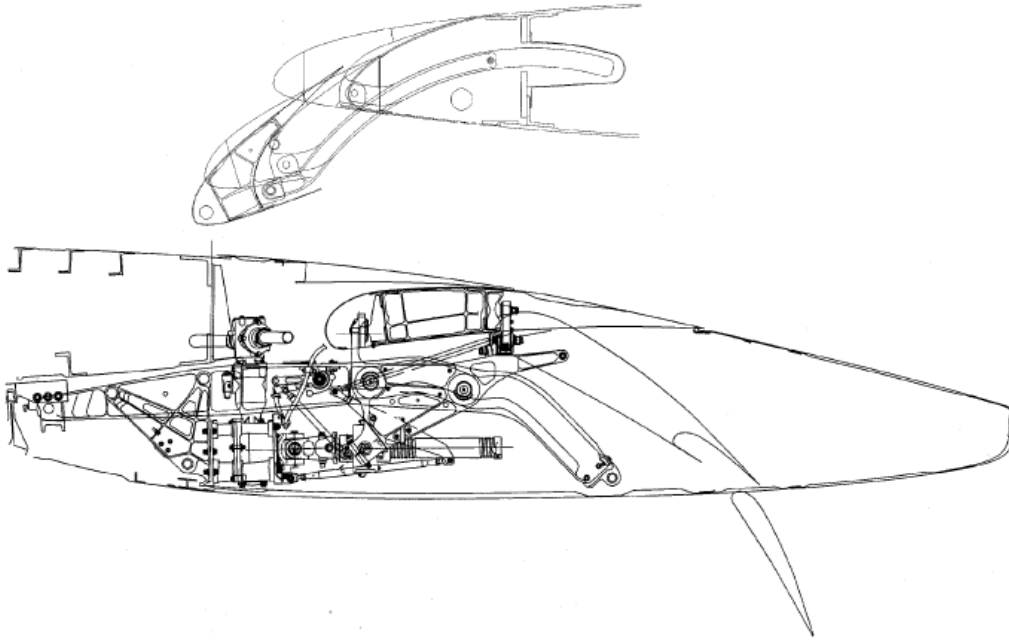


Figure 3.9: Outboard cross-section of 737NG (McLean et al. 1999).

Mechanical control surfaces, especially high-lift devices, can be complex, and their actuation systems require a large number of components. The flaps and leading edge slats require mechanical bearings and tracks to support the motion. Meanwhile, all the motion mechanisms are driven by hydraulic or electronic actuators. It was estimated that a trailing edge triple-slotted flap system alone consisted of 2880 parts (Rudolph 1996). The complex parts of the mechanical control surface significantly increase the cost of manufacture and maintenance, contributing to a significant weight increase. Therefore a simplification of control surfaces and their actuation can potentially reduce the cost and weight of the aircraft. From the history of civil transport aircraft, there is a tendency to simplify high-lift devices to reduce the system complexity, as shown in Figure 3.10. On the latest A350 XWB-900, the Adaptive Dropped Hinge Flap (ADHF) is used with lower complexity and lower cost to maintain (Strüber 2014). The dropped hinge flap is also found on the Boeing 787 (Nelson 2005).

### 3.3 Flow Control

Flow control can be described as manipulating or disturbing a flow environment using a relatively small amount of energy to achieve a favourable benefit for the global flow field, such as separation control, drag or noise reduction. An example of the most simple flow control device is a vortex generator which can often be found on a wing or in an air inlet to control boundary-layer separation. Figure 3.11 shows a schematic of a pair of vortex generators on

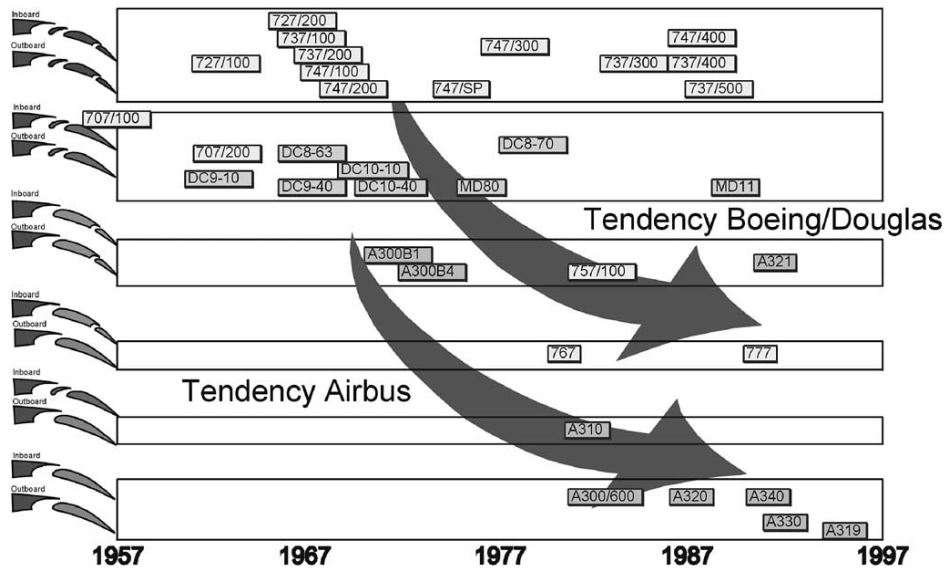


Figure 3.10: The tendency of high-lift systems (Reckzeh 2003).

the upper surface of a wing. Such devices are equivalent to small scale, low aspect ratio wings that generate a tip vortex that trails downstream, mixing the boundary layer with high velocity mainstream flow. Therefore additional momentum is injected into the boundary layer, which helps to suppress separation. Although the form and application of flow control may vary, their fundamental actuation mechanisms are similar, which is to inject energy into the unfavourable flow. According to the energy consumption of the actuation, there are two categories. The passive flow control, which doesn't require additional energy, and the active flow control, which requires external energy to drive an actuator.

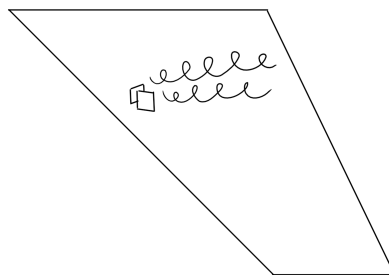


Figure 3.11: Schematic of passive flow control.

### 3.3.1 Passive Flow Control

The method of using geometrical structures to affect fluid flow by generating a vortex, triggering transition, eliminating vortex shedding, etc., is generally classified as passive flow control. It requires no energy and little maintenance therefore has been broadly used. Passive flow

control devices are always in operation even when it is not needed, thus may generate unfavourable drag at the off-design point.

A vortex generator is one of the most basic and widely applied forms of passive flow control devices. Figure 3.12(a) shows a vortex generator array on the upper surface of the wing. Such devices can delay flow separation at low speeds and high AoA, which improves the low-speed performance of the aircraft. Another form of vortex generator can be found on the nacelle of modern transport aircraft, as shown in Figure 3.12(b). This device generates a strong vortex that impinges the wing leading-edge / pylon intersection to energise the local flow and suppress separation at a high AoA.

Military aircraft typically have a cone-cylinder forebody, or strake on the fuselage side to reduce the side force produced by asymmetric vortices at high AoA. Such side force is particularly dangerous during low speed flight since the pilot may lose yaw control and even enter into a stall. Figure 3.12(c) shows a forebody strake on the X-31 research aircraft. Such devices control the forebody vortex system by producing two symmetric vortices that stabilize the aircraft and prevent asymmetric vortices that otherwise may form at high AoA.

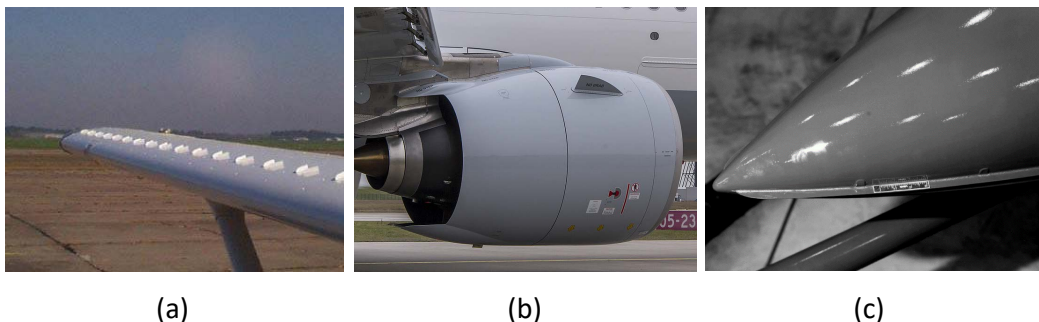


Figure 3.12: Passive flow control devices: (a)Vortex generators to enhance low speed performance, (b)Nacelle Vortex Generator, (c)Forebody strakes (Cobleigh 1994).

### 3.3.2 Active Flow Control

Active flow control generally utilises actuators to inject energy into the flow, typically with the aim of suppressing turbulence to maintain a laminar boundary layer, improving the energy of the local boundary layer, or lift enhancement by increasing the circulation around an aerofoil. In contrast to passive flow control, such as fixed vortex generators, active flow control is adaptive to various flow conditions, and it can be turned off when it is not required. Active flow control always involves energy transfer, usually consumes energy from an external source, and transfers energy to the local flow.

Active flow control techniques have various implementations in the modern aerospace in-

dustry. Figure 3.13 summarises current industrial applications of active flow control (Jones & Joslin 2006, King 2010, Joslin & Miller 2009).

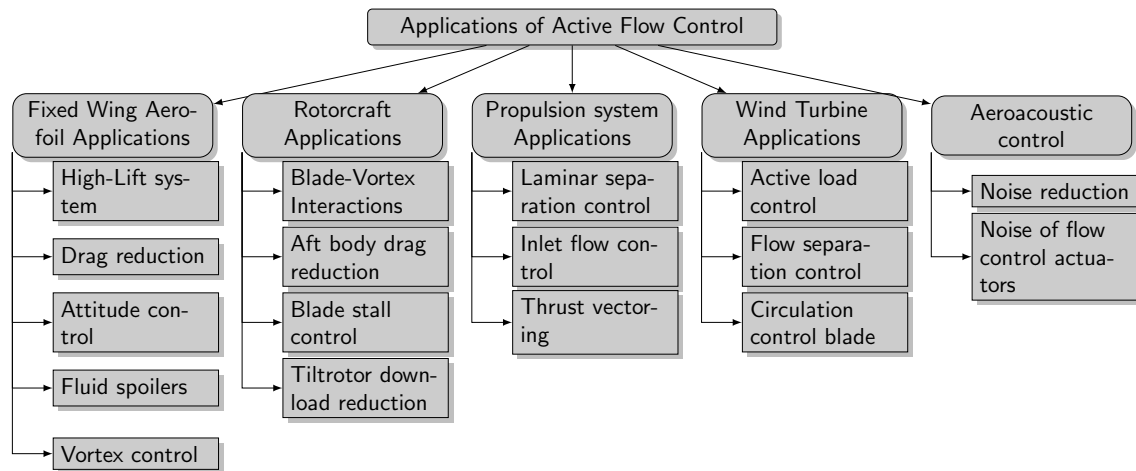


Figure 3.13: Summary of the active flow control implementations (Jones & Joslin 2006, King 2010, Joslin & Miller 2009).

The effectiveness of active flow control has been exemplified in the high-lift system of modern transport aircraft. In recent years, researchers have investigated a variety of experiments that proved active flow control has the potential usefulness of reducing weight as well as operational cost.

A potential application of active flow control, the CCW, has been suggested as a substitute for the conventional wing with slotted flaps and has been studied extensively for decades (McGowan et al. 2004, Golden & Marshall 2010, Buonanno 2009, Buonanno & Cook 2006, Savvaris et al. 2013, Yang et al. 2008, ENGLAR et al. 2009, Cagle 2002, Swanson et al. 2005b, Rogers & Donnelly 2004, Paschal et al. 2012). CCW generally involves a jet sheet that is ejected from near the trailing edge of the aerofoil at a fixed angle or tangent to a flap with a sharp trailing edge (Englar 2000a). Figure 3.14 shows a schematic of the CC flap. The jet from a slot exit on the shoulder of the flap attaches to the upper surface and remains attached in a region that would otherwise be separated. This produces a dramatic lift enhancement compared with the non-blown plain flap.

Compared with conventional mechanical slotted flap systems, the CC flap utilising a plain hinged flap, achieves an equivalent lift increase with a simpler mechanism that potentially reduces weight and maintenance costs. The blowing flap differs from a Coanda jet over a circular trailing edge. Although both configurations create additional circulation by increasing the flow velocity over the upper surface and preventing separation, the blowing flap does not change the rear stagnation point. Whereas on a circular trailing edge, the jet not only entrains

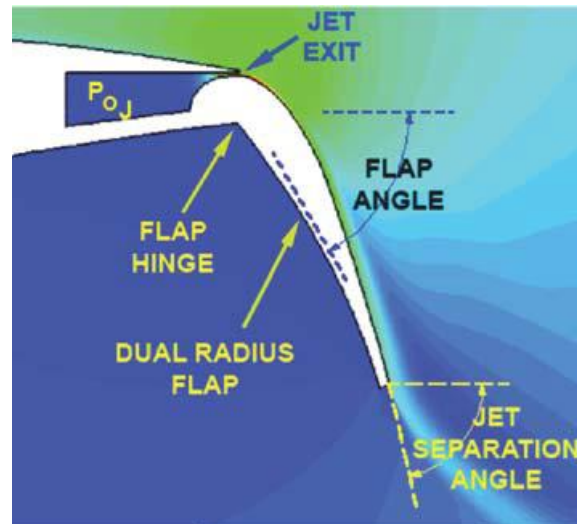


Figure 3.14: The CC blowing flap. (Jones et al. 2013)

the external flow but also moves the stagnation point further downward. From the control side, in the blowing flap configuration, the jet itself can not change the rear stagnation point which is controlled by the position of the flap, compared to the circular trailing edge where the jet can control the stagnation point. Although the lift increment by both configurations is similar (Jones & Joslin 2005).

### 3.3.3 Circulation Control

The active flow control based on jet actuation can be categorised into boundary layer control and CC, depending on the actuation amplitudes. For boundary layer control, a blowing jet with low actuation levels can eliminate flow separation over the wing by injecting energy into the boundary layer or mixing high-energy flow with low-energy boundary layer flow. Since it does not require much energy, a zero net mass flux jet actuator ( introduced in Page 66 ) can be used (Seifert & Pack 1999). Conversely, the CCW uses a high velocity jet to increase the overall circulation around the wing; it requires compressed air to produce a high speed jet and can increase lift significantly (Englar 2005).

#### Engineering application

Research into CC has a long history. Around the 1970s and 1980s, trailing edge CC devices were successfully demonstrated in several experimental studies as well as on a modified US Navy A-6 STOL (Short Take Off and Landing) aircraft (Englar 1979) (Englar et al. 1981). Wind tunnel results showed that a maximum section  $C_L$  (Lift coefficient) of 6.5 can be achieved, while the  $C_{L_{max}}$  of the 3D CCW can be increased by a factor of 2.2. The flight test results of

a demonstration aircraft equipped with a modified CCW showed that the CC can effectively increase the  $C_L$  thus reducing the take-off and landing speed. The highest trimmed lift coefficient achieved was 3.6, compared to 1.79 for the original mechanical flap. The method used on the A-6 aircraft was steady blowing without any controllers, and it was only used as a pneumatic high-lift device, wind disturbance was not considered.

Other applications have been found in transport aircraft and helicopters. Eppel et al. reported an investigation of a Quiet Short-haul Research Aircraft (QSRA) (Eppel et al. 1982). The aircraft has four engines above the wing of which the jet exhaust passes through the upper surface of the wing, as shown in Figure 3.15. Due to the Coanda effect, the exhaust jet from the engines is deflected downward by the curvature of the upper wing surface to reduce the take-off and landing distance. In addition, the trailing edge is modified to a rounded surface with a blowing slot for CC. The CC blowing on the trailing edge produces a further deflection of the exhaust jet of the engines from  $40^\circ$  to  $97^\circ$ . Therefore a large vertical lift is achieved. Eppel et al mention that a control system could be adopted to increase the manoeuvrability as the CC blowing can instantly change the thrust direction without any moving parts (Eppel et al. 1982). This concept is similar to that presented in this thesis.



Figure 3.15: The Quiet Short-Haul Research Aircraft (QSRA) (Huff 2013).

Reader et al. reported an application of CC on a high-speed helicopter rotor (Reader & Wilkerson 1977). CC slots were adopted on the leading and trailing edge of each rotor blade to control the lift at different phase angles periodically. A conventional rotor periodically changes the AoA of each blade in forward flight to avoid stalling the retreating blade and to balance the lift distribution relative to the advancing blade. The study demonstrated that the CC rotor could produce sufficient lift at an advance ratio (the ratio of flight speed to the blade tip speed) of 0.7, which is not achievable by conventional rotors. The application demonstrated not only the lift augmentation of CC but also the fast actuation speeds. This characteristic is also very

important for the application of gust control considered in this research.

In 2004, the NASA Langley Research Center, Office of Naval Research (NASA/ONR) Circulation Control Workshop summarised the relevant research. The applications of CC have also been expanded to propulsion systems and ground vehicles (Jones & Joslin 2005) (Jones & Joslin 2006). Kondor and Moore proposed an application of using CC to improve the off-design performance of a shrouded fan. Annular jet slots were adopted at the inlet and exit of the nacelle to control the flow into the nacelle and the exhaust. As there are no moving surfaces to morph the shroud, this method is simple and cost-effective. Experimental results show that the static thrust coefficient was increased by 30% with the actuation of inlet CC jets. It is a promising technique to improve the performance of vertical take-off and landing (VTOL) aircraft. The advantage of CC can also be used on ground vehicles such as heavy vehicle trailers. Englar has developed a CC device to reduce the drag and improve the safety of heavy ground vehicles (Englar 2000b). The device consists of an upper-blowing slot on the leading edge of the trailer and 4 aft slots on the trailing edge, as shown in Figure 3.16. Wind tunnel results show that the CC reduces drag up to 35% by reducing the flow separation over the trailer. In addition, by actively controlling the blowing, the drag, side force and lift can be controlled to improve the performance of braking and side wind resistance.

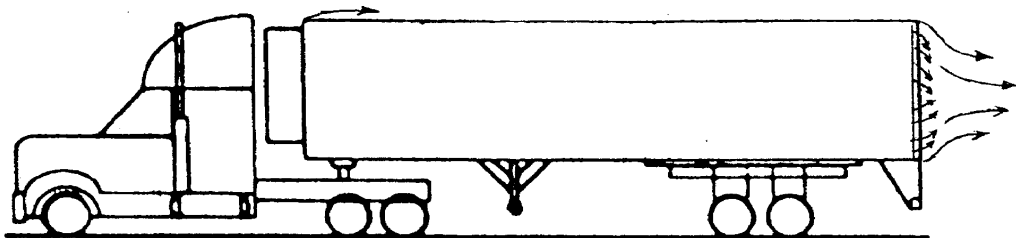


Figure 3.16: The application of CC on heavy vehicles, 4 aft blowing slots and one leading edge blowing slot are displayed (Englar 2000b).

A number of engineering applications were reviewed by N.Wood et al., and future research suggestions were given (Wood & Nielsen 1985). There are two future research areas suggested by Wood et al. that are relevant to the present research: unsteady aerodynamics and 3D aerodynamics. Many applications using CC experience rapidly changing flow conditions and blowing levels. The behaviour of a CC jet in unsteady flow is not fully understood. Moreover, most studies only consider 2D CC aerofoils, and it is necessary to extend this to understand the 3D flow developments, which are less clear, including the effects of sweep and the wing tip vortex. The present research is mainly focused on the unsteady performance of CC.

### Periodic blowing for CC

In the early years, CC mostly used continuous steady blowing. While Ghee et al. investigated the unsteady aerodynamics of CC by using periodic blowing. Results showed that the periodic blowing produces 100% higher lift augmentation (the slope of lift coefficient vs. blowing momentum coefficient,  $\Delta C_L/\Delta C_\mu$ ) than steady blowing (Ghee & Leishman 1992). The maximum  $C_L$  obtained by unsteady blowing is considerably higher than by steady blowing. The periodic blowing experiments also show strong hysteresis effects and phase lag between the blowing actuation and lift response. These effects are perhaps caused by the low actuation frequency in the research, as the periodic blowing is lower than 5 Hz. A broader frequency should be studied to understand the unsteady blowing effects fully.

The periodic blowing was also studied by the NASA-Langley Research Center with a General Aviation Circular Control (GACC) model (Cagle 2002). This wing model was derived from a GAW-1 aerofoil by modifying the trailing edge to a circular Coanda surface. The model was tested in a wind tunnel and a water tunnel. The pulsed blowing frequency was 35 Hz which is much faster than the research by Ghee et al. A maximum  $C_L$  of 3 was achieved when  $C_\mu=0.06$ , while the maximum  $C_L$  without blowing is less than 1.5. This compares with the original GAW-1 aerofoil, without a rounded trailing edge, which had a maximum  $C_L=2$  (McGhee 1980). By using pulsed blowing, the mass flow rate was reduced by 50% for the same lift. Their research also includes dual surface blowing for drag reduction using two slots tangential to the upper and lower surfaces of the circular surface respectively, thereby reducing the drag by 40%. The paper also presents the dynamic pressure distribution around the Coanda surface and the pressure around the trailing edge in response to the pulsed jet. With a 35Hz pulsed jet, the pressure around the trailing edge can respond to the dynamic pressure instantly without obvious delay or hysteresis. This indicated that the wall jet around the Coanda surface has a relatively fast dynamic response, at least for a periodic signal less than 35Hz. However, this paper lacks the time-history comparison between lift response and the blowing momentum coefficient, therefore the phase lag is unknown.

### Transonic and supersonic CC

It has been proved that CC is effective at low speeds, and during the last decade, supersonic applications have also received considerable attention. Robin Schlecht and Scott Anders have evaluated a transonic CC aerofoil and found that the elliptical Coanda surface has better performance than the circular trailing edge (Schlecht & Anders 2007). A parametric study has been conducted to compare the performance of different trailing edge geome-

tries. It was found that a 3:1 ratio (the ratio of the major axis to the minor axis) elliptical Coanda surface on the trailing edge is the most favourable geometry. This gave a maximum  $\Delta C_L=0.625$  at  $C_{\mu}=0.06$ ,  $AoA=6^\circ$  for subsonic condition ( $M=0.3$ ) and a maximum  $\Delta C_L=0.275$  at  $C_{\mu}=0.0085$ ,  $AoA=3^\circ$  for a transonic condition ( $M=0.8$ ). The study presents the effectiveness of CC in transonic flows, however, it only focuses on the steady-state results, and the dynamic or unsteady performance is not considered.

To increase the efficiency of the CC system and expand the application to a higher Mach number, the jet velocity needs to be increased. When the jet velocity is supersonic, a separation problem arises due to the shock wave structures in the jet. Recently, Bradley studied the effects of nozzle geometry for supersonic wall jets (Robertson-Welsh 2017). The characteristics of supersonic jet flow with different slot heights were experimentally investigated, and a mechanism for the separation of the supersonic wall jet was explained. It was found that the adverse pressure gradients cause separation bubbles, where the Mach waves are reflected and create a low-pressure zone which turns the flow towards the curved surface, and eventually, the flow reattaches to the surface. When increasing the nozzle pressure ratio, the reattachment point moves downstream, and the local separation zones are merged. Thus the wall jet will eventually fully separate. The use of a supersonic wall jet also increases control authority and allows a thinner trailing edge for CC to reduce drag. It is also noted that current studies of supersonic wall jets are all focused on continuous steady blowing, and the behaviour of unsteady actuation and the time-history response has not been considered.

### Computational methods for CC

The early studies of CC were mostly experimental, while the modern CFD provides new methods that contribute to a better understanding of CC. The NASA Langley Research Center provided experimental databases of a generic CC aerofoil for CFD code validation (ENGLAR et al. 2009, Paschal et al. 2012). Englar et al. conducted benchmark experiments for a bullet shape CC020-010EJ CC aerofoil (Figure 3.17). A CC wing section was used to perform the wind tunnel test, as shown in Figure 3.18. Surface pressure, lift and pitching moment data with various blowing conditions and nozzle heights were measured and have been used to validate CFD simulations by numerous researchers (Shires & Kourkoulis 2013, Nishino et al. 2010, Hoholis et al. 2016). The shear-stress transport (SST) turbulence model was used in a number of the CFD simulations, and results show that the CFD slightly over-predicts the  $C_L$ , pressure distribution and the velocity profile of the wall jet (Shires & Kourkoulis 2013, Hoholis et al. 2016). The same wing section model was also tested by Paschal et al. using LDV measurements

to provide boundary layer profiles (Paschal et al. 2012). CFD simulations were also performed and showed good agreement with experimental data in terms of pressure distributions.

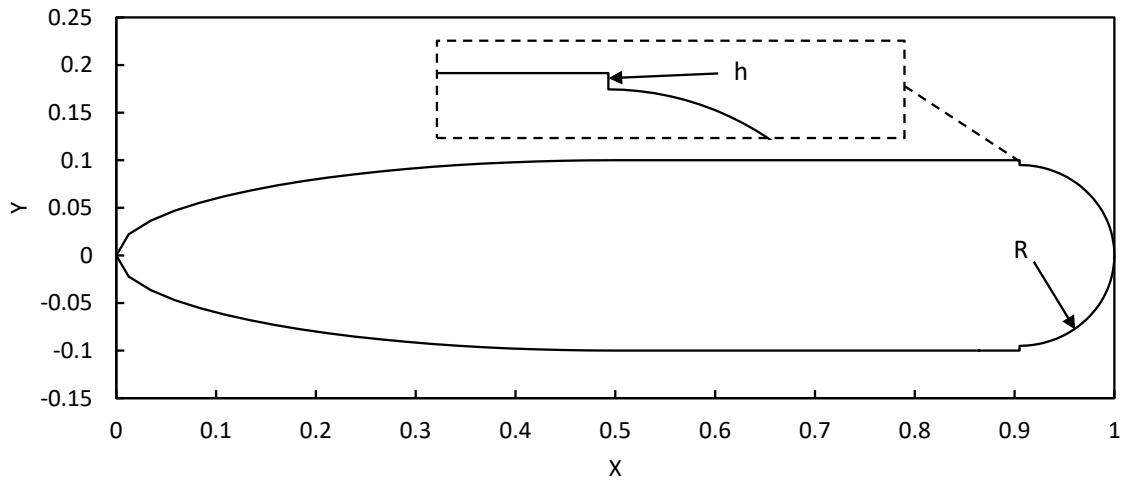


Figure 3.17: The sketch of the CC020-010EJ aerofoil (ENGLAR et al. 2009, Englar 1975a)



Figure 3.18: The CC wind tunnel model (ENGLAR et al. 2009).

The NASA/ONR Circulation Control Workshop also included benchmark databases for an NCCR 1510-7607N CC aerofoil (Figure 3.19) by experimental and CFD approaches. The aerofoil was simulated with various CFD solvers, turbulence models and grids to compare their performance. Such benchmark studies are reviewed in Chapter 5.

Table 3.1 listed the simulation studies of CC from the literature, there are fewer simulations for 3D wings or the full aircraft equipped with CC. One reason is the large computational cost required by such simulations. This is due to the large scale difference between the nozzle (typically less than 0.5mm) and the wing. To obtain a sufficient resolution of the jet flow and its shear layer, high-density meshes must be constructed around the nozzle which is already very small compared to the aircraft. It is not uncommon that the number of cells around the nozzle is larger than in the free stream region. For example, Ciobaca et al. presented a CC

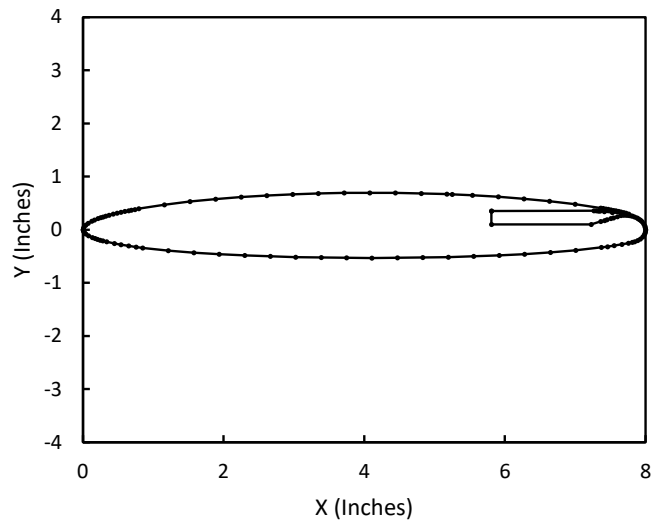


Figure 3.19: The sketch of the NCCR 1510-7607N aerofoil (Jones & Joslin 2005).

aircraft model with wing, fuselage, and engine consisting of 30 million cells (Ciobaca et al. 2013) and require approximately  $1 \times 10^5$  CPU hours for each of the setups. A more complex STOL aircraft model with propeller and CC flap requires 75 million cells (Keller & Rudnik 2015). Also, these 3D simulations are in steady states, the computational cost rises quickly for unsteady simulations. For example, in the unsteady simulation conducted by Yonghong Li (Li & Qin 2020) each setup requires  $1 \times 10^4$  time steps. The present research studied the unsteady behaviour of CC under various actuation frequencies, each setup needs approximately  $1 \times 10^6$  time steps. Considering the large mesh size and number of time steps, 2D simulations are preferred for unsteady CFD and 3D simulations can be used for steady CFD.

### Geometry of the Coanda surface

Although the circular Coanda surface is proven to be effective in lift enhancement, it has certain limitations at the cruise stage due to the considerable drag created when there is no blowing due to the bluff trailing-edge shape and increased wake thickness. Therefore some attention has been paid to the optimisation of the Coanda surface. Figure 3.20 gives examples of some existing Coanda surface designs used on the trailing edge. The circular shape (Figure 3.20 (a)) is a most simple Coanda surface that has a constant curvature. A jet flow is blowing tangentially from the top of the trailing edge and deflected by the circular surface. The maximum flow turning angle is mainly a function of the jet velocity and trailing edge curvature. As displayed in Figure 3.21 on page 62, for a circular shape trailing edge, the relationship between the separation point and the  $C_\mu$  is close to linear (Englar 1975b). Although the curvature of a circular shape remains constant, the jet velocity decreases after it leaves

Table 3.1: Summary of the simulation meshes for CC aerofoil

Authors	Geometry	Turbulence models	Dimension	Mesh size ( $\times 10^6$ )
Slomski et al. (2002)	NCCR 1510-7067N	Full-Reynolds stress model (FRSM) $k - \epsilon$	2D	0.17
Jones et al. (2002)	GACC	SA	2D	0.09
Paterson & Baker (2004)	NCCR 1510-7067N	$k - \epsilon$ $k - \omega$	2D	0.32
Liu et al. (2004)	GTRI-DR BL	SA	3D	N/A
McGowan & Gopalarathnam (2005)	GACC	SA	2D	0.12
Chang et al. (2005)	NCCR 1510-7067N	$k - \omega$ FRSM	2D+3D	0.15
Swanson et al. (2005a)	NCCR 1510-7067N	SA $k - \omega$ FRSM	2D	0.07
Swanson et al. (2005b)	LCC	$k - \omega$ $k - \zeta$	2D+3D	0.11
Baker & Paterson (2006)	CCW-LG	SA $k - \epsilon$ $k - \omega$	2D	0.33
Lee-Rausch et al. (2006)	GACC	SA $k - \omega$	2D	0.36
Slomski, Chang & Arunajatesan (2006)	NCCR 1510-7067N	LES	3D	18
Swanson & Rumsey (2006)	LCC	SA $k - \omega$ $k - \psi$	2D	0.43
Salem Said & Ragab (2008)	Coanda disk	SA $k - \omega$ $k - \epsilon$ FRSM	3D	2.62
Pfingsten & Radespiel (2009)	Transonic aerofoil with dual radius flap	SA	2D+3D	0.7(2D) 6(3D)
ENGLAR et al. (2009)	CC020	$k - \omega$	2D	0.5
Lichtwardt & Marshall (2011)	3D AMELIA aircraft	$k - \omega$	3D	37
Rumsey & Nishino (2011)	GTRI	RANS LES	2D 3D	0.45(RANS) 116(LES)
Ciobaca et al. (2013)	3D civil aircraft	$k - \omega$	3D	30
Keller & Rudnik (2015)	STOL aircraft	SA	3D	75
Li & Qin (2020)	Elliptic	$k - \omega$	2D	0.05

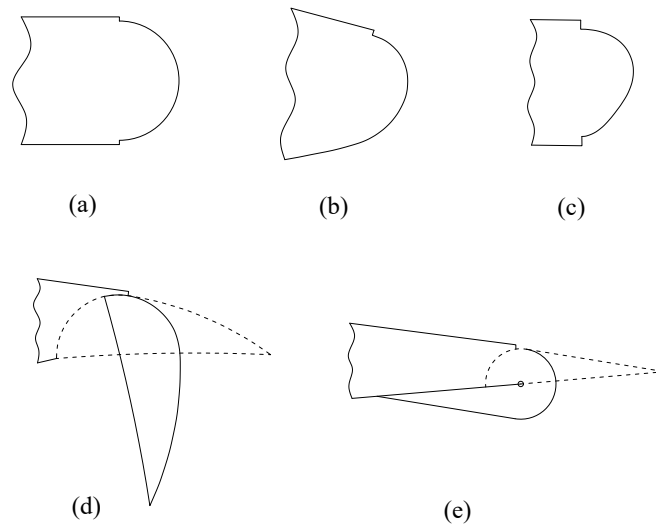


Figure 3.20: Examples of trailing edge surface for CC. (a) Circular (b) Logarithmic spiral (Slomski, Marino, Ebert & Abramson 2006) (c) Multipoint optimisation (Forster et al. 2016) (d) Dual radius (Golden & Marshall 2010) (e) Retractable (Englar 1975b)

the nozzle until it finally separates from the surface. Considering the curvature of the trailing edge, researchers have found that a decreasing curvature delays the separation of the jet flow. Peter A. Chang et al. (Slomski, Marino, Ebert & Abramson 2006) have studied the Logarithmic spiral trailing edge which has a continuously increasing radius from the jet exit, thus the curvature decreases and delays the flow separation. More recently, M. Forster has published an article about the multipoint optimisation of a Coanda surface shape which demonstrated favourable flow deflection both at low speed and high speed conditions (Forster et al. 2016).

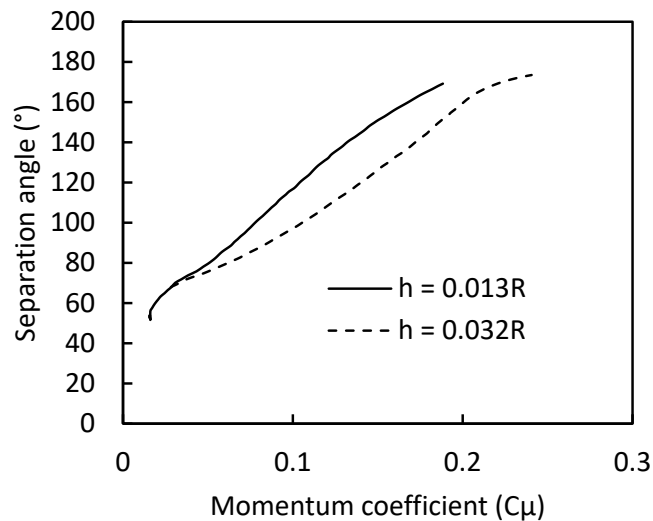


Figure 3.21: The location of the separation point versus  $C_\mu$  with different nozzle height,  $h$ : nozzle height,  $R$ : radius of trailing edge as displayed in Figure 3.17 on page 59 (Englar 1975b).

From another perspective, the three forms of trailing edge shape (Figure 3.20 (a)-(c)) all generate significant drag when blowing is not being used which is unfavourable during the cruise. Although CC has its advantage as a high-lift device, a major problem is that continuous blowing is required even at cruise to reduce the drag caused by the trailing edge. Therefore the dual radius flap (Figure 3.20 (d)) has been investigated (Golden & Marshall 2010). The dual radius flap consists of two arcs with different radius, and the arc with the larger radius is used during a cruise in order to reduce drag. For the landing configuration, the flap drops down with a smaller radius at the jet exit to deflect jet flow and achieves lift enhancement. This design combines the Coanda surface with the previous blowing flap and provides lift augmentation without sacrificing cruise performance. Another form of retractable Coanda flap (Figure 3.20 (e)) has a sharp trailing edge and a circular hinge (Englar 1975b). When the flap is deployed in the high lift configuration, the trailing edge is folded to the lower surface (as shown in the solid outline), and the hinge is exposed as a Coanda surface. Thus jet turning is achieved with minor changes to the aerofoil.

### 3.3.4 Closed-Loop Flow Control

Closed-loop control is a fundamental methodology in control theory. A closed-loop control system compares the actual output signal with the desired value and adjusts the input continuously according to the output deviation. Therefore the controller can amend the output automatically when it is disturbed. An example of the closed-loop control system is the automatic control of aircraft when the autopilot mode is enabled. The flight control computer will monitor the attitude and trim the control surfaces to maintain a level flight and pre-determined flight path. The aircraft may deviate from the desired heading when encountering a crosswind for example, and the autopilot computer will correct the direction without manual intervention. Recently, there has been a growing interest in applying closed-loop control to flow control systems. Closed-loop controllers can extend their effective range of operation and allow them to adapt to various conditions. It also reduces energy consumed by decreasing the actuation level when it is not required.

Closed-loop flow control can be utilized in automatic stall prevention of the wing. In 2002, Mehul P. Patel et al. developed a close-loop separation control system with deployable vortex generators (Patel et al. 2002). The system detected flow separation by monitoring the pressure fluctuation level from a pressure sensor array along the chord. When a stall is detected, the vortex generator array is deployed automatically. The controller was developed using the LabVIEW environment and Data Acquisition Board.

Similarly, Patel et al. also used pressure fluctuation as an indicator of flow separation to trigger the actuator when the incipient stall occurs (Patel et al. 2007). Their study was based on plasma actuators located on the leading edge and designed as an amplitude Peak Sense and Control method. Because the research was mainly for low Reynolds number, the pressure tap was mounted close to the leading edge where a separation bubble could occur at high AoA. Therefore, the method is only effective at a limited range of Reynolds number.

Becker et al. applied a closed-loop control technique to a periodical blowing flap (Becker et al. 2007). Two pressure sensor arrays are mounted beneath the flap, located close to the leading edge and trailing edge respectively, as shown in Figure 3.22. The flow separation over the flap was identified by comparing the differential pressure between the leading edge and trailing edge sensor arrays. If their pressure values are close to each other, which indicates the sensors are in the separation zone, the actuators will deploy and prevent further separation. Since the actuators are only excited when separation is detected, they turn out to be more efficient compared with continuous blowing. However, a major problem with Becker's method is that the actuators only deploy after the separation occurs, which means that the wing will

enter a stall for a short period of time before the reaction of the actuators. This is dangerous in real flight since the aircraft may have lost altitude during the stall.

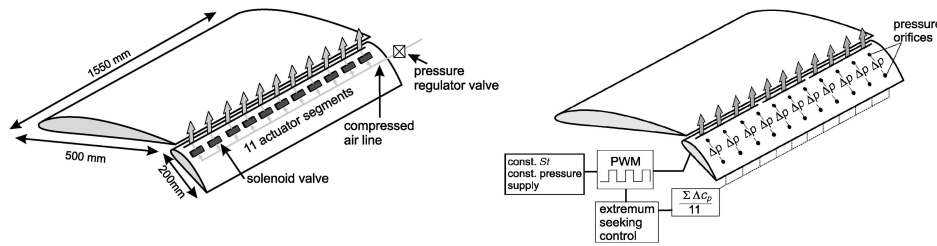


Figure 3.22: Actuator and sensor arrangement of the adaptive closed-loop separation control model (Becker et al. 2007).

The closed-loop flow control is particularly useful in wind gust suppression since the stochastic load on the wing can not be eliminated by steady control. Kerstens et al. conducted experiments with a semicircular wing to actively maintain a constant lift in gusting flow by using variable-pressure pulsed-blowing actuation (Kerstens et al. 2011). The wind gust signal was measured from a hotwire anemometer and  $H_\infty$  controller (the H-infinity controller design method) was used to suppress lift oscillations. In order to establish a robust control system, a dynamic model was obtained by exciting a pseudo-random binary signal (PRBS) and measuring the response with a six-component force balance. Results show that fluctuating lift was significantly reduced by the active controller.

The robust design of a controller deals with the modelling uncertainties of the dynamic system, sensor noise and measurement delays. Such uncertainties are inevitable in experiments, robust design is to assure the stability of the system in a given model family with uncertainties. As a robust design method,  $H_\infty$  approach resolves a control structure to minimise the cost function and satisfy the stability requirements (Skogestad & Postlethwaite 2007), this strategy has been applied in several flow control experiments (Henning et al. 2007, Williams et al. 2010, Heinz, King & Gölling 2010, Kerstens et al. 2011). In these experiments, the controller only deals with active flow control actuators, the actuators are not coupled with the aircraft attitude. This is different to the present study where the longitudinal motion due to gust is considered, and the actuator affects the aircraft motion. Moreover, the present study is based on CFD simulations for both the design process and the test process, the modelling uncertainty is relatively small since there is no mechanical friction, delay or vibrations. The input variable is extracted from instantaneous CFD results so there is no 'sensor noise' compared to experiments. Consequently, robustness is not a concern, and more attention was paid to the multi-variable design of the control structure. However, it is difficult to achieve the desired structure in the  $H_\infty$  approach (Stevens et al. 2015) so it is not suitable for this research.

Further discussion about the selection of controllers is explained in Page 38

Although flight test of flow control has a long history since the 1970s; when Englar first tested CC flap on the A-6 aircraft (Englar 1979). most of the flight tests in the early years were open-loop. Notger Heinz and Rudibert King studied the closed-loop control of lift by a numerical approach (Heinz, King, Höll, Wassen & Thiele 2010). The dynamic response of flow control was identified and a controller was designed. Subsequently, Rudibert King et al. successfully tested a blown flap using a motor glider (King et al. 2013). Figure 3.23 shows the glider and actuation slots on the flap. Two arrays of pressure sensors were located on the flap to measure the pressure gradient which further provides the feedback signal of the controller. Flight results showed that the flow actuators delayed the separation and suppressed disturbances.



Figure 3.23: Stemme S10-VT with two pods for carrying pressurized air and the actuation slots on the flap (King et al. 2013).

On the aspect of control algorithms, novel controllers have been demonstrated by Cai et al. (Cai et al. 2015). An iterative learning control approach was provided to actively increase  $C_L$  and delay separation. Although novel control algorithms are not the focus of the current research, it is a very promising direction for future research.

### 3.4 Actuators and Sensors for Flow Control

As a cross-disciplinary subject, active flow control involves Fluid Mechanics, Electronics, Automatic Control and Manufacturing. Actuators and sensors are fundamental technologies that bridge the gap between theoretical analysis and simulation and industrial applications. It is not feasible to utilise active flow control without the availability of reliable actuators and sensors. This section discusses the progress of relevant technologies and some of the latest flow control devices. Although some of the actuators and sensors are not used in the scope of this thesis, they are based on similar theories and methodologies. A review of such literature contributes to a deeper understanding of the techniques used in this research. Moreover, closed-loop control algorithms were designed in this study, and the input to the algorithms requires sensors

to get attitude, airspeed or AoA information. This review, therefore, discusses the available sensors for closed-loop flow control and their feasibility in engineering applications.

### 3.4.1 Actuators

A considerable amount of literature has been published on flow control actuators. These studies present some novel types of actuators with the latest technology in electronic engineering and micro-electro-mechanical systems, aiming to improve the jet velocity and actuation bandwidth, as well as reduce energy consumption. In terms of excitation methods, flow control actuators are classified into fluidic, moving surface and plasma. Louis and Cattafesta have thoroughly reviewed the progress of flow control actuators as shown in Figure 3.24, and summarized their advantages and drawbacks (Cattafesta III & Sheplak 2011).

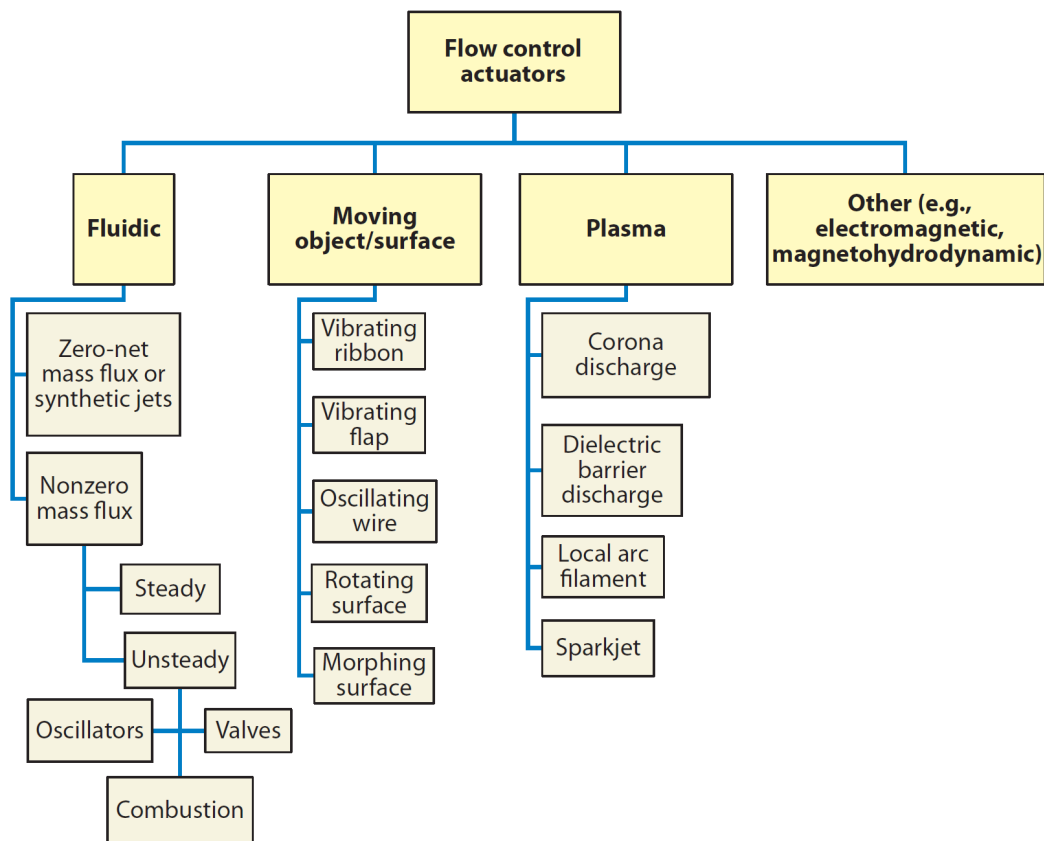


Figure 3.24: A type classification of flow control actuators. (Cattafesta III & Sheplak 2011).

#### Fluidic Actuators

Fluidic actuators, which include Zero Net Mass Flux (ZNMF), pulsed/continuous jet, vortex generator jet (VGJ) (Johnston & Nishi 1990), fluidic oscillators and powered resonance tube (PRT) (Raman et al. 2004), are pneumatically-driven actuators and utilise air jets to affect the

downstream flow.

ZNMF is one of the most widely-used actuators in many different kinds of flow control applications. A basic ZNMF actuator involves a cavity with an orifice and solenoid / piezoelectric components. The cavity volume changes periodically to suck and eject air from the same orifice. Each ejection cycle creates a synthetic jet out of the orifice and injects momentum into the flow. The unique feature is to transfer linear momentum to the flow system without net mass injection across the flow boundary (Glezer & Amitay 2002). It is also an ideal device for feedback flow control due to the convenient regulation of the duty cycle and adjustment of jet velocity.

Pulsed/continuous blowing has successfully demonstrated its effectiveness in separation control, lift enhancement, drag reduction and acoustic applications. It usually requires an external flow source to supply a continuous mass flow and produces a jet through a nozzle or solenoid valve. Compared with ZNMF, the blowing can be much stronger with a sufficient compressed air supply. Thus it is suitable for CC, which requires a particularly high flow rate (Englar 2000a). The main disadvantage of pulsed/continuous blowing is the requirement of a flow source. In laboratory experiments, the mass flow can be supplied conveniently by air tanks or compressors. But in airborne applications, the only feasible source is to bleed air from the engines, which will inevitably influence the thrust. The air bleeding from jet engines has been investigated by Gill et al. (Gill et al. 2007). For a modified AMT Olympus micro jet engine, results show that the engine bleed has a greater effect on the engine's performance at the lower throttle. At 100% throttle, the bleed has an insignificant effect on the thrust, when the throttle is lower than 75%, the thrust is reduced by around 15% due to the engine bleed.

The vortex generator jet, fluidic oscillators and powered resonance tube actuators are not discussed in detail since they are not directly relevant to the current research.

### **Moving Surface Actuators**

Moving surface actuators are excited by a small piezoelectric device, and can fluctuate rapidly but within a narrow range. A Piezoelectric Flap is one of the most commonly-used moving surface actuators and is usually mounted close to the trailing edge for separation control (Seifert et al. 1998). More recently, Morrison et al. presented another small-scale flow actuator based on the piezoelectric effect, using active dimples (Morrison et al. 2006, Dearing et al. 2007). As is shown in Figure 3.25, the excited piezoelectric material can bend the elastomer and generate a depressed dimple. Similar to vortex generators, the active dimple produces a pulsed cavity flow that induces a turbulent boundary layer which is more resistant to separation.

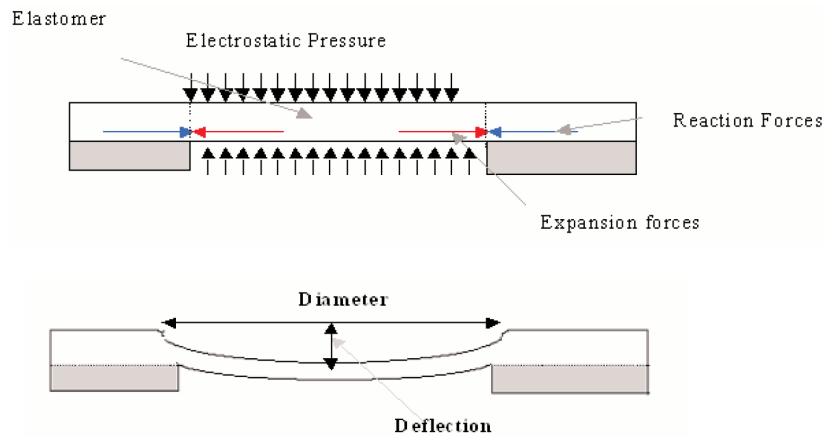


Figure 3.25: Principle of operation of a dimple. (Dearing et al. 2007).

### Plasma Actuators

Actuated by dielectric barrier discharge, plasma differs from the fluidic or moving surface actuator and has no moving parts. A plasma actuator produces a high-velocity synthetic jet triggered by electronic discharge and thus introduces momentum to the flow field. Plasma actuators have been attracting considerable interest since the early years of this century for the advantages of high bandwidth and low mass. However, plasma requires a high voltage, and the velocity output is limited and so is not suited to CC.

### Combustion and Spark Jet Actuators

Recent developments in actuators have focused on high output velocity, fast response and low energy-consuming techniques. Several attempts have been made to develop such high-performance flow control devices. The Combustion-Driven Actuator Concept, presented by T. Crittenden et al. (Crittenden et al. 2001), involves a small-scale combustion chamber with a spark igniter. In each combustion cycle, premixed fuel and oxidizer are injected into the chamber through an orifice on the bottom, and then ignited by the spark to generate a high-speed jet. However, due to limitations of the ignition method, combustion actuators cannot achieve a very high frequency and are not suitable for feedback control. Similarly, the spark jet actuator, invented by Grossman et al. (Grossman et al. 2003), is also driven by electronic discharge. Since no fuel is injected into the actuator, the chamber is heated by a spark directly, resulting in an instantaneous high pressure to drive an air jet. Figure 3.26 explains the three stages of the operation cycle.

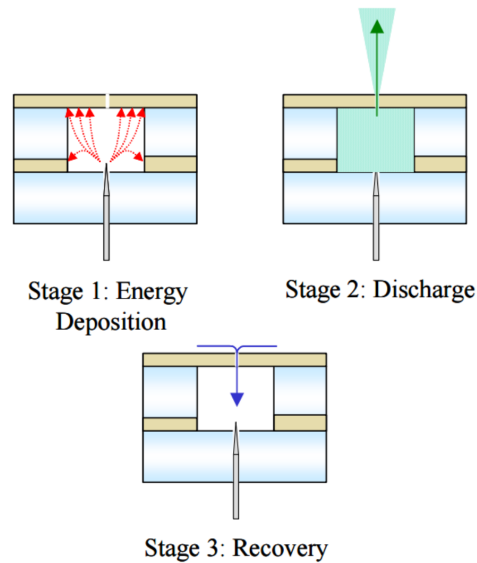


Figure 3.26: Stages of the SparkJet operation cycle (Grossman et al. 2003).

### 3.4.2 Excitation Parameters

Previous investigations have conclusively shown that unsteady actuation has a higher efficiency compared with steady or constant excitation of flow control actuators. In many unsteady actuation applications, an optimised actuation signal with appropriate frequency and amplitude may achieve equivalent augmentation as continuous actuation. Unsteady excitation has been widely used in most actuators, including ZNMF, fluidic oscillators, moving surfaces and combustion/spark jet actuators, since their method of action is inherently periodic. The most basic actuation signal of these actuators is the square wave which is easily amendable for different duty cycles, frequencies and amplitudes. Moreover, there are several researchers that have explored other waveforms for actuation. However, the shape of the waveform may also influence actuation performance. For example, Margalit et al. studied the effect of different signals applied to Piezo-electric actuators on a delta wing model at high AoA (Margalit et al. 2002). Three different input signals of excitation were used in the study, where it was found that burst mode with a small duty cycle is the most effective, as shown in Figure 3.27. Where the BM stands for burst mode and the AM stands for amplitude modulation.

The actuation parameters are restricted by the characteristics of the flow control actuators. Unlike the ZNMF which is mainly based on acoustic signals and can respond to a wide range of frequencies, the pulsed blowing actuator is restricted by the performance of flow valves. Current valves are mainly based on mechanical components to open and close the flow nozzle. The rotating valve, introduced by McManus & Magill (McManus & Magill 1996), is firstly used in separation control, and Figure 3.28 shows a schematic of their rotary valve. The pulsed

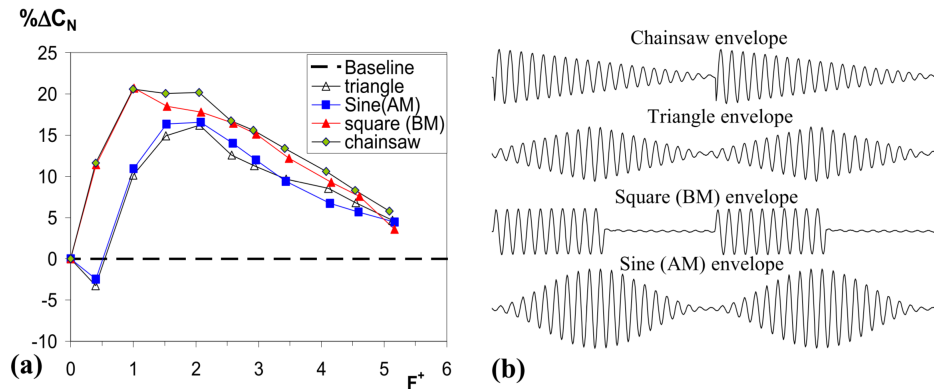


Figure 3.27: The effect of modulating envelope shape on Integral parameters vs. non-dimensional excitation frequency ( $F^+$ ). (a) Normal force coefficient ( $\Delta C_n$ ), (b) Waveform (Margalit et al. 2002).

frequency was controlled by the rotary speed, but the duty cycle is unchangeable. Jones et al. used a high-speed solenoid valve to generate a pulsed flow with variable frequency and duty cycle (Jones et al. 2002) for CC on high-lift systems. To produce a uniform spanwise blowing, each of the actuators is independently controlled. More recently, Choi et al. developed a rotating cap which consists of several orifices covered with a teeth-shape ring (Choi et al. 2006). Each of the orifices opens once during one cycle, as shown in Figure 3.29. This valve has been used to control the supersonic impingement tones, a high amplitude acoustic tone that occurs when a short take-off and vertical landing (STOVL) aircraft hovers close to the ground (Choi et al. 2006).

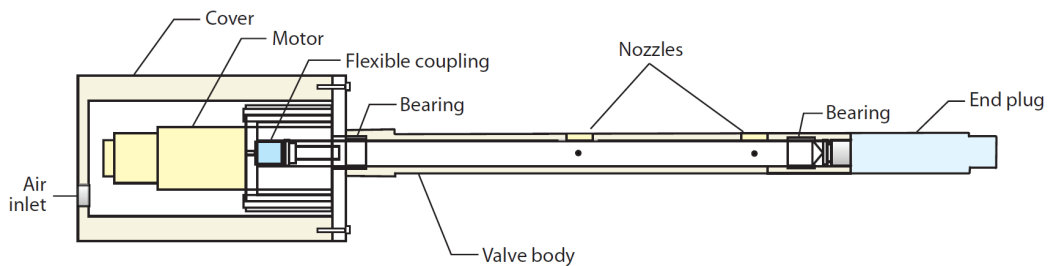


Figure 3.28: Schematic of a rotary valve. (Cattafesta III & Sheplak 2011).

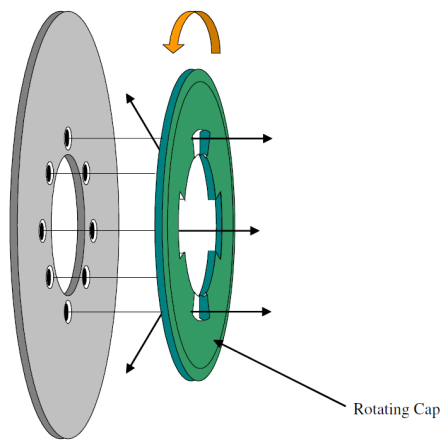


Figure 3.29: Conceptual diagram for rotating cap actuator (Choi et al. 2006).

### 3.4.3 Sensors

Close-loop control also requires sensors to obtain the state of the controlled object. In the implementation of active flow control, sensors are used to acquire information in the local flow field. The flow field information can then be used to evaluate whether a flow separation occurs or to calculate the flow angle and aerodynamic force, for example.

Sensors play an important role in wind tunnel experiments to acquire parameters such as pressure, velocity, temperature and force. Almost all the experimental results are based on direct or indirect measurements of the flow. In the wind tunnel test section, a frequently used device is the multi-component balance, which gives moments and forces in multiple axes. A typical wind tunnel model is also equipped with pressure sensor grids to acquire its pressure distribution over the surface. In addition, a multi-hole probe or hot wire can be used to measure the wake vortices (Chanetz et al. n.d.).

With regard to flow control, especially airborne feedback flow control, only a limited number of sensors are appropriate. Airborne devices are exposed to an extreme temperature range, and vulnerable to contamination or icing. Therefore some of the precise and high-bandwidth laboratory sensors, such as hot wires, are not suitable for in-flight measurement. Moreover, the direct force measurement is difficult to achieve since it is hard to mount a balance on the wing spar, and though it is possible to use strain gauge sensors, their bandwidth is limited.

Wind gusts create flow disturbances and rotation or acceleration of the aircraft body (Williams et al. 2010). This can be obtained from an AoA sensor or inertial sensors such as a gyroscope and accelerometer. The AoA sensors (e.g. vanes) are mounted on the nose of the aircraft to capture the flow angle and feed into the control loop. The inertial sensors can directly provide rotation rate and acceleration in three directions. Such sensors can also be placed in the fuselage to measure the rigid body movement, or in the wing to sense the structural twist and bending (Vartio et al. 2005). Moreover, there are laser-based sensors that can detect the flow velocity using the Doppler effect, such as the multifunction light detection and ranging (LIDAR) system (Cates et al. 2013). The LIDAR can detect the flow velocity and direction at around 500m ahead of the aircraft to provide a preview of the gust information (Hamada et al. 2020). The following table compares the sensors available for gust detection.

Table 3.2: Comparison of sensors for gust detection

Sensor type	Gust preview distance	bandwidth	Weight	Power consumption
LIDAR(Hamada et al. 2020)	500m	1000Hz	83.7kg	936W
Vane (Vartio et al. 2005, UTC 2017)	10 - 20m	Less than 10Hz	≈ 1kg	100 - 400W
Inertial sensor (Honeywell 2021)	0m	≈200Hz	0.02 - 3kg	0.5 - 10W

The LIDAR system provides the longest detection distance ahead of the aircraft; however, it is relatively heavy and unsuitable for small UAVs. The aerodynamic vane has limited bandwidth therefore it can only detect low-frequency gusts. For inertial sensors, although they can not provide preview information of the gust, their high bandwidth and lightweight characteristics are ideal for UAVs. The inertial sensors are equipped in almost every modern aircraft as a standard input of control variables for the autopilot system. For the longitudinal movement, the variables achieved from inertial sensors include axial acceleration  $\dot{u}$ , vertical acceleration  $\dot{w}$  pitch rate  $q$  and pitch angle  $\theta$ . The system states can be directly acquired or estimated according to these variables. These variables are also used in the controller design in Chapter 5 on page 124 and Chapter 8 on page 235. The integration of sensors in control algorithms was discussed in Section 2.6 on page 38.

### 3.5 Applications of Flow Control on Modern Aircraft

The flow control technologies demonstrate opportunities for increased efficiency in the next generation of aircraft. Stanewsky has thoroughly reviewed the cutting-edge progress in flow control as well as adaptive wing technology (Stanewsky 2001). Figure 3.30 summarises some of the flow control applications to be considered in future wing design. In this section, the literature that focuses on modern industrial applications is reviewed. The following applications are either already used on the aircraft, or experimentally tested and will be used in future aircraft.

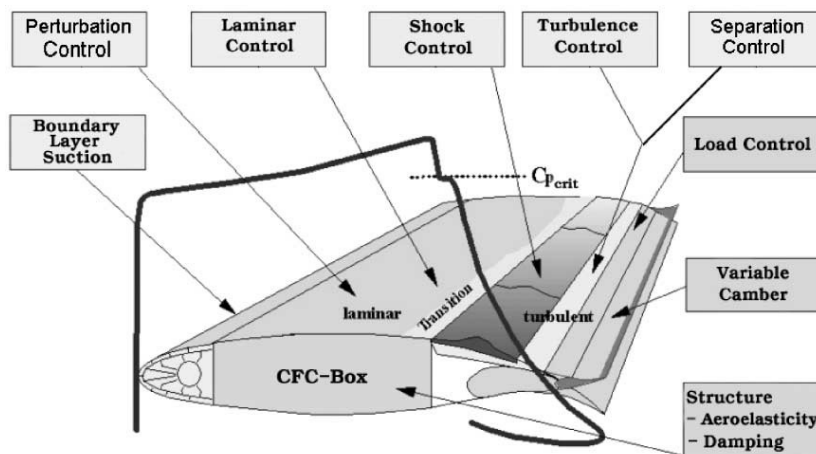


Figure 3.30: Wing-adaptation and boundary layer control devices (Stanewsky 2001).

### 3.5.1 Application on Unmanned Aerial Vehicles

In the field of Unmanned Aerial Vehicles, flow control, especially the CC shows a significant advantage over traditional mechanical control surfaces since it has no moving parts. The FLAVIIR project funded by BAE and EPSRC aims to design low-cost flapless UAVs (Fielding & Smith 2006). The UAV was derived from a pre-existing “Eclipse” aircraft. As a part of the project, conventional mechanical control surfaces were replaced by CC slots, as shown in Figure 3.31. Its demonstration flight is considered to be the first flapless flight with approval from the Civil Aviation Authority (CAA) (Buonanno 2009, Savvaris et al. 2013, Buonanno & Cook 2006).

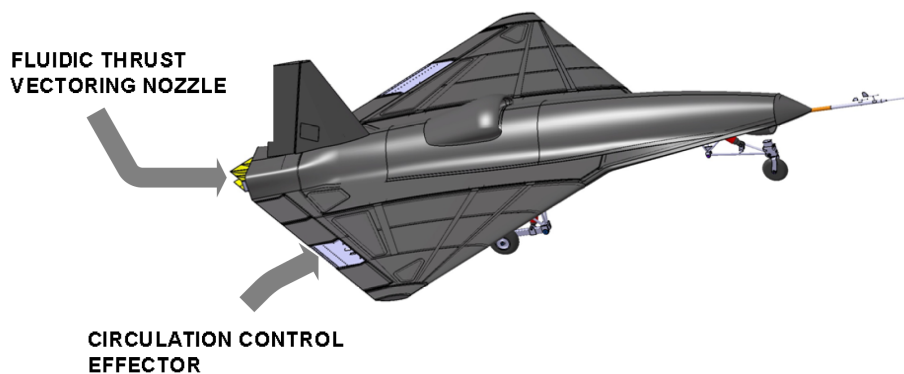


Figure 3.31: The Demon UAV (Buonanno 2009).

Flow control can also provide novel control techniques for delta-wing aircraft which has unique aerodynamic characteristics. The application of flow control to the delta wings focuses on vortex control at high AoA and improves manoeuvrability at level flight. For example, Margalit et al. used piezoelectric actuators on the leading edge of a delta wing to expand the post-stall operation range (Margalit et al. 2002). It is also capable of changing the rolling moment by exciting only certain actuators of the leading edge. Recently, Williams and Seidel combined leading edge and trailing edge actuators on a delta wing UAV model and attempted to control lateral/directional moments by coordinated activation of the actuators (Williams & Seidel 2016). The actuators are located on the apex, mid-span and trailing edge, as is shown in Figure 3.32. Results indicate that pneumatic actuation can produce the moments required for a coordinated turn by changing the symmetrical flow pattern over the surface of the vehicle. Furthermore, flow control devices have the potential to replace mechanical devices such as spoilers. Harley, C.D. has studied the aerodynamic performance of low form factor spoilers (Harley 2011). The Micro Geometric Spoiler and Counter-Flow Fluidic Spoiler

have been compared using CFD URANS methods, a schematic of these spoilers is shown in Figure 3.33. The length of the Micro Geometric Spoiler is very small, it is of a similar order to the thickness of the boundary layer. The Counter-Flow Fluidic Spoiler is a device with a blowing slot that produces a jet sheet in the opposite direction of the free stream flow. Both of them can be used for reducing lift and increasing drag. Results show that the Counter-Flow Fluidic Spoiler has better control linearity and less pitching moment, compared with the Micro Geometric Spoiler. Both spoilers have a low form factor which means they require minimum volume for installation compared with conventional spoilers.

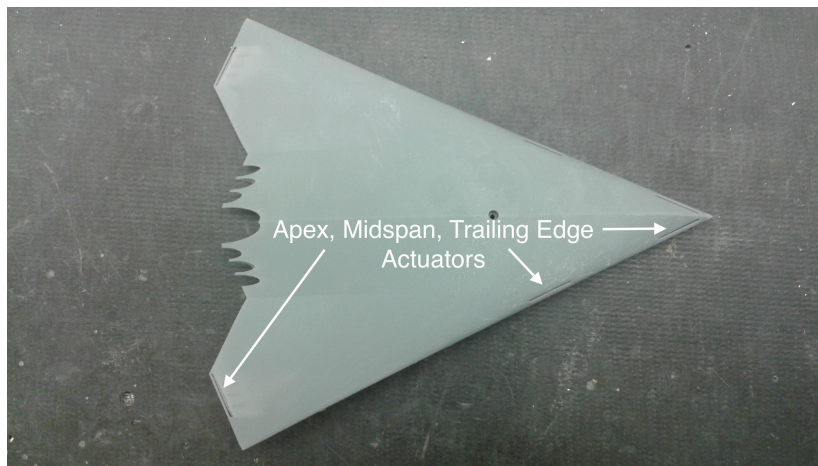


Figure 3.32: Photographs of the hybrid model with actuators on the apex, midspan and trailing edge (Williams & Seidel 2016).

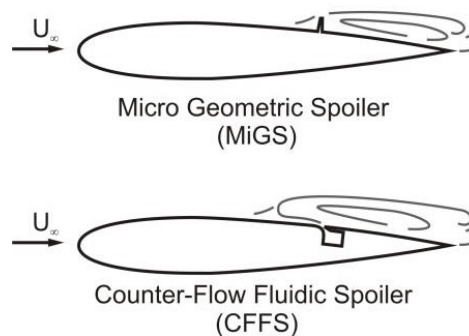


Figure 3.33: The micro geometric spoiler and counter-flow fluidic spoiler (Harley 2011).

### 3.5.2 Application on Civil Transport Aircraft

The next-generation civil transport aircraft requires high-efficiency wings. Advantaged leading and trailing edge concepts with active flow control have the potential to simplify the current high-lift system and reduce the overall weight of the wing. The past decade has witnessed the

rapid development of the active flow concept for future transport aircraft.

NASA Langley research centre has conducted a list of studies towards the active flow control actuators and wing integration, from the development of new pattern high-performance actuators to the comprehensive study of mechanisms (Schaeffler et al. 2002), as well as CFD validation experiments (Jones et al. 2008). In a recent study, a fuselage-wing model (FAST-MAC model) based on a supercritical wing has been studied with experimental and CFD methods, aimed at evaluating the flow control high-lift devices (Milholen et al. 2010) (Jones et al. 2013). A dual radius trailing-edge blown flap definition was adopted in the research. CFD simulation results were compared with wind tunnel Schlieren photographs (showing density contours) and a lambda shock was observed at the adjacent area between the two different radius surfaces, see Figure 3.34 .

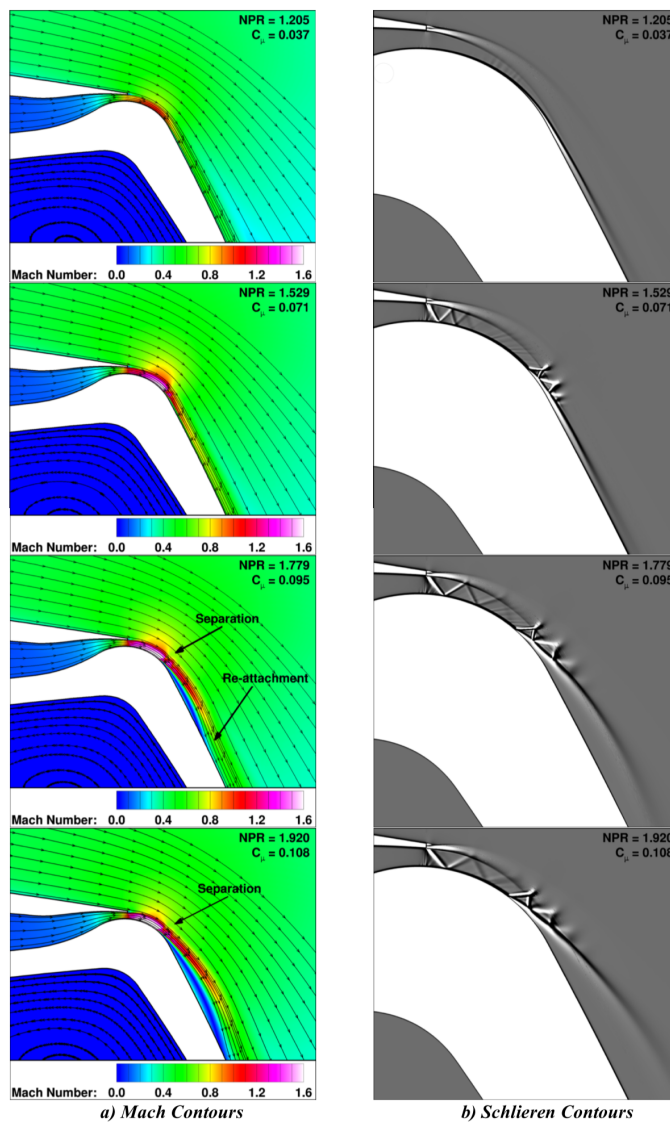


Figure 3.34: 2D CFD simulation and schlieren contours for 60° flap configuration for varying blowing conditions (Jones et al. 2013).

One of the other applications of CC is the AMELIA (Advanced Model for Extreme Lift and Improved Aeroacoustics) project, which introduces a hybrid wing body configuration with a CC flap (Golden & Marshall 2010). The geometry of the flap is investigated to improve the performance of CC.

Similarly, the German Aerospace Centre (DLR) performed experiments and CFD simulations about flow separation control on the high-lift device of civil aircraft. The wind tunnel experiments were based on the DLR-F15 high lift model integrated with leading edge vortex generator jets and trailing edge multiple-slot pulsed blowing (Ciobaca & Wild 2013). Figure 3.35 shows the structure of the wing model and actuation system. Results show that compared with clean configuration, the actuation of the leading edge jet increases the stalling AoA, and the trailing edge blowing rises the  $C_L - \alpha$  (lift coefficient vs. AoA) curve. Both of the actuation used pulsed blowing with a 50% duty cycle. Moreover, the structural influence of the slots has been evaluated by Machunze et al (Machunze et al. 2016), by conducting coupon tests to verify the stress concentration around the slots. A novel flap structure equipped with active flow control devices was designed, and the weight of the flap is around 10% lower than a conventional flap with equivalent lift.

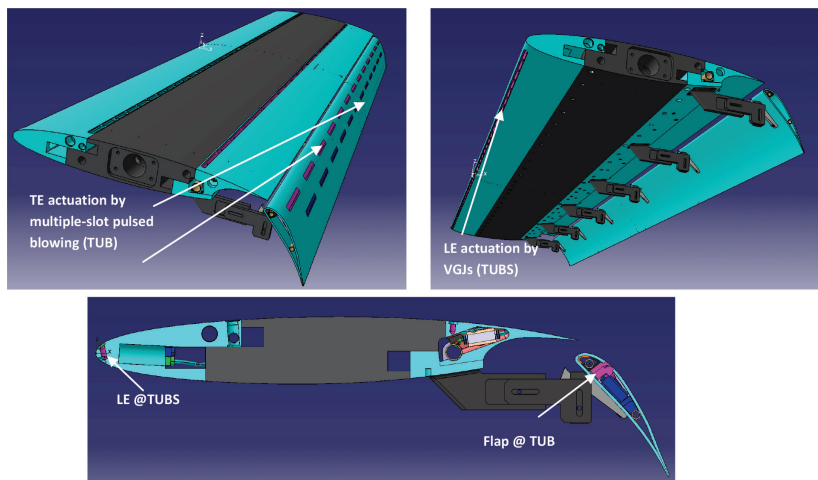


Figure 3.35: The DLR-F15 wing model and actuation system (Ciobaca & Wild 2013).

The latest research project in Germany, the Coordinated Research Center SFB880 project seeks to investigate technologies for environmentally friendly aircraft. The CC flap is one of the approaches that have the potential to reduce take-off and landing distance, therefore, reducing the noise pollution to the ground (Sommerwerk et al. 2016) (Semaan et al. 2019). The aeroelastic effects of the CCW were investigated, and it was found that the active flow control produces special flutter phenomena which are not found in conventional aerofoils. Various approaches were considered to alleviate the flutter. Considering the flutter control,

the present research in this thesis raises the possibility of using CC to alleviate the flutter as the bandwidth of CC is reasonably high, according to the results in this thesis. This will be a future research direction for CC.

As previous studies have demonstrated significant advantages of using active flow control techniques, flight tests have been conducted by researchers to demonstrate their effectiveness in real flight. In 2015, NASA and Boeing tested a full-scale rudder with sweeping jet actuators in order to improve its aerodynamic efficiency and reduce the size of the vertical tail (Whalen et al. 2015). The vertical tail was tested in the wind tunnel and then installed on a Boeing 757 aircraft. Flight test successfully demonstrated the enhancement of yawing control moment. The blowing jets produce a 20% or greater increase in sideforce at maximum rudder deflection. Figure 3.36 presents the photo of the vertical tail and flow control actuators.

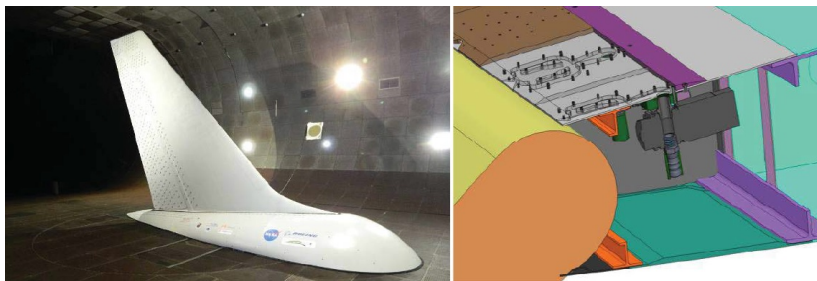


Figure 3.36: The B757 tail model and sweeping jet actuator (Whalen et al. 2015).

Although active flow control has been comprehensively studied at the laboratory level, there is still a gap between laboratory research and industrial application. The integration of a novel high-lift concept is a systematic and complicated problem since the wing structure, pneumatic pipelines and engine bleeding device have to be changed. Jabbar et al. systematically studied the mass, cost and power consumption of different types of flow control methods (Jabbar et al. 2010). The Airbus A320 wing was used as the case study and the trade-off between flow control efficiency and hardware mass was investigated to find the most practical solution. It was estimated that an electromechanical-fluidic system costs 40% mass of the leading edge slat and 5% mass of the trailing edge flap. For a 2h flight mission of an A320 aircraft, the all-electric flow control system costs 0.6% maximum take-off weight and 1% of the mission fuel.

Meanwhile, as one of the most promising techniques for the future civil aircraft, there are still some key issues that affect the application, such as the actuator capability, robustness and noise, the system power, complexity and cost, the failure modes and redundancy considerations (Goldhammer 2009). These issues require a more thorough investigation in future studies.

### 3.6 Gust Alleviation Based on Conventional Control Surfaces

So far there is only a small number of publications use active flow control as means of gust alleviation (Kerstens et al. 2011, De Breuker et al. 2007)(Williams et al. 2010), it is even less in terms of CC (Li & Qin 2020). Hence the scope of the literature review is broader than "circulation control for gust alleviation". Previous sections reviewed general flow control including actuators and sensors. This section focuses on general gust alleviation with conventional control surfaces.

#### 3.6.1 Direct Lift control (DLC)

A frequently used approach to reduce gust influence on the aircraft or passenger is the Direct Lift Control. The lift control of a normal aircraft usually requires a change in the AoA by deflecting the elevator to alter the pitching moment, thus rotating the aircraft. Direct lift control is to increase the total lift by deflecting control surfaces simultaneously without changing the AoA of the wing or attitude of the aircraft i.e. it alters the flight path without movement in other degrees of freedom. Thus the coupling effect of different forces is eliminated, which can increase the manoeuvrability, enhance the flight path control during landing and suppress the effect of disturbances.

Figure 3.37 is an example of vertical movement by direct lift control. To produce a vertical upward movement, the flap (or aileron) is deflected downward ( $\delta_f$ ) and the elevator is turning upward ( $\delta_e$ ) at the same time to compensate for the change in pitching moment. The lift increment due to the flap is  $\Delta L_{\delta_f}$  and an opposite but smaller lift increment is generated by the elevator,  $\Delta L_{\delta_e}$ . Consequently a net vertical force ( $\Delta L_{\delta_f} - \Delta L_{\delta_e}$ ) is produced without changing the attitude of the aircraft. Traditionally, the flap or aileron on the wing act as a direct lift device, while in this research, a CC system is used as an actuator for direct lift control.

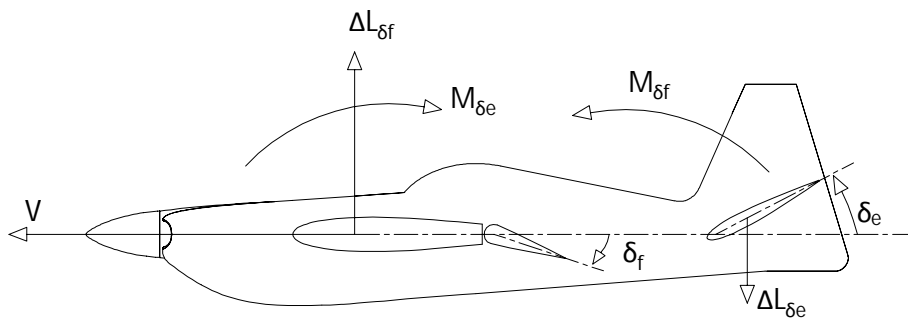


Figure 3.37: The schematic of direct lift control.

Since 1970, direct lift control has been investigated by researchers, aiming at increasing the response of aircraft, by coordinating the rotation of control surfaces to generate a vertical force close to the centre of gravity (Pinsker 1970a) (Pinsker 1970b). In their research, the direct lift control surfaces are usually commanded by the pilot. Later, direct lift control has successfully been utilised on a commercial transport aircraft, the L-1011, as a part of its automatic landing system (LYKKEN & SHAH 1972, Ferrell & Colgren 2003). Such systems are also used in small general aviation aircraft of which the spoiler is used as a direct lift control device (Kohlman & Brainerd 1974). Moreover, direct lift control can effectively improve manoeuvrability, such as the control law of the F-16 aircraft provided by Barfield (BARFIELD & DAZZO 1983).

The other scope of direct lift control is concerning dynamic performance, for the purpose of alleviating dynamic loading. In the 1980s and 1990s, advanced technology testing aircraft system (ATTAS) was used by DLR as a research platform. One of the systems tested was the high-frequency direct lift control in which a set of rapidly deflecting flaps are used (Hahn & König 1992) (Jategaonkar 1993). However, the flight test results show that the DLC flaps are less effective than expected due to their slow deflection rate at high airspeed. It was also evaluated on a Cessna Citation II aircraft by Gerrits, M. for the purpose of improving passenger comfort (Gerrits 1994). Similarly, on the Boeing 787, it was reported that the flaperons and elevators are used to suppress gust loading (Dodt 2011) (Regan & Jutte 2012).

As another form of lift control, a load alleviation system is usually found on modern transport aircraft to instantly modulate lift in order to prevent the wing bending moments from exceeding the designed limit (Matsuzaki et al. 1989, Walton et al. 2014). This method requires rapid sensing of the gust and fast actuation of the control surfaces, while Roland Kelm and Michael Grabietz provided a method to redistribute the lift in the spanwise direction in order to reduce the bending moment at the wing root (Kelm & Grabietz 2000).

While most of the previous direct lift control are using aerodynamic control surfaces such as ailerons, spoilers and flaps, there are new actuators being investigated recently. Xiaoping et al. have evaluated gust alleviation using active flow control approaches. A flow control actuator was placed on the upper surface of an aerofoil and the gust response with different types of flow control was investigated. Results show that active flow control can significantly reduce gust loading (Xiaoping et al. 2011). DeSalvo et al. provided a novel approach of using aerodynamic bleed to actively control the lift (DeSalvo et al. 2019). An array of channels were configured in the wing that connect the upper surface and lower surface. When the channels are open, air will be driven through the wing by the pressure difference. Results show that this aerodynamic bleeding can reduce lift up to 28% and increase lift up to 11%, which indicates

that it could be an effective approach for direct lift control.

#### 3.6.2 Load Alleviation and Ride Smoothing

Load Alleviation and Ride Smoothing (LARS) is one of the engineering applications of direct lift control in operational aircraft, which is relevant to this research. Atmospheric disturbances can cause extraordinary loading on the structure of an aircraft and affect the performance of pilots and passenger comfort. The LARS system is to reduce the influence of atmospheric disturbances by using control surfaces to suppress the dynamic loading on the aircraft. Usually, such atmospheric disturbances occur unpredictably and it is not possible for pilots to react as quickly as needed, thus LARS is automatically controlled by the flight computer and sensors. The sensors are used for detecting the gust or turbulence to provide the magnitude and direction of the disturbance. Such sensors include AoA vanes, acceleration sensors, and more recently, the LIDAR system (Cates et al. 2013).

The workflow of the LARS system is as follows. Firstly, the sensors detect gust or dynamic loading and transmit the data to the flight computer. Secondly, the flight computer compares the gust loading with pilot inputs and the limitation criteria of the aircraft. Finally, the control surfaces are actuated instantaneously to alleviate the dynamic loading.

Although load alleviation and ride smoothing are similar techniques, on modern transport aircraft, the LARS is usually two separate systems. The load alleviation is to alleviate discrete, large-magnitude gust loading which can cause damage to the aircraft structure. It only deploys when the dynamic loading reaches the designed loading limitation and involves a number of control surfaces such as aileron and spoilers. For example, a gust alleviation system was applied to the A320. When the system detects a vertical gust that exceeds the threshold of the positive  $g$  loading, its ailerons will rapidly deflect upward to reduce the loading instantly (Kelm & Grabietz 2000).

While the ride smoothing system is to compensate for the continuous, small-scale and high-bandwidth turbulence that is encountered when the aircraft is flying through clouds or at low altitudes for example. The control surface(s) for ride smoothing can be smaller but actuate more rapidly. On the Boeing 787, such a device is a small control surface between the inner and outer flap (Nelson 2005). On the B-1, the ride smoothing system is two small control surfaces arranged below the canopy (Rainey 1971). It is also reported that the A330 and A340 have similar systems, so the Comfort in Turbulence system improves passenger comfort and flight quality (Regan & Jutte 2012).

In terms of small aircraft such as UAVs, the influence of wind gusts is more critical due

to their smaller inertia. Because of their limited payload and simpler design, there are no control surfaces specifically for gust alleviation. Therefore the ailerons are generally used to suppress gust load. When the flight control computer detects wind gusts from air data or acceleration sensors, it controls both ailerons which move simultaneously up and down to offset the dynamic load on the wing.

Christopher and Christine (Regan & Jutte 2012) have investigated gust alleviation systems in existing operational aircraft and summarised the sensors and actuators they used (Table 3.3). Existing systems are mainly based on conventional mechanical control surfaces such as ailerons, elevators, and dedicated surfaces. The gust information is detected by inertial and aerodynamic sensors. The control surfaces and sensors are integrated with control algorithms to automatically reduce unfavourable loading, therefore reducing structure weight.

Table 3.3: Gust alleviation systems in operational aircraft(Regan & Jutte 2012)

Aircraft	Principle objective	Sensors	Actuation	Improvement
C-5A	Load alleviation and fatigue life extension	Inertial	Symmetric aileron	Empty weight reduction 5.5%
L-1011-500	Load alleviation for wing span extension	Inertial	Symmetric aileron and outboard spoilers	Empty weight reduction 1.25% Drag reduction 3%
B-1	Ride quality	Inertial	Canard-like vanes on nose	Empty weight reduction 4.7%
B-2	Load alleviation and ride quality	Aerodynamic and inertial	Inboard elevons and dedicated surface	Gust load reduced 50%
A320	Load alleviation	Inertial	Ailerons, spoilers, and elevators	N/A
A330 and A340	Load alleviation and ride quality	Inertial	Rudders and elevators	N/A
A380	Load alleviation and ride quality	N/A	N/A	N/A
787	Load alleviation and ride quality	Aerodynamic	Ailerons, spoilers, and elevators	N/A

Methods of gust alleviation for small UAVs are similar to large transport aircraft, although some bulky equipment ( e.g. LIDAR sensor and dedicated surfaces ) are not available due to the limited size of small UAVs. Hence most of the research activities are focused on control laws. For example, Jean et al. have developed a Disturbance Observer Based Control (DOBC) algorithm for gust alleviation of small UAVs (Smith et al. 2016). The algorithm includes an observer to estimate the gust information according to known parameters from the system output and input, incorporated with an LQR controller to alleviate the influence of unexpected gust. Only the elevator and throttle are used, which means the gust is compensated by a simple pitching motion. Results show the altitude variation due to gust is reduced by 60% compared

to the baseline controller, in a 5m/s vertical gust and 15m/s airspeed.

Yang et al. have proposed a non-linear  $H_\infty$  controller to stabilise the attitude and velocity of a fixed-wing UAV in wind gusts (Yang et al. 2012). Both the aileron and elevator are used as control inputs. Simulation results are compared with a typical PID controller in gusty conditions, the  $H_\infty$  controller maintains AoA variation for less than  $5^\circ$  compared to the PID controller for  $15^\circ$ .

Mihai Lungu has developed an auto-landing controller for a fixed-wing UAV (Lungu 2020), a disturbance observer is introduced in the control structure to estimate the gust vector. The elevator and throttle are used to deal with longitudinal gust. During the simulated auto-landing, the UAV subject to gusts maintains the desired trajectory.

Hardware improvement has been conducted by Derrick et al. who developed a 'Flow-Aware Computational Wing', which is enhanced with high-speed pressure sensors on the wing surface and dedicated control surfaces (Yeo et al. 2019). Flight test results indicate a 22% reduction in roll angle and an 18% reduction in roll rate under cruise conditions with disturbances.

These studies introduced improved algorithms for better detection of gust and attitude stabilisation. However, the performance of an algorithm, even with a dedicated control surface, is still limited by the control authority of aerodynamic surfaces, specifically the maximum  $C_L$  that a surface can achieve and the maximum deflection rate.

As previous sections have reviewed cutting-edge flow control techniques, it is possible to replace conventional control surfaces with flow control actuators, especially the CC, adopted with control algorithms that have been tested in existing gust alleviation systems. The following part focuses on the control strategies developed for conventional control surfaces, but also suitable for the present study based on CC actuators.

### 3.7 Gust Alleviation Based on CC

The actuators available for gust alleviation include a spoiler, aileron, elevator and innovative control devices such as active flow control actuators. These actuators can be used either separately or cooperatively (e.g., DLC) to reduce the gust loading. Each of the actuation methods has its own constraints:

Using elevators to pitch an aircraft is the most efficient way in terms of control authority and has less drag penalty, but has significant time lag due to the inertia of the aircraft and unable to perform a high-frequency movement. The time lag can be compensated by feedforward controller using preview gust information from sensors ahead of the wing. Hence it is suitable for the alleviation of low-frequency and high-magnitude gust loading.

Spoilers can reduce lift effectively but are unable to increase lift and cause significant drag penalty, they create flow separation, therefore, bring unfavourable non-linearity to the control loop. Spoilers are usually used ( or actuated with ailerons (Fezans et al. 2019) ) to alleviate vertical loading due to a discrete upward gust to prevent the bending moment on the wing root from exceeding its designed criteria.

DLC is an approach that involves multiple aerodynamic surfaces to actuate simultaneously. However, existing systems based on mechanical control surfaces only have small control authority in terms of changing normal force ( lift ), because these systems use ailerons, elevators, or some special high-speed flaps ( Figure 3.3 ), which are designed to create control moments instead of the lift, such surfaces only have very small effective area, therefore, have little contribution to the lift, compared to pitching the wing.

For some small aircraft, trailing edge plain flaps are also a part of the DLC system; this is possible for small UAVs with low hinge moment and fast deflection rate but not feasible for complex multi-slot flaps on large transport aircraft as they are driven by sophisticated mechanisms in a very slow deflection rate. Consequently, DLC devices can only deal with small amplitude and high-frequency gusts (Fezans et al. 2019).

Section 3.4.1 on page 66 reviewed various types of active flow control actuators. Most of them are not suitable for gust alleviation due to the poor linearity and small control authority. CC has relatively good controllability since it can modify lift almost linearly from zero to  $C_L > 3$  (Friedman et al. 2016). This means it can create an arbitrary lift to compensate for a random gust loading. Therefore, it is ideal for this research.

The increment of sectional lift coefficient by deflecting a plain flap ( the same as ailerons ) is less than 1 (Gudmundsson 2013). In comparison, as a control effector, the CC provides large lift augmentation (up to  $C_L = 9$  (Golden & Marshall 2010)) and wider bandwidth than mechanical control surfaces, according to the results from Chapter 5. Hence using CC for gust alleviation has significant advantages over the previous methods. Moreover, the actuation of CC will create an additional moment which requires an elevator to compensate. This is actually equivalent to the DLC approach, the only difference is that the mechanical control surfaces are replaced by CC actuators. In the present study, the development of control algorithms follows the DLC approach, which means that the CC device is located on the wing in order to change the normal force ( lift ) to alleviate gust loading, while the elevator is used to compensate for the unsteady moment due to CC actuation. This is presented in Chapter 5 and Chapter 8.

It is already known that CC can dramatically change lift. but very few researchers have explored how fast it can change. To evaluate the feasibility of using it to offset unsteady

loading, the first step is to build a dynamic model, which is essential for developing controllers. Currently, studies on CC dynamic response are still rare. One of the studies that are most relevant to the objective of this research has been conducted by Friedman and Arieli, who have investigated the lift build-up process of CC (Friedman et al. 2016), suggesting that the lift variation is similar to the Wagner function (Wagner's theory was explained in Section 2.1.4 on page 11). The study was based on a sharp-edge gust, in which the gust component rises abruptly from  $t = 0$ . He used a step input signal to obtain the lift variation in terms of non-dimensional time  $s$ , and tested it in different blowing momentum coefficients  $C_{\mu_f}$ , shown in Figure 3.38.

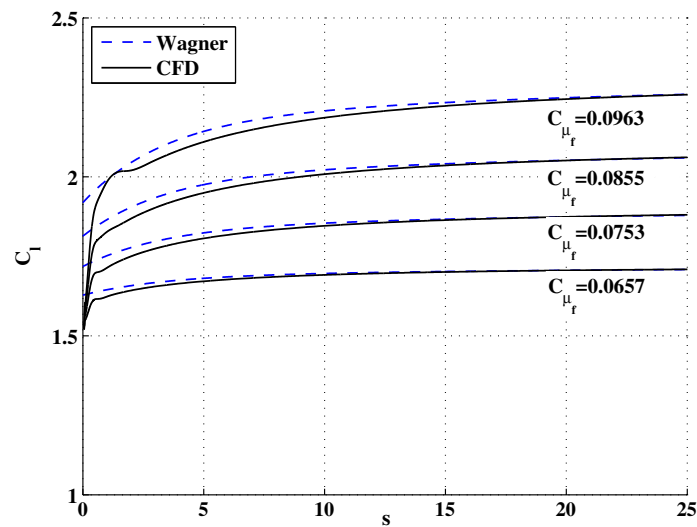


Figure 3.38: The lift build up after a step change in  $C_{\mu}$ , compared with the Wagner's function (Friedman et al. 2016).

As Wagner's curve represents a normal thin aerofoil performing an abrupt change in AoA, the similarity between CC and Wagner's curve indicates that the controllers designed for conventional flap may be applicable to CC, thus simplifying the development of control algorithms. Friedman's results provided an initial study of an elliptical CC aerofoil, but his results were not enough to build a dynamic model of CC due to the lack of different flow conditions, moreover, he didn't compare the dynamics of CC with mechanical flaps. More geometries and flow conditions need to be tested in order to find a universal principle of its dynamic behaviour and to justify its performance in terms of gust alleviation. This research also compares with Wagner's function in Chapter 5, Section 5.2.2 on page 146 and compares with Friedman's results in Chapter 7, Figure 7.19 on page 226.

Recently, Li et al. have investigated the application of using CC for gust alleviation (Li & Qin 2020). An elliptical CC aerofoil has been investigated by CFD at  $M = 0.3, 0.5$  and  $0.8$ .

A discrete 1-cos gust profile ( as shown in Figure 3.4 on page 46 ) was applied on the inlet of the computational domain to generate a discrete flow disturbance, which cooperated with time-varying boundary conditions on the nozzle to offset the unsteady lift. Figure 3.39 shows the lift response at  $M = 0.3$ , where the lift maintains nearly constant with adaptive blowing. The results prove that CC is effective in alleviating unsteady lift when the blowing is actively regulated. However, their research did not vary gust frequencies which is important for the analysis of flight mechanics. In addition, they used a pre-defined profile of boundary conditions without closed-loop control algorithms. The approach is open-loop and only applicable to the scenario where gust information is already known. In real flight, random gusts consist of various frequencies, while the aerodynamic surfaces have limited actuation speed and can only alleviate limited frequencies. This research expands the frequency range of gusts in order to explore the actuation bandwidth of a circulation-control-based flap, and develop a closed-loop system for gust alleviation to compensate for unsteady loading in real time.

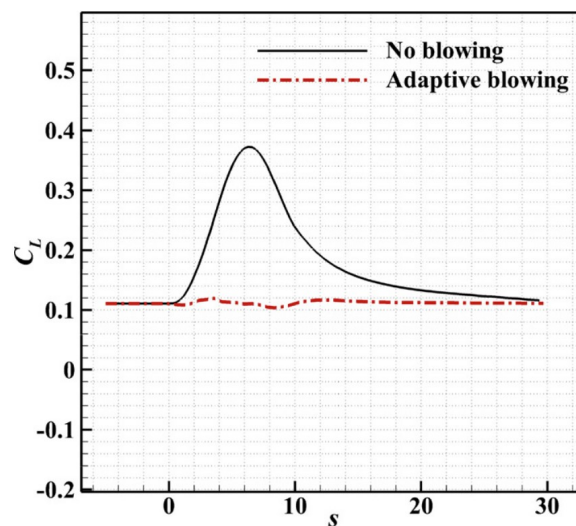


Figure 3.39: The gust response with adaptive blowing compared with no blowing(Li & Qin 2020).

### 3.8 Summary

This chapter reviews literature relevant to this research, from the sources of atmospheric disturbances to the flight control systems of an aircraft, as well as the theories and applications of CC. Although extensive research has been carried out on CC, very few studies have considered dynamic applications for gust alleviation. These studies are mostly conducted by steady state experiments under prescribed conditions, and rarely consider the unsteady environment

(Kerstens et al. 2011, Rosen et al. 2017). In addition, the actuation speed or dynamic response of CC is seldom studied and it is unclear to what extent the gust loading can be reduced. In recent years, major advances in CFD have allowed new approaches to study CC, particularly using unsteady CFD to simulate the dynamic process. The literature review has demonstrated that CFD can give a good prediction of the performance of CC in steady conditions, but importantly it also allows a greater range of parameters to be considered, so CFD is the primary methodology used in this research.

Existing gust alleviation approaches are based on conventional control surfaces, their effectiveness is limited by the actuation speed and magnitude of lift augmentation (Khalil & Fezans 2021). Currently, there is no actuator that has both characteristics at the same time: fast actuation and large lift augmentation. Whereas it is well-explored that CC is effective in lift augmentation, therefore the aim of the research is to develop a gust alleviation mechanism based on CC. From the current state of art, the following objectives have been raised:

1. A need to explore the dynamic performance of CC.
2. A methodology to simulate the unsteady flow under gust conditions.
3. A closed-loop controller for CC to alleviate gust loading.

# Chapter 4:

## Methodology

According to a flow's complexity and the required level of accuracy, the modelling of a flow can be categorised into different levels. Generally, the more accurately a system is modelled, the more computational effort it requires. There is a trade-off between computational effort and accuracy. Figure 4.1 summarises the relevant modelling approaches for this research. The model on the bottom is the most accurate and most closely related to the actual physics but requires large computational resources. Whereas the approaches on the top represent the most simplified models, where assumptions made to simplify the analysis limit their range of applications and/or accuracy. The flow over an aircraft investigated in this research is unsteady, viscous and governed by Navier–Stokes (N-S) equations. These equations are derived from fundamental conservation laws and can model every fluid detail, providing the computational mesh is fine enough to resolve all flow features.

However, in most of the viscous flows, there are no exact solutions of N-S equations, except for some special cases where some terms are zero due to the nature of physics and geometry. For example, the Couette flow, a viscous flow between two parallel infinite-long plates where one plate is moving. The flow patterns in such a flow are straight and parallel to the plate and produce a steady flow field where many terms of the N-S equations are zero. Hence an analytical solution can be achieved without any approximations. Although such an ideal flow does not exist in engineering, practical approximations can be applied to achieve numerical results by using discretisation techniques (transfer continuous partial differential equations to discrete algebraic equations that can be solved numerically rather than analytically). For laminar flows, numerical solutions of N-S equations can produce accurate results. Whereas in turbulent flow, it is challenging to obtain exact results since the flow is highly unsteady and chaotic. Turbulent flows can be modelled by Direct Numerical Simulation (DNS), Large-Eddy Simulation (LES) and Reynolds-averaged Navier-Stokes equations (RANS) (Blazek 2005b). DNS gives the most detailed flow structures but demands high computational efforts; LES methods resolve the larger scale vortices but not flow structures at the smaller scales and therefore are less expensive to compute. The RANS approach models the time-averaged turbulent properties, which is significantly easier to solve than DNS and LES. The discretisation

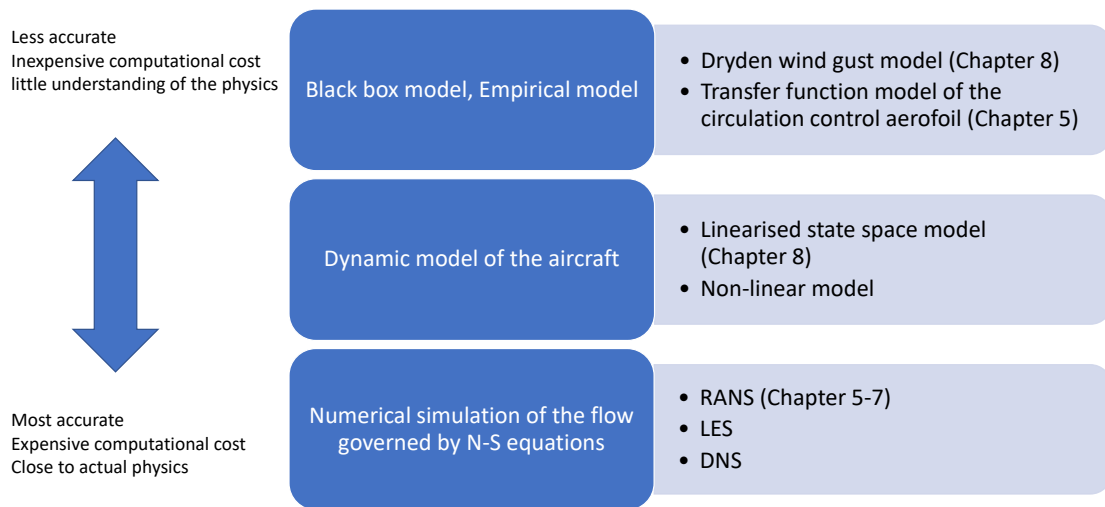


Figure 4.1: Hierarchy of models for flow over an aircraft.

methods and turbulence modelling techniques are explained in detail in this chapter, and why therefore it is the approach used in this research.

Through N-S equations, the aerodynamic forces of an aircraft can be obtained, including lift, drag and moments of the wing or horizontal / vertical stabilizers. These forces and their relationship with AoA or flight speed, can be used to build a dynamic model of the aircraft. Dynamic models, as shown in Figure 4.1, are empirical or mathematical models that are based on CFD or experimental results, and so the details of a flow are not directly modelled. Compared with CFD, dynamic models are easier to solve and are sufficient to analyse the stability of an aircraft, provided the general flow conditions are similar to the original experiment from which the empirical model was derived. Depending on the level of complexity, there are two categories of models, non-linear and linearised models. The former is used when there is a rapid change of orientation where the time-dependent aerodynamic effect occurs; the latter is a simplified model that only considers small changes in the flight condition or slow motion where the aerodynamic coefficients are in a linear region. In Chapter 8 on page 235, a linearised model of the aircraft is used to study the behaviour in continuous gust since the motion caused by a gust is relatively small and can be analysed by linear models.

In control applications, a model will estimate an appropriate output from the available input information without referring to the physical laws and is often referred to as a black box model (Zhang 2010, Keesman 2011). It is used in Chapter 5 on page 124 to describe the relationship between the lift of the aerofoil and the nozzle pressure of the flow control. This

---

model was a transfer function extracted from data sets of time history or frequency response. Compared with CFD simulation, which typically solves the N-S equations for several million cells in every iteration, a single transfer function can produce the dynamic lift variation with acceptable accuracy for many engineering applications. However, one transfer function can only represent a pair of single input and output variables, whilst CFD results contain all the flow variables across the domain. The other method to estimate aerodynamic variables is using empirical data through observations or experiments. For example, to estimate the hinge moment of an aileron by empirical data sets such as those provided by the Engineering Sciences Data Unit ( IHS ESDU )(ESDU 1956-05). This approach is only available to certain aerofoils in conventional configurations. More unique aerofoils, such as flow control aerofoils with a modified geometry, are not generally included in these empirical databases. In addition, modelling the spectrum of wind gusts in the atmosphere requires an empirical function as a filter to the white noise, which is used in Chapter 8 on page 235. Both black box models and empirical models have the least knowledge of the physical laws and the least computational effort, but such models can be suitable for analysing flight dynamics where the motion of a full aircraft model is concerned, and the detailed knowledge of flow phenomena such as boundary layer behaviour and separation are not of interest.

The problems involved in this research require interdisciplinary approaches due to the complexity and non-linearity of CC. The Coanda effect is affected by the geometry of the nozzle and surface, amongst other parameters. This subsequently influences the lift and overall moments, so the flight dynamics need to be analysed. There is no single approach that can analyse all the mechanisms, from flow separation to flight dynamics hence multiple methodologies are used in this research. The initial aerodynamic parameters and geometric study are conducted using steady-state CFD, while the actuation speed of CC is simulated using unsteady CFD. In terms of flight dynamics of the aircraft equipped with CC devices, it is simulated with state-space modelling. Finally, a controller has been designed using the LQR method and developed in Matlab to evaluate potential reductions in gust loading.

This chapter initially introduces the properties and assumptions of the working gas in this research. Subsequently, the fundamental equations of CFD are introduced in Section 4.2.1 on page 94. To be solved by computers, the governing equations can be manipulated to integral forms presented on page 96. According to the flow properties specified in Section 4.1 , suitable discretisation methods are discussed in Section 4.2.2 on page 97. The partial derivative equations can be simplified to algebraic equations by discretisation ( Equation 4.11 on page 98 ) and linearisation ( Equation 4.12 on page 98 ), allowing them to be solved through

numerical methods. Section 4.2.3 on page 102 introduces methods to deal with pressure-velocity coupling problems. Additionally, since turbulent fluctuations are difficult to compute directly from the N-S equations, Section 4.2.4 on page 106 discusses turbulence modelling approaches. Finally, the boundary conditions and mesh generation approaches are discussed in Section 4.2.5 on page 115 and Section 4.2.6 on page 118, respectively. The uncertainties involved in the CFD simulations are summarised in Section 4.2.7 on page 121.

## 4.1 Gas Properties and Assumptions

The selection of the simulation method is highly dependent on the flow properties, so this section provides the properties and assumptions of the working gas used in the following chapters. In this research, all the units are International System of Units (SI units). The aircraft is assumed to be flying in a straight and level attitude in a standard atmosphere (Minzner et al. 1959) at sea level where the following parameters are applied

- Temperature  $T = 288.16$  K
- Free stream pressure  $P = 101325$  Pa
- Density  $\rho = 1.225$  kg/m<sup>3</sup>
- Speed of sound  $a = 340.29$  m/s
- Absolute viscosity coefficient  $\mu = 1.7894 \times 10^{-5}$  kg/(ms)
- Gas constant of air  $R_{air} = 287.05287$  (J/kg)/K
- Ratio of specific heats  $\gamma = c_p/c_v = 1.4$

The working fluid in this research can be treated as perfect gas (Blazek 2005b), for which the state equation is applied.

$$p = \rho RT \quad (4.1)$$

where  $R$  is the specific gas constant ( in this research,  $R = R_{air}$  ). The state equation is used to compute the energy equation in the simulation.

For compressible flows, the state equation links the energy equation, mass conservation and momentum equations. Whereas for incompressible flows, the density is considered as a constant variable, the energy equation can be calculated after the mass conservation and momentum equations if needed, which is the so-called ‘pressure based solver’ in CFD codes. This is discussed in detail in the pressure-velocity coupling in Section 4.2.3 on page 102.

The aircraft is assumed to be flying in an unsteady atmosphere, with a blowing jet for CC, and so the flow is considered to be unsteady, viscous and rotational. The free stream Mach number is around 0.1. The jet flow at the nozzle exit exceeds Mach 0.5 at high pressure blowing, therefore compressible effects need to be considered. The aircraft is also assumed to fly at a relatively low AoA in cruise, and the wing is not near the stall boundary. Additionally, the air properties for low altitude and low speed flight are considered Newtonian fluid, which means the shear stress is proportional to the velocity gradient.

The fundamental assumption for the governing equations of fluid is the continuum assumption. The fluid is a continuous substance without any holes or discontinuities; in contrast to the low density flows in the outer atmosphere that the molecules of gas are far apart. In addition, the derivation of equations relies on the principles that mass, momentum and energy are conserved (Blazek 2005*b*).

## 4.2 CFD methods

A flow can be modelled by solving the governing equations, but it is very hard to find analytical solutions to these equations. However, in most cases, partial differential equations can be solved numerically by the discretization of the domain. Before the invention of practical computers, these equations were solved manually and took massive effort just to calculate a simple geometry. Dating back to the early 1900s, Lewis Fry Richardson attempted to manually solve the governing equations of fluid mechanics regarding the application of a masonry dam and weather prediction (Richardson & Glazebrook 1910, Richardson 1922). The development of CFD closely relied on the evolution of computers. In 1947, Kopal simulated the supersonic flow around a sharp cone with the help of computers, which was considered to be one of the earliest attempts to use computers to obtain solutions for fluid problems (Kopal 1947). During the 1950s and 1960s, CFD was initially used to study the re-entry body problem (Wendt 2008). To solve this challenging problem with a high Mach number, high temperature and chemical reactions, high performance computing and numerical methods are required. Fay and Riddell have contributed to numerical methods of solving non-linear ordinary differential equations of the boundary layer (Fay & Riddell 1958). Blottner has presented a finite difference method to solve the boundary layer equations with chemical reactions (Blottner 1970).

From the 1970s and 1980s, there was an increasing interest in utilising CFD codes for general engineering applications. Several commercial software packages were developed, such as the PHOENICS (Parabolic, Hyperbolic or Elliptic Numerical Integration Code Series) developed by Concentration, Heat & Momentum Limited (CHAM) and the FLUENT, developed by

Fluent Inc. The first version of FLUENT was launched in 1983. The company was finally acquired by ANSYS, Inc. in 2006 (Boysan et al. 2009). Since the early 1980s, commercial CFD codes have solved complex inviscid flows towards applying a complete aircraft or turbomachines. The research activities were then focused on the viscous flows and the more complex turbulent flows (Blazek 2005a). Various methods were used to describe the turbulence, such as the RANS, DNS and LES (Bardina et al. 1980).

In this research, the Ansys Fluent 17.2 was used to solve the simulations. The following sections introduce fundamental theories and equations used in CFD simulation.

### 4.2.1 Navier-Stokes Equations

The fundamental equations to describe flows consist of three governing equations, describing the conservation of mass, energy and momentum (i.e. the application of Newton's second law). It is difficult to directly derive a mathematical model of flows according to the physical principles, as the physical parameters are spatially different, and the substance in the flow travels under various forces. To simplify the flow domain, it is more convenient only to consider a small portion of the fluid. There are two different approaches, one is to consider a control volume that is fixed in space, and the other is to consider a control volume that travels with the fluid with the same particles in the control volume. The former approach gives a conservation form of equations, while the latter approach gives a non-conservation form. These two forms are derived from the same physical principles and can be transformed from one to the other. Depending on the derivation methods, the governing equations have two different forms, the integral form and the differential form. From the mathematical point of view, these various forms describe the same physical phenomenon, but they are suitable for different CFD approaches.

The governing equations can be defined in a cartesian space with  $x$ ,  $y$  and  $z$  axes. The unit vectors on each axis are  $\mathbf{i}$ ,  $\mathbf{j}$ ,  $\mathbf{k}$  respectively. The flow in this cartesian space has a vector velocity field which is defined by

$$\mathbf{V} = u\mathbf{i} + v\mathbf{j} + w\mathbf{k} \quad (4.2)$$

Moreover, a vector differential operator is given by

$$\nabla = \mathbf{i}\frac{\partial}{\partial x} + \mathbf{j}\frac{\partial}{\partial y} + \mathbf{k}\frac{\partial}{\partial z} \quad (4.3)$$

The following sections present the governing equations of unsteady, compressible, 3D flow in the conservation and differential form (Anderson Jr 2016).

The conservation form is derived from the Eulerian approach, considering an infinite small control volume fixed in space. In contrast, the Lagrangian approach uses a fluid element containing constant mass that is moving along with the flow, giving the non-conservation form of momentum equations. Only the left side of the equations are different for non-conservation and conservation form (divergence form). The former is usually presented as substantive derivatives as  $\rho \frac{Du}{Dt}$ , while the latter is presented as  $\frac{\partial(\rho\phi)}{\partial t} + \frac{\partial(\rho\phi u_i)}{\partial x_i}$ , where the convective term  $\frac{\partial(\rho\phi u_i)}{\partial x_i}$  is presented as the divergence of a scalar quantity  $\phi$  multiplied by the velocity vector, representing the net rate of flow of the physical quantity out of the control volume (Versteeg & Malalasekera 2007). Both forms give the same results. However, the conservation form is used here as it is convenient for deriving equations for CFD solvers.

The time-dependent 3D compressible fluid is governed by the following continuity equation:

$$\frac{\partial \rho}{\partial t} + \frac{\partial(\rho u_i)}{\partial x_i} = 0 \quad (4.4)$$

For a Newtonian fluid, the viscosity stresses are proportional to the deformation rate. Thus the viscous stress terms in N-S equations can be rearranged into two parts; one is  $\mu \frac{\partial^2 u_i}{\partial x_j \partial x_j}$ ,  $\mu$  is the dynamic viscosity that relates stress to linear deformations. The other part is included in the momentum source term  $S_M$  (Versteeg & Malalasekera 2007). Hence the momentum and energy equations can be manipulated to a simple form and expressed as:

$$\frac{\partial(\rho u_i)}{\partial t} + \frac{\partial}{\partial x_j} (\rho u_i u_j) = -\frac{\partial p}{\partial x_i} + \mu \frac{\partial^2 u_i}{\partial x_j \partial x_j} + S_M \quad (4.5)$$

$$\frac{\partial(\rho c_v T)}{\partial t} + \frac{\partial(\rho c_v T u_i)}{\partial x_i} = -\frac{\partial(p u_i)}{\partial x_j} + k \frac{\partial^2 T}{\partial x_j \partial x_j} + \Psi + S_e \quad (4.6)$$

where  $\mu$  is the dynamic viscosity,  $k$  is the Thermal conductivity,  $S$  denotes the source term such as body force.  $c_v$  and  $T$  are specific heat and temperature, and  $\Psi$  is the dissipation term due to deformation work on the fluid element.  $S_e$  is the volumetric heat term.

Gravity force is a body force acting on the fluid included in the source terms of the momentum equations. In a fluid element, the pressure difference acting on the vertical direction overcomes gravity. A body immersed in a fluid will experience a buoyancy force as it displaces the fluid. As the air density is very small, the buoyancy force acting on an aircraft is neglectable. The gravity force of a fluid element can be neglected for the governing equations in this research.

In the energy equation,  $S_e$  stands for volumetric heat term. Volumetric heating is produced by radiation from outside the fluid or by the fluid itself if the temperature is very high such

as in the simulation of combustion. Volumetric heating is not considered in this research. The energy equation is derived from the formulation of total energy. The derivation process is omitted here. The total energy contained in a unit mass is the sum of internal and kinetic energy ( $e + V^2/2$ ), where  $V$  is the local velocity magnitude (Anderson Jr 2016). For a low speed aircraft at low altitude, the fluid of external and jet is considered as a perfect gas, and the temperature is less than 1000K (Anderson Jr 2016), where the specific heat is approximately constant, for which the internal energy per unit mass (specific internal energy) is

$$e = c_v T \quad (4.7)$$

where  $c_v$  and  $T$  are specific heat and temperature.

In N-S equations, the compressibility of flow is described by the rate of change of density in time and space, represented by  $\frac{\partial \rho}{\partial t}$  and  $\nabla \cdot (\rho \phi \mathbf{V})$ . In practice, the solution of density depends on the flow solver. If the solver is segregated, the density is treated as a known constant in the current iteration and solved by separate equations. Then the density field will be updated in the next iteration. Otherwise, if the solver is coupled, the density and other variables are solved simultaneously. This is explained further in Section 4.2.3 on page 102.

To derive a set of equations that are suitable for numerical computation, the transport equation can be manipulated by the Gauss divergence theorem for a vector  $\mathbf{a}$ :

$$\int_V \nabla(\mathbf{a})dV = \int_A \mathbf{n} \cdot \mathbf{a}dA \quad (4.8)$$

where  $\mathbf{n}$  is the unit vector normal to the face,  $V$  is the volume of the fluid cell,  $A$  is the enclosed surface over the cell. By integrating the transport equation over a control volume and applying the divergence theorem, Equation ?? can be written in the following integral form:

$$\frac{\partial}{\partial t} \left( \int_V \rho \phi dV \right) + \int_A \mathbf{n} \cdot (\rho \phi \mathbf{V}) dA = \int_A \mathbf{n} \cdot (\Gamma \nabla \phi) dA + \int_V S_\phi dV \quad (4.9)$$

where  $\mathbf{V}$  is velocity vector,  $V$  is the cell volume,  $A$  is the surface over the cell,  $S_\phi$  is the source of  $\phi$  per unit volume. This equation is used for numerical discretisation, which is discussed later.

The governing equations represent a fundamental model of compressible, viscous flows. In most CFD simulations, it is impossible to find an accurate solution to these equations directly. The governing equations are usually simplified and numerically solved by neglecting specific terms. For example, in the incompressible flow where the density is constant or in the inviscid flow where the viscosity is neglected. Moreover, in a turbulent flow, approximate models are widely used to calculate fluctuating properties instead of solving full N-S equations.

A set of equations to describe the gas properties is also required to solve the above equations. Considering the ideal gas law, the conservation equations are supplemented by the followings:

$$p = \rho RT, \quad h = c_p T, \quad R = c_p - c_v, \quad \gamma = c_p / c_v \quad (4.10)$$

these equations are the equation of state of a perfect gas, the enthalpy ( $h$ ), gas constant ( $R$ ) and heat capacity ratio ( $\gamma$ ), where  $c_v, c_p$  refers to the specific heat at constant volume or pressure.

### 4.2.2 Discretisation

The discretisation transfers partial differential equations to algebraic equations that a program can solve, generally based on a mesh system of the flow field. Then the discretised equations are solved by various methods such as pressure correction, Alternating-Direction-Implicit (ADI) and the relaxation technique (John D. Anderson 1995). Figure 4.2 shows a road map of the discretization process from the geometry to the solutions (F. Moukalled 2016).

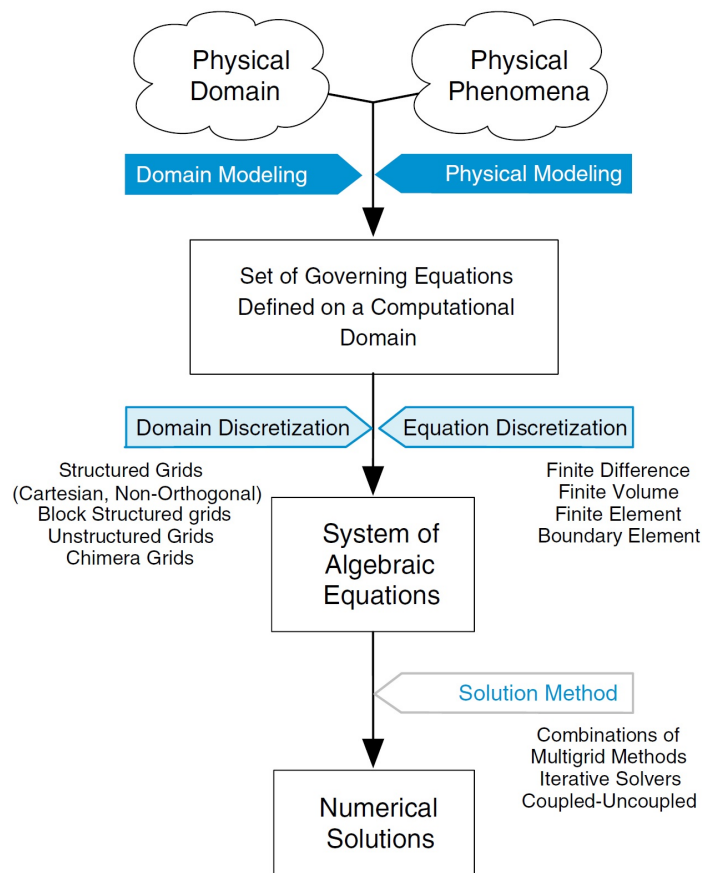


Figure 4.2: The discretization process (F. Moukalled 2016).

### Spatial Discretisation

Spatial discretisation splits the domain into a set of cells or elements, at which the matrix of algebraic equations is calculated. The finite difference, finite element and finite volume are the main methods for discretising the partial differential equations. The finite difference method is derived from Taylor series expansion and replaces the differential with a difference equation. The finite element is mainly used in structural mechanics to analyse the strength or deformation (Zienkiewicz et al. 1977). In the late 1900s, Olivier Pironneau explored its application in fluid dynamics (Pironneau & Pironneau 1989). The Finite Volume Method (FVM) uses finite volumes (divided by the mesh in the flow domain) to represent differential volumes. The FVM can be formulated on unstructured meshes, which is suitable for complex geometry in engineering applications (Patankar 1980).

Ansys Fluent uses the finite volume method for simulation, each cell of the domain is treated as a control volume, and the governing equations of flow are applied. In every computational cell, there are finite numbers of faces. Hence the surface integral of a quantity about a cell is discretised as the summation of its flux at each face. Through this approach, the above-mentioned governing equations can be treated as algebraic equations given by (Ansys 2018):

$$\frac{\partial \rho \phi}{\partial t} V + \sum_f^N \mathbf{n} \cdot (\rho_f \phi_f \mathbf{V}_f A_f) = \sum_f^N \mathbf{n} \cdot (\Gamma_\phi \nabla \phi_f A_f) + S_\phi V \quad (4.11)$$

where  $N$  is the number of faces in a cell,  $\phi_f$  is the value of  $\phi$  at face  $f$ ,  $\mathbf{n}$  is the unit vector normal to the face,  $A_f$  is the face area and  $\mathbf{n} \cdot (\rho_f \mathbf{V}_f A_f)$  gives the mass flux through a face.  $\nabla \phi_f$  denotes the gradient of  $\phi_f$  at the face  $f$ . Figure 4.3 shows an example of two adjacent 2D cells. The cell centroids are marked by  $c_0$  and  $c_1$ ,  $\mathbf{r}$  represents the vector from the cell centroid to the face centre. Apparently, Equation 4.11 can be applied to any type of mesh, so the mesh is not necessarily uniform, and two adjacent cells can have different faces.

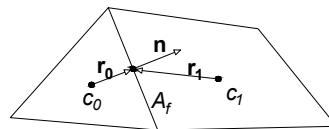


Figure 4.3: Two adjacent cells to illustrate the quantities at the cell centroid and at the faces (Ansys 2018).

Equation 4.11 can be further linearised to the following form (Ansys 2018):

$$a_P \phi = \sum_{nb} a_{nb} \phi_{nb} + b \quad (4.12)$$

where  $nb$  denotes the neighbour cells,  $a_P$ ,  $a_{nb}$  and  $b$  are the linearised coefficients. These coefficients are obtained by manipulations of differencing schemes that will be discussed in the next section. The centre value of the current cell and the neighbour cells are all unknown. To solve these unknown variables, the algebraic equations from each cell build up a large sparse matrix. Then the matrix is solved iteratively by numerical methods.

In Fluent, the fluid variables are stored at the centre of each cell. However, in the discretised scalar transport equation, the value of  $\phi$  and its gradient at cell faces are unknown. Various differencing schemes are used to interpolate the flux at faces given the value at the cell centroid.

### Central differencing

To calculate the flux at cell faces, the simplest method is to interpolate the two cell-centre properties adjacent to the face linearly. For diffusion and source terms of the transport equation, the central differencing method is used, as the influence of diffusion and source is transported in all directions, whereas the convective flux depends on the flow direction. For a strongly convective flow, the influence of the upstream cell is stronger than a downstream cell, so central differencing is not appropriate. In this case, the schemes that are based on the flow direction are used for convective terms. The frequently used schemes suitable for such problems include first/second order upwind and The Quadratic Upstream Interpolation for Convective Kinematics scheme (QUICK) (Leonard 1979).

### First-order Upwind

For convective flow, the variable at a cell face is dominated by upstream cells. The flow direction is not considered by the central differencing scheme, whereas the upwind differencing scheme assumes that the variable is only determined by upstream: The value of  $\phi$  on a face is equal to the value on the centroid of its upstream cell, assuming the centre values represent the entire cell. The upwind differencing only has first-order accuracy (based on Taylor series approximation) and has been used in early CFD codes (Versteeg & Malalasekera 2007). It is the most stable scheme for convective flows but has less accuracy than higher-order schemes.

### Second-order upwind

Similar to the first-order upwind scheme, the second-order upwind scheme also determines the face value according to its upstream cell. In this approach, the gradient of the property at the cell centre is used to compute the face value, given a second-order accuracy of Taylor series expansion (Ansys 2018):

$$\phi_f = \phi + \nabla\phi \cdot \mathbf{r} \quad (4.13)$$

where  $\phi_f$  is the scalar property at the face,  $\phi$  is the property at the centre of the upstream

cell,  $\nabla\phi$  is the gradient of the property, and  $\mathbf{r}$  represents the vector from the cell centroid to the face. In certain cases, when abrupt changes or discontinuities occur in the flow field, the resultant  $\phi_f$  may exceed the maximum or minimum values of the surrounding cells, resulting in unstable salutations. Gradient limiters (Ansys 2018) are introduced to limit  $\nabla\phi$  for flow discontinuities, such as shock waves, to prevalent spurious oscillations. The flow field for the problems in this research is all subsonic without any discontinuities, so the standard limiter is used.

### QUICK

The QUICK scheme combines second-order upwind and central differencing, where the cell centre values of two upstream cells and one downstream cell are used. For a uniform one-dimensional mesh, the face value of  $\phi$  is given by (Ansys 2018):

$$\phi_f = \frac{6}{8}\phi_{i-1} + \frac{3}{8}\phi_i - \frac{1}{8}\phi_{i-2} \quad (4.14)$$

where  $\phi_f$  is the scalar property at the face,  $\phi_i, \phi_{i-1}, \phi_{i-2}$  denotes the cell-centroid properties of the downstream side, upstream side and the one before the upstream cell. The weighted factors on the right side of the equation represent the original form of the QUICK scheme for a uniform mesh. In Ansys Fluent, such factors are not constant. They are dynamically weighted according to iterative solutions to increase the stability of the solver (Ansys 2018).

The QUICK scheme is based on a quadratic interpolation of the neighbour cells. It has a third-order accuracy. Compared with the first/second order upwind scheme, the QUICK scheme introduces more influence from the surrounding cells to reduce discretisation errors.

The differencing schemes will produce a set of coefficients for the linearised transport equation 4.12 on page 98. It is desired that all the coefficients are positive. This implies that an increasing  $\phi$  at one node causes the surrounding nodes to increase. One of the drawbacks of QUICK scheme (Arampatzis et al. 1994) is that the coefficients of the linearised equation are not always positive when the flow is highly convective, which will introduce convergence or stability issues.

Generally, the QUICK scheme is more accurate in meshes that align with the flow direction. In Ansys Fluent, it cannot be used for unstructured, non-hexahedral meshes. For hybrid meshes, if the QUICK scheme is selected, the software only applies the QUICK scheme to hexahedral cells, whereas the second-order upwind scheme is used for non-hexahedral cells. The meshes used in this research include both structured and unstructured mesh. Since the direction of the Coanda jet is not always aligned with the local cells, the second-order upwind scheme is used, which has better accuracy than the first-order upwind.

### Temporal Discretisation

A general form of the temporal discretisation is given by (Blazek 2005b, Versteeg & Malalasekera 2007, Fluent 2011a):

$$\frac{\partial \phi}{\partial t} = F(\phi) \quad (4.15)$$

where  $\phi$  denotes any scalar property,  $F$  denotes spatial discretised equation.

The first-order explicit temporal discretisation is given by (Blazek 2005b, Versteeg & Malalasekera 2007, Fluent 2011a):

$$\frac{\phi^{n+1} - \phi^n}{\Delta t} = F(\phi^n) \quad (4.16)$$

where  $n + 1$  is the value at the future time step, and  $n$  is the current time step. This equation is fully explicit as only old values at the previous time step are needed to compute  $\phi^{n+1}$ .

Explicit equations are solved based on the results from the previous time step. In the function for each cell, only the variable of the current time step in the current cell is unknown. Each algebraic function can be solved individually without any information about the surrounding cells of the current time step.

If the function  $F$  is derived using the value from the future time step ( $n + 1$ ), it is implicit as there are multiple unknown variables at time  $n + 1$ . A first-order implicit temporal discretization equation is given by (Blazek 2005b, Versteeg & Malalasekera 2007, Fluent 2011a):

$$\frac{\phi^{n+1} - \phi^n}{\Delta t} = F(\phi^{n+1}) \quad (4.17)$$

Similar to the linearization process for spatial discretised equations,  $F(\phi^{n+1})$  can be linearised as a function of values at the current cell and neighbour cells. Consequently, the equation of each cell can not be solved individually. Instead, a set of algebraic equations for all the cells over the entire mesh are solved simultaneously to obtain a solution.

A second-order implicit scheme is given by (Blazek 2005b, Versteeg & Malalasekera 2007, Fluent 2011a):

$$\frac{3\phi^{n+1} - 4\phi^n + \phi^{n-1}}{2\Delta t} = F(\phi^{n+1}) \quad (4.18)$$

where  $n - 1$  represents the previous time step. Second-order scheme gives better time accuracy as the information from the two previous steps is used in the equation. This scheme is preferred for the present research into the aerodynamic response of unsteady wind gusts.

For the explicit scheme, the Courant–Friedrichs–Lewy (CFL) condition (the numerical domain of dependence should contain the physical domain of dependence) needs to be satisfied, which means that  $\Delta t$  should be small enough that the distance of any information travelled

with the flow during  $\Delta t$  cannot exceed the vicinity of the neighbour cells (Laney 1998). A Courant number is defined as  $C = U\Delta t/\Delta h$ ,  $\Delta h$  is the character size of the mesh cell. The Courant number should be smaller than 1 for the explicit scheme but can be higher than 1 for the implicit scheme.

It also requires that all cells have the same time step. Therefore the timestep is limited by the small cells in the domain. However, for complex geometries, cells can be highly non-uniform such as the cells at the Coanda nozzle exit, which are very small and in a region of high velocity, whereas cells near the far field are much larger by several orders of magnitude. The time step needs to be smaller than approximately  $10^{-9}$  to satisfy the CFL condition over all cells, which is not practical to achieve.

Implicit schemes avoid the CFL condition by using the entire mesh as a computational domain (Laney 1998). It is unconditionally stable. Therefore there is no restriction on the size of the time step. Using a large time step does not cause stability problems and only affects the accuracy of temporal discretization. However, a smaller time step is still desired to obtain better accuracy.

In practice, there is a trade-off between the time step and convergence. For the flow solvers, a very small time step increases computational effort. To choose an appropriate time step that is stable and efficient to solve and with acceptable accuracy, a set of sensitivity studies were performed and are reported in the next chapter. For most of the simulations in this research, a second-order implicit scheme was used.

### 4.2.3 Pressure-Velocity Coupling

The N-S equations present relations between velocity and pressure. Each velocity component has a transport equation, but there is no transport equation for pressure. For incompressible flow, the continuity equation acts as a constraint for the flow field. If the pressure is correct, the velocity field calculated by momentum equations must satisfy the continuity equation. The governing equations are solved iteratively until a converged solution is reached. Such methods are named pressure-based solvers. For compressible flow, the continuity equation can be used for solving density. Meanwhile, the temperature can be solved by energy equations. Then the pressure can be obtained from density and temperature by the equation of state ( $p = p(\rho, T)$ ). This is the so-called density-based solver, which is usually used in high-speed compressible flow. However, the applications of both pressure based and density based methods are extended in modern CFD codes. For example, although pressure based solvers were originally used for incompressible flow, the energy equations can be solved in the itera-

tion process. As long as the solution is converged in each time step, the pressure based solver can still solve the density field and obtain a flow field for a compressible flow. Note that in the pressure based solver of Ansys Fluent, the kinetic energy ( $e + V^2/2$ ) and the pressure work term  $-p\nabla \cdot \mathbf{V}$  are neglected by default (Ansys 2018). In this research, most of the flows are incompressible, except the flow at the nozzle exit when a slight compressibility effect is presented. The density variation at the nozzle exit is gradual, and there are no shock waves, so it is acceptable to solve the energy equation separately after the momentum equations. Therefore the pressure based method is preferred for better convergence and less computational cost.

There are two categories of pressure-based solvers: segregated and coupled algorithms. The former algorithm sequentially calculates the governing equations and requires several inner iterations in one time step. On the other hand, coupled algorithms solve the continuity and momentum equations simultaneously in one step. Segregated algorithms require less memory compared with coupled algorithms, as only one quantity is solved at a time. However, more iterations are required for convergence. A comparison of the computation sequence of different solvers is presented in Figure 4.4.

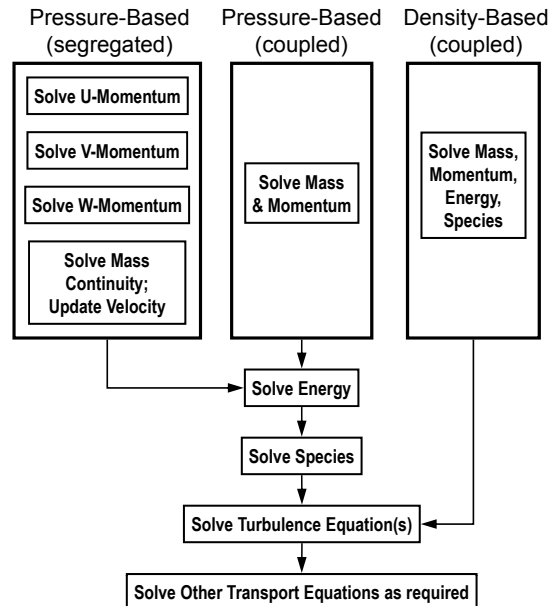


Figure 4.4: The solving sequence of governing equations (ANSYS 2010).

Semi-Implicit Method for Pressure Linked Equations (SIMPLE) and Pressure-Implicit with Splitting of Operators (PISO) are widely used segregated algorithms. The SIMPLE method uses a guessed pressure field to calculate the velocity from momentum equations. Then a pressure correction equation is used to correct the pressure to ensure that the continuity equa-

tion is satisfied. The terminology ‘Semi-Implicit’ comes from the omission of velocity terms in the derivation of pressure correction equations. Through this approximation, the pressure correction  $p'$  is calculated using pressure from neighbour cells only, reducing the complexity of pressure-velocity coupling (John D. Anderson 1995). Figure 4.5 presents a diagram of the calculation process of a transient SIMPLE algorithm.

Based on the SIMPLE algorithm, some less significant terms can be removed in the velocity correction equations, which is the so-called SIMPLEC (SIMPLE-Consistent) algorithm, proposed by Van Doormal and Raithby (Doormaal & Raithby 1984). For some basic laminar flows, using SIMPLEC results in faster convergence. But for complex flow or geometry with high skewness cells, the benefit of SIMPLEC is not significant (Ansys 2018).

The SIMPLE algorithm requires multiple iterations in one time step to make sure the momentum equations are satisfied. On the other hand, the PISO algorithm has an additional neighbour and skewness corrections. For transient flow, the PISO algorithm solves multiple corrections in the solution process (the so-called inner iterations) and therefore does not require iterations in one time step. PISO algorithm is recommended for transient solvers with large time steps as it has an aggressive convergence in a time step (Ansys 2018).

The SIMPLE, PISO, and Coupled algorithms should have similar results when the flow is sufficiently converged. The choice between different methods mainly depends on the computational cost. For transient flows in this research, the time step is set as small as permissible to achieve a good time stepping accuracy. When the time step is sufficiently small, PISO and Coupled methods may not have a significant advantage over the SIMPLE method. So the SIMPLE method is still favourable due to its lowest computational cost per iteration.

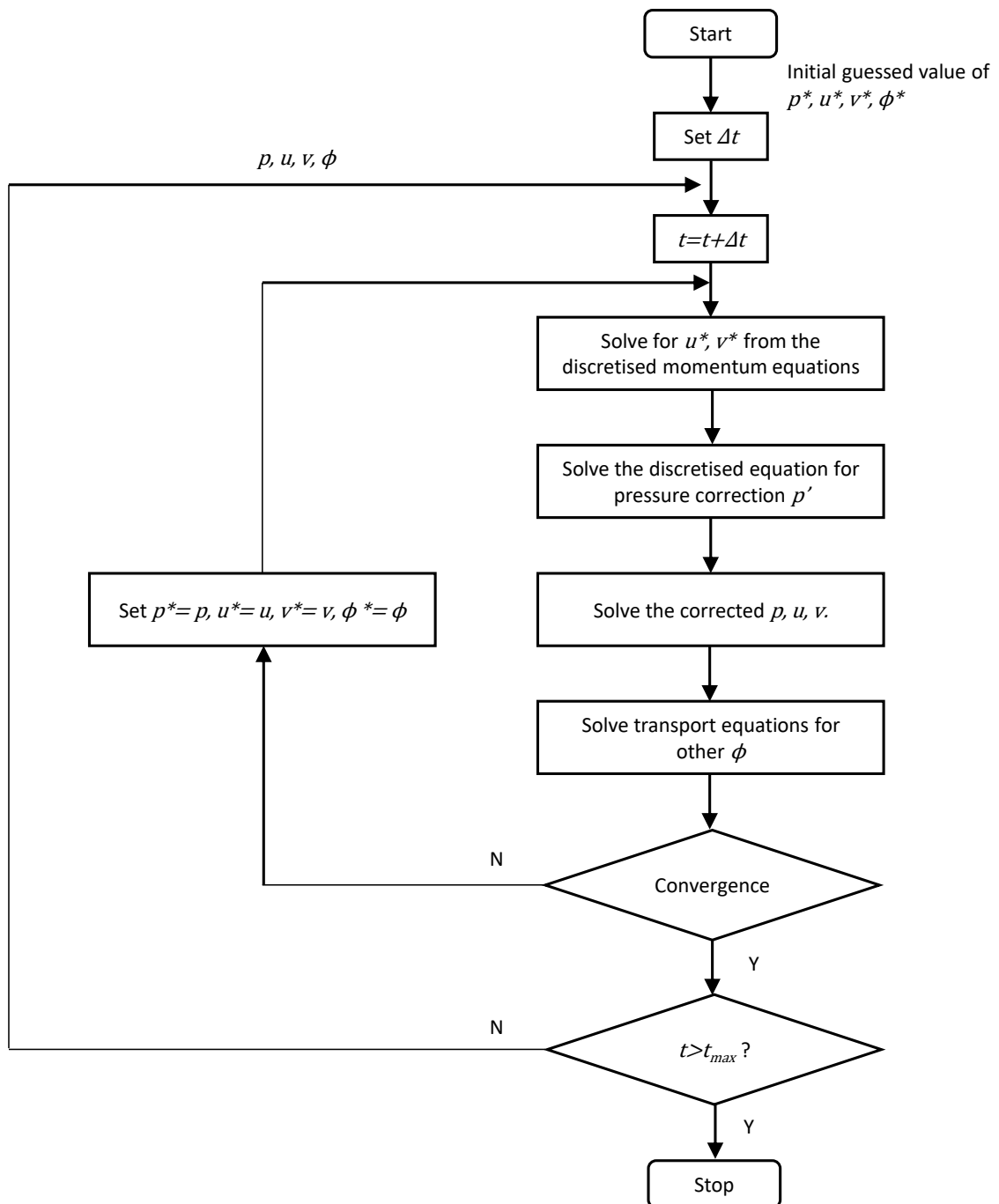


Figure 4.5: Transient SIMPLE algorithm for a 2D domain.  $p$  is the pressure,  $u$  and  $v$  are velocity components,  $\phi$  denotes additional scalars such as turbulent quantities and energy scalars. The  $p^*, u^*, v^*$  are guessed terms,  $p', u', v'$  are correction terms (Versteeg & Malalasekera 2007, Ansys 2018).

#### 4.2.4 Turbulence Model

There are various scales of eddies in a turbulent flow, where large eddies break down into smaller eddies and finally cause dissipation. In this process, the kinetic energy of the fluid is transformed into internal energy. Turbulent flows have a higher friction and heat transfer effect at the boundary of flow or the interface between fluid and solid surface, due to the intensive mixing effect. It occurs in most real engineering applications, for example, the separation of flow over an aircraft wing, the boundary layer at a high Reynolds number and the separation zone of the CC, which is of interest in this research.

#### Comparison of LES, DES and RANS for the Curved Wall Jet Flow

In this research, we are interested in the development of attached boundary layers over curved walls and how they entrain the external flow, and therefore the resulting surface pressure distribution and lift. Clearly, these flows are strongly influenced by turbulence. The eddies in a turbulent flow, such as eddies in the boundary layer and mixing layer, are randomly distributed and rapidly dissipated. These eddies affect the boundary layer growth rate, jet entrainment and wake, and therefore play an important role in the simulation of curved wall jet flow. Using LES with a fine mesh can resolve such eddies to predict a relatively accurate result of pressure distribution and jet separation (Nishino et al. 2010). In the RANS approach, these eddies are not resolved. Instead, only the time-averaged properties are produced with empirical models. The accuracy depends on whether the velocity and turbulent viscosity profiles in the boundary layer and jet are correctly presented by a RANS model. The LES and RANS are combined in the DES approach, in which the near-wall region is solved by RANS equations, and the outer regions, including the wake, are solved by LES. DES has been used for CC applications (Paterson & Baker 2004). However, its accuracy in CC compared with other turbulence models and its ability to capture the curvature effect are not widely reported.

The challenges of modelling the curved wall jet flow are primarily due to the entrainment effect. Neuendorf and Wygnanski (Neuendorf & Wygnanski 1999) have investigated the velocity and Reynolds stress profiles of a curved wall jet, showing a significantly stronger entrainment effect compared with plane wall jet (Neuendorf & Wygnanski 1999). Large eddies in the mixing layer (the shear layer on the outer side) play a major role in entraining the external flow and broadening the jet, and generating additional instabilities that enhance the turbulence level in the shear layer. This effect is not precisely solved by some RANS models, which are based on the Boussinesq hypothesis (Wilcox et al. 1998), and calibrated by relatively simple geometries such as back step, plane wall boundary layers and mixing layer flows

(Spalart & Allmaras 1992).

Swanson and Rumsey have studied the velocity and shear stress profiles of the flow over the Coanda surface (Swanson & Rumsey 2009). The jet solved by Spalart-Allmaras (S-A) and  $k - \omega$  models are relatively thin and have a higher maximum tangential velocity  $U_{max}$  (around 20% to 30% higher) than experimental results, indicating that these models under-predict the broadening effect compared with experiment. The higher  $U_{max}$  leads to a delayed jet separation. As shown in Figure 4.6, where SARC represents the S-A model with curvature correction, c represents coarse mesh containing 18996 cells, m represents medium mesh containing 75984 cells, f represents fine mesh containing 303936 cells. Note the near-wall velocity profiles at  $\theta = 90^\circ$  in (Figure 4.6 (f)), the experimental result is separated while the CFD results are still attached. As a result, the curved wall jet predicted by RANS models have relatively later separation and therefore higher lift coefficient than experiments.

In spite of the deficiencies reported by Rumsey using these turbulence models, in other studies, the RANS approach has demonstrated very good performance for predicting the overall lift and pressure distribution, especially at low Mach number and low blowing momentum coefficients, compared with experimental results (Lui et al. n.d., Jones et al. 2002, Liu et al. 2004, McGowan & Gopalarathnam 2005, Swanson et al. 2005a, Baker & Paterson 2006, Lee-Rausch et al. 2006, Swanson & Rumsey 2006, Salem Said & Ragab 2008, Pfingsten & Radespiel 2009, Keller & Rudnik 2015, Paterson & Baker 2004, Swanson & Rumsey 2009). Although Rumsey's RANS results predicted a lift coefficient that was 12% to 17% higher than using LES (Rumsey & Nishino 2011), this is probably because the geometry used by Rumsey used a very large circular trailing edge, and therefore the lift coefficient is more sensitive to the accuracy of the separation position. Additionally, in order to capture the effects of boundary layer transition, Rumsey modelled a wavy transition strip near the leading edge on the lower surface, and forced the RANS turbulent model to activate after the transition point ( a normal RANS model runs fully turbulent ). These manipulations may lead to a deviation in lift compared to other researchers.

As the performance of the RANS model is dependent on the geometry, mesh, working condition and solver, in order to find a suitable turbulence model for the presented flow problem, a validation of different turbulence models will be discussed in the next chapter.

This research is not seeking to find the most accurate turbulence model for predicting steady state flow but is mainly focused on the dynamic response of lift and its influence on aircraft flight dynamics. To achieve this objective, a series of different input signals were applied to the boundary condition, for example, sinusoidal wave and step signal. For the

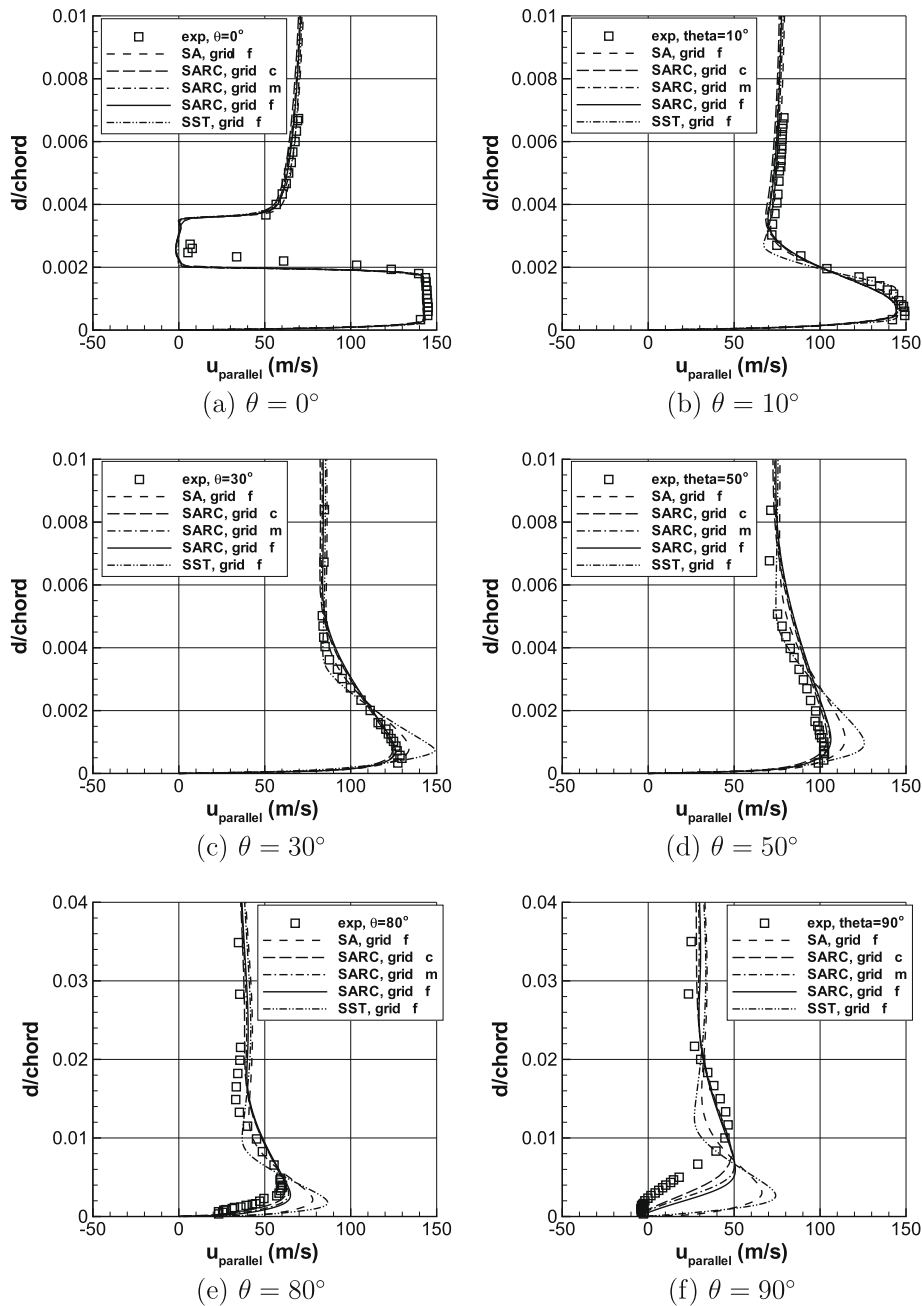


Figure 4.6: Mean velocity profiles of a curved wall jet with external flow,  $C_\mu = 0.03$ ,  $d$ : normal distance to the wall,  $u_{\text{parallel}}$ : tangential velocity component (Swanson & Rumsey 2009).

spectra analysis, signal waves in different frequencies have to be performed, and this analysis requires a large number of time steps (the order of magnitude is around  $10^6$  time steps for this research). Table 3.1 on page 61 has already compared the computational costs for CC applications in various geometry types and models. Additionally, Table 4.1 listed the CPU core-hours requirement of different turbulent approaches for the CC aerofoil. Although the LES simulation for steady state flow is achievable (Rumsey & Nishino 2011), the spectra analysis

of  $10^6$  time steps is very expensive considering that the RANS approach can achieve results with a similar accuracy at a significantly lower cost. Furthermore, the bandwidth range of the spectra analysis is around 0.5 - 50 Hz which covers the typical atmospheric gust / turbulence range that could influence the flight mechanics. This frequency range is much lower than the turbulent unsteadiness found within a shear layer for example, so there is no need to resolve the eddies in turbulent flow, only if the actuation frequency of the CC is comparable to the turbulence frequency (for example, high frequency pulsed blowing or ZNMF jets, where LES or DES should be employed) (Casey et al. 2000). In this research, only continuous blowing was used. In summary, RANS models are still preferred in this research given that their accuracy at low blowing momentum coefficients is acceptable.

Table 4.1: Computational expense of different turbulence modelling methods.

Modelling type	LES (Itsariyapinyo & Sharma 2018)	DES (Paterson & Baker 2004)	RANS
Mesh size (million)	10 - 100	1 - 10	0.1 - 0.5
CPU hours for $10^6$ time steps	$10^5$	$10^4$	$10^3$

### RANS Approach

The general form of the unsteady N-S equations is given in Equation 4.5 on page 95. These equations govern all types of Newtonian flows, including turbulent flow. Considering the mean characteristics of turbulent flow, the flow variables can be treated as a summation of the mean component and fluctuating component, expressed by mean value  $U, V, W$  and fluctuation value  $u', v', w'$ , as stated in Section 2.1.2 on page 9. The velocity components in the N-S equations (Equation 4.5 on page 95) can be replaced by

$$u = U + u' \quad v = V + v' \quad w = W + w' \quad (4.19)$$

Consequently, Reynolds averaged N-S equations can be obtained by replacing velocity components with mean and fluctuating components (Ansys 2018):

$$\frac{\partial \rho}{\partial t} + \frac{\partial}{\partial x_i} (\rho u_i) = 0 \quad (4.20)$$

$$\frac{\partial}{\partial t} (\rho u_i) + \frac{\partial}{\partial x_j} (\rho u_i u_j) = -\frac{\partial p}{\partial x_i} + \mu \left( \frac{\partial^2 u_i}{\partial x_j \partial x_j} \right) + \frac{\partial}{\partial x_j} \left( -\overline{\rho u'_i u'_j} \right) \quad (4.21)$$

where the  $u_i, u_j$  is the fluid velocity.

The  $-\overline{\rho u'_i u'_j}$  is the turbulent stress terms, these additional terms are negative because they are originally on the left side of the equations. The turbulent fluctuation terms are not included

in the continuity equation because the time-averaged divergence of a fluctuating vector quantity equals its mean component. Therefore in the continuity equation, the fluctuation terms are eliminated. Meanwhile, the density fluctuations caused by turbulent stress terms are neglected if the fluctuation component is of the order of 5% of the mean flow velocity (Versteeg & Malalasekera 2007). The density provides a linkage between energy, momentum and continuity equations. If the density variation caused by turbulent fluctuations is neglected, such fluctuations do not influence the energy equation. As a result, in low speed flows for this research, fluctuation terms do not exist in the energy equation.

### Eddy Viscosity Hypothesis

The eddies in a turbulent flow cause additional shear stress by momentum exchange which is known as ‘Reynolds stress’. As shown in the RANS equation system, the following terms are six additional stresses in a turbulent flow (Versteeg & Malalasekera 2007):

$$-\overline{\rho u'^2}, -\overline{\rho v'^2}, -\overline{\rho w'^2}, -\overline{\rho u'v'}, -\overline{\rho u'w'}, -\overline{\rho v'w'} \quad (4.22)$$

In the RANS approach, the Reynolds stress terms are predicted by turbulence models. A number of RANS turbulence models are available and widely used, including the S-A model,  $k - \varepsilon$  model,  $k - \omega$  model and Reynolds stress model. Except for the Reynolds stress model, which solves all stress terms in different directions, the other three turbulence models are based on the Boussinesq Hypothesis that Reynolds stress terms are proportional to the deformation rate of the fluid element (Versteeg & Malalasekera 2007):

$$\tau_{ij} = -\overline{\rho u'_i u'_j} = \mu_t \left( \frac{\partial U_i}{\partial x_j} + \frac{\partial U_j}{\partial x_i} \right) - \frac{2}{3} \rho k \delta_{ij} \quad (4.23)$$

where  $k = \frac{1}{2} (\overline{u'^2} + \overline{v'^2} + \overline{w'^2})$  is the turbulent kinetic energy,  $\mu_t$  is turbulent viscosity.  $\delta_{ij} = 1$  when  $i = j$ ,  $\delta_{ij} = 0$  when  $i \neq j$ . The turbulent viscosity  $\mu_t$  is assumed to be isotropic, which reduces the computational cost compared with the Reynolds stress model but also introduces inaccuracies in some complex flows where the anisotropy is significant. There is an additional assumption for RANS models that the flows are fully turbulent throughout the domain, i.e. the transition from laminar to turbulent boundary layer is not modelled.

In the Boussinesq Hypothesis, turbulent viscosity  $\mu_t$  is treated as a constant, which is inaccurate when a solid wall is present. A solid wall produces a blocking effect so that in the layer immediately close to the wall, the turbulent fluctuation is reduced. To address this problem, in some later RANS models such as  $k - \varepsilon$ ,  $k - \omega$  and S-A model, the wall-blocking effect is modelled by damping functions to give a better solution in the near wall region.

$$\frac{\partial}{\partial t}(\rho E) + \frac{\partial}{\partial x_i} [u_i(\rho E + p)] = \frac{\partial}{\partial x_j} \left[ \left( k + \frac{c_p \mu_t}{Pr_t} \right) \frac{\partial T}{\partial x_j} + u_i (\tau_{ij})_{eff} \right] + S_h \quad (4.24)$$

where  $k$  is the thermal conductivity,  $E$  is the total energy, and  $(\tau_{ij})_{eff}$  is the deviatoric stress tensor (Note  $(\tau_{ij})_{eff}$  is not solved in the pressure-based solver).

$$(\tau_{ij})_{eff} = \mu_{eff} \left( \frac{\partial u_j}{\partial x_i} + \frac{\partial u_i}{\partial x_j} \right) - \frac{2}{3} \mu_{eff} \frac{\partial u_k}{\partial x_k} \delta_{ij} \quad (4.25)$$

$Pr_t = \frac{c_p \mu_t}{k_t}$  is the turbulent Prandtl number and by default, it is set to 0.85 at the wall.  $k_t$  is the turbulent thermal conductivity. The turbulent Prandtl number is analogous to the Prandtl number which refers to the ratio of energy dissipated by friction to the energy transported by thermal conduction (Anderson Jr 2016).

For this research where the maximum flow velocity appears at the nozzle exit where  $M < 0.5$ , and the freestream  $M < 0.2$ . As mentioned in Section 4.2.3 on page 102. The turbulent fluctuation terms have a small influence on the density field. Therefore the Favre averaging ( density-weighted averaging ) is not used in the methodology (Versteeg & Malalasekera 2007, Anderson Jr 2016).

The following section introduces governing equations of frequently used RANS models.

### $k - \varepsilon$ Model

To calculate the Reynolds stress term according to the Boussinesq hypothesis, a more accurate and practical method to calculate the eddy viscosity factor is required.  $k - \varepsilon$  model introduces two factors to construct an equation of the eddy viscosity, the turbulent kinetic energy ( $k$ ) and the turbulent dissipation rate ( $\varepsilon$ ). The  $k$  and  $\varepsilon$  can be solved by two transport equations with empirical coefficients from experiments. There are additional empirical damping functions to correct the dissipation rate close to the wall (Jones & Launder 1972). Even so, the prediction of flows involving the separation and reattachment of the boundary layer is questionable. Hence the  $k - \varepsilon$  model is usually restricted to high Reynolds number attached-flow applications (Blazek 2005b).

The transport equations of the  $k - \varepsilon$  model are given as follows (Blazek 2005b) (Fluent 2011a).

$$\frac{\partial}{\partial t}(\rho k) + \frac{\partial}{\partial x_i} (\rho k u_i) = \frac{\partial}{\partial x_j} \left[ \left( \mu + \frac{\mu_t}{\sigma_k} \right) \frac{\partial k}{\partial x_j} \right] + G_k + G_b - \rho \varepsilon - Y_M + S_k \quad (4.26)$$

$$\frac{\partial}{\partial t}(\rho \varepsilon) + \frac{\partial}{\partial x_i} (\rho \varepsilon u_i) = \frac{\partial}{\partial x_j} \left[ \left( \mu + \frac{\mu_t}{\sigma_\varepsilon} \right) \frac{\partial \varepsilon}{\partial x_j} \right] + C_{1\varepsilon} \frac{\varepsilon}{k} (G_k + C_{3\varepsilon} G_b) - C_{2\varepsilon} \rho \frac{\varepsilon^2}{k} + S_\varepsilon \quad (4.27)$$

where  $G_k$  is the generation of turbulence kinetic energy due to velocity gradients.  $G_b$  is the generation of turbulence kinetic energy due to buoyancy.  $Y_M$  describes the effect of compressibility on turbulence.  $C_{1\varepsilon}, C_{2\varepsilon}, C_{3\varepsilon}, \sigma_k, \sigma_\varepsilon$  are constants.  $S_k$  and  $S_\varepsilon$  are user-defined source terms. The turbulent viscosity  $\mu_t$  in the N-S equations is therefore given by

$$\mu_t = C_\mu \rho \frac{k^2}{\varepsilon} \quad (4.28)$$

where  $C_\mu$  is a dimensionless constant. The above constants are different for various models, in Ansys Fluent, these are given by

$$C_\mu = 0.09, \sigma_k = 1.00, \sigma_\varepsilon = 1.30, C_{1\varepsilon} = 1.44, C_{2\varepsilon} = 1.92 \quad (4.29)$$

The original  $k - \varepsilon$  model was developed by assuming the molecular viscosity is negligible, so it is unsuitable for boundary layer flows where the viscous sublayer can not neglect (Fluent 2011a). For flows around an aerofoil, the solution of the boundary layer is important to determine the flow separation and surface drag. The Shear-Stress Transport (SST)  $k - \omega$  Model was developed to produce a better prediction in the near-wall region.

### SST $k - \omega$ Model

The damping functions of the previous  $k - \varepsilon$  model are unreliable in some flow conditions, so the  $k - \omega$  model was developed, which has a better wall treatment. The  $k - \omega$  model solves a specific rate of dissipation of kinetic energy ( $\omega$ ) instead of  $\varepsilon$ . The  $k - \omega$  model has a better performance of predicting near-wall behaviour than the  $k - \varepsilon$ , while the latter is more robust in free stream flows. The SST  $k - \omega$  model, contributed by Menter (Menter 1994), combines the advantages of both the  $k - \omega$  model and the  $k - \varepsilon$  model. The  $k - \omega$  is used in the mesh layers that are close to the wall, while the  $k - \varepsilon$  is used in the cells away from the wall. A blending function is used to smoothly transit from the near-wall layers to the cells in free stream flow. The SST  $k - \omega$  model also includes a viscosity limiter to further reduce the shear stress of the flow close to the wall, which better agrees with the experiments. This model is favourable in predicting separation locations and in cases with adverse pressure gradients (Menter & Rumsey 1994).

The transport equations of  $k$  and  $\omega$  is given by (Blazek 2005b)(Fluent 2011a):

$$\frac{\partial}{\partial t}(\rho k) + \frac{\partial}{\partial x_i}(\rho k u_i) = \frac{\partial}{\partial x_j} \left( \Gamma_k \frac{\partial k}{\partial x_j} \right) + G_k - Y_k + S_k \quad (4.30)$$

$$\frac{\partial}{\partial t}(\rho \omega) + \frac{\partial}{\partial x_i}(\rho \omega u_i) = \frac{\partial}{\partial x_j} \left( \Gamma_\omega \frac{\partial \omega}{\partial x_j} \right) + G_\omega - Y_\omega + S_\omega \quad (4.31)$$

where  $G$  represents the generation of  $k$  and  $\omega$  due to velocity gradients,  $Y$  is the dissipation due to turbulence,  $S$  represents the source terms defined by users,  $\Gamma$  is the effective diffusivity given by (Menter 1994):

$$\begin{aligned}\Gamma_k &= \mu + \frac{\mu_t}{\sigma_k} \\ \Gamma_\omega &= \mu + \frac{\mu_t}{\sigma_\omega} \\ \mu_t &= \alpha^* \frac{\rho k}{\omega}\end{aligned}\tag{4.32}$$

where  $\sigma$  is the turbulent Prandtl number.  $\alpha^*$  is a correction coefficient for low-Reynolds number. In the SST  $k - \omega$  model,  $\mu_t$  is further limited considering the transport of the turbulent shear stress.

At a solid wall, the turbulent kinetic energy  $k$  is zero. The  $\omega$  at the wall is given by:

$$\omega_{wall} = \frac{\rho (u^*)^2}{\mu} \omega^+\tag{4.33}$$

where,  $\mu$  is the dynamic viscosity of air,  $\omega^+$  is a function of the wall  $y^+$ ,  $u^*$  is the dimensionless velocity parallel to the wall. In the solver, this function is automatically blended from the viscous sublayer to the log-law region, which is insensitive to the mesh resolution near the wall (Ansys 2018).

### S-A One-Equation Model

In the viscous sub-layer of the boundary layer, the profile of the turbulent kinematic viscosity ( $\nu_t$ ) is not linear. In the S-A model, a new parameter  $\tilde{\nu}$  is defined which is linked to  $\nu_t$  ( $\mu_t/\rho$ ) by a transport equation. The profile of  $\tilde{\nu}$  in the near-wall region is close to a linear distribution, so it is easy to be solved numerically. The S-A model has only one equation to solve  $\tilde{\nu}$ , so it requires less computational effort than the SST  $k - \omega$  model (Spalart & Allmaras 1992). It predicts good results for the boundary layer with adverse pressure gradients and has fast and robust convergence. S-A model has been widely used in aerospace engineering and shows good agreement with experiments (McDaniel et al. 2007). However, the S-A model has limitations, such as the inaccuracy when the length scale changes abruptly (Fluent 2011a). For example, a jet flow discharged from a rounded nozzle.

In addition, it is less reliable to predict homogeneous, isotropic turbulence and free shear flows. The flows in this research include jet sheet, shear layer and curved wall jet. As mentioned in Section 4.2.4 on page 106, the results predicted by RANS models, including the S-A model, generally have good agreement with experimental results in terms of lift coefficients (Jones et al. 2002, Liu et al. 2004, McGowan & Gopalathnam 2005, Swanson et al. 2005a, Baker & Paterson 2006, Lee-Rausch et al. 2006, Swanson & Rumsey 2006, Salem Said & Ragab

2008, Pfingsten & Radespiel 2009, Keller & Rudnik 2015), but have relatively small spreading effect for the jet sheet (Rumsey & Nishino 2011). The accuracy is also relevant to the shape of the geometry. Hence further validation is required to evaluate the level of accuracy for the specific application in this research, which is discussed in Chapter 5 on page 124.

The standard S-A model is used in this research, in which the modified turbulent viscosity  $\tilde{\nu}$  is described by the following transport equation (Spalart & Allmaras 1992) (Fluent 2011a):

$$\frac{\partial}{\partial t}(\rho\tilde{\nu}) + \frac{\partial}{\partial x_i}(\rho\tilde{\nu}u_i) = G_\nu + \frac{1}{\sigma_{\tilde{\nu}}} \left[ \frac{\partial}{\partial x_j} \left\{ (\mu + \rho\tilde{\nu}) \frac{\partial \tilde{\nu}}{\partial x_j} \right\} + C_{b2}\rho \left( \frac{\partial \tilde{\nu}}{\partial x_j} \right)^2 \right] - Y_\nu + S_{\tilde{\nu}} \quad (4.34)$$

On the left side, there are temporal derivative and convection term, which are similar to a general transport equation. On the right side,  $G_\nu$  denotes the production of turbulent viscosity due to shear, for example, the velocity gradients in the boundary layer. The terms in the square bracket correspond to diffusion. These terms describe the spread of turbulent viscosity from high intensity area to low intensity area. For example, the spread of a wake. The constant  $c_{b2} = 0.622$  is the coefficient of the non-linear part of the diffusion term, which is calibrated with experimental data to produce a more accurate wake.  $\sigma_{\tilde{\nu}} = \frac{2}{3}$  is the turbulent Prandtl number.  $Y_\nu$  is the destruction term, which is used to model the blocking effect of the wall in the near-wall region.  $S_{\tilde{\nu}}$  is the source term which is not considered here.  $\tilde{\nu}$  is the modified turbulent viscosity and  $\nu$  is the molecular kinematic viscosity. The relation between turbulent eddy viscosity and modified turbulent viscosity is given by the following equation (Spalart & Allmaras 1992):

$$\mu_t = \rho\tilde{\nu}f_{v1} \quad (4.35)$$

where  $f_{v1} = \frac{\chi^3}{\chi^3 + C_{v1}^3}$  is the viscous wall-damping function,  $\chi \equiv \tilde{\nu}/\nu$  is an intermediate variable.  $C_{v1} = 7.1$  is a constant. At the wall,  $\tilde{\nu} = 0$ , whereas in the freestream,  $\tilde{\nu} = \nu_t$ .

The turbulent parameters for the free stream are defined in the far field boundary condition by the turbulent viscosity ratio  $\mu_t/\mu$ , which is proportional to the turbulent Reynolds number  $Re_t \equiv k^2/\varepsilon\nu$ . The solver then calculates the inlet boundary  $\tilde{\nu}$  according to a specified turbulent viscosity ratio. In this research,  $\mu_t/\mu$  is set to 10 (Fluent 2011b), which is a relatively large value to simulate the gusty atmosphere. The turbulence intensity in the boundary layer is usually significantly higher than the ambient flow. Hence the turbulent settings at far field boundary have little influence on the boundary layer around the aerofoil (Fluent 2011b). For the pressure inlet condition in the plenum chamber of the CC aerofoil,  $\mu_t/\mu$  is also set to 10.

### 4.2.5 Boundary Conditions

The governing equations of CFD can describe different types of flow, from supersonic to low speed, in various altitudes and various geometries of the domain. To specify a flow field in a certain situation, initial conditions and boundary conditions are required. Boundary conditions define the physical constraints of the computation domain and the flow parameters in the far field. In the simulation of gust response, the dynamic gust profile is also defined by the far field boundary condition. The main boundary types used in this thesis are listed as follows.

#### Walls

Wall boundary is used for the geometry of the aircraft, the nozzle chamber (except the nozzle inlet boundary condition) and the Coanda surface at the trailing edge. The wing surface, for example, is defined as a solid wall as the flow near the wing is not able to penetrate through the surface. The normal component of velocity near the surface is zero. For a viscous flow near a stationary wall, the tangential velocity of the fluid nearest to the surface is also zero, which is the no-slip condition. The velocity components of the fluid layer adjacent to the surface are,

$$u = v = w = 0 \quad (4.36)$$

where  $u, v, w$  are the x, y, z components of the velocity. Additionally, if the temperature of the wall is known as a constant  $T_w$ , the temperature of the fluid adjacent to the wall is

$$T = T_w \quad (4.37)$$

In the other situation, when there is no heat transfer between the wall and the fluid, which is the adiabatic wall condition

$$\left( \frac{\partial T}{\partial n} \right)_w = 0 \quad (4.38)$$

Although the actual surface of the material has complex heat transfer with the fluid, most of the situation can be assumed by either the adiabatic wall or a constant temperature (John D. Anderson 1995).

The mesh distribution near the wall is another important factor in simulating the boundary layer flow precisely. For example, the  $y^+$  of the first mesh layer adjacent to the wall. For a coarse mesh (e.g.,  $y^+ > 10$ ), the wall function (Wilcox et al. 1998) can be applied to describe the flow profile near the wall by existing models. If the mesh near the wall is very fine, and  $y^+ \leq 1$ , the boundary layer flow can be solved directly without wall functions (Blazek 2005b).

In Ansys Fluent, a  $y^+$  insensitive treatment for the near-wall region is applied (for  $k - \omega$  and S-A turbulence model). This treatment ensures that the solution is blended from the viscous sublayer, the buffer layer, to the log-law region. There is no strict requirement for the thickness of the first layer adjacent to the wall ( e.g. less than  $y^+ = 1$  so that the first layer is thinner than the viscous sublayer ). While in Fluent, even if the first layer covers the buffer layer or log-law region, a reasonable profile can be solved by the blended formulation. However, a sufficient amount of layers within the boundary layer is still necessary to deliver a good resolution in the near-wall region and resolve flow separation. The number of layers is recommended as 10 - 20 to cover the boundary layer (Fluent 2011b). This is checked in the validation case in the next chapter.

In terms of the pressure at the solid wall, it can be extrapolated from the interior of the domain (Blazek 2005b) using the pressure at the centre of the first cell next to the wall, or using extrapolation of pressure on the first and second mesh layers for higher accuracy.

### Far Field

The Pressure far field is used in the 2D and 3D simulations, which defines the free stream condition with designated Mach number, total pressure, temperature and flow angles. The far field boundary is far away from the model and should not reflect the instability waves from the model. The pressure far field boundary is only used in compressible flow using the ideal-gas model (Fluent 2011a). The outer boundary is required to be placed far enough from the model. It can not be used for multi-phase models and constant-density models. In the 2D simulations of the aerofoil, a circular shape far field was defined, while in the 3D cases the far field was a semi-sphere shape. Figure 4.7 shows the boundary settings in this research, the far field was set as a pressure far field condition. In company with the ideal gas law so the domain is treated as compressible flow in Ansys Fluent.

For subsonic flows, two Reimann invariants are used to calculate the flow properties:

$$\begin{aligned} R_{\infty} &= v_{n\infty} - \frac{2c_{\infty}}{\gamma - 1} \\ R_i &= v_{n_i} + \frac{2c_i}{\gamma - 1} \end{aligned} \quad (4.39)$$

where  $v_n$  is the normal velocity,  $c$  is the speed of sound,  $\gamma$  is the ratio of specific heats for ideal gas. Variables with a subscript  $\infty$  are the free stream values specified at the boundary and the variables with  $i$  are interior values. Then the normal velocity and speed of sound on the boundary are given by:

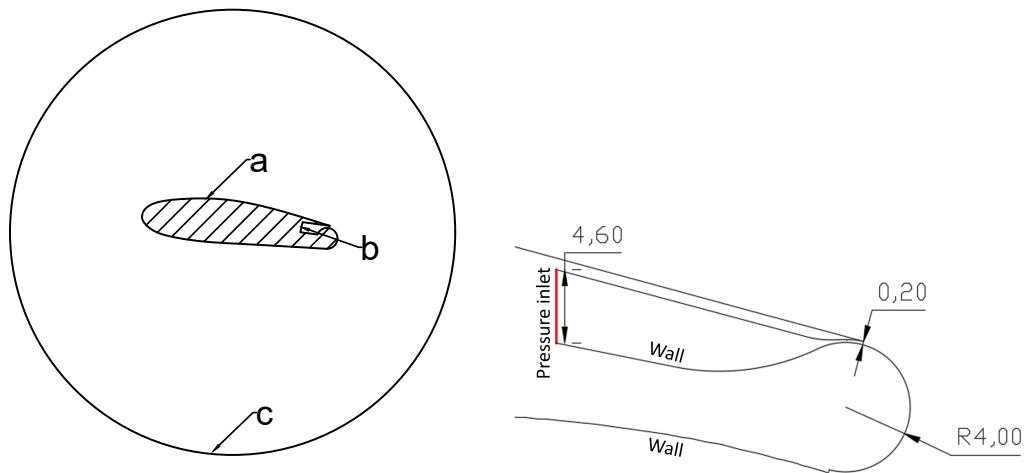


Figure 4.7: The schematic of the boundary settings. (a) wall, (b) inlet, (c) far field. The right figure shows a close-view of the nozzle.

$$\begin{aligned} v_n &= \frac{1}{2} (R_i + R_\infty) \\ c &= \frac{\gamma-1}{4} (R_i - R_\infty) \end{aligned} \quad (4.40)$$

Using  $v_n$  and  $c$ , in addition to tangential velocity and entropy, the other flow variables can be solved (Fluent 2011b).

### Inlet / Outlet

Ansys Fluent provides different types of inlet and outlet conditions, as listed below.

- Velocity inlet, defines the velocity and scalar variables at the flow inlet
- Pressure inlet, defines the total pressure and other variables at the flow inlet
- Mass flow inlet, defines the mass flow rate for compressible flow
- Pressure outlet, defines the static pressure at the flow outlet

In the simulation of CC, the boundary inside the plenum chamber is defined as a pressure inlet (i.e. surface 'b' in Figure 4.7). The nozzle of the plenum chamber is usually controlled by pneumatic valves where the pressure is known but the velocity is not, thus the pressure inlet condition is suitable for this situation.

For compressible flow, the velocity inlet boundary condition is not useable, therefore the pressure inlet condition is used in the nozzle chamber and a total pressure is specified. The relation between pressure and velocity for the isentropic flow of ideal gas is given by the

following formulation:

$$\frac{p'_0}{p'_s} = \left(1 + \frac{\gamma - 1}{2} M^2\right)^{\gamma/(\gamma-1)} \quad (4.41)$$

where  $p'_0$  is the total pressure specified on the boundary, and  $p'_s$  is the static pressure from the adjacent cell in the flow domain. This equation can be used to calculate the Mach number and other flow variables (Fluent 2011*b*).

### Symmetry Plane

A symmetry plane can be used when the flow is symmetrical to a plane. The symmetry plane boundary condition has the following features (Blazek 2005*b*):

- There is no flux transport across the plane.
- The normal velocity at the plane is zero.
- The gradient of a scalar in the normal direction is zero.
- The gradient of tangential velocity in the normal direction is zero.
- The gradient of normal velocity along the plane is zero.

On the cells adjacent to the symmetry plane, the scalars and velocity components are resolved by assuming there are ‘dummy cells’ on the other side of the plane which have the same values. In this research, the 3D aircraft model was split by a symmetry plane on the centre of the fuselage, and only half of the aircraft was solved. The propeller was not considered so there was no asymmetrical propeller wake. Assuming the flow is symmetrical to the centre of the fuselage, the symmetry plane boundary condition is therefore applied.

### 4.2.6 Mesh Generation

Meshing is the process of discretising the computational space and the surface of the geometry, so that the conservation equations and turbulence models can be applied to each cell. Different meshing approaches greatly influence the data transfer between cells and the flow near the walls. Whilst the meshing is also influenced by the shape of the model. Meshing is an important and time-consuming stage during the simulation, but a high-quality mesh can dramatically reduce the computational time and increase accuracy.

There are two types of mesh, structured and unstructured. In a structured mesh, all the cells are mapped and stored by a regular index. The mesh has a uniform and ordered topology, and the mesh cells with adjacent index are also connected in the physical mesh. According to

the shape of the geometry, the C, H and O types of topology can be used, as shown in Figure 4.8. The C shape is suitable for an aerofoil with a sharp trailing edge and round leading edge. Whereas the H shape is suitable for the supersonic aerofoil with both a sharp leading edge and trailing edge. The O shape can be applied to most of the geometries except a zero-thickness trailing edge. An advantage of structured meshes is that cells are better aligned with the local flow direction, which can improve the accuracy of the simulation, particularly where shear layers are present.

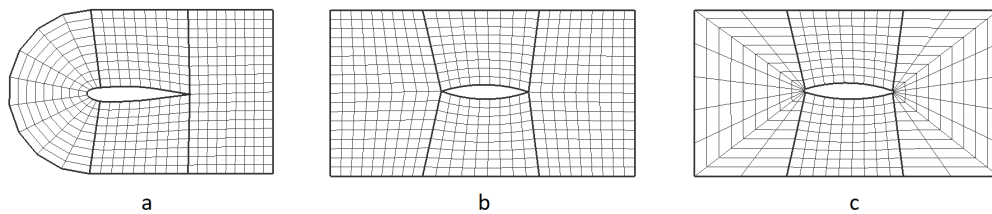


Figure 4.8: The topology of structured mesh. (a) C-shape, (b) H-shape, (c) O-shape.

When the geometry becomes complex with twisted surfaces or gaps, the structured mesh is no longer suitable. In this case, the unstructured mesh has a better performance. It has no ordering or uniform index, the neighbouring cells can not be determined by the index (Blazek 2005b). Various types of cells are used in unstructured meshing, as shown in Figure 4.9.

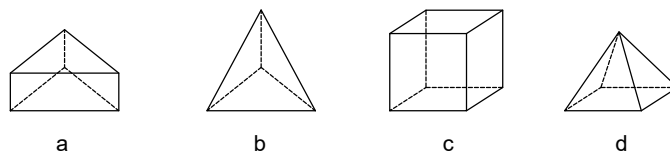


Figure 4.9: The cells of unstructured mesh. (a)prism, (b)tetrahedral, (c) hexahedral, (d)pyramid.

The unstructured mesh has advantages over structured mesh for complex geometries, at corners or sharp edges, and local refinement zones can easily add to unstructured meshes without affecting other regions. While in structured meshes, local refinement may lead to an increased number of cells away from the refined region. Unstructured cells can be any shape including triangles and quadrilaterals for 2D, tetrahedral and hexahedral for 3D. These shapes are more adaptive to sharp edges or corners.

Prism mesh is usually used in the near-wall boundary layers, where the flow is mainly tangent to the wall. Prisms are stretched to thin layers to capture the velocity profile due to viscosity. Tetrahedral and hexahedral meshes are used in the volume domain as they can

fill in complex geometries. The pyramids are used as an interface between prism layers and tetrahedral mesh.

The geometry in this research has narrow gaps and twisted surfaces, and there are difficulties in meshing the prism layers and the mesh inside the jet slot. When using a structured meshing approach, the plenum chamber and the jet nozzle slot can mesh easily, but the highly-twisted transition surface between the wing root and the fuselage is very difficult to mesh. Whereas when an unstructured approach is used, it can easily mesh complex surfaces and fill the volume mesh, but there will be too many cells in the long and narrow jet slot (length:885mm, width: 0.2mm). The best method is using structured mesh inside the chamber and nozzle, while using unstructured mesh for the volume mesh. This is discussed further in Chapter 6.

Pointwise V18.1 was used to generate these hybrid meshes, using an anisotropic tetrahedral extrusion (i.e. the 'T-Rex' tool ) to deal with the transition from prism to volume mesh (Pointwise n.d.). Firstly, it extrudes from the wall with anisotropic mesh, and then each point grows at a user defined growth rate with triangular cells, until reaches the maximum layers or the new cells are isotropic, or collide with other layers. The T-Rex extrusion can smoothly transition from anisotropic to isotropic mesh. Figure 4.10 shows an example of the T-Rex meshing for a 2D aerofoil.

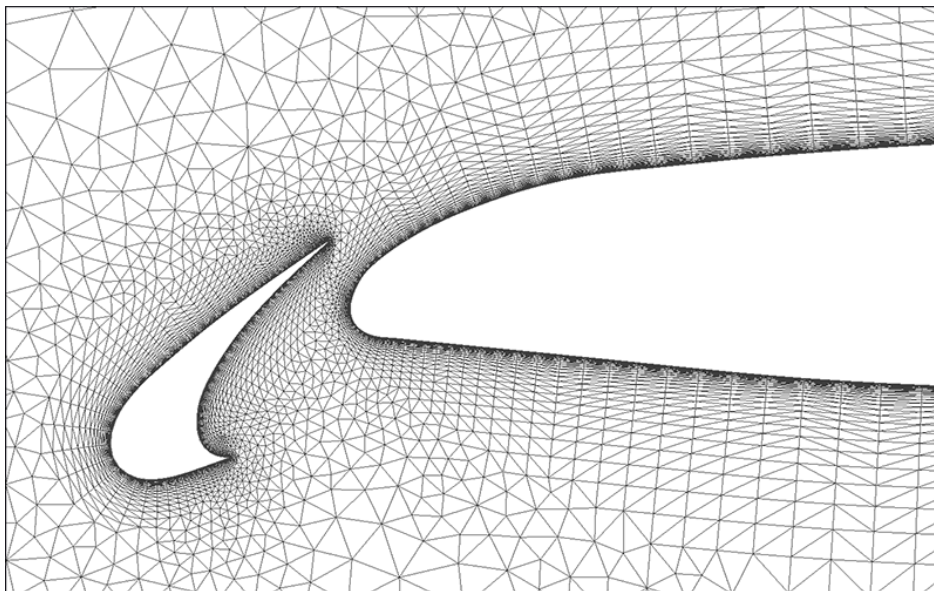


Figure 4.10: T-Rex meshing of a multi-element aerofoil (Pointwise n.d.).

### 4.2.7 Numerical Errors

This section is a summary of the factors that influence the accuracy of simulation both in space and time. The reasons for errors are discussed and methods of improvement are given.

#### Mesh Induced Errors

Mesh-induced errors are caused by insufficient mesh resolution and low quality cells. In the Finite Volume method, the flow domain is composed of millions of control volumes. Differential equations are discretised to algebraic equations in each of the control volumes, assuming the flow variables are linearly distributed in the control volume. With a higher mesh resolution, the results of algebraic equations are more close to the non-linear differential equation. For strong shear flows, high speed jets, and flow over a geometry with large curvature, the gradients of flow variables are much stronger than a flow over an aerofoil. Insufficient mesh resolution in these areas may produce incorrect separation points or unphysical spreading of the jet since these large velocity gradients are not captured sufficiently (Jasak 1996).

For the CC problem, it is important to obtain an accurate solution for the jet broadening and jet separation. Except for choosing the right turbulence model and flow solver, the mesh at the nozzle exit and trailing edge should be sufficient to capture the mixing layer, and the number of nodes on the radial and tangential direction of the Coanda surface should be sufficient. According to the study by Swanson and Rumsey (Swanson & Rumsey 2009) on a CC aerofoil with S-A model, the difference of lift coefficient predicted by a fine mesh and a coarse mesh is around 5% at  $C_{\mu}=0.03$ , this difference increased to 11% at  $C_{\mu}=0.226$ .

The mesh quality is another important factor that greatly impacts the convergence and final results. Mesh quality is evaluated by a variety of parameters. For example, the aspect ratio, which is the ratio of maximum length to the minimum length of one cell (the aspect ratio of tetrahedral cells is the ratio of the radius of the circumscribed sphere to the inscribed sphere divided by 3 (Versteeg & Malalasekera 2007)). The definition of aspect ratio is different for various flow solver and meshing packages, but their purpose is the same which is to describe the stretching of a cell. High aspect ratio cells can be found around the corner of two walls or close to the trailing edge. These cells are unfavourable and may cause slow convergence due to differencing errors. Local refinement is needed to reduce high aspect ratio cells. Before each flow simulation, a coarse mesh can be used to perform an initial simulation which gives a picture of the flow. Subsequently, refinement is gradually added to the mesh until the simulation results are independent of the mesh density.

The non-orthogonality is another source of errors. On the interface between two adjacent

cells, the flux normal to the face is calculated in the computational process of discretised N-S equations. More specifically, the diffusion term is formulated as the summation of flux over all the faces enclosed around a cell (Equation 4.11 on page 98). Mesh non-orthogonality and skewness are two factors that deteriorate the accuracy of simulation as a result of inaccurate face flux. Figure 4.11 shows two adjacent unstructured cells,  $c_0$  and  $c_1$  are the cell centroid,  $\mathbf{n}$  is a unit vector normal to the face,  $\mathbf{S}$  is the surface vector,  $\mathbf{T}$  is the cross-diffusion term,  $A_f$  is the surface area,  $\mathbf{r}_0$  and  $\mathbf{r}_1$  are vectors connecting the cell centroid and the face centre. If the surface vector  $\mathbf{S}$  and the vector from cell centroid  $c_0$  to  $c_1$  are not co-linear, the cells are non-orthogonal. In this case,  $\mathbf{S} = \mathbf{r}_1 + \mathbf{T}$ .

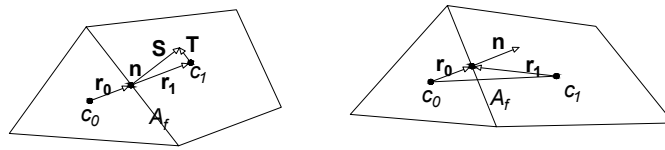


Figure 4.11: Non-orthogonal (left) and skewed (right) cells (Ansys 2018).

Because vector  $\mathbf{T}$  can not be directly derived from cell centroid values on  $c_0$  and  $c_1$ ,  $\mathbf{T}$  is treated explicitly from  $\mathbf{S}$  and  $\mathbf{r}_1$  using previous solution (F. Moukalled 2016). This process introduces instabilities and inaccuracies in the flux results.

The inaccuracy is further increased when the line connecting  $c_0$  and  $c_1$  does not intersect with the face centre, shown in Figure 4.11(right), which is called skewed cells. Additional interpolation is required to obtain the value on the face centre from line  $c_0c_1$ . To avoid inaccuracy due to non-orthogonal and skewed cells, every effort should be made to ensure the mesh is orthogonal and satisfy the solver requirements of mesh quality.

### Differencing Scheme Induced Errors

The discretization of non-linear differential N-S equations is fundamentally using Taylor series representation of the differential equation (Versteeg & Malalasekera 2007). For a function,  $\phi(x)$ , the Taylor series of  $\phi(x + \Delta x)$  is given by the following equation. The higher-order truncated terms are neglected so that a simple algebraic equation can approximate  $\phi(x)$ :

$$\phi(x + \Delta x) = \phi(x) + \left(\frac{\partial\phi}{\partial x}\right)_x \Delta x + \left(\frac{\partial^2\phi}{\partial x^2}\right)_x \frac{\Delta x^2}{2} + \dots \quad (4.42)$$

The power of the truncated terms is called the order of difference approximation. A higher-order approximation has less error but is more difficult to solve. In this research, a second-order differencing scheme was used for both spatial and temporal discretization. For temporal

discretization, the time stepping accuracy is also important for the prediction of dynamic response. This is ensured by sensitivity studies prior to every flow problem.

### **Turbulence Modelling Errors**

Turbulence modelling is another major source of error for CFD simulations. CC problem is generally difficult to accurately predict by CFD due to the strong entrainment effect by high speed jet around a circular surface. CFD simulations may overpredict the lift coefficient compared with experimental results because the jet spreading by CFD simulations are relatively weak ( see Figure 4.6 ), resulting in delayed jet separation.

The simulation conducted by Takafumi Nishino et al. shows that LES gives 6.8% higher lift than the experimental result when  $C_{\mu}=0.044$ . In comparison, the simulation conducted by Swanson and Rumsey using S-A model with curvature correction produces 13.8% higher lift than experiments at  $C_{\mu}=0.03$ . On the other hand, as mentioned in Section 4.2.4 on page 106, other researchers have obtained better accuracy using RANS methods at  $C_{\mu} < 0.1$ . Overall, the turbulence model significantly influences lift results, steady and unsteady validations are needed to ensure the deviation in the lift is acceptable.

## **4.3 Summary**

This chapter introduces the computational methodologies used in this research. The fundamental Navier-Stokes equations, turbulence models, solver and meshing techniques, are discussed. Finally, several reasons that affect the accuracy of simulation are concluded.

The simulations in this research involve unsteady 2D or 3D external flows in the range of  $M = 0.1$  to  $0.3$ . The flow is mainly incompressible but includes some regions of weakly compressible flow in the nozzle where the Mach number is up to  $0.5$ . There are no shock waves, and a compressible solver with a pressure-based segregated algorithm is sufficient.

The geometries used in this research are relatively complex, including sharp edges and thin gaps. It is difficult to build high-quality structured meshes. Hence both structured and unstructured meshes were used. This also determines the selection of differencing schemes and turbulence models. The second-order upwind scheme is suitable in this case since the 3D mesh may include non-hexahedral cells which may not be applicable to some other schemes. Considering the unique features of the mesh, RANS models are preferred. They have good accuracy to predict the separation and pressure distribution, and a reasonable computational cost considering the large number of iterations required. The RANS models, including other simulation settings, are validated in the next chapter.

# Chapter 5:

## The Preliminary Study of a 2D CC Aerofoil

This chapter is a preliminary study of the performance of CC using a relatively simple CC aerofoil. A steady-state CFD simulation process was initially validated using published wind tunnel data. Subsequently, unsteady validation was conducted using an analytical curve for the sharp edge gust encounter problem. Then the frequency response of the CC aerofoil was obtained from unsteady CFD simulations, the response results were used for comparison with conventional mechanical flap and tuning a controller. The performance was verified in a novel closed-loop simulation coupling CFD analysis with a control algorithm by regulating the boundary condition according to the intermediate variables obtained in each simulation step. Results show that the CC can suppress the gust load effectively and maintain a constant lift.

### 5.1 Validation

#### 5.1.1 The General Aviation Circulation Control (GACC) aerofoil

The study uses the existing GACC aerofoil developed by Jones et al. (Jones et al. 2002) and shown in Figure 5.1. The GACC aerofoil was modified from the GAW-1 aerofoil, a low-speed 17% thick aerofoil, by transforming its sharp trailing edge to a circular Coanda surface, as shown in Figure 5.1(b). A backward facing step is located on both the upper and lower side of the Coanda surface with a dimension of  $h/c = 0.0011$ , where  $h$  is the step height, and  $c$  is the aerofoil chord. In the present study, only the upper step is used as a jet exit for CC. An internal plenum chamber is located upstream of the jet exit that supplies high pressure air to a convergent nozzle. Except for the modifications to the trailing edge, the remaining aerofoil shape is the same as the GAW-1 aerofoil.

A GACC model was tested in the Basic Aerodynamics Research Tunnel in Langley Research Center by Jones et al. (Jones et al. 2002) to obtain lift increments and surface pressure distributions for different angles of attack and nozzle pressure ratios. In the present study, a 2-D CFD analysis of this aerofoil was conducted with and without blowing to validate the mesh and physics approach by comparing results with those from this experiment.

A common parameter to quantify blowing for CC is the momentum coefficient ( $C_{\mu}$ ) given

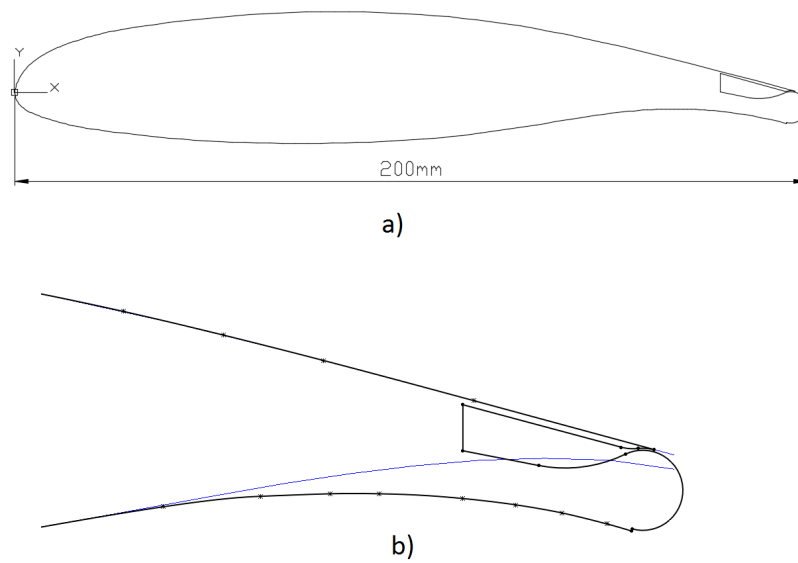


Figure 5.1: (a)The geometry of the GACC aerofoil. (b)Comparison with the original GAW-1 aerofoil (blue curve)

by equation 5.1, where  $h$  and  $w$  are the nozzle height and width respectively,  $C$  is the chord length,  $b$  is the span. The  $\rho$  and  $U$  are the density and velocity, while the subscript  $\infty$  is used to denote the free stream conditions, and  $J$  is the jet conditions at the nozzle exit. However, since the nozzle exit velocity is not uniform (as shown in Figure 5.12 (left)), and the nozzle height is typically very small,  $C_\mu$  is difficult to measure experimentally (ENGLAR et al. 2009). Therefore blowing is more conveniently defined by the nozzle pressure ratio (NPR) given by equation 5.2, where  $P_{tJ}$  is the plenum stagnation pressure and  $P_\infty$  is the freestream pressure.

$$C_\mu = \frac{2hw}{Cb} \frac{\rho_J}{\rho_\infty} \frac{U_J^2}{U_\infty^2} \quad (5.1)$$

$$NPR = P_{tJ}/P_\infty \quad (5.2)$$

In order to relate Equation 5.1 and Equation 5.2, the nozzle exit velocity  $U_J$  can be expressed by NPR through the following derivation, assuming an isentropic expansion of the flow through the convergent nozzle.

The jet Mach number at the nozzle exit is

$$M_J = U_J/a \quad (5.3)$$

where  $a$  is the speed of sound given by (Anderson Jr 2016)

$$a = \sqrt{\gamma RT_\infty} \quad (5.4)$$

where  $\gamma$  is specific heat ratio,  $R$  is gas constant and  $T$  is the static temperature.

The pressure can be linked to the Mach number by (Anderson Jr 2016), page 579

$$\frac{P_{tJ}}{P_{\infty}} = \left(1 + \frac{\gamma - 1}{2} M_J^2\right)^{\frac{\gamma}{\gamma - 1}} \quad (5.5)$$

Combining the above equations, the jet exit velocity is obtained

$$U_J = \sqrt{\frac{2\gamma RT_{\infty}}{\gamma - 1} \left[ \left(\frac{P_{tJ}}{P_{\infty}}\right)^{\frac{\gamma - 1}{\gamma}} - 1 \right]} \quad (5.6)$$

Use the following equation to replace  $T_{\infty}$  by  $T_{tJ}$

$$\frac{P_{tJ}}{P_{\infty}} = \left(\frac{T_{tJ}}{T_{\infty}}\right)^{\frac{\gamma}{\gamma - 1}} \quad (5.7)$$

The jet exit velocity can be written as (ENGLAR et al. 2009).

$$U_J = \sqrt{\frac{2\gamma RT_{tJ}}{\gamma - 1} \left[ 1 - \left(\frac{P_{\infty}}{P_{tJ}}\right)^{\frac{\gamma - 1}{\gamma}} \right]} \quad (5.8)$$

### 5.1.2 Mesh and Boundary Conditions

It was necessary to validate the CFD process, including both mesh and physics models, to establish an accurate representation of the real world from the perspective of the intended uses of the model. For this study, this meant comparing outputs from the steady CFD model with measured wind tunnel results published by Jones et al. (Jones et al. 2002). The strategy for ensuring the CFD model is validated was;

1. Choose a suitable size for the computational domain such that the far field boundaries are not too close so as to influence the flow around the aerofoil, and not too large to become computationally expensive.
2. Ensure that the mesh is sufficiently fine to adequately resolve pressure gradients and off-surface flow features, achieved by a mesh independence study.
3. Ensure the near wall mesh is sufficiently fine to resolve boundary layer development.
4. Once the mesh model is established, a suitable physics model is selected. As discussed in the previous chapter, based on literature, the SIMPLE flow solver was selected to solve the RANS equations.
5. Since turbulence models are based on empirical data, it was necessary to select the best model for the type of flow being considered, which is discussed in the next section.

6. Establish the boundary conditions on all surfaces needed to represent the flow physics.

Figure 5.2 displays the dimensions of the aerofoil, plenum chamber, nozzle exit, Coanda surface and far field. A pressure inlet boundary condition was applied to the plenum chamber, a no-slip condition was used on the aerofoil surface, and the pressure far field was used for the free stream conditions on the domain boundaries. Although a uniform velocity inlet boundary condition could be used to establish the jet flow (Shires & Kourkoulis 2013), most previous research included the plenum chamber to give a more representative jet velocity profile due to the development of boundary-layers within the plenum.

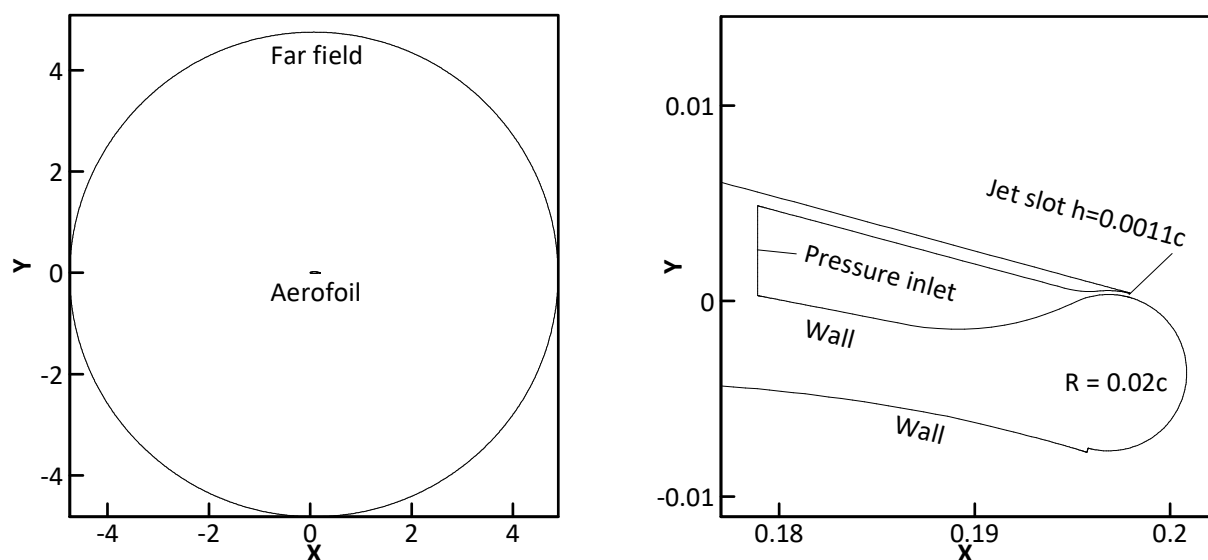


Figure 5.2: Boundary conditions and dimensions of the nozzle ( m ), for GACC aerofoil.

Existing literature suggests that the far field boundary should be 10 to 40 chord lengths away from the aerofoil for CC cases (Jones & Joslin 2005, Swanson & Rumsey 2009, Friedman et al. 2016). A sensitivity study for different far field distances was conducted using 10c, 25c, 100c at  $C_{\mu} = 0.017$ . Results of pressure distribution are shown in Figure 5.3 . It was found that different domain sizes have a minor influence on the pressure distribution. Their differences are only visible in the zoomed view. The 25c curve is relatively closer to the 100c curve so the solution can be considered independent of domain size when it is larger than 25c. The distance of 25c has been used for this study.

Structured meshes were generated using ANSYS 17.2 ICEM. A mesh independence study involved producing an initial baseline mesh and then successively coarsening and refining this baseline mesh, in a consistent manner, by changing the mesh base size by a fixed percentage each time. A mesh independent result is obtained when a monitored variable, such as the aerofoil lift coefficient ( $C_L$ ), no longer changes. This would imply that pressure gradients

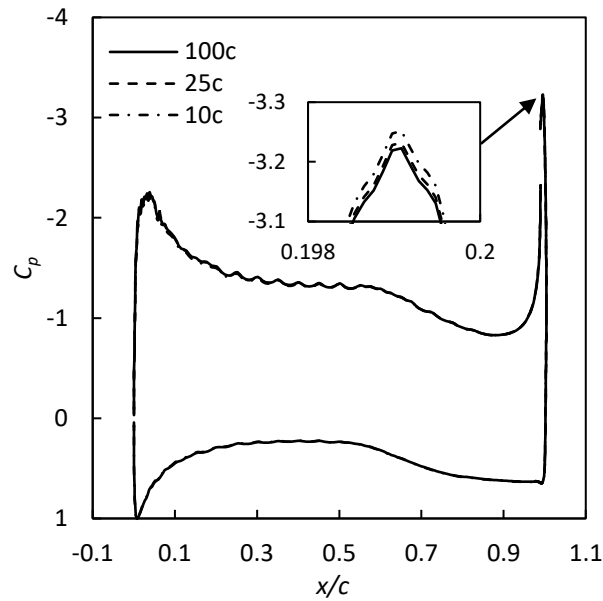


Figure 5.3: Sensitivity study for far field distance of 10, 25, 100 chord length, at  $C_\mu = 0.017$ ,  $M = 0.1$ .

and off-surface features are fully captured at this level of mesh refinement. Four meshes were generated ranging in size from 86,211 to 211,811 cells.

Flow solutions were obtained for each of these meshes using Ansys Fluent 17.2. Simulations were performed at a freestream Mach number of 0.1, assuming sea level ISA conditions and  $0^\circ$  AoA, with a modest momentum coefficient of  $C_\mu = 0.025$ . The chord Reynolds number of  $Re = 4.6 \times 10^5$  matches that of the experiment (Economou et al. 2008). Since the flow is mildly compressible, the pressure-based compressible solver is used, and the SIMPLE (Semi-implicit Method for Pressure Linked Equations) algorithm is selected to solve the pressure-velocity coupling problem. The ideal gas is used with an initial temperature of 288K for simulation. In terms of the discretization approach, the second-order upwind finite volume method is used for spatial discretization, and the second-order implicit method is used for temporal discretization. The S-A turbulence model was initially used for the mesh independence study, and a further study of different turbulence models is reported in the next section.

Figure 5.4, shows the percentage difference in lift determined for each of the 4 mesh sizes, where  $C_{Lref}$  represents the lift coefficient for the finest mesh level. The figure shows that a mesh of 149,001 cells gives a reasonably independent result and an acceptable accuracy of predicted lift coefficient, and was therefore used for all further CFD analyses presented in this chapter.

To ensure the near wall mesh is sufficient to resolve boundary layers, the thickness of the

first layer adjacent to the wall is 0.012mm, giving a Wall  $y^+$  less than 1.

Figure 5.5 illustrates this mesh and the refinement added to capture interactions between the jet and external flow streams. In summary, there were 511 points around the aerofoil surface, 120 points around the circular trailing edge and 30 points across the nozzle exit.

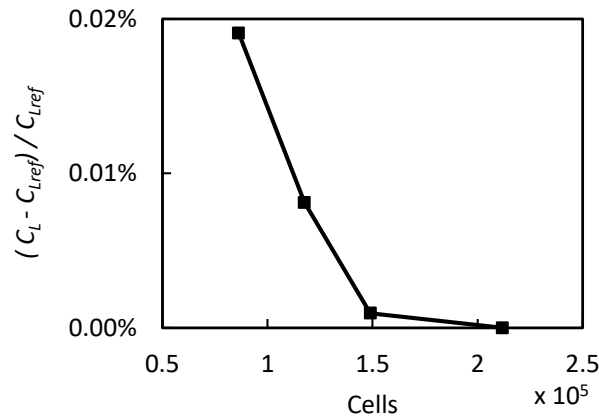


Figure 5.4: The variation of lift coefficient over increasing mesh scale with SIMPLE method and S-A turbulence model, GACC aerofoil,  $M=0.1$ ,  $AoA=0$ ,  $C_\mu = 0.025$ .

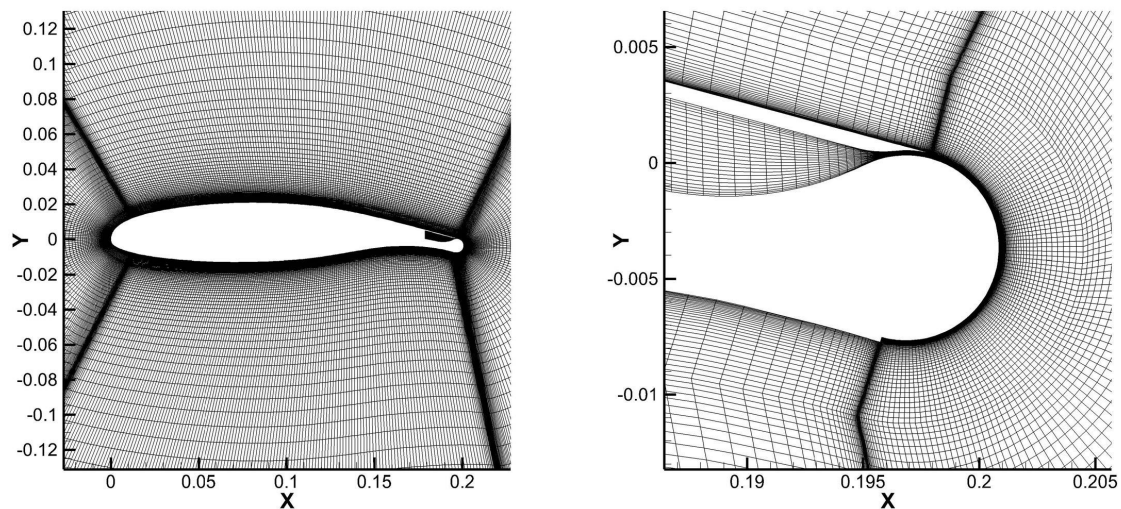


Figure 5.5: The mesh of the GACC geometry with 149,001 cells.

### 5.1.3 Validation Result for steady and unsteady simulations

#### Steady Validation

Firstly the turbulence models are validated. Due to the high relative jet velocity and the complex shear flow that results, as well as the boundary-layer separation/reattachment mechanism around the Coanda surface, the prediction of CC using CFD is a significant challenge

(Economon et al. 2008). A workshop to evaluate appropriate meshing, boundary condition, turbulence model and solver strategies for CC (Economon et al. 2008) recommended three standard turbulence models:  $k - \varepsilon$ ,  $k - \omega$  SST and S-A. Each of these was evaluated for the range of cases given in Table 5.1 and results compared with experiment. The S-A model was found to predict a higher lift coefficient and lower drag coefficient than both  $k - \varepsilon$  and  $k - \omega$  models which gave similar results. In addition the rear stagnation position predicted with the S-A model most closely matched the experimental result. Based on the conclusion from literature, in this study, a further comparison of the  $k - \omega$  and S-A models was made with steady blowing.

Jones et al. have provided wind tunnel results of the GACC aerofoil (Jones et al. 2002), which is used as a baseline for CFD validation. The experiment was conducted in the LaRC Basic Aerodynamics Research Tunnel (BART) which has a test section of  $0.71\text{m} \times 1\text{m} \times 3\text{m}$ . The model is a wing section with a  $0.2\text{m}$  chord and is equipped with pressure tappings, force balance and air supply. However, due to a lack of pressure tappings around the trailing edge, the pressure data is too sparse to be used for integrating  $C_L$ , and so the  $C_L$  results were only obtained from the force balance. This brings a potential issue that the balance data is different to sectional  $C_L$  due to junction flows and wall effect, particularly for large AoA, so only low AoA and low  $C_\mu$  data sets are used for validation. Table 5.1 gives the available  $C_\mu$  range used in the experiment for CFD comparison (Jones et al. 2002).

Table 5.1: The plenum chamber conditions for various blowing momentum coefficients ( Reference pressure:  $101325\text{Pa}$ ,  $T=288\text{K}$ ,  $\gamma=1.4$ ,  $R=287$  ).

$C_\mu$	$U_J(\text{m/s})$	$P_{tJ}(\text{Pa})$	NPR	$\dot{m}$ (kg/s)
0.007	75.9	104343	1.036	0.014
0.017	126.5	110003	1.099	0.024
0.025	150.2	112803	1.143	0.029
0.06	222.03	129364	1.366	0.047

A comparison of the  $k - \omega$  SST and S-A models was made with steady blowing,  $C_\mu = 0.017$  and  $0.025$ , over the range of AoA  $-6^\circ$  to  $6^\circ$  as shown in Figure 5.6. The author also stated that the test rig had a leakage issue, so the wind tunnel results are less confident for higher AoA (Jones et al. 2002). The present study was primarily for low AoA, close to  $0^\circ$ , therefore the validation is sufficient to cover the flow conditions in this study. It can be seen that both models give the correct trend of  $C_L$  for various AoA. The  $k - \omega$  SST model predicts roughly 12% lower lift for all AoA in both  $C_\mu$  settings. Whereas the S-A model gives a lift

coefficient that more closely matches the wind tunnel results. For  $C_\mu = 0.025$ ,  $\text{AoA} = 2^\circ$  to  $6^\circ$ , there is a deviation with wind tunnel results, probably caused by air leakage of the test rig or wall-interference, since the wind tunnel data is obtained from the force balance. The S-A model was then selected for all the following simulations. Note the curvature correction is used according to the study by Swanson et al. (Swanson & Rumsey 2009).

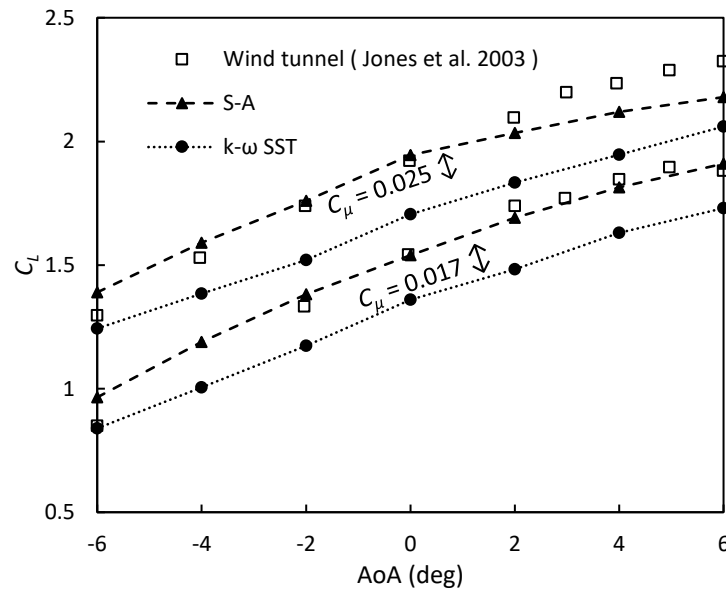


Figure 5.6: Comparison between  $k - \omega$  SST model, S-A model and experimental data. (2D GACC aerofoil in CFD compared with a 2D wing section model in the wind tunnel,  $C_\mu = 0.017$  and  $0.025$ ,  $M=0.1$ ,  $\text{Re}=4.6 \times 10^5$ )

In the existing literature regarding CFD solvers for the study of CC, the SIMPLE (Semi-Implicit Method for Pressure Linked Equations) and PISO (Pressure-Implicit with Splitting of Operators) methods are frequently used (Sellars et al. 2002)(Subhash & Dumas 2013). In this research, three different solvers, SIMPLE, SIMPLEC (Semi-Implicit Method for Pressure Linked Equations-Consistent) and PISO, were compared with a steady blowing at  $C_\mu=0.025$ ,  $\text{AoA}=0^\circ$ . Figure 5.7 shows the residuals of three solvers for the initial 10000 iteration steps. The SIMPLE method is the most robust and has a good convergence, better than the SIMPLEC and PISO, Whilst the PISO method gives the worst convergence results. Figure 5.8 shows the time history of  $C_L$  solved by the three solvers. All three solvers gave identical  $C_L$ , and the results of SIMPLE and SIMPLEC were exactly the same. Whereas the result of PISO was very unstable, which was probably caused by the bad convergence. Compared with the experimental result for the same condition ( $C_L=1.923$ ), the SIMPLE and SIMPLEC gave  $C_L=1.980$  and all three models slightly over-predicted  $C_L$ . To compare the computational cost, three cases with different solvers were solved using a High-Performance Computing Cluster with

8 processors for each case. Table 5.2 compares the time and memory costs. The SIMPLE and SIMPLEC methods were faster than PISO, while PISO used the smallest memory. In the current research, computational time and robustness are the main considerations, as well as accuracy, since the meshes are relatively large due to the complex geometry. Therefore, the SIMPLE method is used in the present research.

Table 5.2: The computational effort of different solvers for 10,000 steps.

Method	Wall clock time	CPU time	Maximum memory
SIMPLE	1h 35min	12h 30min	843 MB
SIMPLEC	1h 36min	12h 39min	785 MB
PISO	1h 55min	15h 7min	774 MB

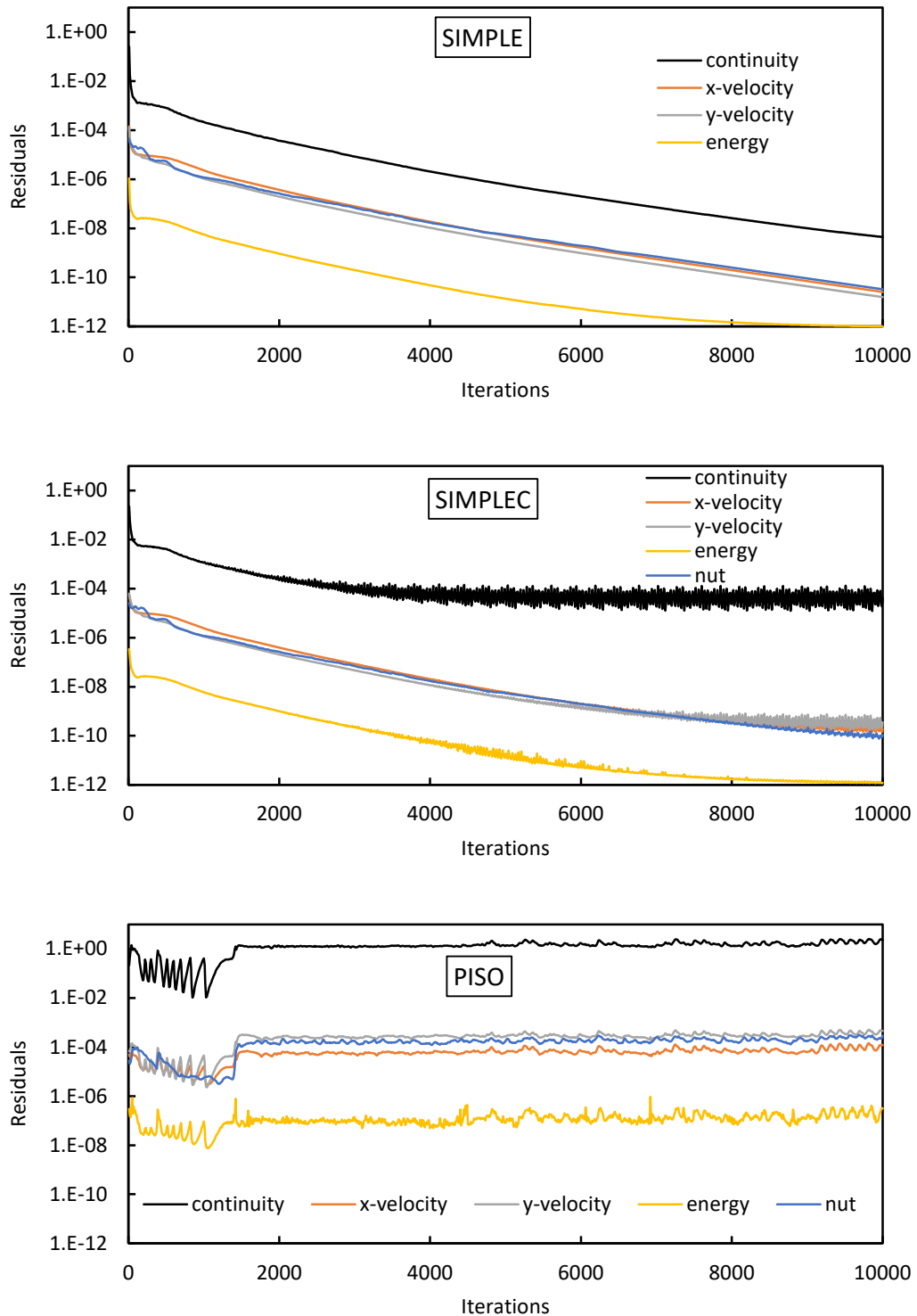


Figure 5.7: Comparison of the residuals between SIMPLE, SIMPLEC and PISO methods. (GACC aerofoil,  $C_\mu = 0.025$ ,  $M=0.1$ ,  $Re=4.6 \times 10^5$ )

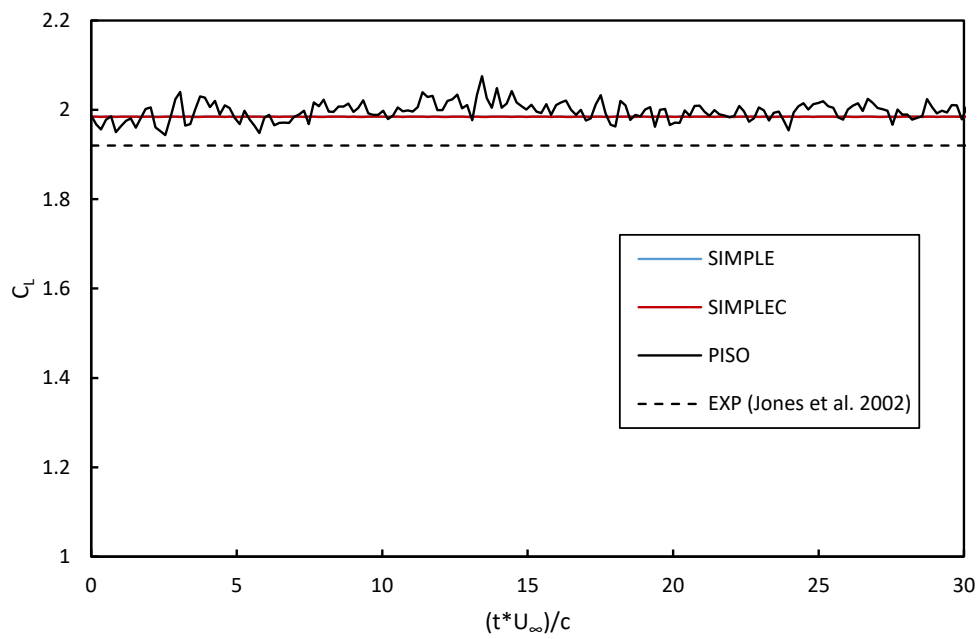


Figure 5.8: Comparison of the time-history  $C_L$  using SIMPLE, SIMPLEC and PISO methods. (GACC aerofoil,  $C_\mu = 0.025$ ,  $M=0.1$ ,  $Re=4.6 \times 10^5$ )

To expand the flow conditions of validation, the aerofoil performance was evaluated over the range of momentum coefficients given in table 5.1 on page 130 for  $\text{AoA} = 0^\circ$  and using the S-A model. Figure 5.9 compares the results of present CFD, reference CFD, and wind tunnel. The figure shows that significant increments in  $C_L$  can be achieved using CC and that CFD is effective at predicting these increments, giving good agreement with the experiment in terms of magnitude and slope ( $\Delta C_L / \Delta C_\mu = 50$ ). The present result is closer to the wind tunnel compared to other CFD results.

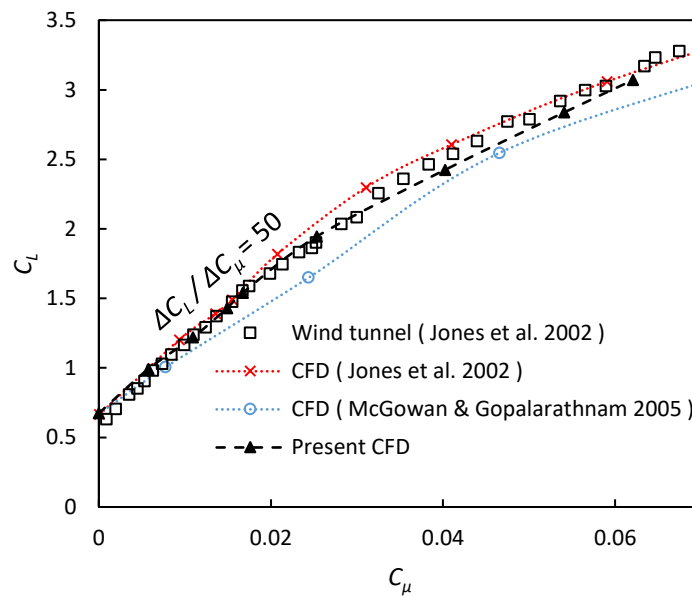


Figure 5.9:  $C_L$  vs.  $C_\mu$  of the GACC aerofoil at  $M = 0.1$ , unsteady S-A model,  $\text{AoA} = 0$ , time step = 0.0001s. Compared with experimental data.

Figure 5.10 presents the pressure coefficient distribution over the aerofoil surface for  $C_\mu = 0.06$ . The CFD data agrees well with the experiment on both the suction and pressure surfaces, including the peak suction value around the Coanda surface. It is identical to the CFD results conducted by Jones et al. who also used the S-A model (Jones et al. 2002).

Figure 5.11 presents the variation of  $C_L$  with  $\text{AoA}$  for four different momentum coefficients. In general, the present CFD is in very good agreement with the experiment, the maximum deviation appears at  $C_\mu = 0.025$ ,  $\text{AoA} = 6^\circ$ , which is 0.14 lower than the wind tunnel  $C_L$  and it is acceptable. All CFD results are identical for  $C_\mu = 0$ , indicating good agreement for the unblown cases. Note both of the reference CFD simulations used the S-A model. However, the CFD conducted by McGowan predicts 15% lower  $C_L$  for  $C_\mu = 0.025$  which is worse than the present CFD.

Figure 5.12 illustrates the velocity vectors at the nozzle exit and at the rear stagnation (separation) point around the Coanda trailing edge. The jet flow remains attached to the

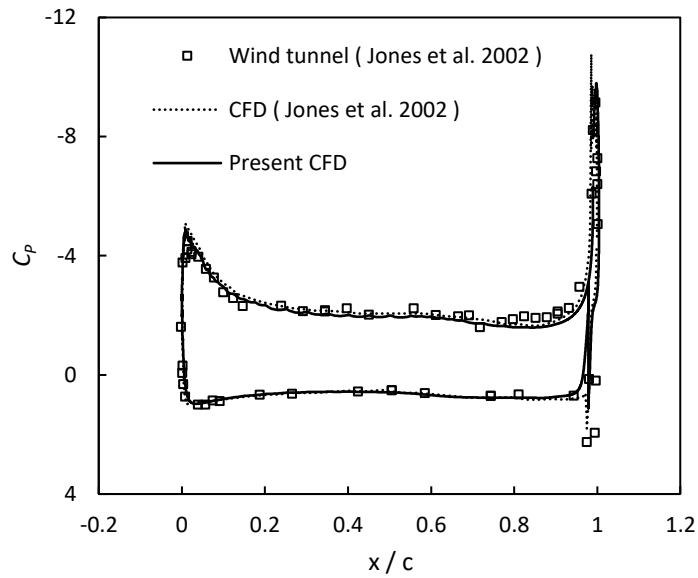


Figure 5.10: The surface distribution of pressure at  $C_{\mu} = 0.06$ ,  $M = 0.1$ , compared with experimental data, for the GACC aerofoil.

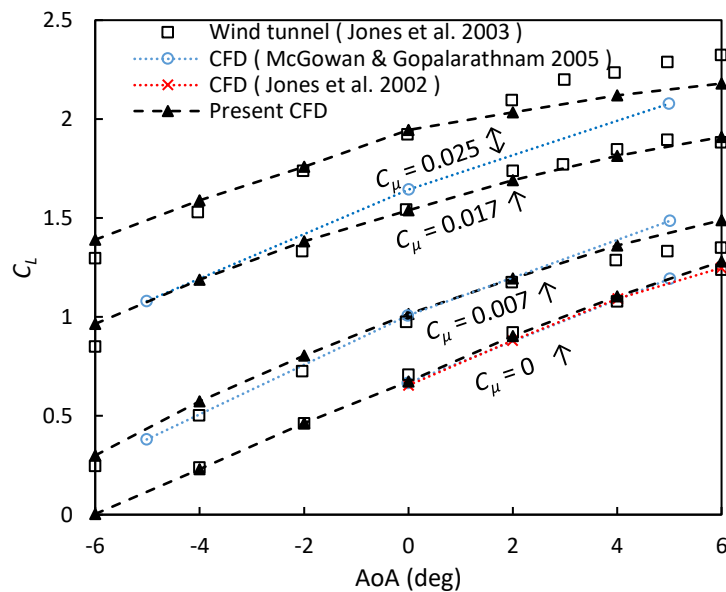


Figure 5.11:  $C_L$  vs. AOA of the GACC aerofoil in different blowing momentum coefficients at  $M = 0.1$ . Compared with experimental data.

Coanda surface for a significant distance causing a rotation of external flow that it entrains. The attached boundary layer becomes thicker as it decelerates around the trailing edge before finally separating from the surface.

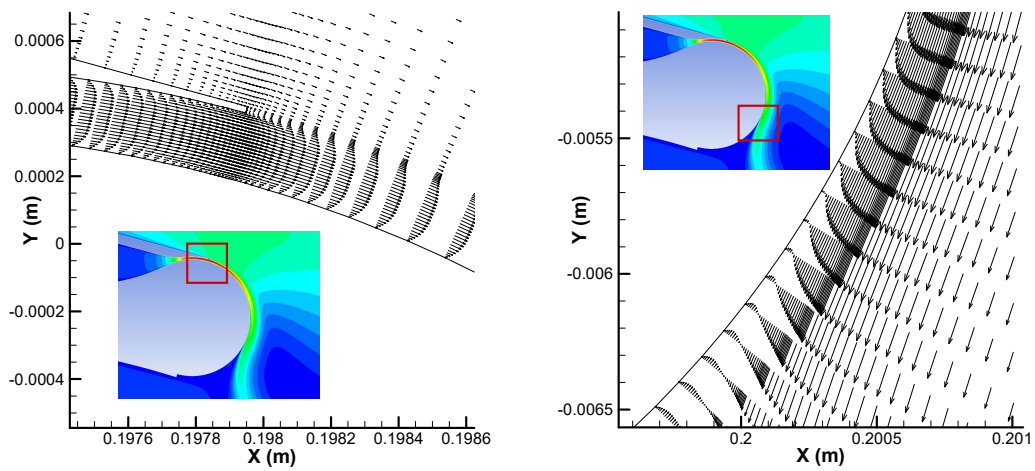


Figure 5.12: The velocity profiles on the trailing edge of the GACC aerofoil at  $C_{\mu} = 0.015$ ,  $M=0.1$ . Left, nozzle exit. Right, separation point on the round trailing edge.

### Unsteady Validation

For the purpose of analysing dynamic performance, one of the gust models that has been widely used is the sharp edge gust (Raveh 2007, Medina et al. 2017, Zaide & Raveh 2006, KARAKAŞ 2020). Assuming an aircraft that is initially flying in a quasi-steady state in calm air, encounters a uniform vertical gust with a velocity of  $w_g$ , the interface between the calm air region and the gust region is a step change in velocity. Although an ideal sharp edge gust is not realizable in actual flight or in a wind tunnel, it can be studied by analytical methods or CFD simulations to understand the time history of incremental lift after it encounters a gust. Analytical solutions for this lift response to a sharp edge gust have been derived by Hans Georg Küssner (Küssner 1936, Jones 1940), and are used here to validate the unsteady CFD simulations. Küssner developed an exponential equation 5.9 for a flat plate experiencing a unit step gust in an incompressible flow. The function was extended from a theory of non-uniform motion of a thin aerofoil in potential flow initially given by Wagner (Jones 1940).

$$\Psi(s) = 1 - 0.5e^{-0.13s} - 0.5e^{-s} \quad (5.9)$$

In this equation,  $\Psi(s)$  is the lift variation with non-dimensional distance travelled,  $s = 2U * t/c$ , over the time period  $t$ . Note the coefficients may have been modified slightly by other references (Leishman 1994, Wright & Cooper 2008, von Karman & Sears 1938), but this study has adopted the coefficients approximated by William Sears et al. (Sears 1941).

Although the Küssner function is derived for a thin flat plate, a thin symmetrical aerofoil should also give similar results (Ghoreyshi et al. 2018). A NACA0012 aerofoil was selected for the unsteady validation with a unit chord. Figure 5.13 shows the structured mesh generated using the Pointwise software, which has 807,000 cells with a circular-shaped domain dimensioned so that the far field boundary is approximately  $10c$  from the aerofoil. There are 808 points around the aerofoil and 1001 points in the wall normal direction. The thickness of each mesh layer is gradually increased from  $1 \times 10^{-5}m$  at the aerofoil surface, to  $0.01m$  in the free stream region. Beyond this, the edge length is kept uniform to ensure a relatively fine mesh in the freestream flow to reduce the numerical dissipation of the gust front. The final mesh has a wall  $y^+$  value less than 0.7.

Although the previous GACC aerofoil was meshed using ICEM software, the mesh for the NACA0012 aerofoil was generated by Hyperbolic Extrusion using Pointwise software. In this approach, a marching front could be extruded from the wing surface to the far field. Despite the non-uniform distribution of points on the aerofoil surface, the Hyperbolic Extrusion method produces a high quality orthogonal mesh, and a smooth transition from a high to low

density region to capture the propagating front, and avoids high aspect ratio cells near the far field, relative to the previous mesh strategy using ICEM (since the block topology used in ICEM is more suited for complex geometries). For both cases, similar parameters (including first layer thickness, growth rates and algorithm, and point distribution over the aerofoil surface) were used for the near wall region in order to achieve consistency between the two mesh approaches.

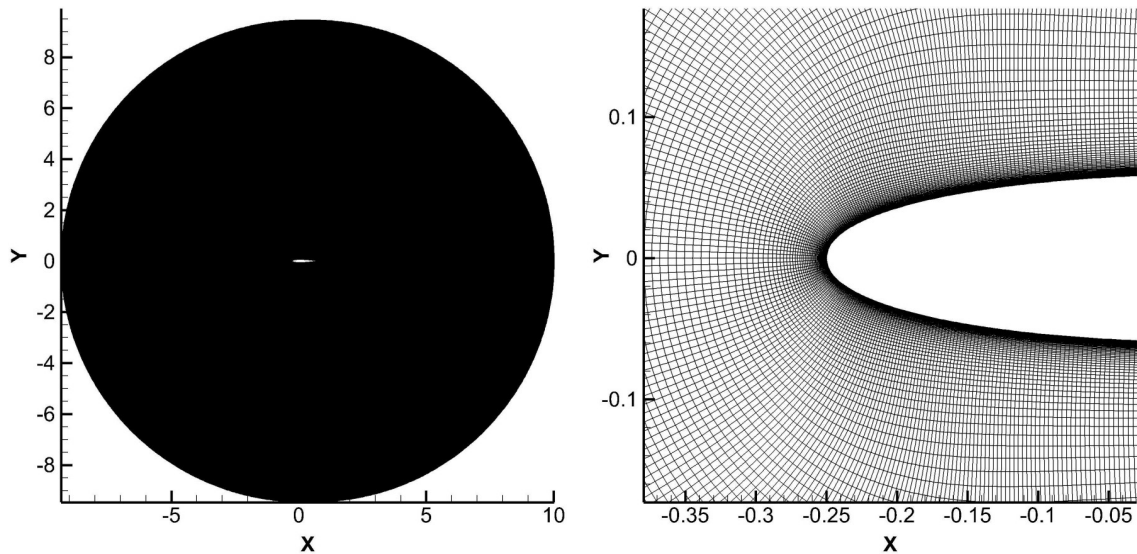


Figure 5.13: The computational mesh for unsteady validation of NACA0012 aerofoil, left: the computational domain with a uniform density from the aerofoil to the far field, right: the mesh distribution near the wall.

A sharp edge gust is realized by applying an initial vertical velocity component to every cell in a specific field ahead of the aerofoil (Förster & Breitsamter 2015, Bartels 2012, Li & Qin 2020), or by imposing an unsteady gust profile on the inflow boundary (Ghoreyshi et al. 2018). The first method may cause convergence issues due to the discontinuity at the interface and is not available in most solvers. The second method is easily realizable but the gust front may be smeared due to numerical dissipation as the gust front travels from the inflow boundary to the leading edge of the aerofoil. In this study, the latter approach was used, with a high mesh density upstream of the aerofoil to reduce numerical dissipation and a user-defined function (UDF) that specifies a vertical gust front at the inflow boundary. Since this boundary has a circular shape, the gust front passes each element on the boundary at a different time, determined by the UDF. Thus, assuming  $x$  is the cell centre on the  $X$  axis, the vertical velocity component of each face on the boundary is controlled using the function;

$$w_g(t) = \begin{cases} 0, & (t - t_0) < (x - x_0)/u \\ w_0, & (t - t_0) \geq (x - x_0)/u \end{cases} \quad (5.10)$$

where  $x_0$  is the initial position of the gust front which is on the far left end of the computational domain,  $t_0$  is the time when the gust starts moving,  $w_0$  is the vertical component of the gust velocity,  $u$  is the free stream velocity. This function describes when the gust front passes each face on the far field. Figure 5.14 displays an instantaneous vertical velocity distribution that clearly shows the gust front located at  $x=-5.5\text{m}$ , as it travels from left to right. On the left side, a uniform vertical gust velocity  $w_g = 1\text{m/s}$  is applied, whilst on the right side, the vertical velocity is zero. Simulations were performed for 2 streamwise velocities,  $U_\infty = 34\text{m/s}$  ( $M_\infty = 0.1$ ) and  $U_\infty = 68\text{m/s}$  ( $M_\infty = 0.2$ ), giving a chord Reynolds number,  $\text{Re} = 2.31 \times 10^6$  and  $4.62 \times 10^6$  respectively. At  $t=0$ , the initial position of the gust front is  $x=-10\text{m}$ . The penetration speed of the gust is the same as the free stream velocity,  $U_\infty$ .

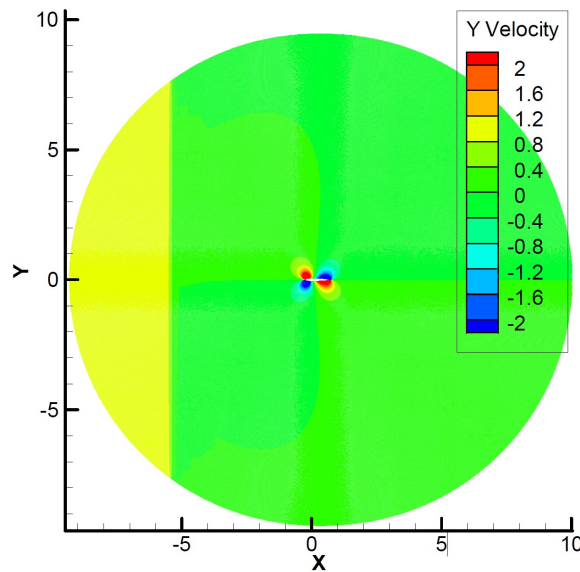


Figure 5.14: The vertical velocity field ( m/s ) showing the gust front marching from the left side of the domain, NACA0012 aerofoil.

Unsteady simulations were initialised from a fully converged simulation with steady boundary conditions ( $U_\infty = 34\text{m/s}$  or  $U_\infty = 68\text{m/s}$ ,  $\text{AoA}=0^\circ$ ,  $T = 288\text{K}$ ), prior to the UDF being used to create the gust front. As the gust front passes the aerofoil, a time history of  $C_L$  is recorded and compared with analytical results. Figure 5.15 gives the unsteady validation results for both  $M_\infty = 0.1$  and  $M_\infty = 0.2$  cases. Simulated results are in very good agreement with analytical solutions as well as simulated results from other researchers. Note there is a small lag compared with the analytical curve due to numerical dissipation. Considering two

adjacent cells in the flow domain, since the velocity components are defined at the centroid, the discretization scheme will create a gradient over the distance between the two centroids, so a perfectly sharp edge is not achievable except for some custom codes (Li & Qin 2020). Consequently, it is difficult to determine the exact time when the gust front arrives at the leading edge, and it is assumed to correspond to the time when  $C_L$  increases to 5% above the steady state value, leading to a small inaccuracy in the interaction time and the lag that was observed compared with analytical results.

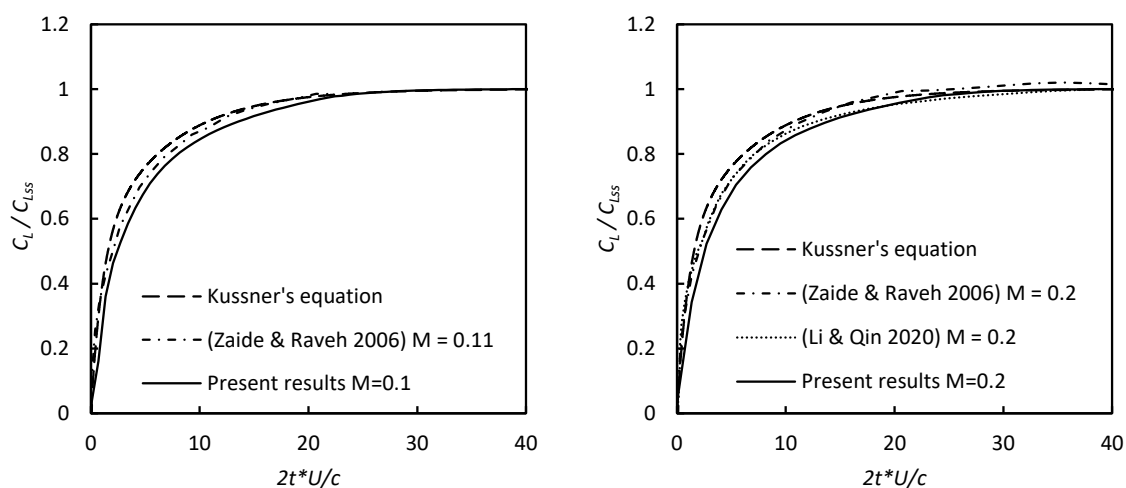


Figure 5.15: Unsteady validation results of the NACA0012 aerofoil encountered a sharp edge gust, left:  $M_\infty = 0.1$ , right:  $M_\infty = 0.2$ .

## 5.2 Study of the CC dynamic response

### 5.2.1 Time step sensitivity study

An understanding of the dynamic characteristics of CC is essential to develop a suitable control system. Typically the dynamic characteristics of conventional (mechanical) control surfaces can be obtained in sub-scale wind tunnel tests to measure hinge moments in order to size actuators. The actuation with respect to CC is by means of varying the NPR ( $P_{tJ}$ ). In this section, the dynamic response is evaluated for steady and unsteady load cases to derive a numerical model that can be used in the control algorithm design. The dynamic lift response to NPR changes can be evaluated using CFD with a step or sinusoidal pressure in the plenum chamber.

Since the controller design requires accurate response data, the time-step settings in the transient solver were examined to ensure that the temporal variations of lift are physical i.e.

the time step must be small enough to ensure a stable time-accurate solution. A time-step independence study was performed specifying a sinusoidal plenum chamber stagnation pressure with a 10 Hz frequency and an amplitude range of 0 - 20kPa (gauge pressure), with 10 inner iterations per time step.

As mentioned in the previous chapter, the implicit scheme has no requirement for the CFL condition. The selection of the time step is based on the dynamic results. As long as the time step is smaller enough to capture the shape of the lift variation, and the sampling frequency is twice faster than the maximum frequency of the input signal, the flow can be considered independent of time step settings.

Figure 5.16 shows the  $C_L$  response with time for time-steps in the range 0.01ms to 5ms, with the sinusoidal NPR starting after 0.5s. Clearly with a time step greater than 0.5ms it is not possible to capture the physical response, whereas for a time step less than 0.1ms the response is adequately captured. Consequently, a time step of 0.1ms was selected for all further calculations, which gives a reasonable computational expense (i.e. 12s simulation time requires 176 CPU hours).

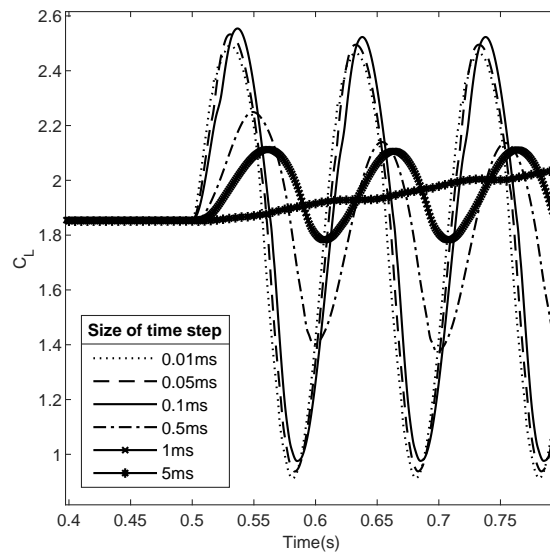


Figure 5.16: Simulated lift coefficient response with different time steps, GACC aerofoil,  $M = 0.1$ ,  $C_{\mu} = 0.025$ .

### 5.2.2 Comparison of the response of CC and mechanical ailerons

The dynamic response of mechanical control surfaces depends on the actuation speed of servo motors. A typical servo motor has a time constant of the order of 0.1s (Nelson et al. 1998). This is sufficient to damp the short-period mode but not able to alleviate gust loading that has

a higher frequency. A fast-actuation effector developed by Elisa and Israel (Phillips & Wygnanski 2013) has a maximum deflection rate of approximately  $300^\circ/s$ , this control surface can potentially be used to compensate high frequency gusts. Figure 5.17 shows their experimental rig of a NACA 0021 aerofoil with a flap driven by a pneumatic cylinder giving a maximum deflection angle of  $30^\circ$ . This experimental result is compared with the GACC aerofoil in terms of lift response to a rapid actuation.

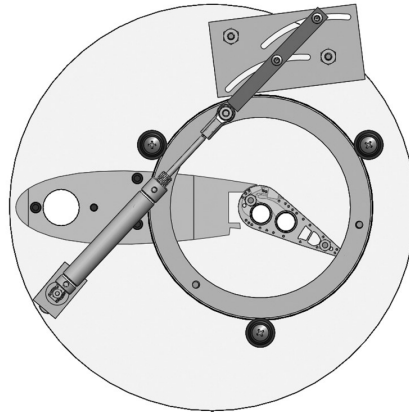


Figure 5.17: The experimental rig for a fast-actuation flap, with NACA0021 aerofoil (Phillips & Wygnanski 2013).

Figure 5.18 compares the lift response to a step input for GACC aerofoil (the same curve in Figure 5.15) and mechanical flap. Due to the inertia of a mechanical flap, it is impossible to rotate instantaneously. In the experiments reported by Elisa and Israel (Phillips & Wygnanski 2013), three actuation speeds were presented, with a fast actuation taking  $t * U/c \approx 2.67$  to complete a  $30^\circ$  rotation, a medium actuation taking  $t * U/c \approx 3.67$  and a slow actuation taking  $t * U/c \approx 5.33$ . The three vertical dashed lines in Figure 5.18 denote these times for the mechanical flap to fully rotate to 30 degrees, and then be suddenly halted by a stopper (Phillips & Wygnanski 2013). Simulated results in the present study for CC are included in Figure 5.18 for comparison with the measured results for a mechanical flap reported in (Phillips & Wygnanski 2013). These simulations assume an instantaneous change to NPR since by contrast, the opening of a valve to control the plenum pressure can be less than 0.5ms (SMC n.d.).

The initial rate of increase in  $C_L$  is higher for the CC than the mechanical flap, but both systems achieve 95% of the steady state  $C_L$  in  $t * U/c \approx 7$ . However, Elisa and Israel only provide unsteady results at  $Re = 200,000$ ,  $U_\infty = 10$  m/s due to performance restrictions of their experimental setup. In order to compare the response at a higher Re number ( $Re = 460,000$ ,  $U_\infty = 34$  m/s), assuming that the mechanical flap rotates at the same speed as  $U_\infty = 10$  m/s

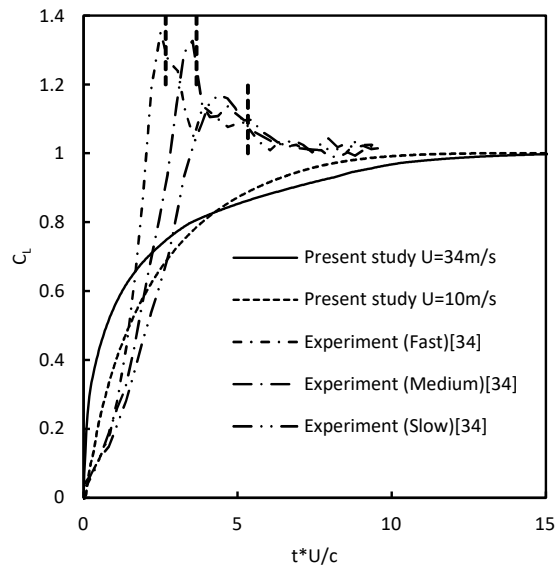


Figure 5.18: Lift response to a step input for GACC aerofoil and mechanical flap.

( although the rotation speed is probably slower due to higher aerodynamic load ), which is approximate  $300^\circ/s$ , shown as the dotted line in Figure 5.19. At  $U_\infty = 34\text{m/s}$ , the difference between GACC and mechanical flap becomes apparent if we change the horizontal axis to physical time as displayed in Figure 5.19. The step response of typical actuators on aircraft in operation is also plotted as a grey area which will be explained later. For the GACC aerofoil, the step response is faster with a higher velocity. This is affected by the non-dimensionalised  $t * U/c$ . The  $C_L$  in terms of  $t * U/c$  for GACC is not sensitive to free stream velocity  $U$  (as well as  $Re$ ), as the ‘fluidic effector’ of GACC aerofoil changes lift by moving the rear stagnation point, the movement of rear stagnation point happens instantly at  $t=0$ . The response curve for GACC actually represents the response of the fluid around the aerofoil. For different free stream velocities, the response time of the fluid around an aerofoil is nearly constant in terms of  $t*U/c$ , but positively correlated with  $U$  in terms of physical time  $t$ . While for the mechanical flap, the angular rate in terms of physical time is constant in various velocities (or becomes slower at a higher velocity due to increased hinge load).

According to Theodorsen’s research (Theodorsen & Mutchler 1935), the unsteady lift response to an arbitrary motion of the flap is the summation of circulatory lift and non-circulatory lift. The former is the lift due to the change of circulation of the aerofoil, including the dynamic stall vortex ( DSV ). The latter is caused by the displacement of the surrounding fluid due to flap deflection, the fluid around the flap is accelerated, which requires additional force from the flap, this force does not change net circulation but temporarily increases lift, named as non-circulatory lift (Taha & Rezaei 2019). Circulatory lift is a function of non-

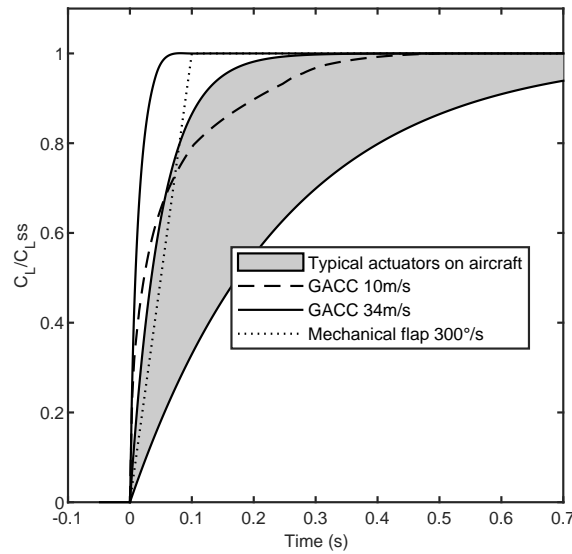


Figure 5.19: Comparison of the GACC actuation and typical plain flaps of the lift response to a step input over physical time.

dimensional time ( $t * U/c$ ), if the circulation of aerofoil changes abruptly, the time history curve of lift can be approximated as a Wagner function (Theodorsen & Mutchler 1935). This function is independent of aerofoil geometry and Reynolds number, assuming it is potential flow and incompressible. In comparison, the dynamic response of non-circulatory lift depends on the size of aerodynamic surfaces, rotation rate and acceleration. A mechanical flap that is turning downward generates an additional positive lift. It may also create a DSV which passes over the upper surface of the flap, therefore, creating a peak in the time history of  $C_L$ , as shown in Figure 5.18. In order to evaluate the dynamic performance of GACC and mechanical flap, the time when  $C_L$  reaches a steady state can be evaluated. This ‘settling’ time (when the lift reaches 95% of the steady state value) depends on the slowest component of circulatory or non-circulatory lift. For a mechanical flap, the settling time is always longer than the time of flap rotation, when the flap reaches the desired position and stops, the fluid needs additional time to settle down. This is clearly shown in Figure 5.18. Unlike the mechanical flap, the GACC aerofoil is equivalent to an infinitely small flap located at the trailing edge of the aerofoil. It can change the rear stagnation point abruptly without adding a non-circulatory lift or DSV as there is no moving part on the aerofoil, the lift response is just a function of convective time  $t * U/c$ . As a result, the settling time of GACC is shorter than a mechanical flap at  $U_\infty = 34$  m/s or at a higher velocity.

Note the deviation rate of  $300^\circ/\text{s}$  is a relatively fast actuation rate found in the reference (Phillips & Wynanski 2013). However, in practice, the angular rate of aerodynamic surfaces

on aircraft is usually slower. Most of the mechanical aerodynamic surfaces are linked to servo motors which can be modelled by first-order systems, assuming the transfer function is  $G(s) = 1/(\tau s + 1)$ , their time constant  $\tau$  is in the range of 0.05 - 0.25 (Nelson et al. 1998). The step response of a typical first-order system reaches 95% of its steady state value at  $t = 3\tau$ . Corresponding to the angular rate  $40^\circ/s - 200^\circ/s$ , assuming the maximum deviation angle is  $30^\circ$ , the step response within this range is plotted in Figure 5.19 as a grey area which falls behind GACC aerofoil. The settling time of the mechanical flap is equivalent to non-dimensional time  $t * U/c = 17$  to  $85$ . Compared to the GACC aerofoil which has a settling time around  $t * U/c = 7 - 9$ , it is even faster at higher velocity.

Another interesting finding is that the lift response of GACC due to step change in nozzle pressure is surprisingly close to the Küssner function, shown in Figure 5.20. However, the Küssner function describes a sharp edge gust passing over a thin flat plate, which is a different scenario to the GACC aerofoil. This is probably because the sudden actuation of a blowing jet on a GACC aerofoil changes the boundary condition of the aerofoil, while the gust passing over a flat plate is equivalent to a sudden change in the boundary condition of the surrounding fluid. In both scenarios, the settling time is fundamentally how fast the flow converged to a steady state. Discarding the difference in boundary conditions, the steady state of both scenarios is similar as their Mach number, Reynolds number and steady state  $C_L$  are the same. Therefore it is possible to use the Küssner function to describe a dynamic process for CC. This also indicates that the lift response of GACC to unsteady nozzle inputs is not a simple first-order system, but it is likely to be a higher order system like the Küssner function. In addition, the Wagner function (Equation 5.11) is also plotted in Figure 5.20. Wagner function describes lift response to a step change in AoA for a flat plate (Leishman 1994). This function also has a similar shape compared to GACC results except for the non-zero initial conditions ( $\phi(s = 0) = 0.5$ ). The initial condition is non-circulatory dominated due to displacement of surrounding air caused by indicial motion (Leishman 1994). However there are no moving parts in a GACC aerofoil, and the lift is mainly caused by circulation, which means the initial condition of GACC is different from the Wagner function. Friedman and Arieli have reported a similar comparison between the lift response of CC and Wagner function (Friedman et al. 2016), results showed a good correlation, but not as close as the Küssner function. This will be compared with more results in Chapter 7.

$$\phi(s) = 1 - 0.2048e^{-0.0557s} - 0.2952e^{-0.333s} \quad (5.11)$$

A further analysis was performed considering different input frequencies and amplitudes

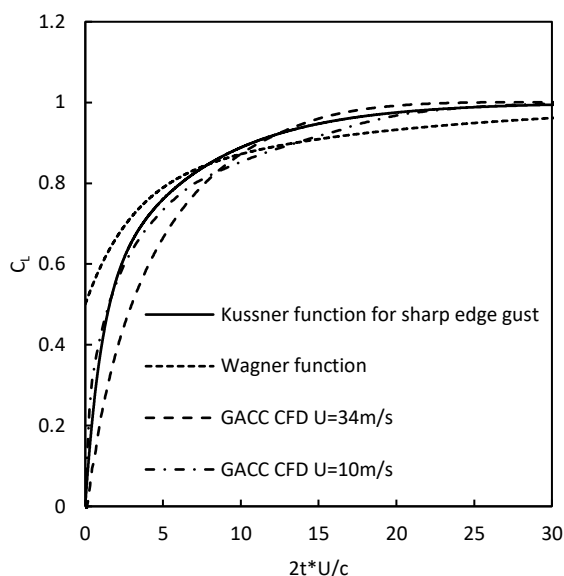


Figure 5.20: Comparison of the lift response of GACC aerofoil to a step input and the Küssner and Wagner function.

for the plenum stagnation pressure to determine the frequency response. In the CFD simulation of this aerofoil, the input variable is the nozzle pressure and the output is lift. However, when analysing the bandwidth of CC, it is more convenient to compare the magnitude ratio between the dynamic  $C_L$  (with sinusoidal blowing) and the quasi steady  $C_{L_{ss}}$ . Which gives an intuitive comparison of how the magnitude of  $C_L$  reduces with higher frequency. The relationship of nozzle pressure and  $C_{L_{ss}}$  at steady state is given by:

$$C_{L_{ss}} = f(C_\mu) \quad (5.12)$$

The  $f(C_\mu)$  is the steady-state lift response to different nozzle pressures and can be obtained from Figure 5.9 on page 135, according to the steady state CFD simulations.

However, when  $C_\mu$  is dynamically varying at high frequency (e.g. 10Hz to 100Hz), the lift no longer follows the input signal, and the amplitude of the output  $C_L$  decays. There is also a time lag between the input signal and the output signal. Figure 5.21 is a schematic of the desired  $C_L$  and the actual  $C_L$ . If the lift responds immediately to any frequency of  $C_\mu$ , the lift should equal to the corresponding steady state value  $C_{L_{ss}}$  at any time, as shown by the 'Target  $C_{L_{ss}}$ ' curve. The degradation of output can be quantified by the magnitude decay and the phase lag. The former is the ratio between the magnitude of  $C_{L_{ss}}$  and the actual (measured)  $C_L$ , expressed in logarithmic scale by the convention in signal processing. This determines how much gust loading can be alleviated at this frequency. The latter is the time lag between the two signals, expressed by the phase of the sinusoidal signal, assuming the frequency is  $\omega$ .

A large time lag deteriorates the controller's performance.

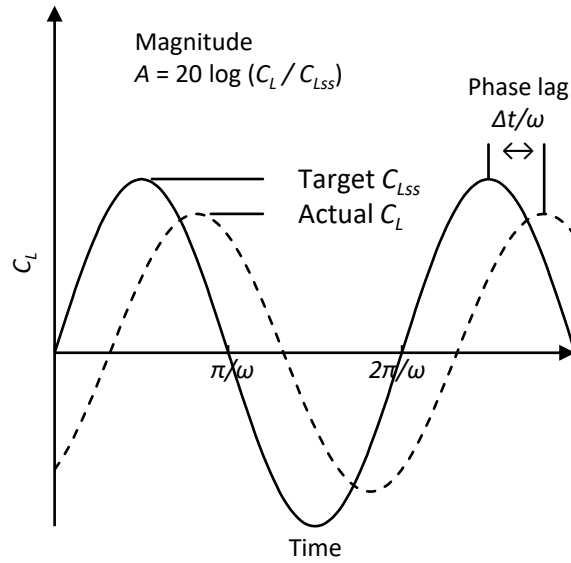


Figure 5.21: Response of lift to a sinusoidal input.

Figure 5.22 shows a Bode diagram of the frequency response. A frequency range from 3.14 to 314 rad/s and input amplitudes of  $\pm 1\text{kPa}$  and  $\pm 10\text{kPa}$  were considered. In addition, a freestream Mach number  $M_\infty = 0.2$  was also considered with an amplitude of  $\pm 1\text{kPa}$ . The response of a mechanical flap governed by a first-order transfer function is also plotted for comparison, using the same assumptions as in Figure 5.19 on page 145.

From Figure 5.22, the dynamic performance of GACC aerofoil is significantly better than mechanical flaps. When the magnitude of lift response is reduced to -3dB (0.707 of the quasi-steady value), the mechanical flap is in the range of 4-20 rad/s compared with GACC at 60-101 rad/s. In terms of the phase lag, the mechanical flap reaches  $-45^\circ$  in the range of 53-77 rad/s, compared with GACC at 90-97 rad/s. The higher bandwidth of CC means that it can be used in some scenarios that require fast actuation, for example, gust alleviation. While in practice, the bandwidth of CC may be limited by the actuation speed of pneumatic valve (Buonanno & Cook 2006, Buonanno 2009). However, it is much easier to increase the bandwidth of a valve than an aerodynamic surface which has a much stronger aerodynamic load. Additionally, it is found that the amplitude response of a stronger fluctuation ( $\pm 10\text{kPa}$ ) is faster than a smaller fluctuation ( $\pm 1\text{kPa}$ ). The cause of this response is still unknown and further study is needed. Also, a higher free stream Mach number ( $M_\infty = 0.2$ ) gives a faster response than the lower Mach number ( $M_\infty = 0.1$ ), this can be explained by the previous context about the step response in the time domain, that the response of GACC is actually the response of surrounding fluid. If the horizontal scale is in physical time, the response is faster as the free

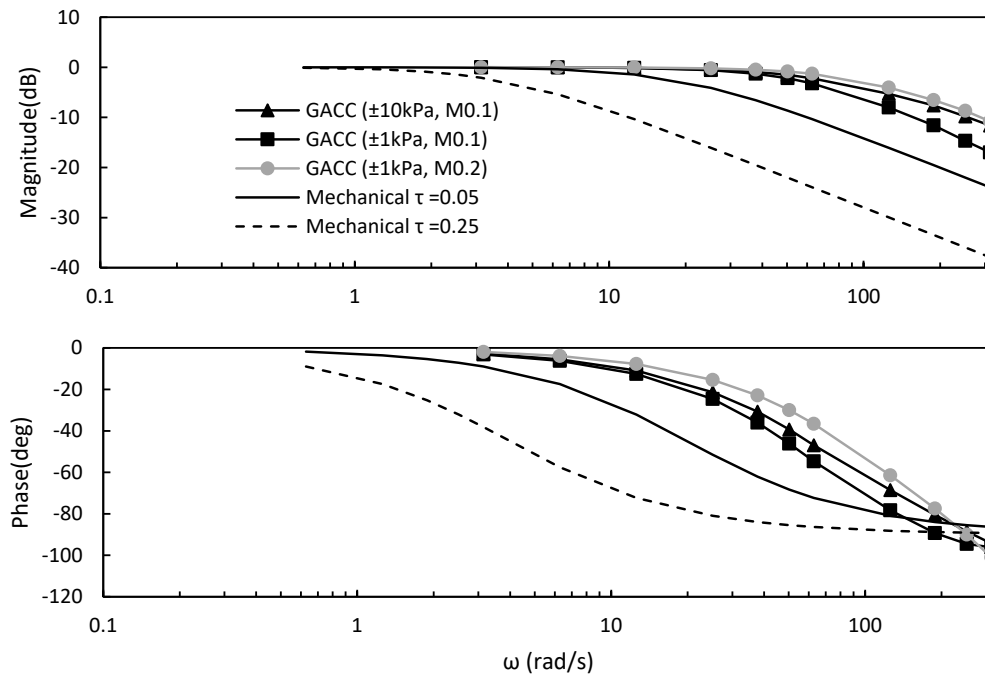


Figure 5.22: Comparison of amplitude and phase response with different nozzle pressure range and velocity.

stream velocity is higher, which is the case for Figure 5.22. However, if the horizontal scale is in non-dimensional time, the response is almost consistent for different Mach numbers. The relation between lift response and Mach number is further compared in Figure 7.11 on page 217, which includes higher Mach numbers up to  $M = 0.3$ .

In the feedback control algorithm design, it is crucial to identify the lift response to wind gusts. The CFD performs unsteady simulations with  $P_{t,J}$  constantly equal to 10 kPa. Time-varying axial directional wind gusts are implemented in the CFD simulations via the dynamic freestream conditions at the inlet by specifying sinusoidal Mach number changes with time between 0.09 and 0.11 with a frequency range of 0.5 to 10 Hz. Time-varying vertical gusts are also implemented from the far field with a wind gust velocity range of 0 to 6.8 m/s and a frequency range of 0.5 to 10 Hz. The steady longitudinal velocity component is equal to 34 m/s,  $M = 0.1$ . Figure 5.23 shows the Bode diagram for axial and vertical wind gusts.

Figure 5.23 shows that the magnitude for axial gust does not change significantly with higher frequencies compared to vertical gust, which is the case in a similar experimental study by Kerstens (Kerstens et al. 2011). The lift responses have the natural frequency to the axial and the vertical wind gusts around 4 Hz and 6 Hz, respectively.

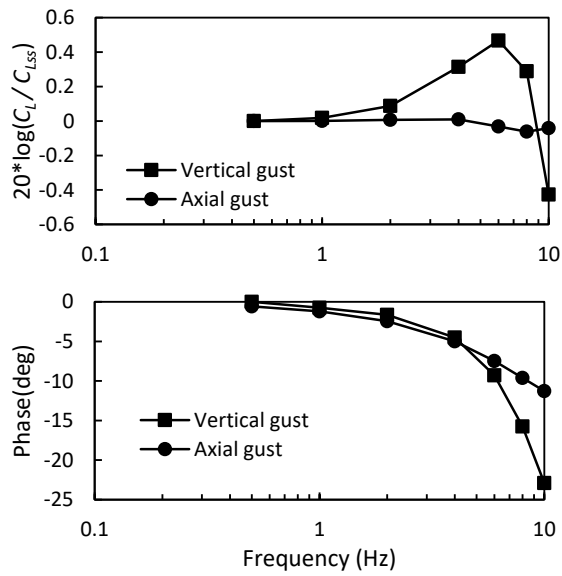
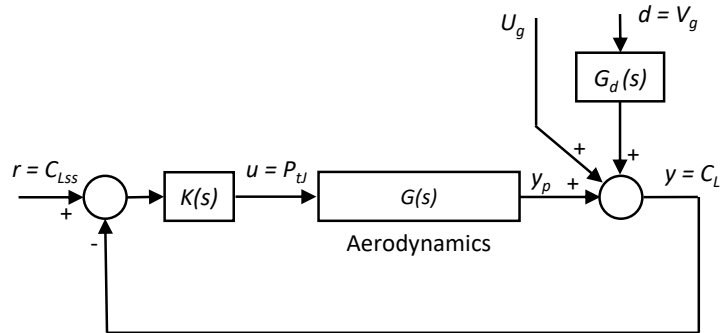
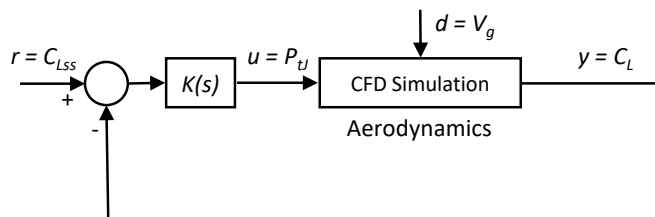


Figure 5.23: Lift response to axial gust, GACC aerofoil,  $P_{t,J}=10\text{kPa}$ ,  $M = 0.1$ ,  $\Delta U_g = \pm 3.4\text{m/s}$ ,  $\Delta V_g = 6.8\text{m/s}$ .



(a) The architecture for controller tuning



(b) The architecture for testing

Figure 5.24: The schematic of the system: (a) for controller tuning, (b) for CFD in the loop testing.

### 5.3 Circulation control algorithm design & CFD verification

According to the information on frequency response in terms of various nozzle pressure inputs and external gusts, a feedback control algorithm can be designed.

Figure 5.24 shows the block diagram of the feedback CC system. The architecture in Figure 5.24 (a) is used for tuning the controller, where the transfer function of the aerodynamics plant model,  $G(s)$ , and the wind gust model,  $G_d(s)$ , are to be identified,  $C_{L_{ss}}$  is the reference command, and  $K(s)$  is the CC algorithm to be designed.

The vertical wind gust has a dominant effect on lift perturbations than the axial wind gust as confirmed in Figure 5.23. In this section, only the vertical wind gust is considered in the control design. The maximum loading due to vertical wind gusts is also one of the primary considerations for wing structure design. Once the controller,  $K(s)$ , is designed, the controller performance can be verified in the CFD simulations. Figure 5.24 (b) shows the CFD solver in the control loop for the verification process, where the gust input,  $d = V_g$ , becomes a variable for the far field boundary of the CFD simulations.

To design the CC algorithm, one of the standard system identification methods uses the frequency responses shown in Figure 5.22. Consider the case of  $M = 0.1$  and  $P_{tJ} = 10$  kPa in Figure 5.22 to design the circulation feedback controller. The system identification toolbox in Matlab is used, where the identification method chooses the best algorithm among several optimization algorithms (Ljung 2022). The order of the system is through trial and error, it is found that the minimum order to fit all the measured results is 2. The system identification finds a second-order transfer function as follows:

$$G(s) = \frac{-5.174 \times 10^5 s + 3.907 \times 10^8}{s^2 + 5.26 \times 10^6 s + 3.947 \times 10^8} \quad (5.13)$$

As shown in Figure 5.25, it fits the frequency response almost perfectly.

Among many feedback control algorithms, the PID control is the most widely used algorithm proven by its simplicity and effectiveness (Åström & Hägglund 2001). Based on the system identified, Equation 5.13, which is a stable second-order system, the PID is also an appropriate choice. The PID controller structure is given by

$$u(t) = k_p e(t) + k_i \int_0^t e(\tau) d\tau + k_d \frac{de}{dt} \quad (5.14)$$

where  $k_p$ ,  $k_i$  and  $k_d$  are the gains to be determined, and  $e(t)$  is the error equal to  $r - y = C_{L_{ss}} - C_L$ . The gains were tuned to achieve a settling time of approximately 0.04 seconds for a step input of  $r = C_{L_{ss}}$ , giving  $k_p = 1.78$ ,  $k_i = 0.0032$ ,  $k_d = 0.0061$ .

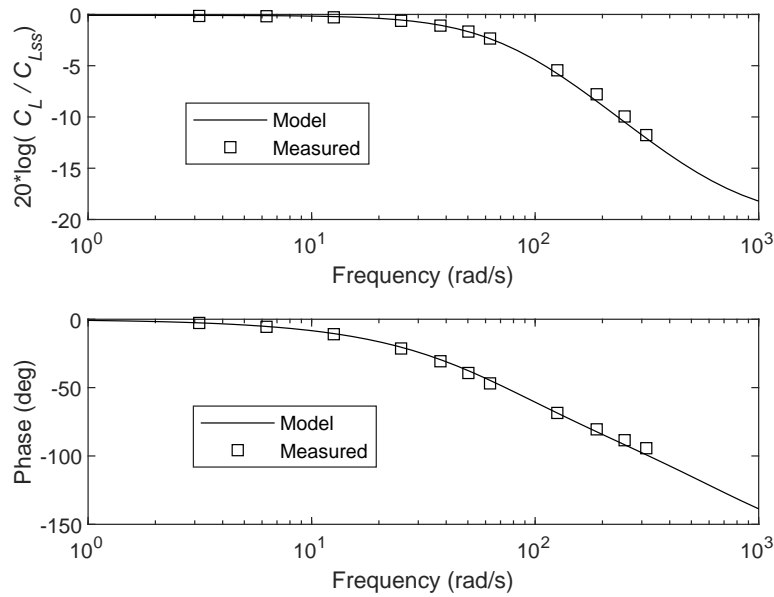


Figure 5.25: System identification for the lift response at  $M=0.1$ ,  $P_{t,J} = 10$  kPa, GACC aerofoil.

To test the gust suppression performance of the PID controller, the same sinusoidal vertical gust profile that has been implemented for Figure 5.23 is used as the output disturbances. The maximum variation of  $C_L$  with and without a controller is compared, providing  $C_{L_{controlled}} / C_{L_{uncontrolled}}$  in different frequencies. Figure 5.26 shows that the unsteady lift is dramatically reduced by 81.3% for low frequency gusts at 0.5 Hz. For other frequencies, the controller also effectively suppresses the gusts.

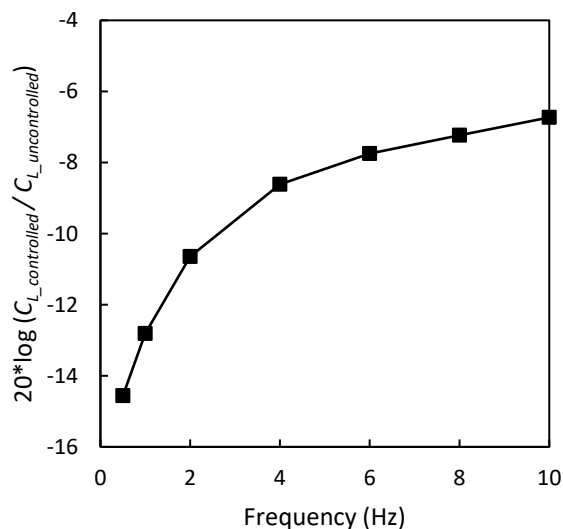


Figure 5.26: Gust suppression performance of the tuned PID controller with identified plant model, simulated without CFD.

To verify the performance of the PID controller, it is coupled to the Fluent URANS solver.

The solver provides real-time gust alleviation control for the GACC aerofoil. The User Defined Function (UDF) is used to program Equation 5.14. The UDF script in the unsteady CFD simulation allows the PID controls the lift by adjusting the nozzle pressure in response to wind gust loading.

A 1-cosine vertical gust profile used in the far field boundary is given by (Cook 2012)

$$V_g = \frac{V_{gm}}{2} \times \begin{cases} 1 - \cos(2t), & \text{for } t_0 \leq t < \pi/2 \\ 1 + \cos(2t), & \text{for } \pi/2 \leq t \leq \pi \\ 0, & \text{otherwise} \end{cases} \quad (5.15)$$

where the maximum vertical gust velocity,  $V_{gm}$ , is equal to 7% of the freestream velocity,  $t_0$  is the gust initiated time equal to 3s, and  $t$  is the time in seconds. The profile is shown in the top figure in Figure 5.27.

The CFD simulation coupled with the control algorithm is equivalent to a wind tunnel experiment conducted in the reference(Kerstens et al. 2011). The wind gust information is measured from the CFD simulation variables at each time step. The measured values are fed to the PID controller through the UDF, which calculates the nozzle pressure value. The nozzle pressure value controls the circulation in the CFD simulation for the next time step calculations. This framework to evaluate the CC performance is cost-effective and flexible compared to a wind tunnel experiment.

Figure 5.27 shows the CFD simulation results of the CC system in the time domain. For the uncontrolled case with a constant plenum chamber pressure equal to 11.1 kPa, the  $C_L$  increases caused by the vertical gust after  $t=3s$ . On the other hand, when the circulation controller is active, the chamber pressure reacts and successfully maintains a constant lift in response to a gust of wind. The chamber pressure decreases rapidly, and  $C_L$  remains the same value as before the wind gust, while the  $C_L$  for the uncontrolled case increases by 0.227 from the initial value. For the controlled case, the  $C_L$  deviation is only 0.008. The maximum deviation of  $C_L$  is dramatically reduced by 96.5%. Also, there is no significant overshoot or oscillation, which is desired for the flight controller since it is well-damped and does not cause additional unsteadiness to the control loop. For a small UAV, a disturbance that is equivalent to  $\Delta C_L = 0.227$  can cause a bad trajectory following and increase structure load. This result indicates that CC has enough control authority and bandwidth to suppress a moderate discrete gust.

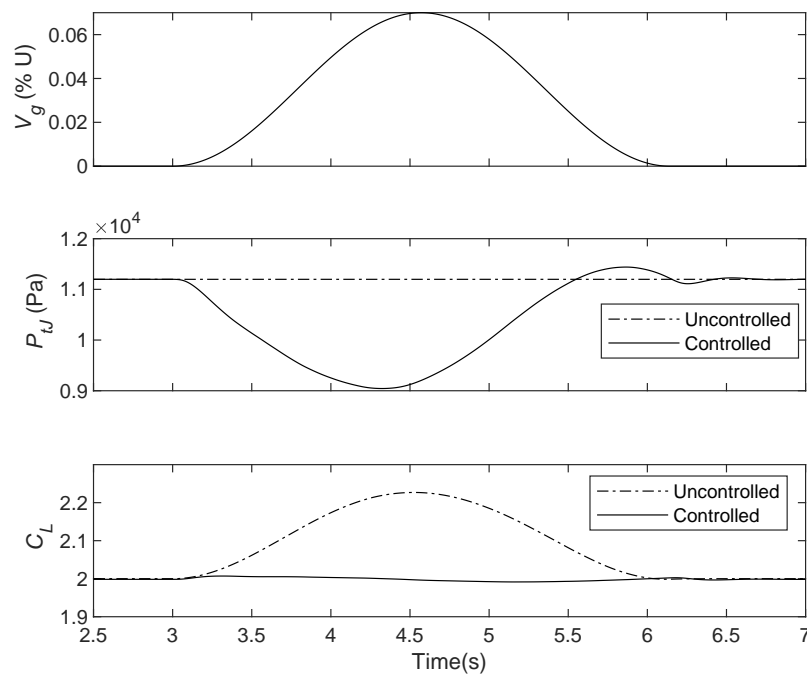


Figure 5.27: The time-history variation of the variables under 1-cosine vertical gust at M0.1, simulated with CFD, GACC aerofoil with blowing.

## 5.4 Summary

A CFD validation of the general aviation CC aerofoil showed that lift and pressure coefficient data predicted by steady CFD was consistent with the experiment. Further unsteady validation presented a good agreement with analytical results and other references for a sharp edge. A time step gust independent study was also performed, and results show that the time history of lift becomes consistent when the time step is smaller than  $10^{-4}$ s. The dynamic characteristics were then investigated for a sinusoidal plenum chamber pressure using transient CFD (URANS) simulations and the validated mesh and physics model settings. By varying the frequency and magnitude of the sinusoidal chamber pressure, the frequency response was obtained. The dynamic characteristics of CC were compared with published performance data for a conventional mechanical flap, and the actuation speed of CC was found to be approximately twice as fast as a typical mechanical actuator when  $U_\infty = 34$ m/s. Regarding frequency response, the max bandwidth of CC at the magnitude of -3dB is 101 rad/s, which is 5 times faster than a typical mechanical actuator. The  $-45^\circ$  phase lag of CC is 97 rad/s, which is approximately twice as fast. Comparing CC and mechanical flaps indicates therefore that CC can be used as a high bandwidth, low lag actuator for gust alleviation applications.

The dynamic response information was then used to design a feedback controller for gust

alleviation. The system identification algorithm provides the transfer functions, and the PID controller uses the transfer function to tune the control gains. The effectiveness of the PID controller in compensating the vertical wind gusts was evaluated using the CFD simulation coupled with the controller. The proposed CFD simulation method successfully demonstrated the effectiveness of closed-loop CC in unsteady flows.

To the best of the author's knowledge, it is the first time that the dynamic response of CC has been conducted, and has been compared with that of a mechanical flap, for gust alleviation or indeed other applications. Moreover, the CFD simulation coupled with a feedback controller provided a novel approach to simulating the closed-loop system in a high-fidelity flow domain. It is ideal for various non-linear control applications involving unsteady fluids, where low-order transfer function models are difficult to achieve due to the complex nature of unsteady flows.

This chapter is a preliminary study with a simple gust profile, and good dynamic performance is demonstrated. The following chapters focus on applying this technique to a 3D aircraft wing considering the motion in continuous gusts. The dynamic performance of a CC aerofoil is subsequently expanded to consider different shapes in various flow conditions to study the mechanism of the unsteady process.

# Chapter 6:

## Steady State Study of the Datum Aircraft

In the previous chapter, a 2D aerofoil was investigated, and a closed-loop controller was designed for a single discrete cosine shape gust. The aerofoil was stationary when encountering the gust for the simplicity of implementation and flow simulation. Results showed the effectiveness and high bandwidth of the CC aerofoil for gust alleviation. However, new questions are raised: How does it influence the aircraft dynamics, if pitching and plunging motions are considered? How does CC perform when the aircraft is in motion, the wing is 3D, and the gust is continuous?

This chapter conducted steady state 3D flow simulations to obtain static aerodynamic derivatives. These derivatives, in addition to the dynamic model from Chapter 7, are used for the 3D simulation of flight in unsteady gusts presented in Chapter 8. The above-mentioned questions are also addressed in Chapter 8.

To better understand the effectiveness of CC on a 3-D wing and how it affects flight dynamics, a datum aircraft was computationally explored. The datum aircraft was used for aerodynamic study, flight dynamics and controller design. In order to choose an aircraft that can fulfil all the requirements for the purpose of this study, the following issues should be considered.

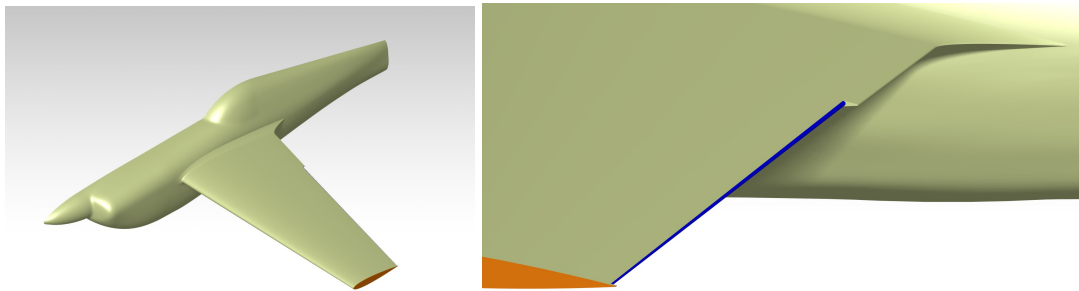
1. The aim of this research is to improve the gust resistance of small civilian UAVs. The size of the aircraft geometry for this research should be reasonably small and designed for low speed flight. Although there is an existing research model adopted with CCW, the Fundamental Aerodynamics Subsonic / Transonic-Modular Active Control model (Milholen et al. 2010), it is for large transport aircraft, which is not suitable for this research.
2. The wing should have a simple layout which is easy to modify. To compare the effectiveness of the conventional flap and CC device, the original flap of the datum aircraft is modified to a CC slot. It is expected that the geometry of the wing and control surfaces are relatively simple to reduce the workload for meshing.
3. It is expected that the datum aircraft have an existing documented aerodynamic database

---

(lift and drag coefficients, pitch moments, etc.) to validate the CFD codes.

4. It is expected that the datum aircraft have aerodynamic derivatives for simulating flight dynamics (e.g., longitudinal stability, gust response). This research includes a simulation of the flight dynamics with the actuation of CC. If using CFD to acquire all the aerodynamic derivatives, the computational effort is massive. Therefore, a documented aircraft model with aerodynamic derivatives is required.
5. It is expected that there is an existing CAD (Computer-Aided Design) geometry for the aircraft, otherwise it is very time-consuming to build a new CAD model.

This aircraft is a 33% scaled Zivko aerobatic aircraft with half wing and fuselage ( Figure 6.1 ), it was based on the parameters from the book written by Brian Stevens et al. (Stevens et al. 2015). The stability and control derivatives of the aircraft are given in the reference. This aircraft is not the original Zivko aerobatic aircraft, but a scaled model which has been used as a remote-controlled model aircraft. It has a span of 2.65m and has a simple tapered wing with a pair of flaperon, which is ideal for this research. The stability derivatives were sufficiently documented in the literature. As the CFD simulations haven't included a tailplane, the stability derivatives are not achievable from CFD. The flight dynamics of this aircraft are analysed in Chapter 8 on page 235 using existing derivatives in the reference.



(a) The left wing and fuselage.

(b) The modified trailing edge.

Figure 6.1: The geometry of the 33% scale Zivko Edge 540T aircraft with a NACA0013 aerofoil and a modified CC trailing edge.

Since the wing trailing edge is modified to a blunt edge, the static aerodynamic derivatives related to the wing and flap are different to the reference (Stevens et al. 2015).

$C_L$ ,  $C_D$ , and  $C_M$  are obtained from CFD instead of using the original database, given by the following equations. Their results are provided in Section 6.7.1 on page 194

Dynamic pressure:

$$q_\infty = \frac{1}{2} \rho_\infty V_\infty^2 \quad (6.1)$$

Lift coefficient:

$$C_L = \frac{L}{q_\infty S} \quad (6.2)$$

Drag coefficient:

$$C_D = \frac{D}{q_\infty S} \quad (6.3)$$

Moment coefficient:

$$C_M = \frac{M}{q_\infty S l} \quad (6.4)$$

where  $S$  is the reference area,  $l$  is the reference length.  $C_M$  is calculated about the centre of gravity. The centre of gravity is designed at  $0.25 \bar{c}$  for a stable configuration.

The following derivatives can be calculated from the force and moment results and used for the small-perturbation equations in Section 2.5 on page 31.

Clean wing:  $\frac{\partial C_D}{\partial V}$ ,  $\frac{\partial C_L}{\partial V}$ ,  $\frac{\partial C_M}{\partial V}$ ,  $\frac{\partial C_D}{\partial \alpha}$ ,  $\frac{\partial C_L}{\partial \alpha}$ ,  $\frac{\partial C_M}{\partial \alpha}$

Circulation control actuator:  $\frac{\partial C_{D_{dlc}}}{\partial \eta_{dlc}}$ ,  $\frac{\partial C_{L_{dlc}}}{\partial \eta_{dlc}}$ ,  $\frac{\partial C_{M_{dlc}}}{\partial \eta_{dlc}}$ , where  $dlc$  refers to the CC actuator,  $\eta_{dlc} \propto C_\mu$ .

Because the tailplane is excluded in the CFD simulation, the derivatives related to the tailplane, such as  $\frac{\partial C_{DT}}{\partial \alpha_T}$ ,  $\frac{\partial C_{LT}}{\partial \alpha_T}$  are obtained from the reference (Stevens et al. 2015).

The following table shows the basic parameters of the model.

Table 6.1: Aircraft parameters

Item	Parameter
Span	2653mm
Tip chord length	288mm
Root chord length	595mm
MAC	460mm
Wing area (Left wing)	0.5167 m <sup>2</sup>
Aerofoil	NACA0013
Centre of gravity ( $x_{cg}$ )	0.25 $\bar{c}$

This chapter is organised in the following way: The first section presents a validation of the CFD analysis of the aircraft. Firstly, a 3D half-wing-body model was used and simulated for various AoA and flap deflection angles. The dimensions of the aircraft are shown in Figure 6.2 . Except for the modifications on the trailing edge, the model with conventional flap and CC have precisely the same shape. The results were compared with the data from the literature to validate the CFD methodology, including mesh resolution and solver settings. Secondly, a CC flap was designed through a parametric study to find a suitable radius and understand the steady state performance, simulated initially in 2D. Subsequently, the modified wing-body

model was simulated by 3D CFD. A hybrid mesh was used to generate an appropriate mesh domain for the model with a complex nozzle geometry. During the simulation, a strong vortex sheet was found when simulated with the thinner trailing edge. To further investigate the cause of the unstable vortex, various flight conditions were examined. Additionally, the span-wise extent of the CC was studied to compare the full-span and half-span nozzle performance. Finally, the  $C_L$ ,  $C_D$ , and  $C_M$  data of the wing-body model were obtained and compared with the 2D case and mechanical flap.

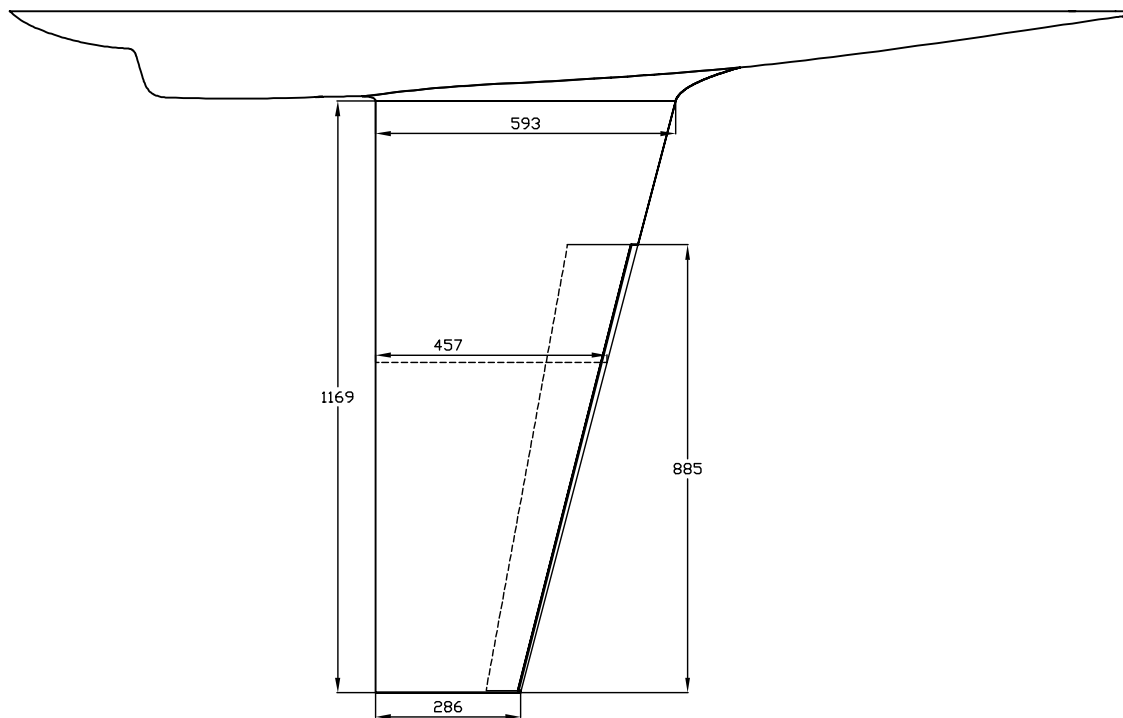


Figure 6.2: The dimensions of the 33% scale Zivko Edge 540T aircraft (mm).

## 6.1 CFD Validation of the Datum Aircraft with Mechanical Flap

According to the reference aircraft, a geometry was established. The purpose of this section is to obtain the aerodynamic parameters of the aircraft through CFD and compare them with the wind tunnel data from the reference (Ol et al. 2013). The primary concern is the  $C_L$  and  $C_D$  with and without the flap, so only the wing and half fuselage were modelled. Figure 6.3 shows the unstructured mesh of tetrahedral elements that have been used in the study. The inflation layer of triangular prism cells was used to capture the boundary layer. Increased density regions have been added to the leading edge, trailing edge and the edge of the flap. Also, an increased density region is added at the wake zone, as shown by the slice of Figure 6.3.

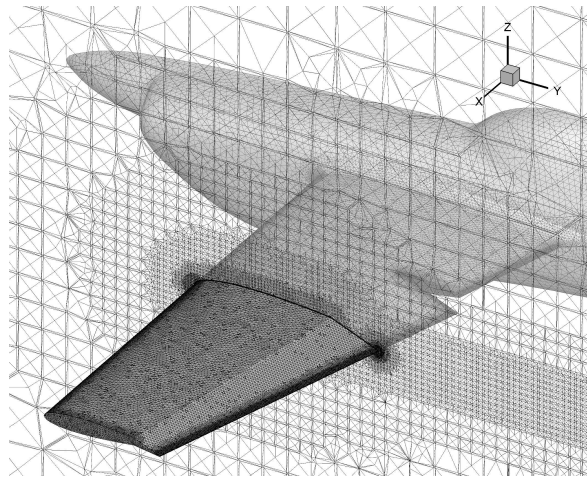


Figure 6.3: Unstructured tetra mesh for the half-wing-body, 33% scale Zivko Edge 540T with flap.

The far field boundary is a semi-circular shape with a radius of  $100c$  ( $c =$  mean aerodynamic chord), shown in Figure 6.4 (e). For the coarse mesh, the maximum edge length on the wing is  $4\%c$  and reduced to  $0.07\%$  on the flap corner, trailing edge and around the nearly-tangent feature lines in the aft of the wing-body junction. There are 800 points in the spanwise direction on the leading and trailing edge, 200 points around the aerofoil and 5 points across the trailing edge.

On the upper and lower wing surface, the anisotropic triangles are used to reduce the area ratio (Figure 6.4 (a)). These cells transition smoothly from the isotropic triangles on the wing surface to the high aspect ratio cells on the thin trailing edge.

The thickness of the first prism layer is  $0.011\text{mm}$ , with a growth ratio of 1.2 and 20 layers in total. Over the wing surface, the prism layers grow until the thickness of the last layer is

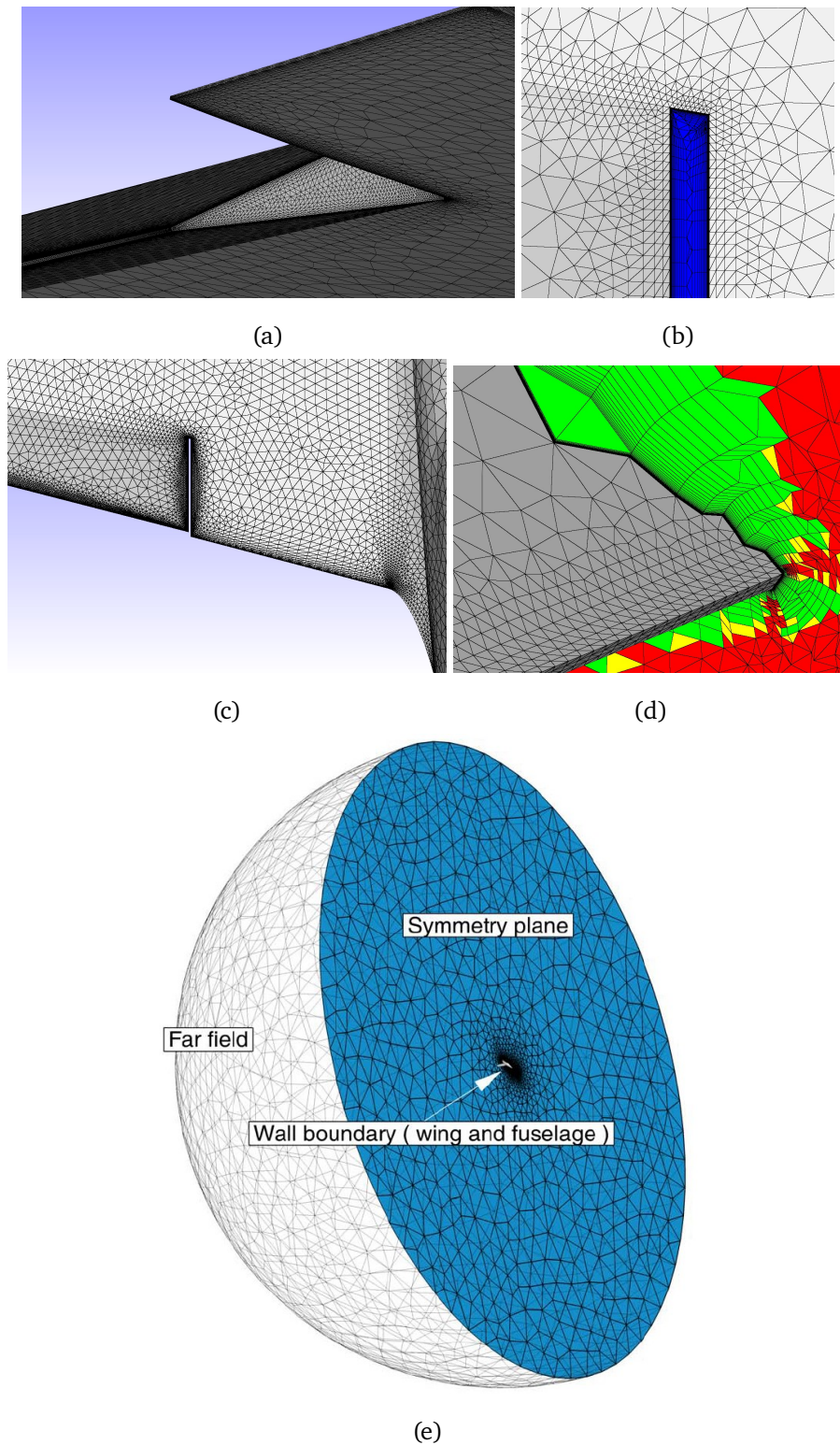


Figure 6.4: The mesh details near the trailing edge and far field for the half-wing-body, 33% scale Zivko Edge 540T with flap. (a) the surface meshes on the flap, (b) the volume mesh in the gap region, (c) the top view of the wing-body junction region, (d) the volume mesh near trailing edge, (e) the far field and symmetry plane.

comparable to the edge length of the volume cells, in which case the volume ratio (the ratio between the largest volume and smallest volume in adjacent cells) criteria can be satisfied. Otherwise, the prism layer stops growing locally if the skew criteria fail. On the other hand, in the gap region where there is not enough room for the growth of the prism layer, it collapsed and replaced with tetrahedral volume meshes, as displayed in the blue region in Figure 6.4 (b). These spacing settings are gradually reduced for denser meshes listed in Table 6.2 except for the prism layers, which remain constant for different mesh resolutions.

Table 6.2: Mesh independent study of the 33% scale Zivko Edge 540T aircraft with mechanical flap at  $M = 0.1$ .

mesh	number of cells	$C_L$	Deviation
1	3063406	0.686	3.6%
2	4307360	0.697	2.0%
3	7301873	0.710	0.2%
4	10015291	0.712	-

Then the mesh independence study was performed using four meshes shown in Table 6.2. The solver is configured using the SIMPLE method and second-order upwind scheme with an S-A turbulence model. The four meshes are all running at  $M=0.1$  until converged. The results are shown in Figure 6.5 , and since the mesh with 7.3 million cells was reasonably independent, it was used in the following studies. In this research, no wall functions were used. The first prism layer next to the wall is placed in the viscous sub-layer ( $y^+ < 5$ ) to capture the near-wall region correctly (Fluent 2011a). The  $y^+$  value is displayed in Figure 6.6 . The value on most of the area is around 1, which means the prism layer (inflation layers near the wall) is fine enough.

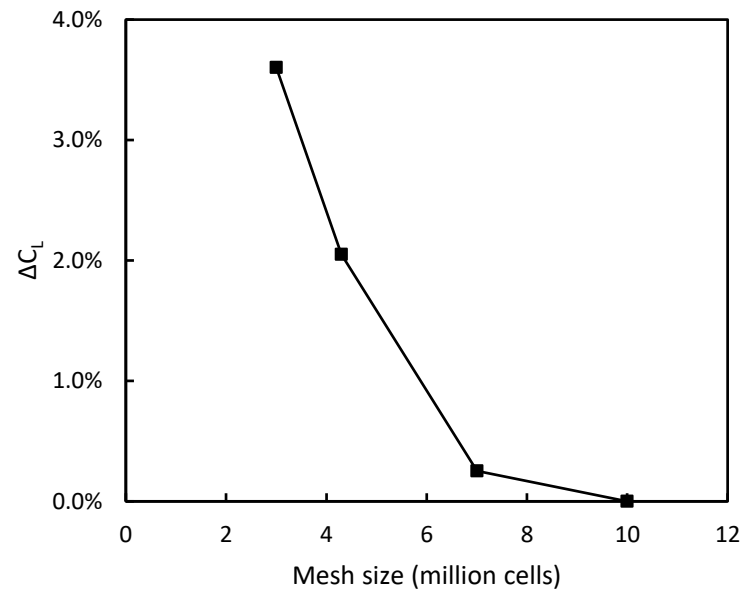


Figure 6.5: Lift coefficient of different mesh densities, for the 33% scale Zivko Edge 540T aircraft with mechanical flap at  $M = 0.1$ .

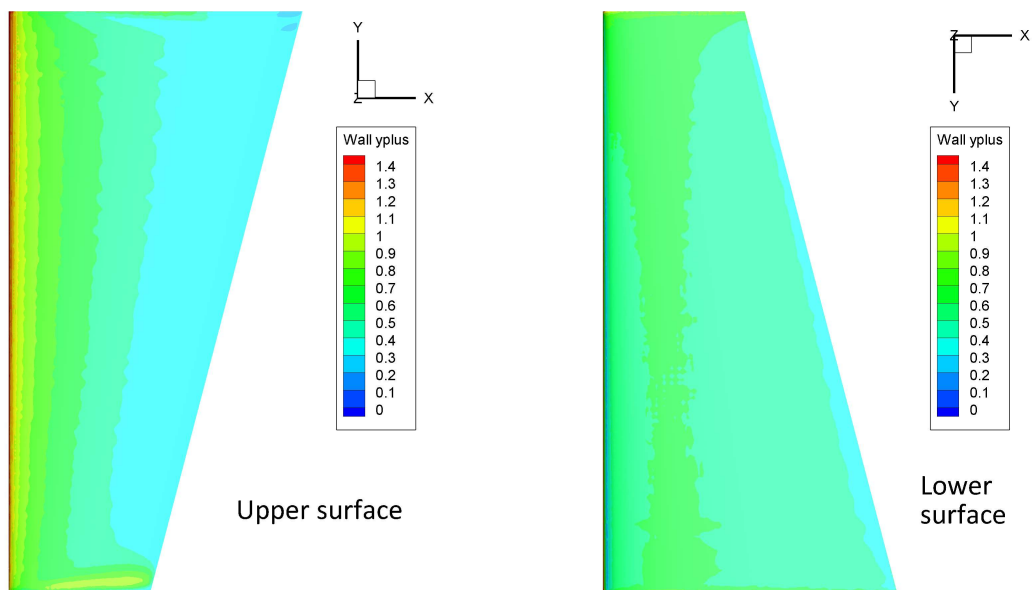


Figure 6.6: Contour of  $y^+$  value for the tapered NACA0013 wing at  $M = 0.1$ ,  $AoA = 0$ .

A validation has been conducted to verify the flow solver using published wind tunnel data for the same aircraft. Michael OL et al. have conducted a wind tunnel test for the sub-scaled Edge 540 aerobatic aircraft in a vertical wind tunnel (Ol et al. 2013). In the experiment, the flow velocity is 9.14m/s,  $Re = 140,000$ . The aerofoil thickness is 9%, compared to 13% in the present CFD simulation, wing span is 1041mm, compared to 2653mm in the present CFD simulation. Hence the CFD geometry is temporarily scaled, and the flow velocity is reduced to match the experiments. The aerofoil thickness is also reduced to 9%. These changes are only applicable in the results shown in Figure 6.7 . All the other simulations in the present research use a 2653mm span and 13% thickness.

Figure 6.7 shows the  $C_L$  and  $C_D$  for various AoA and flap deflection. The solid line depicts the present CFD results. The lift curves show good agreement with experiments at low AoA, while the CFD curve stalls a little earlier than the experiment. The  $C_L$  in terms of flap deflection also agrees with experimental data. For the drag results, CFD under-predicts  $C_D$  for  $AoA < 12^\circ$  and various flap angles. This is probably due to the absence of a propeller in the CFD model. While in wind tunnel experiments, the propeller is stationary for power-off tests. In addition, the wind tunnel model is a hobby-type aircraft fabricated with carbon and wood, the size and shape of the geometry have limited accuracy and experience surface deflection with the aerodynamic load. For example, the actual aerofoil shape of the wind tunnel model is slightly different from a standard curve due to manufacturing defect (Ol et al. 2013). Overall the CFD results match experiments reasonably well at low angles of attack.

A further comparison with the aerodynamic derivatives from reference (Stevens et al. 2015) - Page 648 for the same aircraft is presented in the following section.

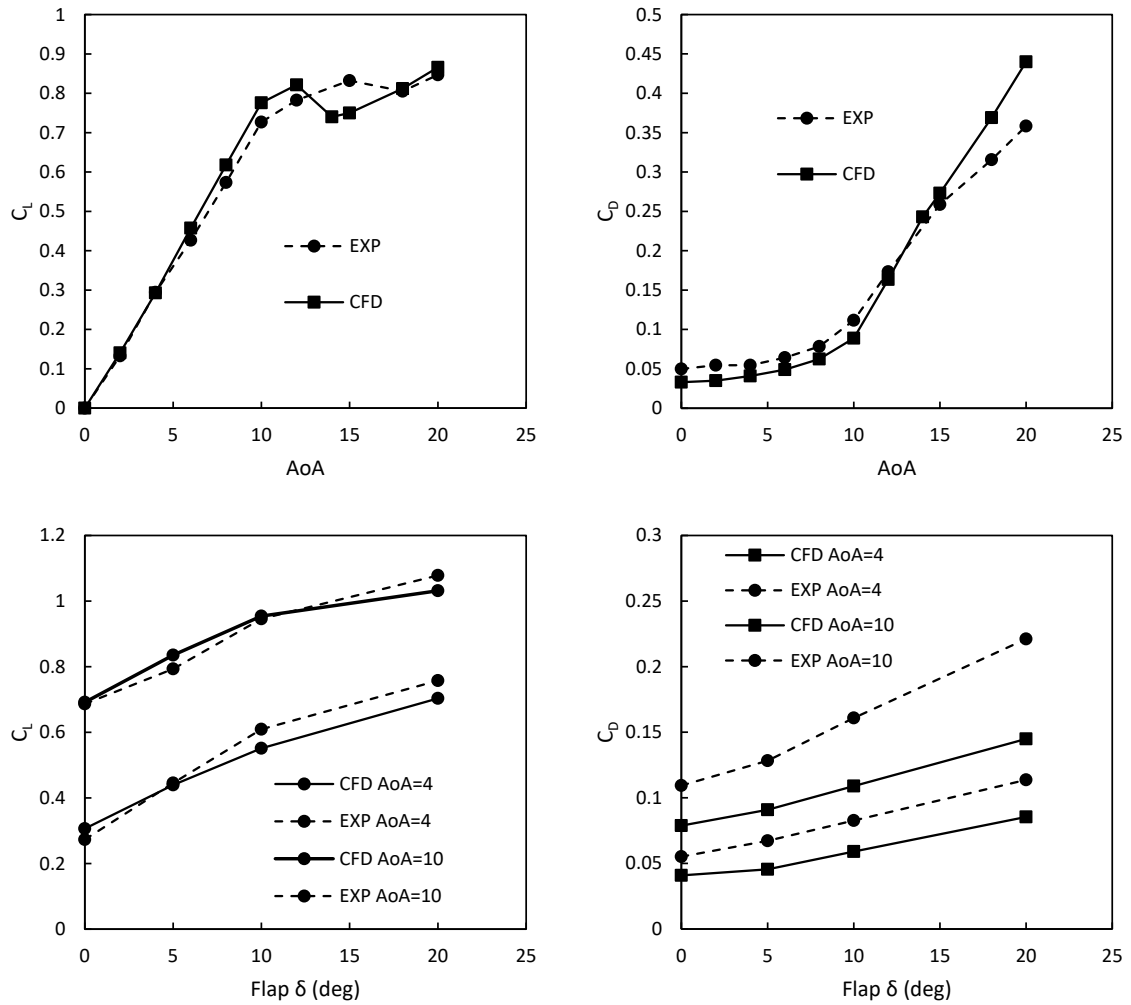


Figure 6.7: Validation of the present CFD results with wind tunnel data for the 9% thickness wing-body model(Ol et al. 2013) at  $Re=140,000$ , top:  $C_L$  and  $C_D$  vs. AoA for clean wing, bottom:  $C_L$  and  $C_D$  vs. flap deflection at  $AoA=0$ .

Subsequently, the original model ( 2653mm span and 13% thickness ) is used to compare with the database provided by Brian Stevens et al. (Stevens et al. 2015). A set of 3D CFD simulations with various AoA and flap settings have been performed. Figure 6.8 shows the results of  $M=0.1$  and various AoA from  $0^\circ$  to  $16^\circ$ . It can be seen that the stall AoA is around  $15^\circ$ . It is also found in the pressure distribution plot in Figure B.5.c, when  $AoA=16^\circ$ ,  $FLAP=0^\circ$ , the flow at the inboard region was separated.

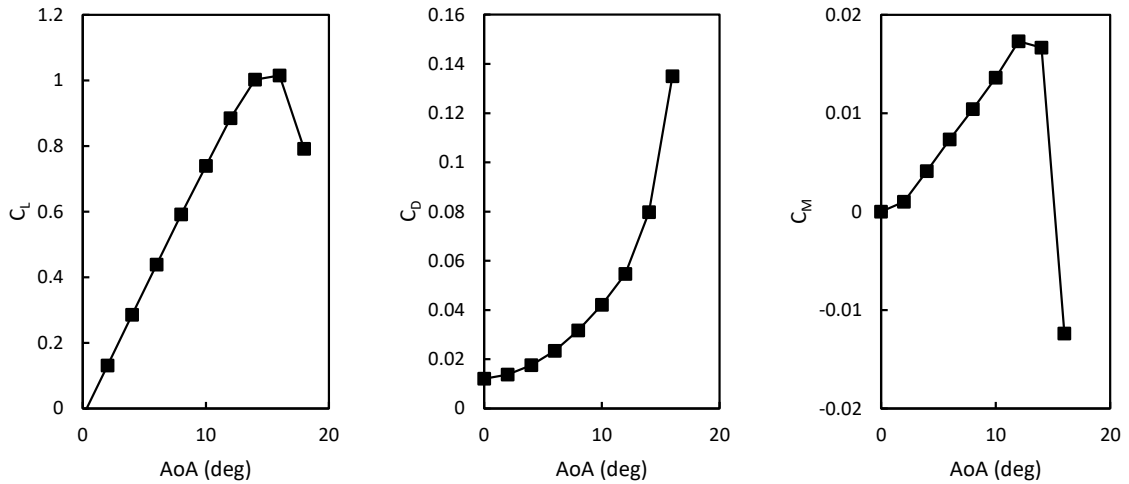


Figure 6.8: Lift, drag and pitch moment coefficients of the 3D wing-body model in various AoA (33% scale Zivko Edge 540T aircraft with NACA0013 aerofoil,  $M = 0.1$ ).

Figure 6.9 shows the results with flap deflection from  $0^\circ$  to  $25^\circ$ . The maximum effective deflection angle is around  $25^\circ$ . The flow separation over the wing or flap is the main reason that the maximum lift is limited for conventional mechanical control surfaces.

The results obtained from CFD simulation are then compared with the reference from the literature (Stevens et al. 2015) to validate the accuracy of the CFD solver, As shown in Table 6.3. The flap effectiveness ( $\tau_a$ ) is the lift coefficient increment by the flap, divided by the lift coefficient by AoA at the same angle, given by the following equation

$$\tau_a = \frac{C_{L\delta}}{C_{L\alpha}} \quad (6.5)$$

where  $C_{L\delta}$  is the lift coefficient increment by the flap deviation,  $C_{L\alpha}$  is the lift coefficient increment by increasing AoA. The CFD results closely match the data from the literature, except the lift is a little lower. As the referenced literature doesn't provide accurate geometry dimensions, the geometry was derived from the datasheet of a full-scale aircraft from the manufacturer (Zivko 2003). It is possible that the geometry used in this CFD is slightly different from that in the literature.

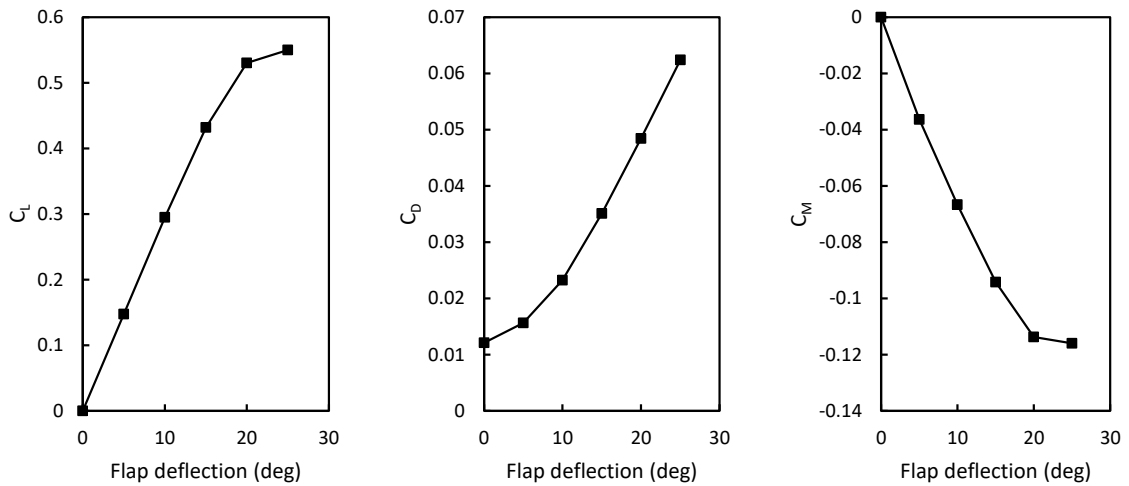


Figure 6.9: Lift, drag and pitch moment coefficients of the 3D wing-body model in various flap deflection angle (33% scale Zivko Edge 540T aircraft with NACA0013 aerofoil,  $M = 0.1$ ).

Table 6.3: Comparison of the literature reference data and the CFD results (33% scale Zivko Edge 540T aircraft with NACA0013 aerofoil,  $M = 0.1$ )

Item	Literature	CFD
Lift curve slop	4.6	4.23
$C_L$ at AoA=0	0	0
Max Cl	1.1	1.01
Cd at AoA=0	0.01	0.012
Flap effectiveness ( $\tau_a$ )	0.4	0.4

As the results are reasonably close to the reference data, in the following study, the lift, drag and moment of the wing and flaps are based on the present CFD, while the stability derivatives are based on the given data from the literature. The purpose of flight dynamics simulation is to demonstrate the feasibility of applying CC, not an accurate quantitative study. The accuracy of the derivatives is acceptable.

## 6.2 Re-design of the trailing edge for CC

This section describes a re-design of the trailing edge shape of the wing section to include CC using 2D CFD simulation. The original NACA0013 aerofoil used in the datum aircraft has been modified as a CC aerofoil. A plenum chamber and a Coanda shape trailing edge have been added. The combination of slot height and the trailing edge radius strongly affect the drag performance, so a parametric study was therefore undertaken to get the best performance.

However, the shape parameters were not derived from a detailed optimisation study. The relationships of slot height and radius were given by Englar et al. (Englar & Williams 1971), and an effective design region was provided. In this study, four different combinations within Englar's design region were used to find a suitable trailing edge shape for the datum aircraft flying at a low Reynolds number.

The chord length of the aerofoil is 460mm, which is equal to the Mean Aerodynamic Chord (MAC) of the datum aircraft. Four meshes of different nozzle dimensions are generated, as shown in Figure 6.10 . The sizes of the four TE configurations are shown in Table 6.4.

Table 6.4: Circulation control trailing edge parameters, r: TE radius, h: Nozzle height, c: Chord length (33% scale Zivko Edge 540T aircraft with NACA0013 aerofoil and modified circular trailing edge).

TE configuration	r (TE radius)	h (Nozzle height)
$h/r=0.1, r/c=0.01$	4.6mm	0.46mm
$h/r=0.1, r/c=0.005$	2.3mm	0.23mm
$h/r=0.05, r/c=0.02$	9.2mm	0.46mm
$h/r=0.05, r/c=0.01$	4.6mm	0.23mm

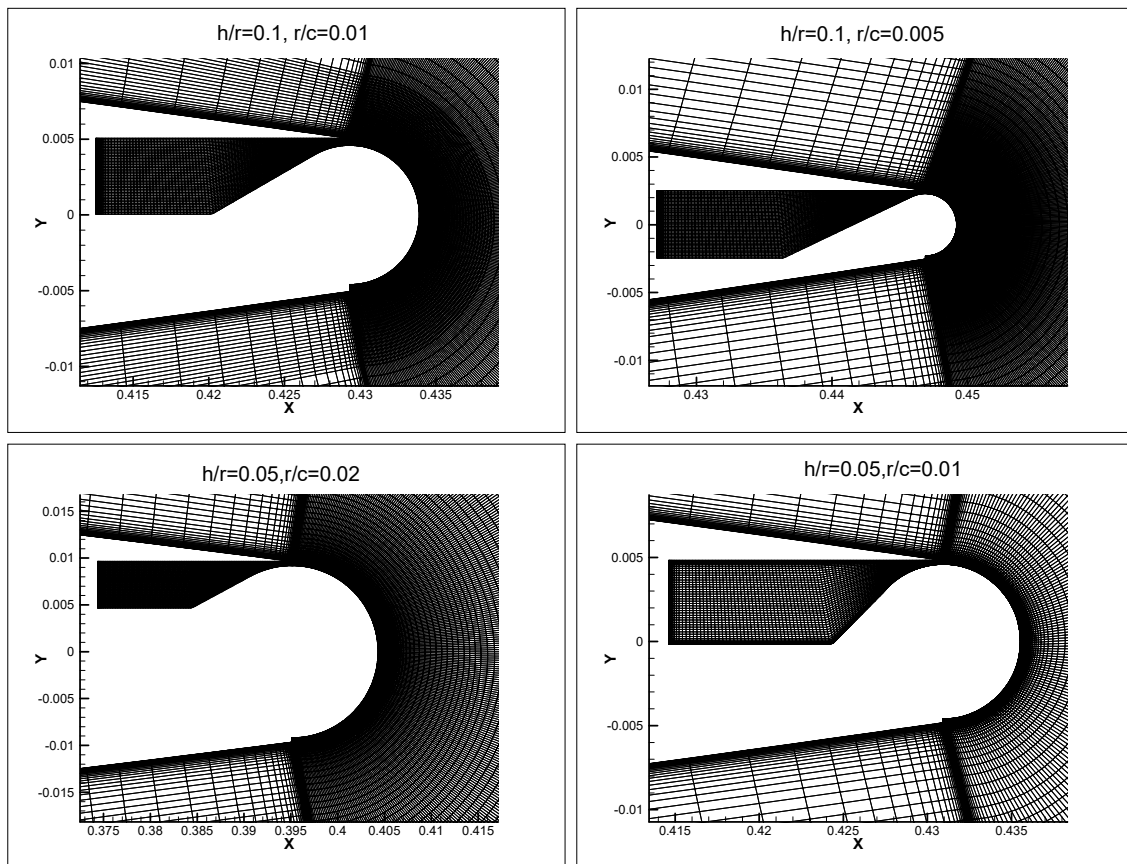


Figure 6.10: Trailing edge configurations by modifying the NACA0013 aerofoil. h: Nozzle height, r: TE radius, c: Chord length.

Figure 6.11 and Figure 6.12 compare the lift and drag coefficients under various  $C_{\mu}$ . Apparently thicker trailing edge and larger nozzle height will generate higher lift. The configurations of  $h/r=0.1$ ,  $r/c=0.01$  and  $h/r=0.05$ ,  $r/c=0.02$  give much higher  $C_L$  and  $C_D$  than the others. The  $h/r=0.1$ ,  $r/c=0.005$  and  $h/r=0.05$ ,  $r/c=0.01$  have similar drag performance, but the latter gives higher lift. In this study, the CC is considered a means of gust alleviation and is used during the cruise. The gust alleviation doesn't need as much lift increment as a high-lift device, but a lower drag coefficient is desired. Therefore the configurations of  $h/r=0.1$ ,  $r/c=0.005$  and  $h/r=0.05$ ,  $r/c=0.01$  was selected for the following 3D simulation as their maximum  $C_L$  is enough for the purpose of gust alleviation.

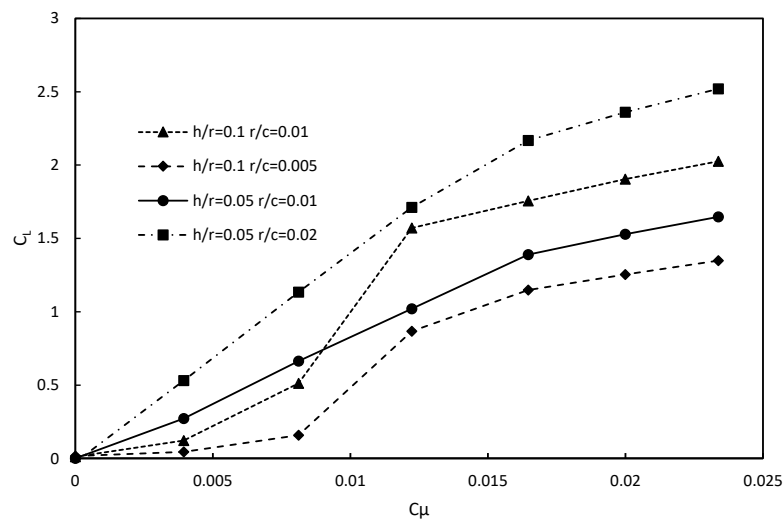


Figure 6.11: Lift coefficient of the 4 configurations of the modified NACA0013 aerofoil under different  $C_{\mu}$ . AoA=0, M=0.1.

### 6.3 Hybrid Meshing of the Aircraft with CC Wing

The meshing for the CCW is challenging, and it is difficult to mesh the geometry using the conventional unstructured or structured method. Firstly, the fuselage of the aircraft has some unique surfaces which are difficult for structured meshing. For example, the surface between the wing and fuselage is twisted and has a very thin, sharp trailing edge. Secondly, the feature on the trailing edge nozzle is very small; therefore the mesh must be fine enough to capture the local flow. Finally, the mesh should be equivalent to the case with the mechanical flap to compare the performance of the mechanical and CC flaps.

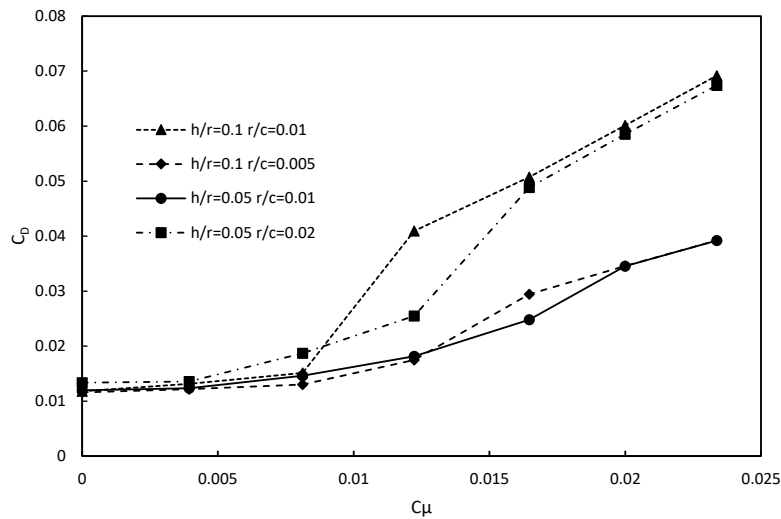


Figure 6.12: Drag coefficient of the 4 configurations of the modified NACA0013 aerofoil under different  $C_{\mu}$ . AoA=0, M=0.1.

### 6.3.1 Unstructured Tetra Meshing

In this case, pure tetra mesh is unsuitable as there is a very thin slot on the trailing edge. The thinnest part is only 0.1mm. To resolve the flow at the blowing slot, the local cells have to be very small, which results in a large number of cells along the spanwise. Therefore the total number of volume cells is very large (above 10 million cells). As this study includes many unsteady simulations of which the time step is relatively small, it is expected to use a small mesh to reduce the computational cost.

To generate a fine mesh at the blowing slot with an acceptable amount of cells, the anisotropic hexahedral mesh is probably the best method since it can be stretched spanwise and retain a sufficiently high density in the flow direction. This is a standard method for lifting surfaces. However, the wing geometry has a taper ratio and complex structures along the jet slot, so it is difficult to stretch the cells. For example, the wing root area and the corner of the nozzle are expected to use fine mesh to capture the vortex, but the cells inside the plenum chamber are expected to be stretched as there is no spanwise flow in the chamber. It is not possible to only stretch the mesh inside the chamber. The mesh is inevitably very large when using a normal unstructured meshing technique.

### 6.3.2 Structured Meshing

The previous 2D study used structured meshing, and to maintain consistency, the 3D-hexa mesh has been tried. Structured Hexa mesh can generate a fine mesh with fewer cells which

is beneficial for the dynamic CFD as it requires a very small time step. However, there are some difficulties when generating a hexa mesh due to the highly twisted surface on the fuselage and body-wing junction area. Figure 6.13(a) shows the junction area (in red). The surface has a small radius at the leading edge and a large radius near the trailing edge. The junction between the trailing edge and fuselage creates some highly skewed elements, structured meshing failed to generate a usable mesh for this aircraft after several attempts.

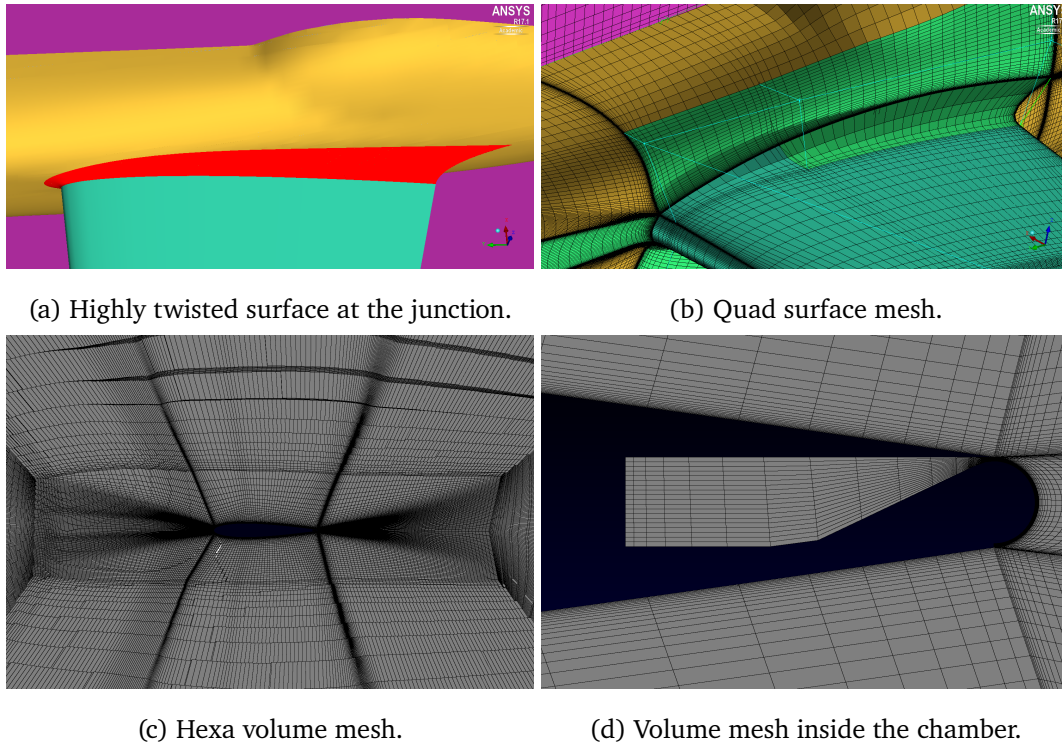


Figure 6.13: Structured mesh for the 33% scale Zivko Edge 540T wing-body model with CC trailing edge.

### 6.3.3 Hybrid Meshing

Considering the mesh quality and size, hybrid meshing is probably the best choice for this geometry. Therefore the trailing edge and the blowing slot are built with hexa mesh while all the other parts are tetrahedron and triangular prism. The hexa mesh was placed inside the plenum chamber and wrapped around the Coanda surface to reduce mesh size and align with the local flow. Figure 6.14 (a) shows the unstructured surface mesh around the wing and fuselage. Figure 6.14 (c) shows the tetra volume mesh. Whereas inside the nozzle chamber and around the Coanda surface are structured mesh, shown in Figure 6.14 (b) and the cross-section in Figure 6.14 (d). As the spanwise flow along the trailing edge is weak and has little impact on the CC effectiveness, the structured mesh is stretched to reduce the number of cells.

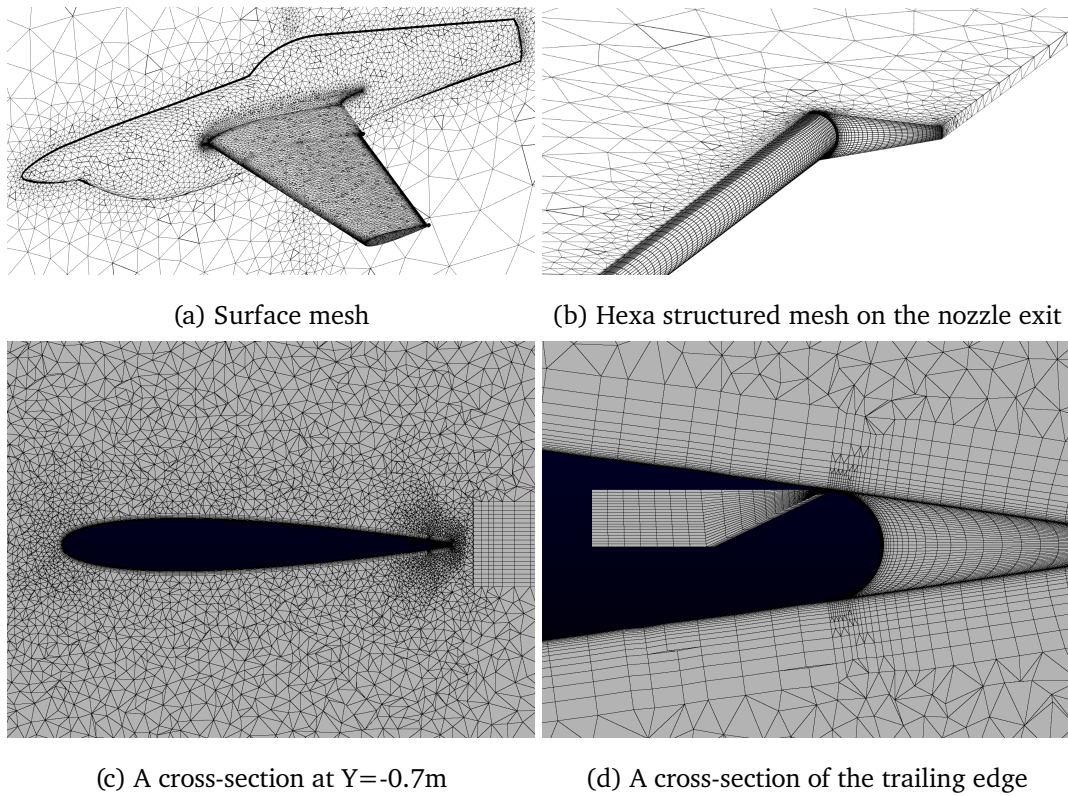


Figure 6.14: Hybrid mesh for the 33% scale Zivko Edge 540T wing-body model with CC trailing edge.

A mesh independence study was carried out and the mesh was refined from 5 million to 15 million as shown in Figure 6.15 . The  $\Delta C_L$  is the percentage difference to the finest mesh. Through the mesh independence study, the 7.9 million mesh gives a close value to the finest and has been used in the following sections.

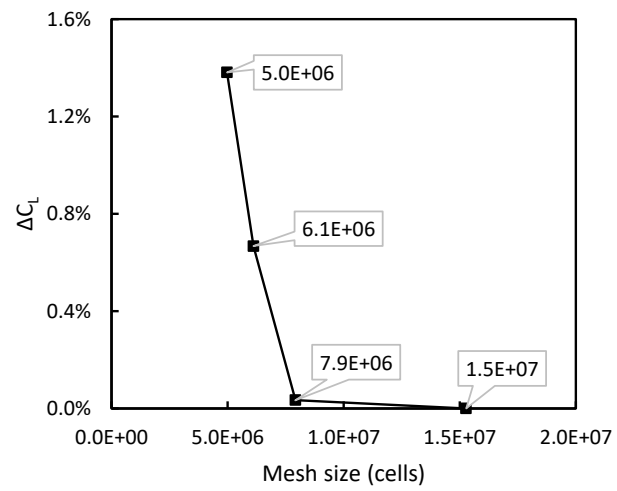


Figure 6.15: Mesh independent study for the 33% scale Zivko Edge 540T wing-body model with hybrid mesh at  $C_\mu = 0.01$ ,  $M = 0.1$

## 6.4 3D Effect of the Trailing Edge Coanda Surface

The previous section studied different nozzle configurations in 2D. In this section, a 3D simulation was conducted. The trailing edge of the 3D wing-body model was redesigned, and a blowing slot was added according to the dimension from the previous 2D case. The spanwise length of the slot is the same as the mechanical flap. As the 3D wing has a taper ratio, the chord length is not constant. In the 3D geometry, the ratio between the TE radius and the chord length remains the same. The slot height and radius are scaled according to the local chord. The  $h/r=0.1$ ,  $r/c=0.005$  configuration case was first selected as it has the smallest drag.

In the simulation, an unanticipated result is that the separation of the jet sheet around the trailing edge is unstable and results in unsteady vortex patterns. Figure 6.16 shows the vortex system at the wake zone. The jet sheet from the nozzle first travels around the Coanda surface but then becomes unstable and generates a few counter-rotating vortices. Figure 6.16 (b) and (c) shows the streamlines coloured by X-vorticity. The red colour indicates an anti-clockwise rotating vortex, and the blue indicates the vortex rotates in the opposite direction. The definition of vorticity can be found in Section 2.1.4 on page 11. A series of vortices are formed from the trailing edge. The vortex close to the wing root is very strong as the inboard wing doesn't generate lift at zero AoA. The nature of the inboard vortex is similar to the edge vortex from a mechanical flap. However, as shown in Figure 6.16 (b) and (c), the vortices on the left side are much weaker, which indicates the vortex sheet is influenced by the 3D effect of the wing and is not uniform along the span.

Generally, the air jet from the blowing nozzle is a thin sheet that wraps around the trailing edge and then separates from the Coanda surface. The separation point on any cross-sectional slice of the wing remains the same. Thus there should be a straight separation line on the cylindrical trailing edge. However, the separation line is unique in this case. Figure 6.16 (d) shows the pressure distribution on the cylinder trailing edge surface. The boundary between blue and red indicates the separation position of the jet sheet, which looks like a sinusoidal wave. At some point, the separation happens very early, but the others separate very late or even recirculate to the bottom of the wing. This unstable separation then generates a series of vortex patterns.

There are several factors which are probably responsible for the vortex sheet, for example, the edge vortex due to spanwise lift distribution, the low Reynold's number effect at the trailing edge, or the non-uniform flow from the nozzle exit. Several simulations were undertaken to

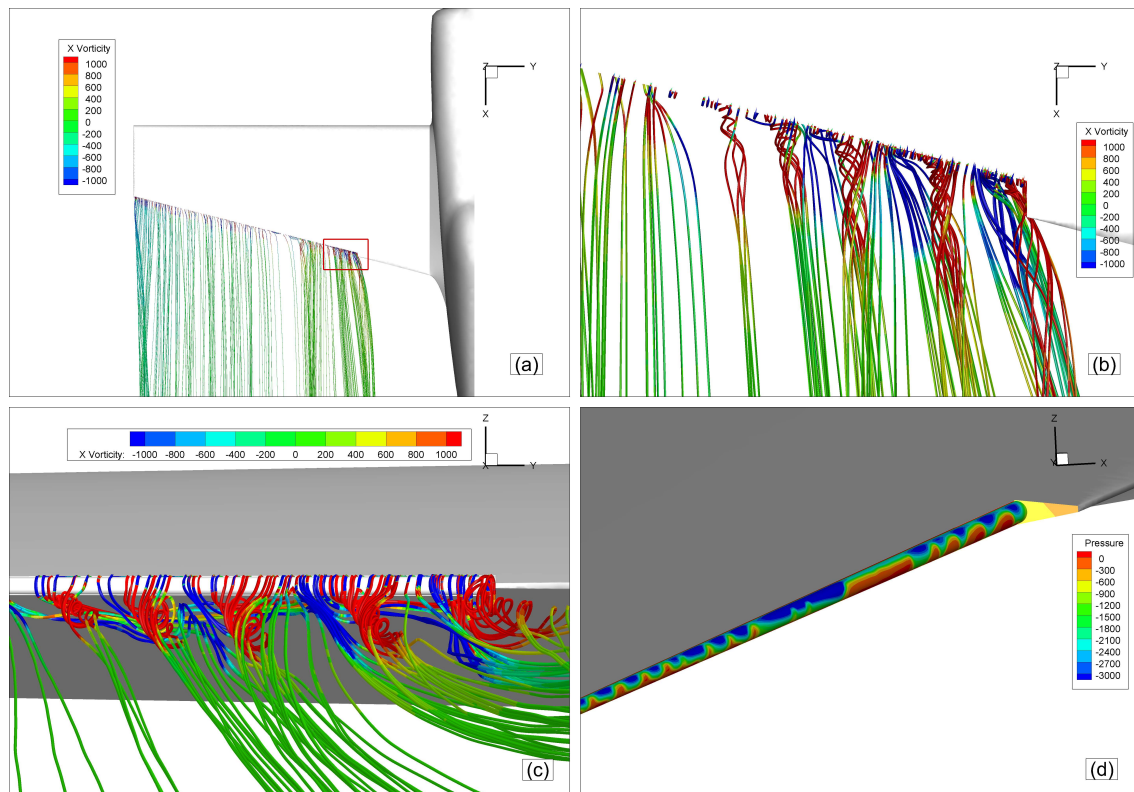


Figure 6.16: The streamline view of the vortex patterns at  $M = 0.1$ ,  $C_{\mu}=0.01$ , for the 33% scale Zivko Edge 540T wing-body model.

find out the potential reasons.

#### 6.4.1 Flow Field at the Nozzle Exit

The vector field from two cross-sections was plotted to compare the velocity profile between early-separation and late-separation positions. As shown from Figure 6.17, two slices at  $y=-0.942\text{m}$  and  $y=-0.955\text{m}$  are marked as red vertical lines on the pressure contour. The  $y=-0.942\text{m}$  slice is on the early separation point where the flow separates just after the nozzle, whereas the  $y=-0.955\text{m}$  slice shows the late separation where the flow keeps attached till the bottom of the cylinder trailing edge. The velocity profile at the two slices is plotted together to compare the flow conditions. Obviously, the flows from the two slices are almost identical at the nozzle exit. Then the  $y=-0.942\text{m}$  slice separates at an early stage, but the  $y=-0.955\text{m}$  slice remains attached. This indicates that the flows at the nozzle exit are identical at different spanwise positions. Therefore the unstable separation is not caused by the flow condition at the nozzle exit.

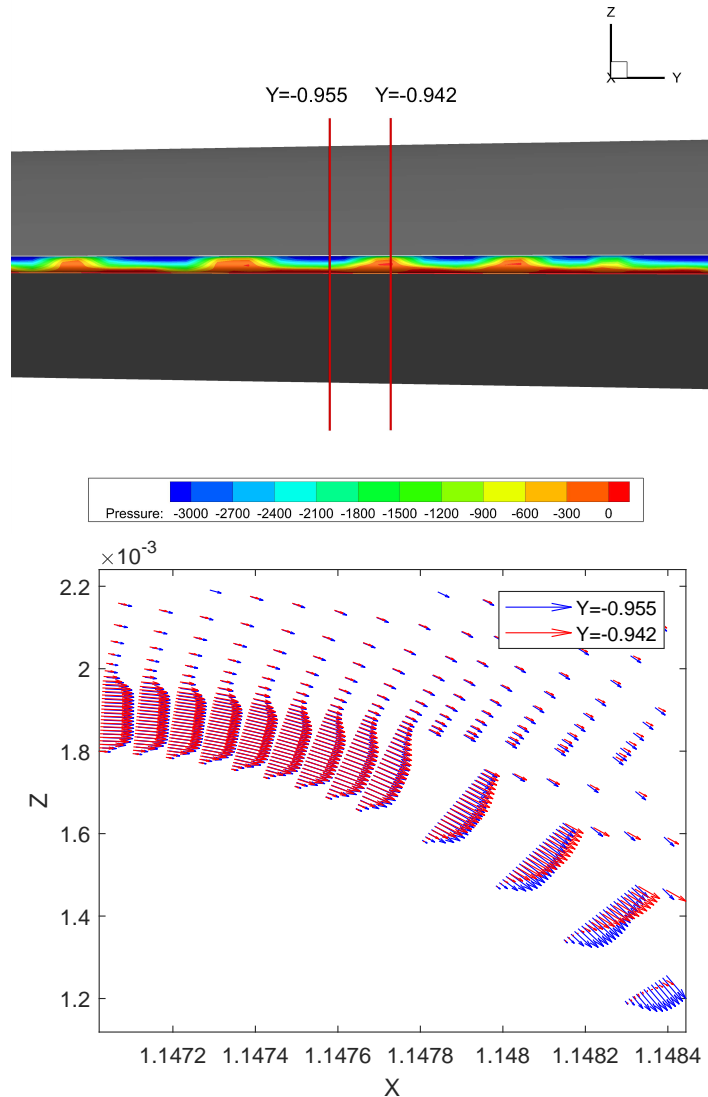


Figure 6.17: The vector field of the vortex patterns at  $M = 0.1$ ,  $C_{\mu}=0.01$ , for the 33% scale Zivko Edge 540T wing-body model.

#### 6.4.2 The Flow Field Without the Edge Vortex

In the original mesh, the symmetry plane cut through the fuselage, as shown in Figure 6.4 on page 161 (e) and Figure 6.18 on page 179 (b). To eliminate the effect of the edge vortex, the fuselage and inner wing are removed, the symmetry plane is moved outboard (in the  $-Y$  direction) therefore the rest of the wing has a full-span blowing slot, as shown in Figure 6.18 on page 179 (a). The root of the wing is a symmetry plane therefore the spanwise flow is restricted. If the unstable separation of the Coanda surface is caused by the edge vortex, the separation should become stable. However, as shown in Figure 6.18 on page 179, there was no significant difference between the modified wing (a, c, e) and the original wing-body case (b, d, f). The vortices in wake flow (Figure 6.18 on page 179 (c)) are identical to the original

case (Figure 6.18 (d)), which means there is no relation between the unstable phenomenon and the edge vortex.

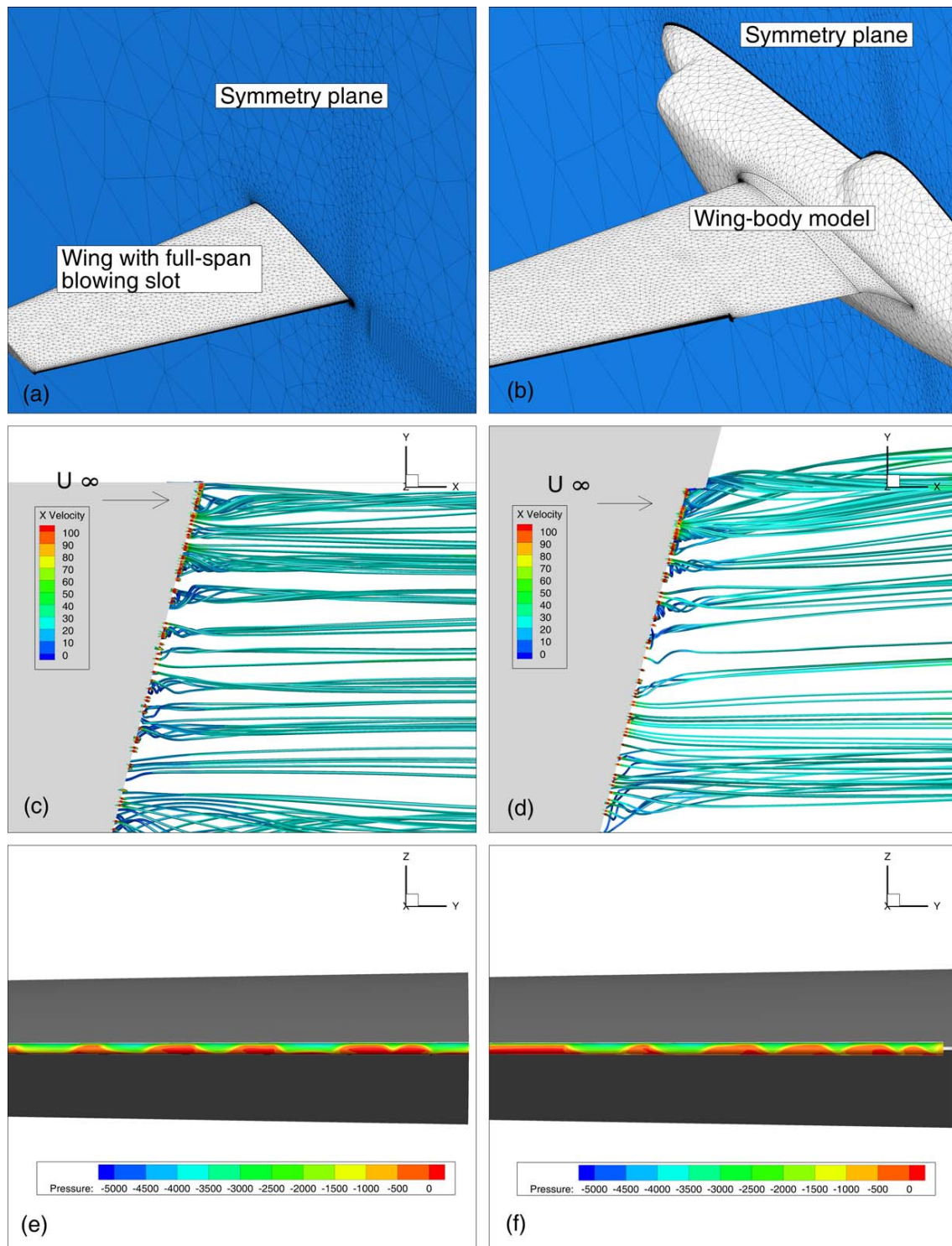


Figure 6.18: The vortex patterns of the modified wing and the original wing-body case at  $M = 0.1$ , nozzle pressure 7500Pa,  $C_{\mu}=0.01$ , 33% scale Zivko Edge 540T model. (a): modified wing geometry, (b): original wing-body geometry, (c): streamlines of the modified wing, (d): streamlines of the original wing-body case, (e): pressure distribution of the trailing edge of the modified wing, (f): pressure distribution of the original wing-body case.)

To investigate the influence of the taper ratio, the flow field of the finite wing is compared with a simplified wing-section case, which is extruded from the 2D aerofoil with no swept and taper ratio, displayed in Figure 6.19 . The section span is 100mm and has 100 points in the span direction. The streamlines have weaker vertices compared with Figure 6.16 on page 176, the wavy flow pattern still appears further downstream. Although there is no obvious counter-rotating vortex pairs, the streamlines with positive and negative helicity (dot product of the vorticity and the velocity vector  $(\nabla \times \mathbf{V}) \cdot \mathbf{V}$ ) are staggered. Figure 6.19 (c) and (d) are cross-sectional slices at the wave peak and valley respectively, coloured by helicity. It can be seen that the helicity is very strong in the mixing layer on the outer side of the jet and has an opposite direction in (c) and (d). Therefore, these flow structures are most likely caused by an unstable mixing layer downstream of the nozzle lip and independent of spanwise perturbations. For a finite tapered wing, the wavy flow pattern is enhanced by the spanwise velocity component and developed into a strong counter-rotating vortex sheet.

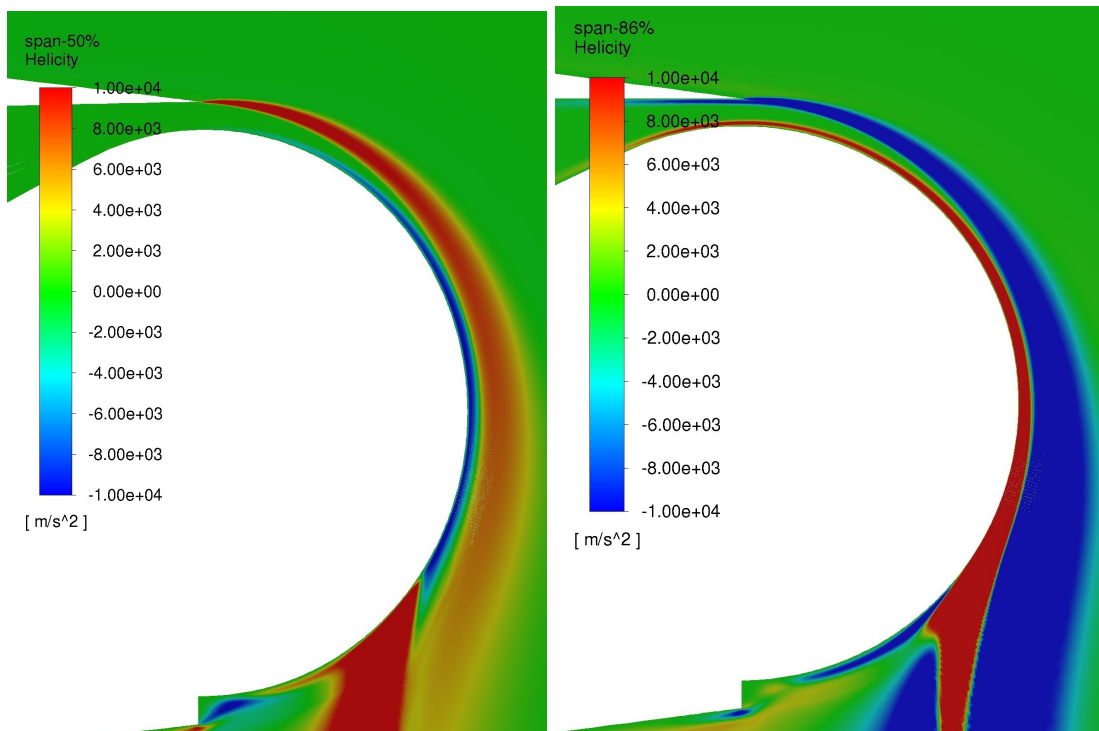
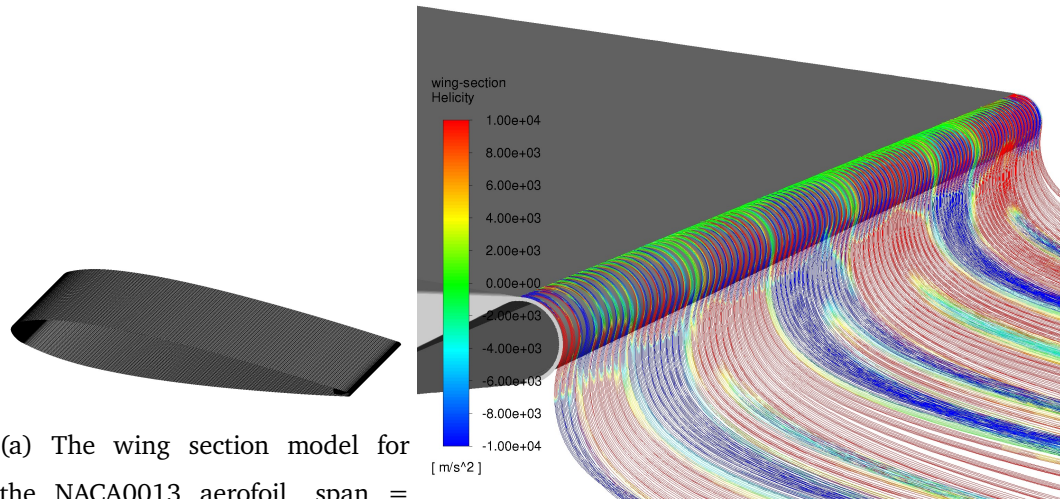


Figure 6.19: The jet sheet for a wing section model with a modified TE NACA0013 aerofoil, nozzle pressure 7500Pa,  $M = 0.1$ .

### 6.4.3 Trailing Edge Thickness

From the previous study, there was no evidence that the vortex patterns and the unstable separation at the trailing edge were caused by the nozzle condition or the edge vortex. The other possible explanation for these vortices is that the trailing edge is too thin. To reduce the drag during the cruise, a very thin trailing edge has been used. The previous 2D study shows that although the lift enhancement of a thin trailing edge is lower than a thicker trailing edge, it can still provide enough lift for gust alleviation and obviously has a much smaller drag coefficient. Although there is no stability issue in the 2D simulation of the  $h/r=0.1$ ,  $r/c=0.005$  configuration, the flow field in the 3D simulation is very different due to the spanwise flow. On the 3D finite wing, the thin trailing edge has a very high curvature which means the flow is easy to separate, and it is likely that the spanwise flow component deteriorates the stability of the jet sheet, which makes the separation unstable.

To understand how the trailing edge thickness influences the 3D flow field, a thicker trailing edge ( $h/r=0.05$ ,  $r/c=0.01$ ) from the 2D cases was used. Figure 6.20 compares the flow field of the two different trailing edge configurations at the same flow condition. Figures on the left (Figure 6.20 (a), (c)) show the streamlines and pressure distribution of the thicker trailing edge, and the figures on the right (Figure 6.20 (b), (d)) show the thinner trailing edge. Obviously, the thicker trailing edge gives a better flow field. The streamlines from the thicker trailing edge are smooth and straight, while the thinner trailing edge generates a few vortices. The pressure distribution view presents the separation line on the Coanda trailing edge. It is apparent that the separation line on the thicker trailing edge is almost straight, except for a short area near the inner edge due to the edge vortex. However, the separation on the thinner trailing edge shows a wavy distribution that indicates the jet sheet is unstable and produces intermittent vortex patterns.

From the previous comparison cases, it is almost certain that the trailing edge thickness is the cause of unstable separation. The thicker trailing edge has a low curvature so that the jet flow is easy to attach to the Coanda surface. However on the thin trailing edge, the curvature is very high, and the jet sheet easily separates at an early stage instead of travelling to the bottom of the trailing edge.

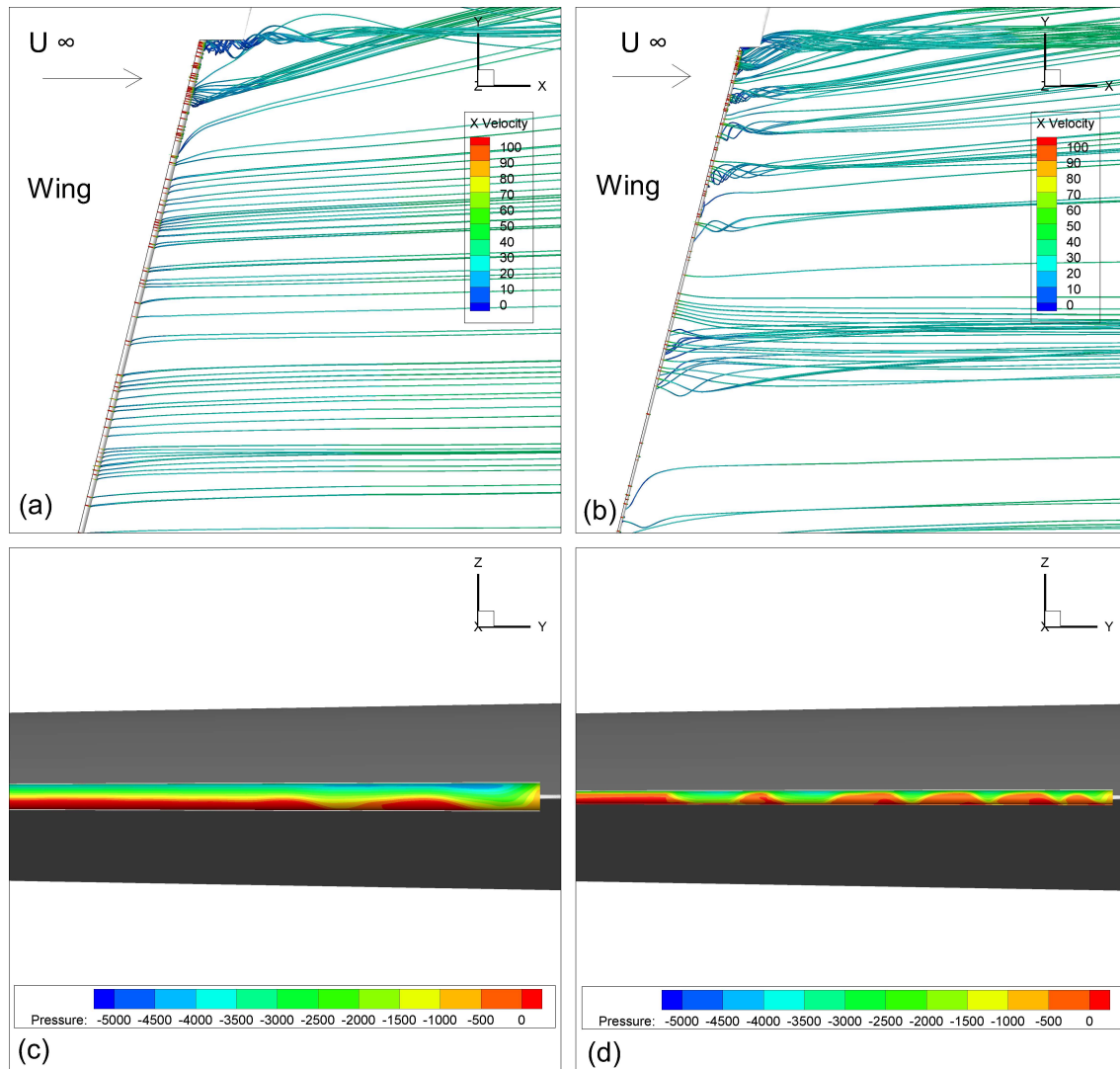


Figure 6.20: Streamlines and trailing edge pressure distribution of the thicker trailing edge ( $h/r=0.05$ ,  $r/c=0.01$ ) and the original thinner trailing edge ( $h/r=0.1$ ,  $r/c=0.005$ ) at  $M = 0.1$ , nozzle pressure 7500Pa,  $C_{\mu}=0.01$ , 33% scale Zivko Edge 540T model. (a): streamlines of the thicker trailing edge, (b): streamlines of the original thinner trailing edge, (c): pressure distribution on the trailing edge showing a straight separation line (d): pressure distribution showing an unstable separation line.)

Few studies have been conducted on the wavy meandering vortices over a convex surface associated with a wall jet Gross & Fasel (2008), Dunaevich & Greenblatt (2020). Dunaevich has observed similar vortices in a water tunnel (Dunaevich & Greenblatt 2020). The experimental apparatus is a cylinder with a tangential slot, as shown in Figure 6.21 (a). The cylinder model has a radius  $R = 20\text{mm}$ , span  $b = 200\text{mm}$  and slot height  $h = 1\text{mm}$ . The flow visualisation result is shown in Figure 6.21 (b), in which the slot is at the bottom of the figure and the flow direction is upward. The water jet from the slot is dyed to visualise the flow. A wavy flow pattern is observed downstream of the slot, the streamwise counter-rotating vortices are very similar to the present CFD results, except the size of wavy vortices shown in Figure 6.21 (b) is much smaller than ones in Figure 6.16 on page 176. This can be quantified by the wavenumber  $\alpha = 2\pi h/\lambda$  ( $\lambda = \text{wavelength}$ ). In the present CFD results,  $\alpha = 0.046$ , compared to 0.6 in the experiment (Dunaevich & Greenblatt 2020). This is probably due to the different flow conditions: the present research has a larger jet Reynolds number ( $Re_h = \frac{U_j h}{\nu}$ ) of 1533, compared to  $Re_h = 19 - 253$  in the experiment. Also, there is no external flow in Dunaevich's experiment.

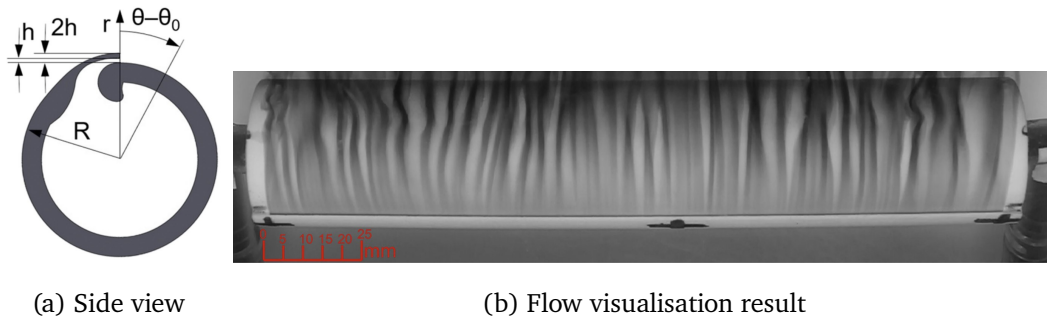


Figure 6.21: The side view of the research model and the wavy vortices conducted in a water tunnel, the slot is at the bottom of figure (b), flow direction is upward,  $Re_h = 63$  (Dunaevich & Greenblatt 2020).

Dunaevich suggested a slot height based Gortler number  $G' = \frac{U_j h}{\nu} \sqrt{\frac{h}{R}}$  to evaluate the fluid stability over a convex wall jet. Figure 6.22 is a stability map of  $G'$  vs.  $\alpha$ . Theoretically, the region above the neutral stability curve is unstable (Dunaevich & Greenblatt 2020). The test cases conducted by Dunaevich, and the present CFD results are all in this region. In addition, increasing the trailing edge thickness ( $R$ ) will move  $G'$  downward towards the stable region so that the flow is relatively stable for a larger  $R$ . It is very likely that the wavy flow pattern shown in Figure 6.16 on page 176 is a similar type of centrifugal instability (Saric et al. 1994) as the one observed by Dunaevich (Dunaevich & Greenblatt 2020). This instability results from the centrifugal force applied to the mixing layer between the jet sheet and external flow,

and is enhanced by the spanwise velocity component due to the taper ratio. However, further study of flow instability is out of the scope of this research.

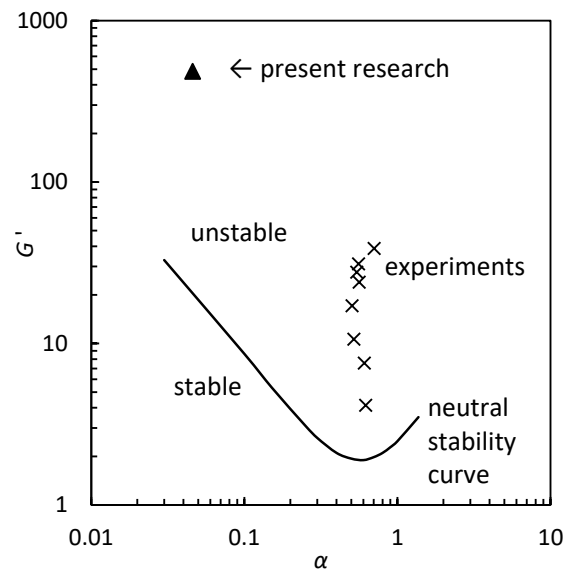


Figure 6.22: The stability map of slot height based Gortler number  $G'$  in terms of wavenumber  $\alpha$  (Dunaevich & Greenblatt 2020)

In practice, the wing trailing edge should not be too thick since a thick trailing edge creates significant drag. Figure 2.14 on page 30 shows the pressure distribution around a Coanda surface, the suction peak downstream of the nozzle creates a strong force component in the axial direction, resulting in a large drag coefficient. As shown in Figure 6.12 on page 171, the two thicker aerofoil  $h/r=0.1$ ,  $r/c=0.01$  and  $h/r=0.05$ ,  $r/c=0.02$  has twice as large drag coefficients than the other two configurations. As a result, the following chapters use the  $h/r=0.05$ ,  $r/c=0.01$  configuration for a stable jet and less drag penalty.

## 6.5 Spanwise Velocity Distribution

The boundary condition of the nozzle was set to pressure inlet ( the same BC as in Figure 5.2 on page 127 ), which means the pressure inside the plenum chamber is uniform along the span. Because the tip chord is smaller than the root chord, to maintain a constant ratio between the local TE and chord length, the slot height and TE radius are scaled by the local chord. Consequently, the velocity and  $C_\mu$  along spanwise are not consistent. In this section, the spanwise distribution of velocity is studied to obtain an accurate  $C_\mu$ . Figure 6.23 displays the velocity components in both X and Y directions when the nozzle pressure was set to 7500Pa. The trailing edge is inclined which affects the direction of the jet sheet and forces the jet to turn outward, which results in a spanwise velocity component. When calculating the  $C_\mu$ , both X and Y velocities are considered and the result is shown in Figure 6.24 . From the root to the tip, the nozzle height is scaled from 0.25mm to 0.11mm, the local  $C_\mu$  is reduced from 0.01 to 0.009 accordingly. The average  $C_\mu$  is 0.0096, compared to a 2D aerofoil at the same nozzle pressure which is 0.012. Table 6.5 listed the 2D and 3D  $C_\mu$  at various nozzle conditions, the 3D velocity is the velocity magnitude at mid-span. The exit velocity for different nozzle pressure is in good agreement between the 2D aerofoil and 3D wing. As expected, the  $C_\mu$  of the 3D wing is different from the 2D result, which is 6% to 15% lower, this is attributed to the fact that the nozzle geometry varies along the span, but  $C_\mu$  is originally defined for a 2D geometry. However, the difference does not affect the dynamic response. The average  $C_\mu$  is still used in the following study.

Table 6.5: The  $C_\mu$  of the 2D modified NACA0013 aerofoil and 3D tapered wing under various pressure settings.

Nozzle pressure (Pa)	2D velocity (m/s)	2D $C_\mu$	3D velocity (m/s)	3D $C_\mu$
2500	67.5	0.0039	69.0	0.0036
5000	96.9	0.0081	98.5	0.0068
7500	118.9	0.0122	120.5	0.0101
10000	138.0	0.0165	139.0	0.0133
12500	152.0	0.0200	157.6	0.0165
15000	164.4	0.0234	170.4	0.0197

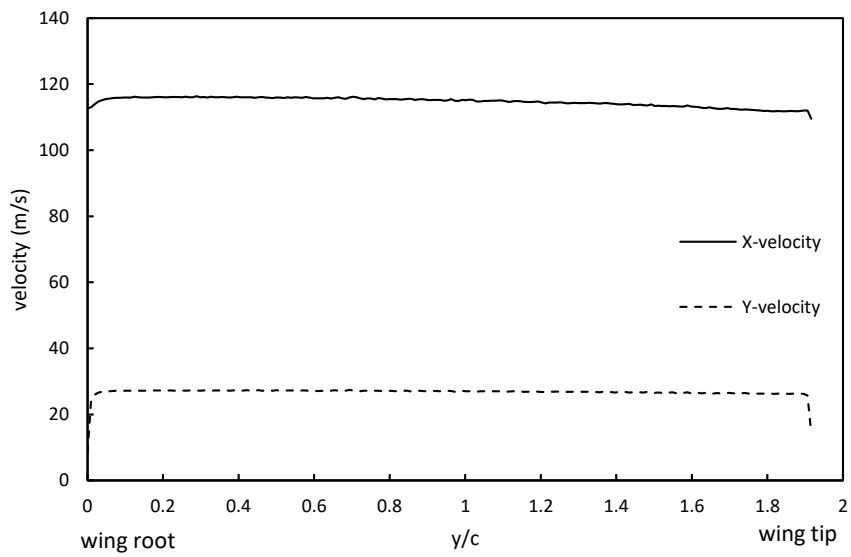


Figure 6.23: The axial(X) and spanwise (Y) velocity distribution from the wing root to the wing tip (Nozzle pressure = 7500Pa, 33% scale Zivko Edge 540T wing-body model).

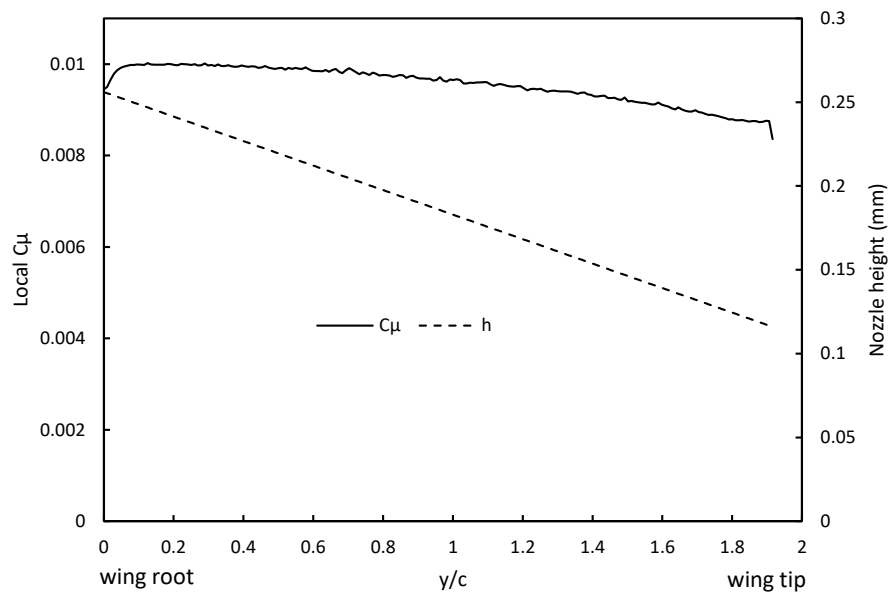


Figure 6.24: The local nozzle height and  $C_{\mu}$  from the wing root to the wing tip (Nozzle pressure = 7500Pa, 33% scale Zivko Edge 540T wing-body model).

## 6.6 Spanwise Effect of the CC Flap

The CC can generate a very high lift coefficient which might be higher than required. The previous study was based on a full-span nozzle, its spanwise length is the same as the original mechanical flap in order to compare the lift increment. However, a smaller spanwise extent

may be sufficient to generate an equivalent lift, with reduced pumping requirements and also reduced drag since the CC does increase the profile drag. Considering the energy cost, it is unclear which nozzle has higher efficiency. The following study investigates the nozzle with different spanwise lengths to determine if flap effectiveness can be achieved with a part-span flap at a reduced cost (in terms of pumping requirements). Two different configurations have been investigated, the inner-half-span and the outer-half-span, the spanwise length of each is half of the previous nozzle. As shown in Figure 6.25.

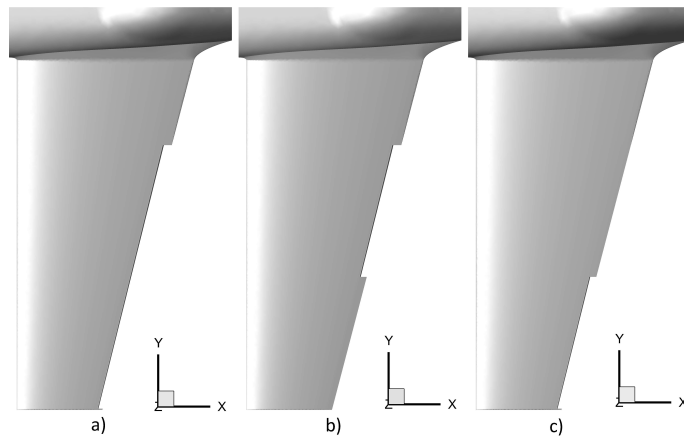


Figure 6.25: The geometries of the half-span cases, 33% scale Zivko Edge 540T wing-body model. a) original nozzle, b) inner half-span nozzle, c) outer half-span nozzle.

Figure 6.26 shows the lift coefficient with various blowing momentum coefficients. The  $C_L$  of the outer-half-span case is significantly lower than the inner-half-span because the outer half has a shorter chord length and is affected by the tip vortex.

To compare the energy cost of the various configurations, the mass flow rate has been recorded. As the outer half-span configuration failed to provide enough lift, only the inner-half-span and the original full-span configuration have been compared. Figure 6.27 shows the mass flow rate at the nozzle boundary and the energy consumption under various  $C_L$ .

For a given mass flow rate and pressure, the relation between enthalpy rise and the pump shaft power is provided by the following equation, assuming an adiabatic compressor (Atkin & Courtenay 2002).

$$h_{t2} - h_{t1} = c_p (T_{t2} - T_{t1}) = \frac{\eta_{mech}}{\dot{m}} P_{shaft} \quad (6.6)$$

where  $h$  is enthalpy,  $c_p$  is the specific heat capacity at constant pressure. Subscript  $t$  is the total condition, and subscript 1 denotes the inlet condition of the pump, this is either from the engine compressor or from the free stream. Here we use free stream condition. Subscript

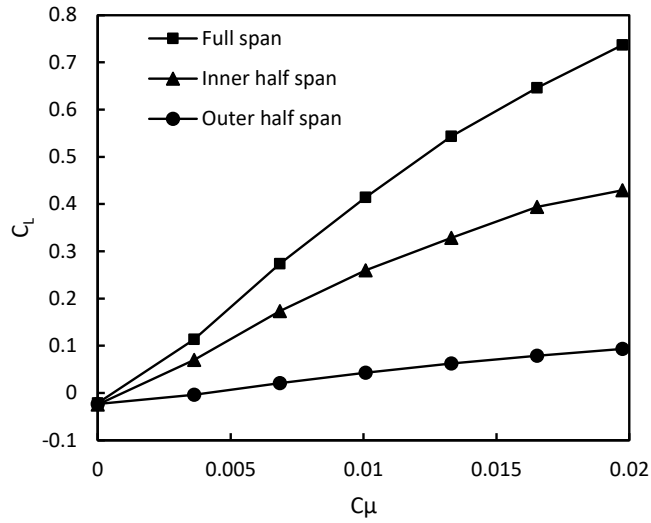


Figure 6.26: Lift coefficient of various blowing momentum coefficient with full-span nozzle, inner half and outer half at  $M = 0.1$ , 33% scale Zivko Edge 540T wing-body model.

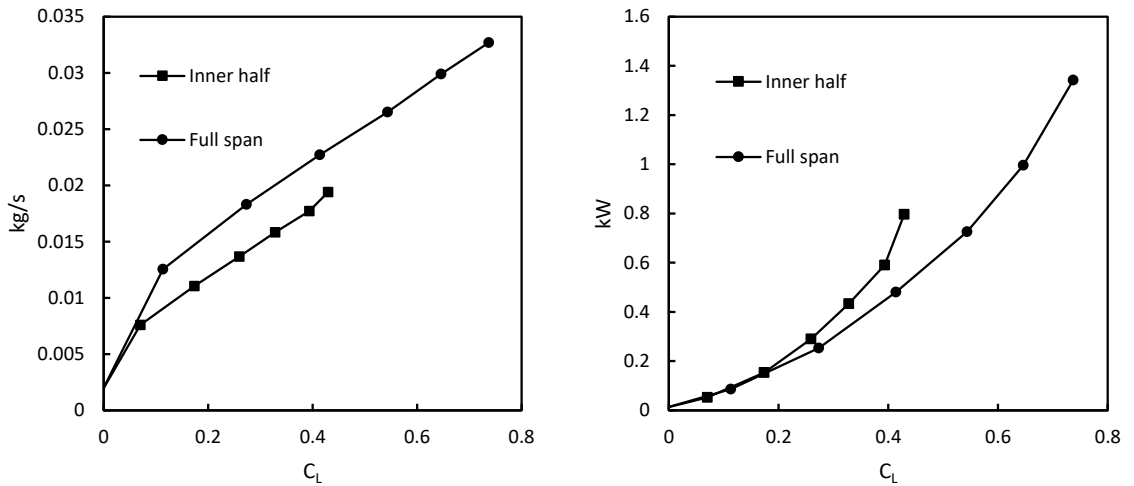


Figure 6.27: The mass flow rate and power consumption under various lift coefficients with full-span nozzle and inner half nozzle at  $M = 0.1$ , 33% scale Zivko Edge 540T wing-body model.

2 denotes the inlet condition of the plenum chamber.  $\eta_{mech}$  is the mechanical efficiency of the pump.  $\dot{m}$  is the mass flow rate and  $P_{shaft}$  is the power.

The isentropic efficiency is given by

$$\eta_{isen} = \frac{T'_{t2} - T_{t1}}{T_{t2} - T_{t1}} \quad (6.7)$$

where  $T'_{t2}$  is the isentropic total temperature

The change in total pressure is given by

$$\frac{P_{t2}}{P_{t1}} = \left( \frac{T'_{t2}}{T_{t1}} \right)^{\frac{\gamma}{\gamma-1}} = \left[ 1 + \eta_{isen} \left( \frac{T_{t2}}{T_{t1}} - 1 \right) \right]^{\frac{\gamma}{\gamma-1}} \quad (6.8)$$

According to the above equations, the pump power required can be calculated by

$$P_{shaft} = \frac{\dot{m}c_p T_{t1}}{\eta_{pump}} \left[ \left( \frac{P_{t2}}{P_{t1}} \right)^{\frac{\gamma-1}{\gamma}} - 1 \right] \quad (6.9)$$

where  $P_{t2}$  is the stagnation pressure in the plenum chamber which is equal to the stagnation pressure  $P_{tJ}$  at the jet exit,  $P_{t1}$  is the stagnation pressure at the inlet of the pump. Assuming the inlet condition of the pump is the same as the free steam, thus  $p_{t1} = 101325Pa$ ,  $T_{t1} = 288K$ ,  $c_p = 1.00kJ/kg.K$ ,  $\gamma = 1.4$ . The pump efficiency varies for different types, but an electric turbo compressor with an efficiency of 64% (Pegasus 2017) is assumed. According to Equation 6.9, the required pump power for different  $C_L$  is calculated and shown in Figure 6.27 .

Obviously for the same  $C_L$ , the full-span configuration requires a higher mass flow rate, but uses less energy compared to the inner-half-span configuration ( when  $C_L > 0.2$  ). The higher energy consumption for the inner-half-span configuration is probably a result of the strong cross-flow component which can be seen in Figure 6.28 (e) and Figure 6.29 on page 192(e). The cross-flow consumes additional energy and creates low pressure region on the lower side of the wing surface which further decreases lift. In Figure 6.27 , when  $C_L = 0.43$ , the inner-half-span configuration requires 59.2% more energy than the full-span configuration. Also, the slope of energy vs.  $C_L$  is steeper at this point, but the slope of  $C_L$  vs.  $C_\mu$  is flatter ( Figure 6.26 ), indicating an inefficient lift enhancement. In comparison, the full-span configuration can achieve much higher  $C_L$  with a reasonable increment in mass flow rate and energy consumption and a more uniform flow as shown in the following figures.

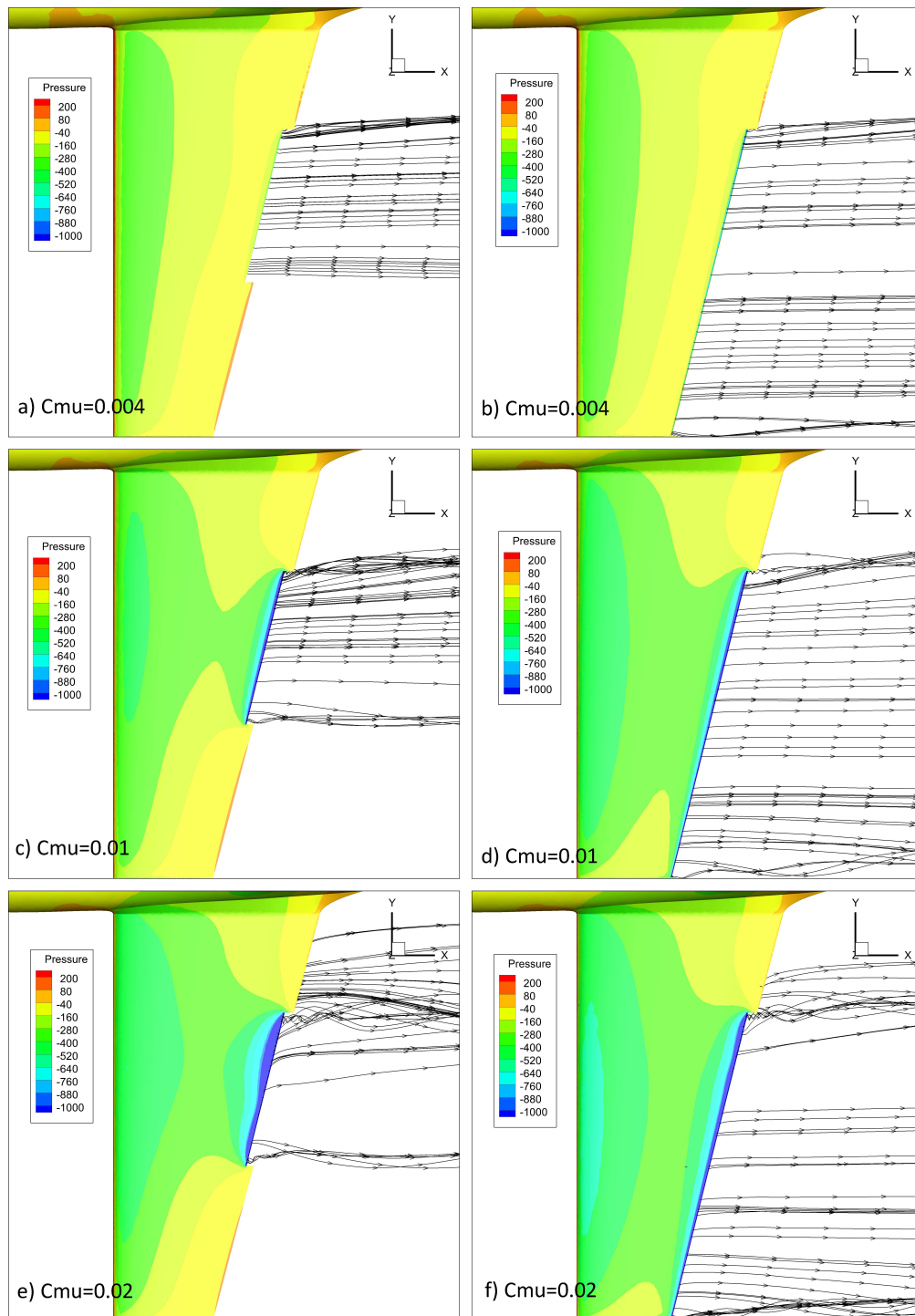


Figure 6.28: The streamlines and pressure distribution of the upper surface at  $M = 0.1$ , 33% scale Zivko Edge 540T wing-body model, (a) (c) (e): half span, (b) (d) (f): full-span.

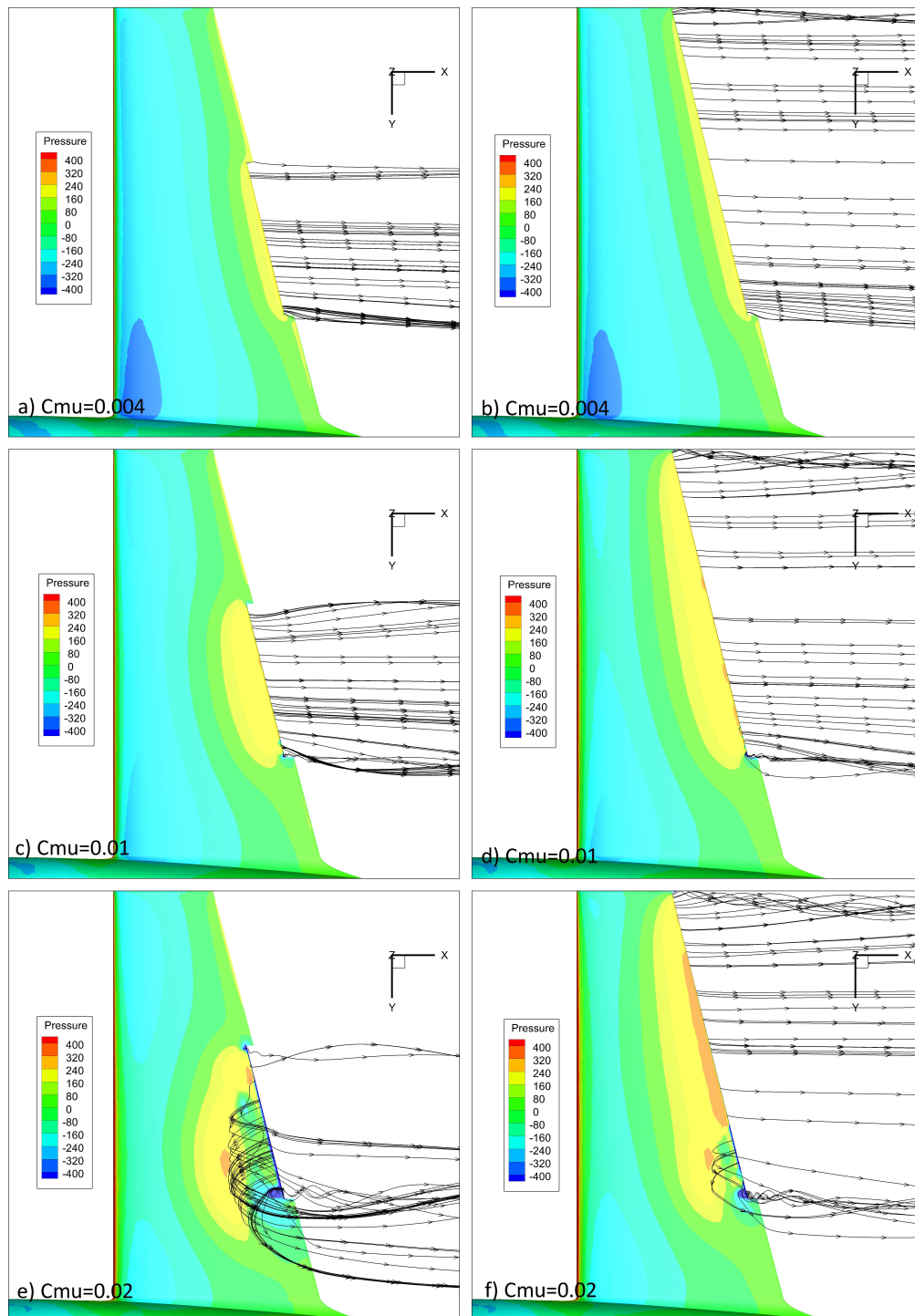


Figure 6.29: The streamlines and pressure distribution of the lower surface at  $M = 0.1$ , 33% scale Zivko Edge 540T wing-body model, (a) (c) (e): half span, (b) (d) (f): full-span.

When the blowing momentum coefficient of both configurations is lower than 0.01, the streamlines are stable and uniform, as shown in Figure 6.28 on page 191 (a)-(d). However the flow of the inner-half-span case is severely deteriorated at  $C_{\mu} = 0.022$  (Figure 6.28 on page 191-(e)). Meanwhile, Figure 6.29 shows the lower side of the wing where the spanwise flow is observed. The jet sheet at the lower side of the wing moves inbound to the fuselage which attributes to the separation and instability of the flow. Therefore the  $C_L$  of the half-span nozzle is limited. The streamlines of the full-span configuration (Figure 6.28 on page 191-(f)) also show spanwise flow, but only the streamlines close to the fuselage are directed inbound, which has a minor influence on the overall jet sheet. In conclusion, when  $C_L > 0.2$ , the full-span nozzle needs less energy compared to the inner-half-span nozzle to achieve the same  $C_L$ . The full-span nozzle produces a uniform jet sheet downstream without strong cross flow beneath the wing as found in the inner-half-span case. Hence the full-span nozzle is used in the following studies. When  $C_L < 0.2$ , both configurations have similar energy consumption, if the aircraft only requires a small  $\Delta C_L$  for gust reduction, the half-span slot is suitable since it has lower drag.

## 6.7 Simulation Results of the CC Half Wing-body Model.

### 6.7.1 Steady State CFD Results of the 3D Wing-body Model

A set of CFD simulations with the trailing edge of  $h/r=0.05$ ,  $r/c=0.01$  have been conducted at various  $C_{\mu}$  and AoA at  $M=0.1$ . Figure 6.30, 6.31, 6.32 show the  $C_L, C_D, C_M$  results of the 3D wing. The CC significantly increases  $C_L$  by 0.7-0.8, though the  $C_{\mu}$  is still at a very low level (less than 0.025). The relationship of  $C_L$  vs.  $C_{\mu}$  at different AoA is almost linear which is favourable for the controller design. Despite its efficacy, the CC shows drawbacks that it generates large drag and pitching moment, as shown in Figure 6.31 and 6.32. When deploying the CC, the thrust and elevator need to be adjusted to compensate for the additional drag and pitching moment.

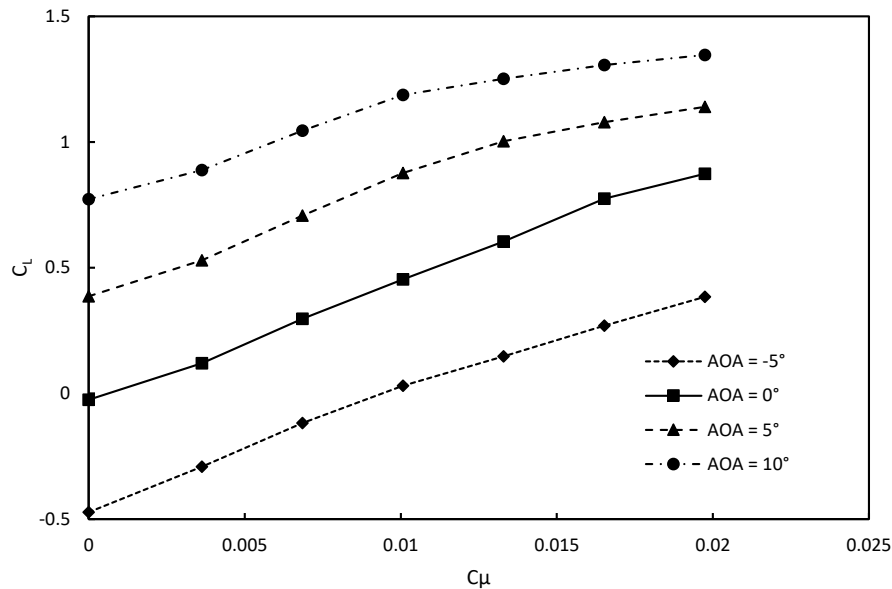


Figure 6.30: The lift coefficients of the 33% scale Zivko Edge 540T wing-body model in various AoA,  $M = 0.1$ .

It is found that with higher  $C_{\mu}$ , the jet sheet attaches to the lower surface of the wing and the streamlines are turning inward. The reason for the inward flow is probably due to the taper ratio of the wing. The jet stream is firstly turned by the Coanda surface and then stays perpendicular to the trailing edge of the wing. As the trailing edge is not perpendicular to the freestream, consequently the jet stream is not parallel to the freestream. A close view of the flow direction at the trailing edge can be found in Figure 6.37 on page 202 which will be discussed in the next section.

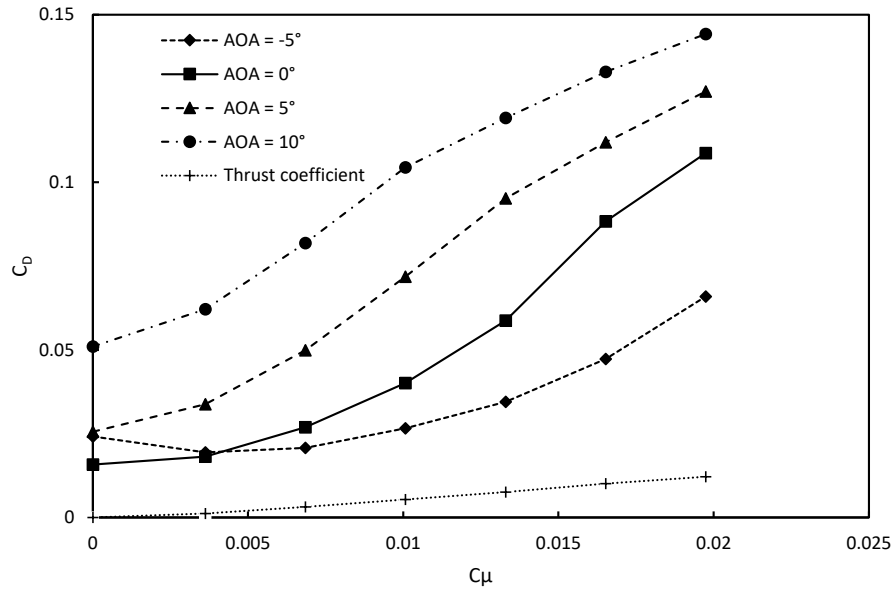


Figure 6.31: The drag coefficients and nozzle thrust of the 33% scale Zivko Edge 540T wing-body model in various AoA,  $M = 0.1$ .

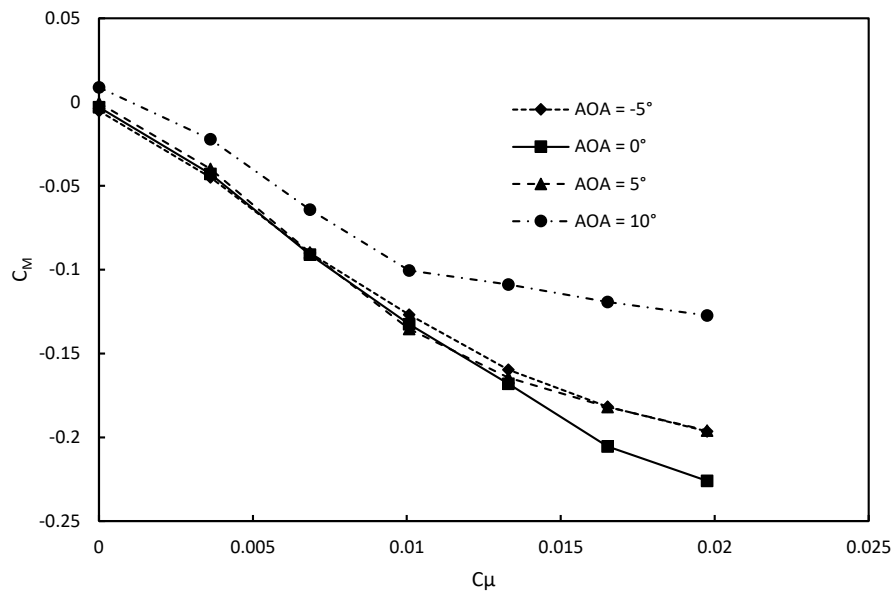


Figure 6.32: The pitch moment coefficients of the 33% scale Zivko Edge 540T wing-body model in various AoA,  $M = 0.1$ .

## 6.7. SIMULATION RESULTS OF THE CC HALF WING-BODY MODEL.

Based on the CFD results and reference (Stevens et al. 2015), a list of the variables for flight dynamics is summarised in Table 6.6. The variables are used to establish the small perturbation model provided in Section 2.5 on page 31.

Table 6.6: Parameters for the simulation of flight dynamics

Item	Nomenclature	Value
Air density	$\rho$	1.225
Weight	m	13.15
Pitch inertia	$I_y$	2.033 $m^2kg$
Mean aerodynamic chord	c	0.46m
Induced drag coefficient	$k_T$	0.08
The slope of $C_L$	$\frac{\partial C_L}{\partial \alpha}$	4.6
The slope of $C_D$ at equilibrium point	$\frac{\partial C_D}{\partial \alpha}$	0
Drag coefficient due to velocity	$\frac{\partial C_D}{\partial V}$	0
Lift curve slope of the tailplane ( $\alpha_1$ )	$\frac{\partial C_{LT}}{\partial \alpha_T}$	3.6
Lift curve slope about elevator angle ( $\alpha_2$ )	$\frac{\partial C_{LT}}{\partial \eta}$	0.5
Velocity	$V_0$	34
Wing area	$S$	1.208 $m^2$
Initial lift coefficient	$C_L$	0.15
Initial drag coefficient	$C_D$	0.01
Tailplane area	$S_T$	0.279
Tail moment arm	$l_T$	1.128m
The slope of $C_m$	$\frac{\partial C_m}{\partial \alpha}$	-1.32
Effectiveness of the CC	$\frac{\partial C_{L_{dlc}}}{\partial \eta_{dlc}}$	39.5
Drag slope of the CC	$\frac{\partial C_{D_{dlc}}}{\partial \eta_{dlc}}$	5.0
Moment slope of the CC	$\frac{\partial C_{M_{dlc}}}{\partial \eta_{dlc}}$	10.3
The rate of change of downwash angle at the tailplane with AoA	$d\varepsilon/d\alpha$	0.5

### 6.7.2 Comparisons Between 3D Wing and 2D Aerofoil

The performance of CC on a 3D wing may be reduced compared with the 2D aerofoil due to its tip effects and taper ratio. This section compares the lift performance of the 3D wing and the 2D aerofoil to better understand the effect of the spanwise flow, tip vortex, down-wash and the fuselage which are not considered in the 2D simulations.

Figure 6.33 compares the lift coefficient of the 3D wing and 2D aerofoil without blowing.

It is expected that the 2D  $C_L$  is higher due to the downwash created by the wing, considering the aspect ratio of the wing is 5.7 and there is no wingtip device on the model. However, the three-dimensionality is significant in blowing conditions. Figure 6.34 shows the comparisons at  $C_\mu = 0$  to 0.02 and two different AoA. The  $C_L$  curve of the 2D aerofoil is dramatically higher than the slope of the 3D wing.

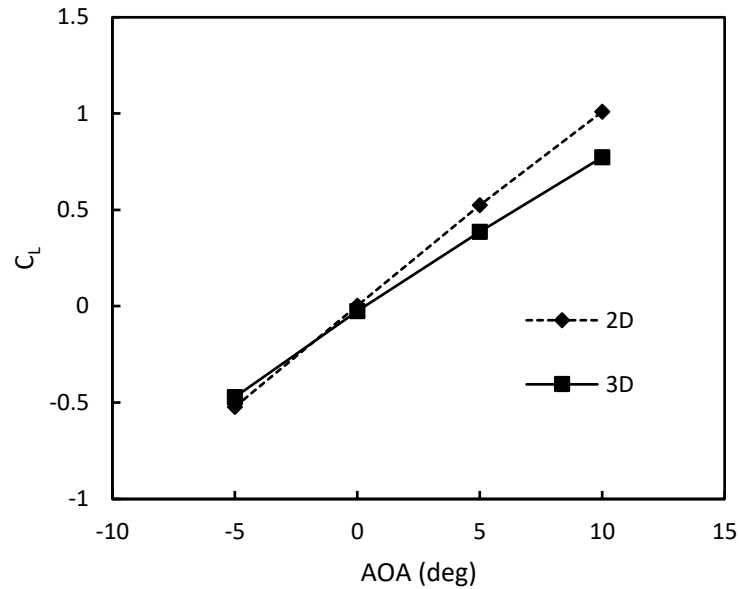


Figure 6.33: The lift coefficient of the 2D NACA0013 aerofoil and 3D tapered wing without blowing at  $M = 0.1$ .

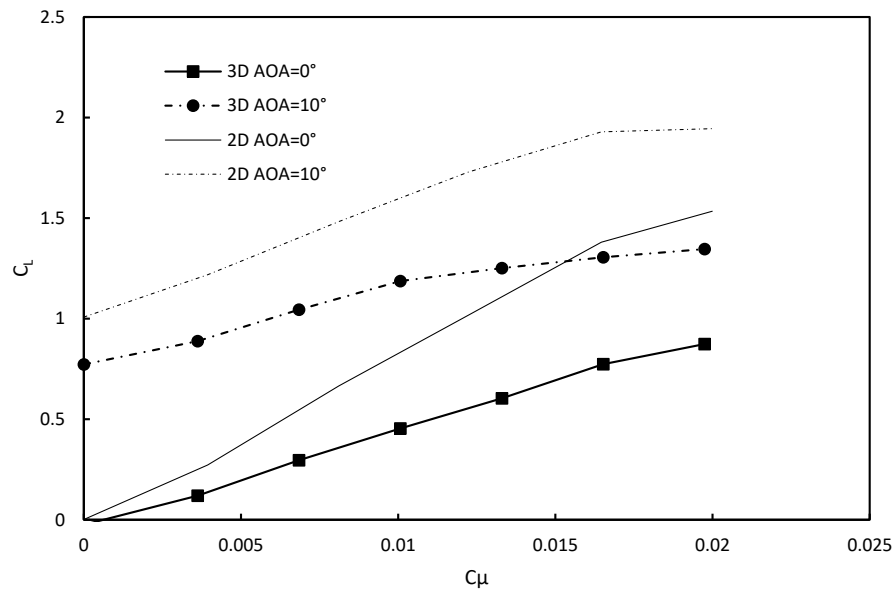


Figure 6.34: The lift coefficient of the 2D NACA0013 aerofoil and 3D tapered wing with blowing at  $M = 0.1$ .

Figure 6.35 and 6.36 on page 201 show the comparison of the 2D aerofoil and a mid-span slice of the 3D wing. From the  $C_p$  curves, it can be seen that the 2D aerofoil has a stronger suction on the upper surface close to the leading edge, this is because the 2D case has significantly higher  $C_L$ , and the front stagnation point is lower. The streamlines of the jet sheet, as shown in Figure 6.35, Figure 6.36 (c),(d), are similar, but the velocity magnitude near the jet exit of the 3D section seems to be stronger than the 2D. This is attributed to the additional spanwise flow components.

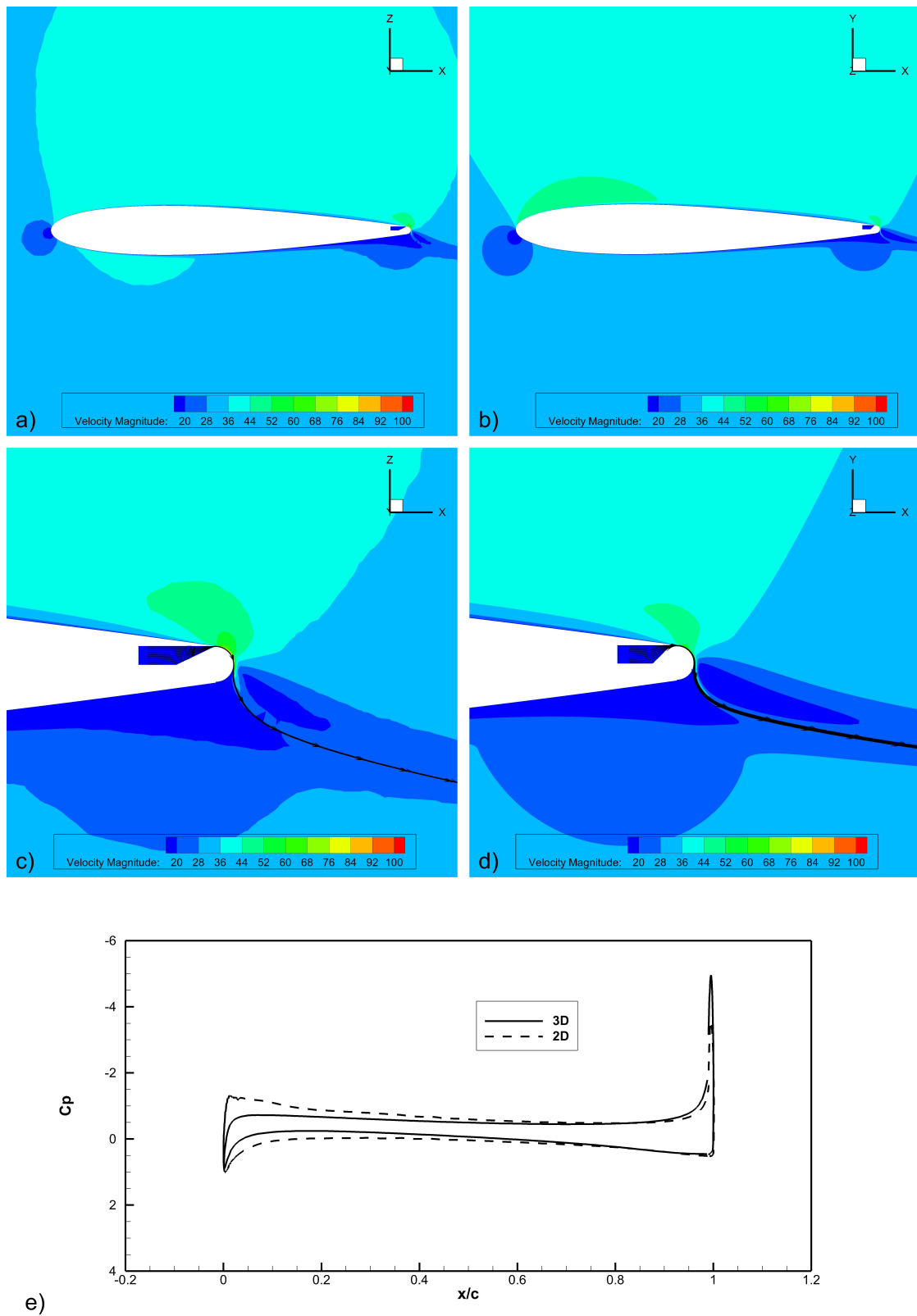


Figure 6.35: Comparison of the 2D NACA0013 aerofoil (b, d) and mid-span slice of the 3D tapered wing (a, c) at  $C_{\mu} = 0.01$ ,  $AoA = 0$ .

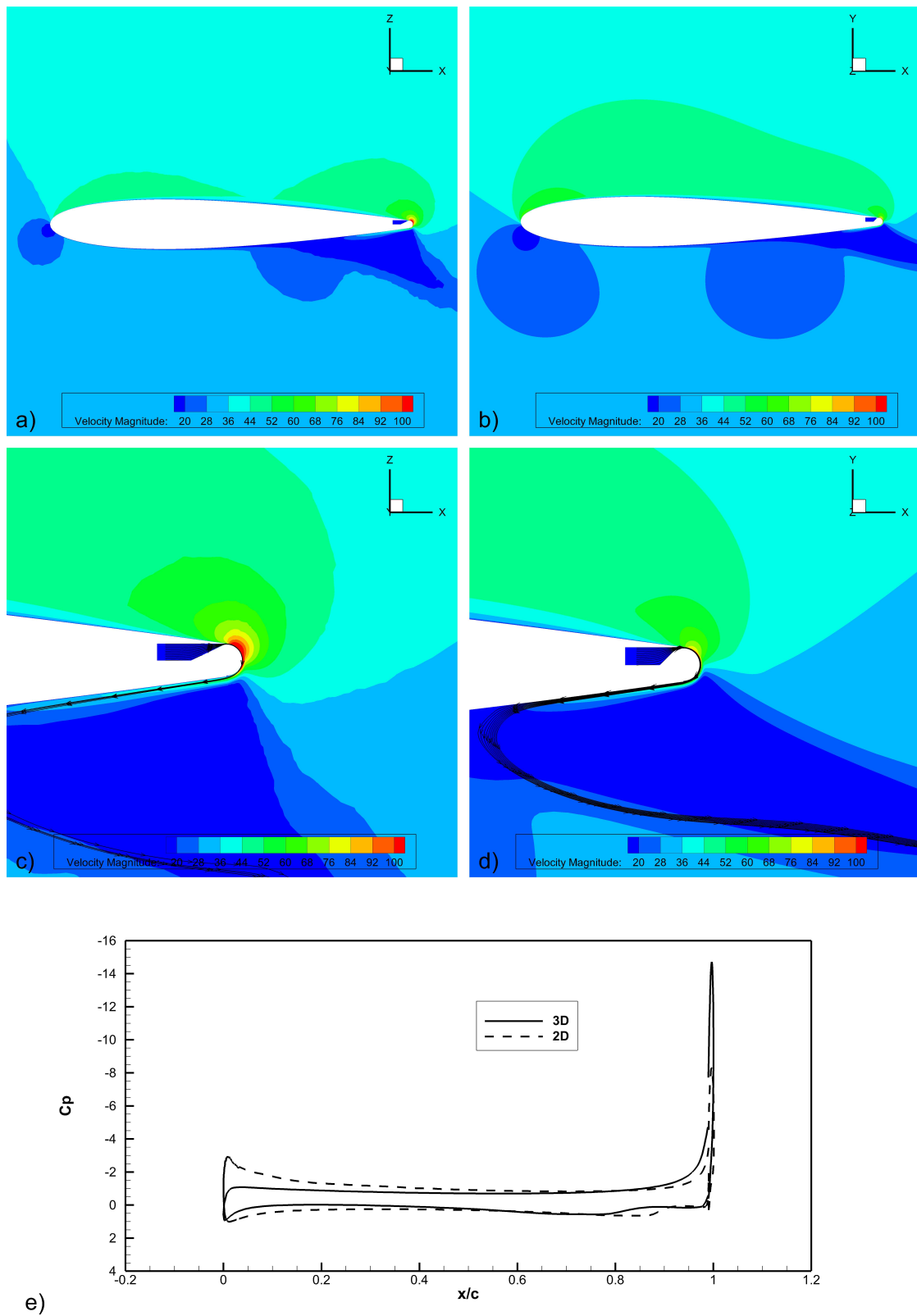


Figure 6.36: Comparison of the 2D NACA0013 aerofoil (b, d) and mid-span slice of the 3D tapered wing (a, c) at  $C_{\mu} = 0.02$ ,  $AoA=0$ .

To understand the three-dimensionality, Figure 6.37 shows the 3D streamlines of the wing at  $C_{\mu} = 0.01$  on the X-Y plane. The upper surface of the wing was set transparent so the streamlines inside the plenum chamber can be seen. Interestingly, although the direction of the velocity on the inlet boundary is the same as the free stream, the jet turns outward at the trailing edge. The direction of the flow around the Coanda surface keeps perpendicular to the axial direction of the circular surface. It is a possible explanation of the lower  $C_L$  compared with 2D aerofoil because the velocity component in the X direction is slower. Whereas at higher  $C_{\mu}$ , the jet sheet turns to the lower surface of the wing and turns inward, generating a great spanwise flow and deteriorating the lift. Also, the downwash effect by the tip vortex and the edge vortex at the wing root is another factor that reduces the  $C_L$  of the 3D wing.

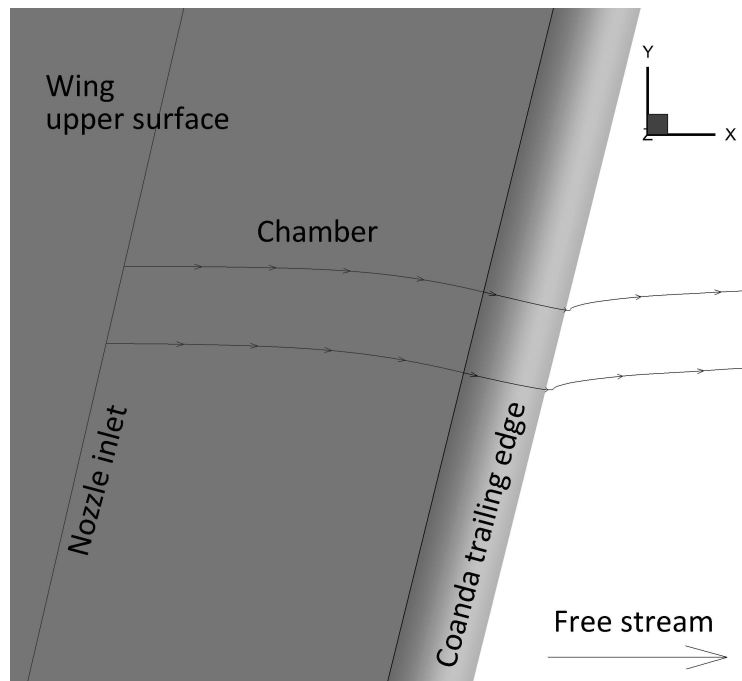


Figure 6.37: x-y plane at  $C_{\mu} = 0.012$ ,  $AoA=0$  for the 3D tapered wing.

### 6.7.3 Comparison of the CCW and the Mechanical Flap

In the current study, the spanwise length of the CC nozzle is the same as the mechanical flap on the datum model. As the CC can increase lift dramatically, only a small  $C_{\mu}$  is needed to generate an equivalent lift to the mechanical flap. Figure 6.38 compares the  $C_L$  of mechanical flap and CC. The input parameters of both methods are different so the horizontal axis is set to  $C_L$  to compare the input requirement. The first vertical axis is the flap deviation angle and the secondary vertical axis is the input  $C_{\mu}$  of CC. It can be seen that the maximum  $C_L$  of the mechanical flap is 0.55 at  $25^\circ$  while the CC creates the same  $C_L$  at only  $C_{\mu} = 0.015$  which is much lower than its maximum  $C_L$ . Figure 6.39 shows the drag polar of the mechanical flap and CC, CC creates a slightly higher drag when  $C_L < 0.5$ . Subsequently, the mechanical flap is stalled and the  $C_D$  of CC is increasing linearly. Figure 6.40 shows the pitching moment in which the CC creates a higher  $C_M$  than the mechanical flap by around 30% for the same  $C_L$ .

For the application of gust loading reduction in this study, obviously, the CC has a higher control authority and should therefore be able to compensate for severe turbulence or gust loading compared with a mechanical flap. Meanwhile, the CC creates a higher pitching moment which would need to be compensated by the elevator.

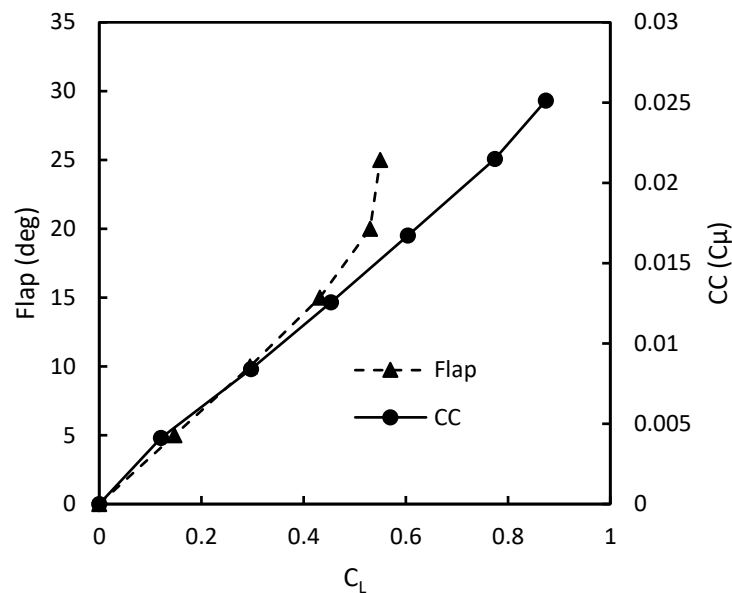


Figure 6.38: The  $C_L$  of the 3D tapered wing with modified CC trailing edge and the original mechanical flap of the 33% scale Zivko Edge 540T at  $M = 0.1$ ,  $AoA=0^\circ$ ,  $C_{\mu} = 0 - 0.02$

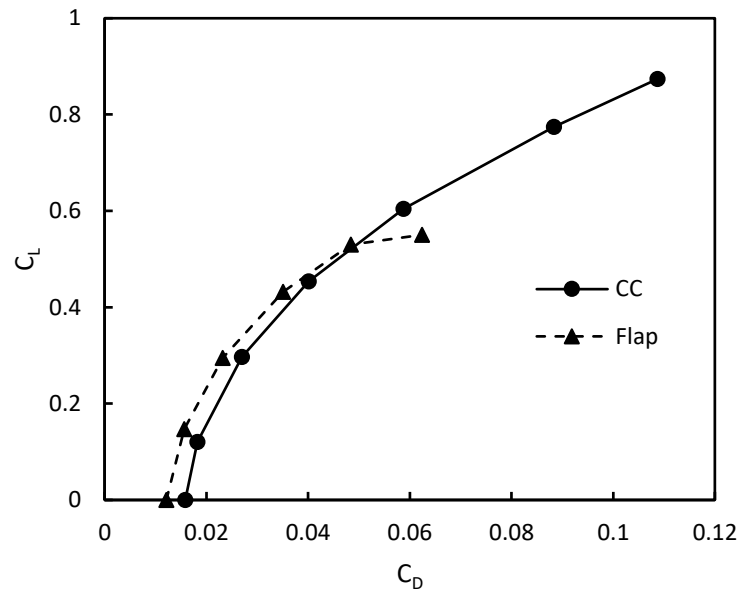


Figure 6.39: The drag polar of the 3D tapered wing with modified CC trailing edge and the original mechanical flap of the 33% scale Zivko Edge 540T at  $M = 0.1$ ,  $AoA=0^\circ$ ,  $C_\mu = 0 - 0.02$

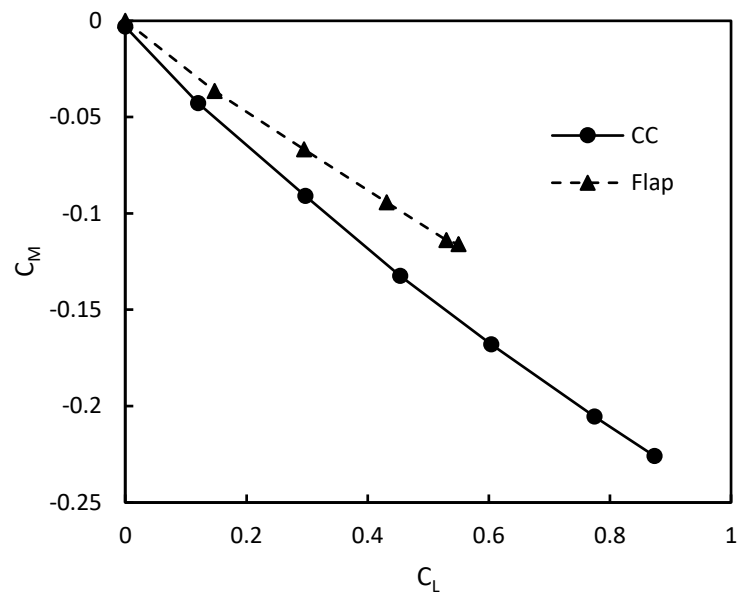


Figure 6.40: The  $C_M$  of the 3D tapered wing with modified CC trailing edge and the original mechanical flap of the 33% scale Zivko Edge 540T at  $M = 0.1$ ,  $AoA=0^\circ$ ,  $C_\mu = 0 - 0.02$

## 6.8 Summary

In this chapter, a datum aircraft was used to validate the simulation results. The geometry used in the simulation has a wing, flap, and fuselage. The propeller, undercarriage and tail were removed to simplify the simulation.

The second section of this chapter was to study the trailing edge shape for CC, consequently, this shape was used in the 3D geometry of the aircraft. Then the geometry with a modified CC trailing edge was meshed and simulated. An additional study was conducted to compare the efficiency of half-span CC and full-span CC configurations.

Due to the three-dimensionality of the wing, there was a strong spanwise flow that caused unique unsteady vortices. Such vortices were also investigated in this chapter. The results suggested that a thicker trailing edge can eliminate the unsteady vortices with a more consistent separation point.

Finally, the simulation results of the 2D and 3D CC wing, as well as with the mechanical flap were compared and analysed. Following the equations provided on Page 157, the results obtained in Section 6.7.1 on page 194 are used as static derivatives to complete the small perturbation aircraft model presented in Chapter 2.

# Chapter 7:

## The Dynamic Performance of CC

The previous chapter provides steady state simulation of the aircraft with CC. A dynamic model is therefore required to design a controller. This chapter investigates the dynamic performance of the CC aerofoil. Firstly a time step sensitivity study is conducted. Then the flow field at different time is recorded and analysed. Subsequently, the step responses in various flow conditions are compared. Finally, a dynamic model is provided for the controller design in the next chapter.

### 7.1 2D Step Response of the CC Flap

From the dynamic point of view, uncertainty still exists about the factors that affect the dynamic response. It is also difficult to find experimental data for validation as there is little related research, to the best of the author's knowledge. This research is based on the numerical simulation and the solver settings affect the dynamic results. Therefore, similar to Chapter 5, an essential first step is to find out the effect of time step size. The initial condition is  $M=0.1$  with  $AoA = 0^\circ$  and no CC blowing. This condition was running in CFD for a period of iterations (10000 time steps) until it converged and the lift was constant. Initially, a fully converged steady state solution is obtained. Then a step signal was applied to the inlet of the plenum chamber, where the nozzle pressure ( $P_{LJ}$ ) was raised from 0 to 10kPa. From this point onwards, the time history of the  $C_L$  was recorded and is presented in Figure 7.1 using different time steps. These show that a smaller time step results in a faster step response of the lift coefficient. When the time step is less than 0.00001s, the step response curve no longer changes and is independent of the time step, as shown in Figure 7.1 . Therefore the following study of the dynamic response uses a time step setting of at least 0.00001s which is equivalent to  $7.4 \times 10^{-4}c/U_\infty$ . This time step is similar to that reported by Notger Heinz et al., which was  $2.1 \times 10^{-3}c/U_\infty$  (Heinz, King, Höll, Wassen & Thiele 2010) in a similar study.

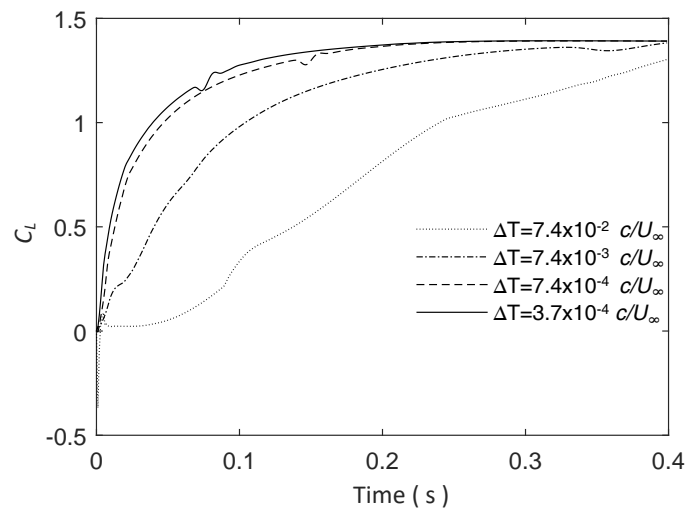


Figure 7.1: Step response of  $C_L$  when  $P_{t,J}$  increased by 10kPa, for the modified TE NACA0013 with various time step settings from  $10^{-3}$ s ( $7.4 \times 10^{-2}c/U_\infty$ ) to  $5 \times 10^{-6}$ s ( $3.7 \times 10^{-4}c/U_\infty$ ) at AoA=0,  $M = 0.1$  and 10 inner iterations per time step.

## 7.2 Flow Field in Different Phase

The step response of the lift in the previous result indicates that the CC is non-linear. As shown in Figure 7.2, there is a rapid increase in  $C_L$  at the beginning, then the rate of change reduces until a drop occurs at  $T=0.15s$ , and eventually,  $C_L$  reaches the desired level. Figure 7.2 also shows the velocity at the centre of the nozzle exit. A steady nozzle jet velocity is established almost instantly when a step input is applied. In comparison, the response of the  $C_L$  is much slower, which indicates the time lag of the  $C_L$  is mainly caused by the re-distribution of the flow around the aerofoil, not by the flow inside the plenum chamber.

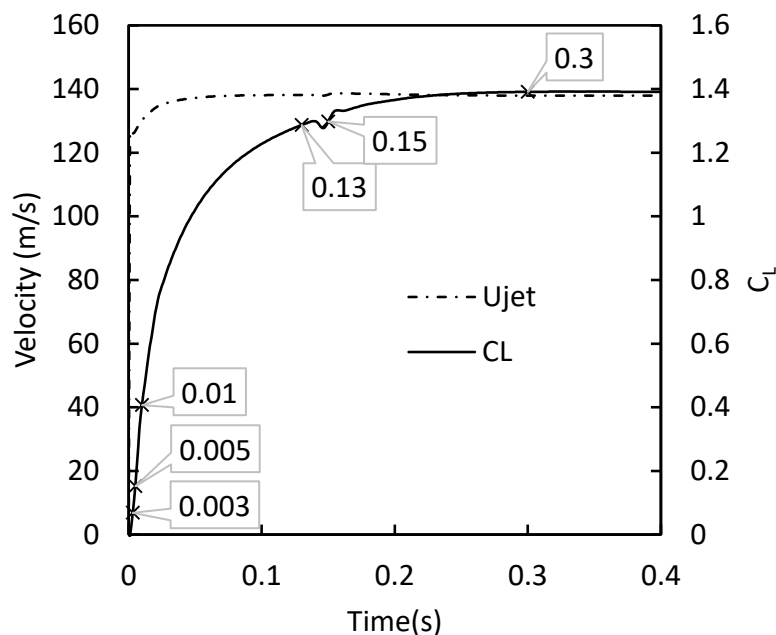


Figure 7.2: Step response of  $C_L$  and jet velocity on the nozzle exit when  $P_{t,J}$  increased by 10kPa, for the modified TE NACA0013, plenum pressure rises from 0Pa to 10kPa at  $T=0s$ .

Further investigation is required to study the flow field development. Therefore 6 frames of flow field have been recorded, as shown in Figure 7.3. It is apparent that the jet sheet attaches to the trailing edge very quickly as soon as the step input is applied, as shown in  $T=0.003s$ ,  $T=0.005s$  and  $T=0.01s$  frames in Figure 7.3. However, during this period, the pressure contours around the upper and lower surfaces of the aerofoil do not show any significant changes. This is also evident from the pressure distribution curves in Figure 7.4 on page 210, noting that the left part of the  $T=0.003s$  and the  $T=0.005s$  curves are almost the same, which means that the pressure distribution near the leading edge is not affected by the trailing edge before  $T=0.005s$ .

From  $T=0.01s$  to  $T=0.13s$ , the separation point where the jet stream separates from the

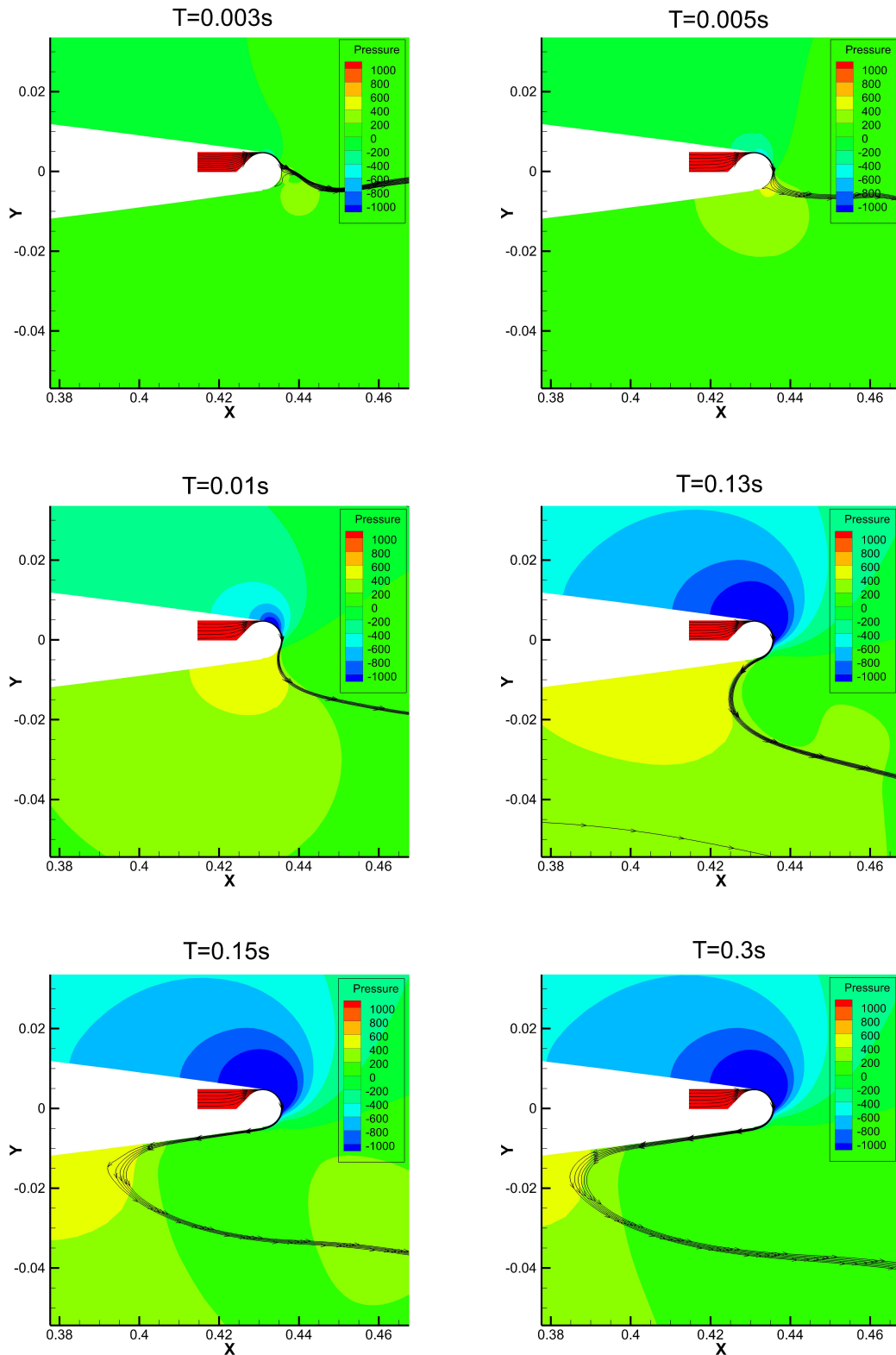


Figure 7.3: Phases of the flow field and streamlines at different stages when  $P_{tJ}$  increased by 10kPa, for the modified TE NACA0013,  $M = 0.1$ ,  $AoA = 0$ .

trailing edge moves downward for only a short distance. But the direction of the airflow subsequently reverses to flow ahead of the trailing edge with a significant downward curvature, as

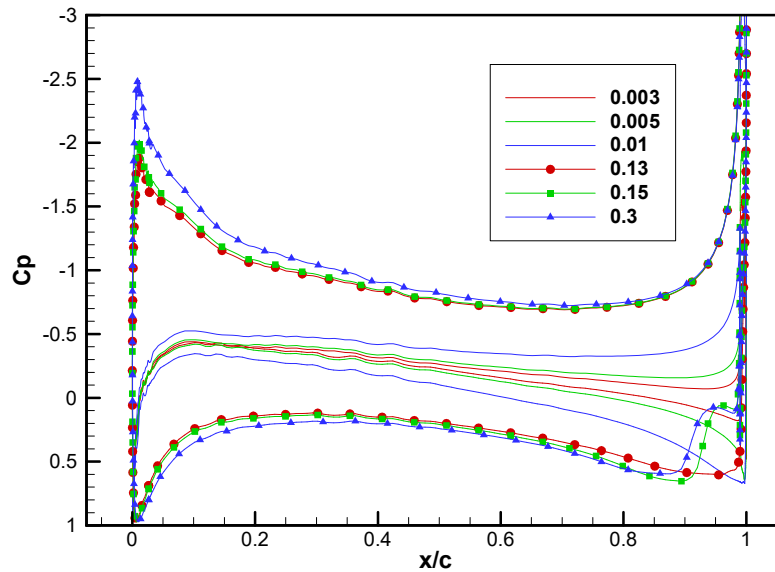


Figure 7.4: The pressure distribution of different phases when  $P_{t,j}$  increased by 10kPa, for the modified TE NACA0013,  $M = 0.1$ ,  $AoA = 0$  ( Legend: time in seconds ).

shown in the streamlines of  $T=0.01s$  and  $T=0.13s$  from Figure 7.3 . The pressure distribution also changes notably from  $T=0.01s$  to  $T=0.13s$ , as shown in Figure 7.2 on page 208, 64% of  $C_L$  is built up during this period.

From  $T=0.13s$  to  $T=0.15s$ , there is a small drop in the  $C_L$  in Figure 7.2 on page 208. This could be explained by the fact that the jet stream attaches to the bottom of the aerofoil within a short time, as shown in Figure 7.3 . In the  $T=0.13s$  frame, the separation point of the jet stream is at the bottom of the trailing edge. Then it rapidly slides forward to the lower surface of the aerofoil, which is shown in the  $T=0.15s$  frame. Moreover, the  $T=0.15s$   $C_p$  curve in Figure 7.4 indicates there is a significant 'step' on the lower surface close to the trailing edge, which is not seen in the  $T=0.13s$  curve. This 'step' is a low pressure zone, caused by the high-speed jet being attached to the lower surface, it contributes to the  $C_L$  drop at  $T=0.13s$ . After  $T=0.15s$ , the  $C_L$  recovers and the overall  $C_L$  is still rising towards a new equilibrium state. The 'low-pressure zone' has no influence on the trend of the curve.

From  $T=0.15s$  to  $T=0.3s$ , the shape of the jet stream roughly remains consistent. Also, it can be seen from the  $C_p$  curves in Figure 7.4 that the step on the lower surface curve moves forward from  $T=0.15s$  to  $T=0.3s$ , which indicates that the separation point slides forward. From the  $C_p$  curves of  $T=0.15s$  to  $T=0.3s$  on the upper surface, the front suction peak rises, but the aft pressure remains the same profile.  $C_L$  rises less than 10% in this period and approaches the steady state.

Figure 7.5 is a schematic of the stages of the step response, which summarises the devel-

opment of the flow. The step input of pressure on the plenum chamber generates a jet stream from the nozzle. This jet stream first attaches to the Coanda trailing edge in a short period of time, which is shown in stage (a). During stage (a), the pressure distribution close to the leading edge roughly remains steady, but there is a significant change in the pressure distribution close to the trailing edge. The maximum rate of increase in  $C_L$  appears in stage (a). During stage (b), the overall pressure distribution changes simultaneously, but the rate of increase of the  $C_L$  is lower and non-linear. However, stage (b) contributes most of the lift increment. The following stage (c) starts with a drop of the  $C_L$  caused by the jet stream attaching to the lower surface of the aerofoil. Then the shape of the jet stream remains roughly consistent, and the  $C_L$  rises until it is equivalent to the steady state. Stage (c) contributes very little further lift increment. In summary, the Coanda jet first affects the flow field around the trailing edge, then gradually affects the overall pressure distribution. Finally, the flow field near the trailing edge remains unchanged, but the pressure distribution near the leading edge keeps changing until it reaches a steady state.

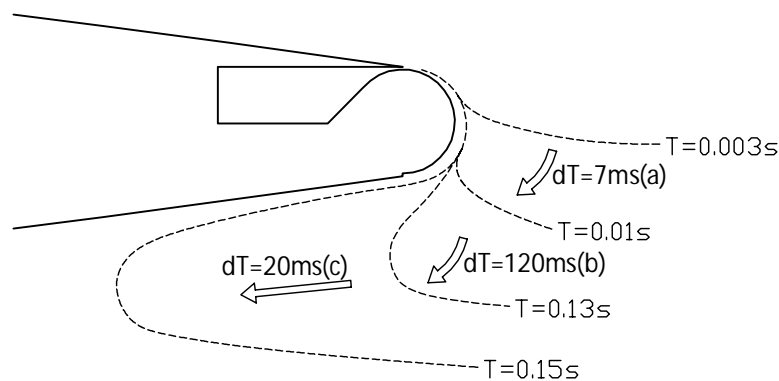


Figure 7.5: The schematic of the jet stream variation on different phases, when  $P_{t,J}$  increased by 10kPa, for the modified TE NACA0013,.

As a non-linear system, it is also important to study the lift response when the blowing is switched off because it might be different from switching on, which is the hysteresis effect. Firstly the chamber pressure was defined as 10kPa, and the steady CFD case was converged and run for two physical seconds. Then the chamber pressure was stepped down to 0Pa, and the subsequent unsteady flow was simulated to record the variation of the lift and nozzle velocity. As shown in Figure 7.6, it is apparent that the velocity on the jet nozzle and the  $C_L$  both reduce very fast from the beginning. The velocity drops to zero at  $T=0.04s$ , whereas the  $C_L$  drops 0.78 within 0.03s, compared with the previous response (when blowing starts), where the  $C_L$  rises by 0.84 in 0.03s.

Four frames of the flow field have been recorded, as shown in Figure 7.7 on page 213. The

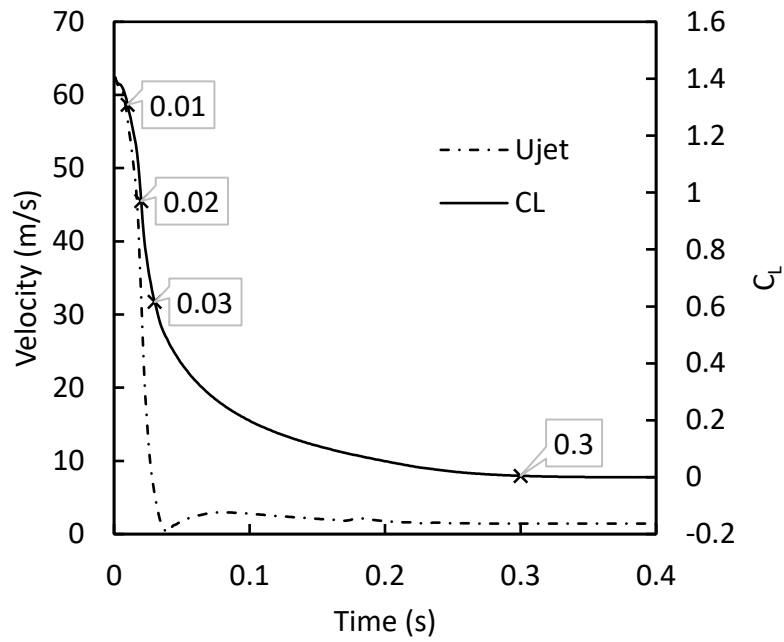


Figure 7.6: Step response of  $C_L$  and jet velocity on the nozzle exit, when  $P_{t,J}$  drops from 10kPa to 0Pa at  $T=0s$ , for the modified TE NACA0013.

jet stream is attached to the lower surface at  $T=0.01s$  but then immediately separates after the  $T=0.02s$  frame. Although in a short period of time, the flow field around the trailing edge changes significantly from  $T=0.01s$  to  $T=0.03s$ . But from  $T=0.03s$  to  $T=0.3s$ , there is a very small difference around the trailing edge.

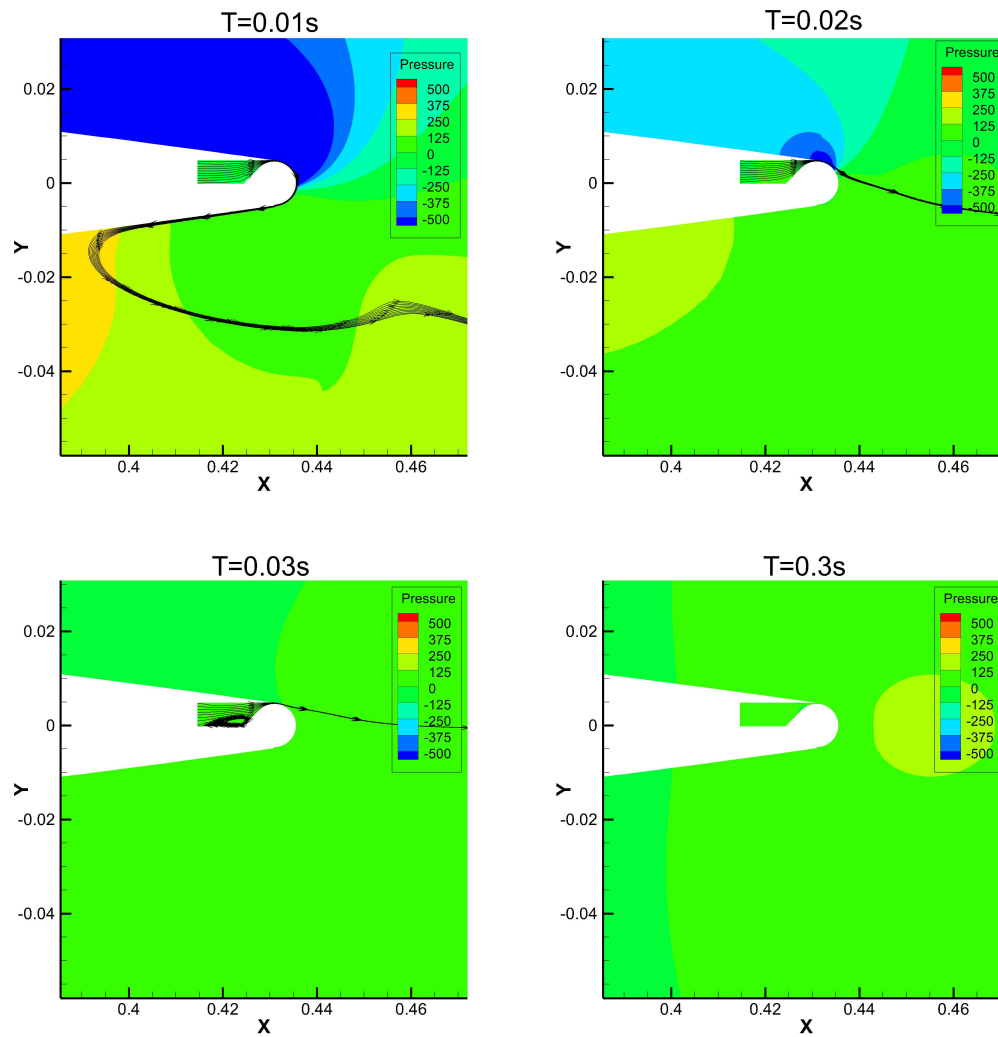


Figure 7.7: Phases of the flow field and streamlines at different stages when  $P_{t,J}$  drops from 10kPa to 0Pa at  $T=0s$ , for the modified TE NACA0013.

Figure 7.8 shows the pressure distribution in different frames. After switching off the blowing, the pressure near the trailing edge reduces at first, which can be seen from the  $T=0.01s$  and  $T=0.02s$  curves in Figure 7.8. Then from  $T=0.03s$  to  $T=0.3s$ , the pressure distribution near the leading edge gradually reaches a steady state. The flow field development is similar to the previous rising case, with the jet stream firstly affecting the trailing edge region, and subsequently, the front region is affected.

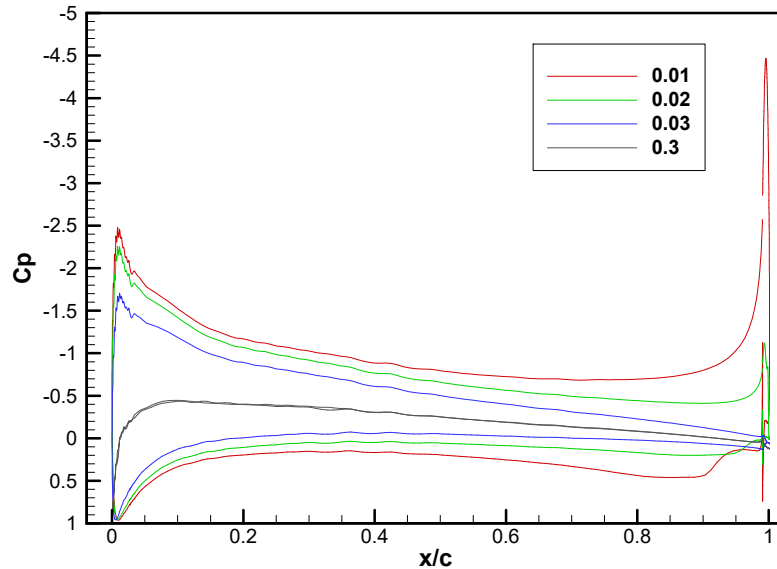


Figure 7.8: The pressure distribution of different phases when  $P_{tJ}$  drops from 10kPa to 0Pa at  $T=0s$ , for the modified TE NACA0013 ( Legend: time in seconds ).

As shown in the step response results, the lift increment is smooth at the beginning of the step signal when the separation point is on the Coanda surface. As the separation point moves to the lower surface of the aerofoil, as shown in  $T=0.13s$  and  $T=0.15s$  in Figure 7.3 on page 209, the lift curve shows a 'bump', since the separation point is quickly marching forward. Therefore when the CC is used for gust alleviation, it is better to regulate the chamber pressure to keep the separation point on the Coanda surface to avoid the lift 'bump', which could otherwise introduce disturbance to the aircraft. In addition, the lift response seems slower for higher chamber pressure which will be discussed later ( see Figure 7.13 on page 219 - 8.6kPa ). However, this is probably dependent on the aerofoil geometry. For example, there is no 'bump' in the time history of lift in Friedman's results (Friedman et al. 2016), and the response speed is not sensitive to different chamber pressure ( or  $C_{\mu}$  ). This is discussed in Section 7.3.4 on page 226.

## 7.3 Factors of the Dynamic Response of CC

Many factors affect the dynamic response. This section describes a parametric investigation to extend the knowledge and understanding of the critical parameters in the dynamic process of CC. The parameters interested in this study are as follows.

- Study the time history  $C_L$  curve with different mesh densities.
- Investigate the influence of the free stream Mach number on the response speed of the CC.
- Investigate the step response of the CC aerofoil with different trailing edges and nozzle heights.
- Investigate the step response of different nozzle pressure.

### 7.3.1 Mesh Density

A mesh independence study for steady cases can be achieved by monitoring the lift while increasing the mesh size. Similarly, to obtain a mesh-independent dynamic response, the time history  $C_L$  is monitored as a dominant factor. Five meshes were prepared with cell counts ranging from 0.075 million to 0.42 million. These cases were all run for one second without blowing, and then a nozzle pressure of 10kPa was applied on the boundary condition from  $T=0s$ , and the time step used was 0.00001s. The time history curves are shown in Figure 7.9 . There is no significant difference between the different mesh densities, and the settling time is roughly the same. From Figure 7.9 , the slope of the five curves is similar initially. Then at around  $T=0.1s$ , the  $C_L$  rate of increase is lower for the finer mesh. At  $T=0.1s$ , the jet is attached to the trailing edge, and the pressure around the aerofoil changes simultaneously. This can be seen in Figure 7.4 on page 210, from  $T=0.01$  to  $T=0.13$ . As the changing of the flow field involves all the mesh around the aerofoil, therefore the mesh density has a stronger impact at this stage. At the point after  $T=0.2s$ , all the meshes reach the same  $C_L$ , which means the overall settling time is the same even with various mesh densities.

### 7.3.2 Freestream Velocity Effect

When the blowing jet changes abruptly, it is likely that the settling time is related to the freestream velocity. This indicates a need to understand the influence caused by various Reynolds numbers. Firstly a few steady state cases were simulated, and the relationship between the  $C_L$  and the nozzle pressure under different Mach numbers were recorded as shown

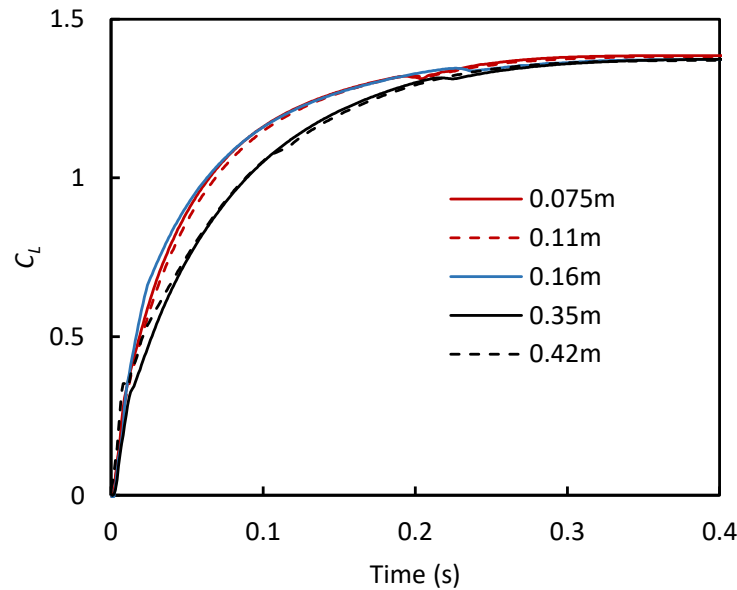


Figure 7.9: Lift response with different mesh, when  $P_{tJ}$  rises from 0Pa to 10kPa at  $T=0s$ , for the modified TE NACA0013.

in Figure 7.10 . At the higher freestream velocity, the  $C_L$  achieved is much lower with the same nozzle pressure. For a higher Mach number, the differential velocity between the jet and freestream is smaller, which affects the separation point of the jet. Also, the boundary behaviour might be different with higher freestream velocity.

To compare the lift response with the same  $C_L$  increment, the  $C_L$  curves in Figure 7.10 are interpolated to find the correct nozzle pressure setting for a 0.3  $C_L$  increment. The nozzle pressure settings are 2.68kPa, 7.43kPa and 13.9kPa for freestream Mach numbers 0.1, 0.2 and 0.3, respectively. The step response results are shown in Figure 7.11 . The time was normalised to convective time ( $t*U_\infty/c$ ) to compare the response curve under the same scale. It is apparent that the step responses of different Mach numbers are very similar, and there is only a slight difference for the initial slope. This means the dynamic response of CC is not significantly affected by the Mach number at low speeds.

### 7.3.3 Nozzle Pressure Effect

The relation between nozzle pressure and the  $C_L$  in the steady state has been investigated in the previous chapter. The steady state  $C_L$  curve and the previous step response curve both show strong non-linearity. Generally, the lift rises faster at the beginning and then slows down after the jet stream attaches to the lower surface of the aerofoil. Therefore it is necessary to explore the dynamic characteristics at different stages during the development of the Coanda

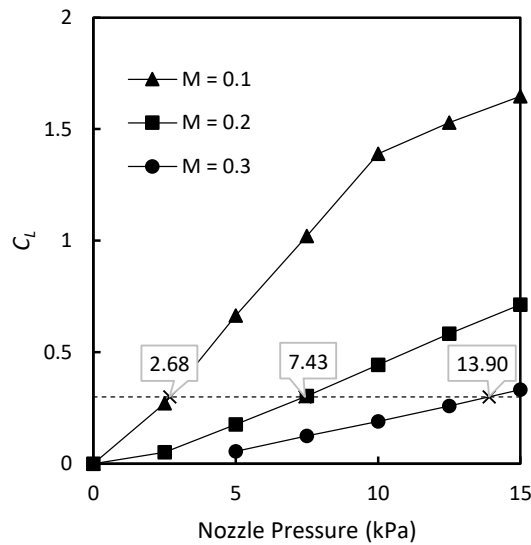


Figure 7.10: Steady state  $C_L$  vs. nozzle pressure with different Mach number for the modified TE NACA0013.

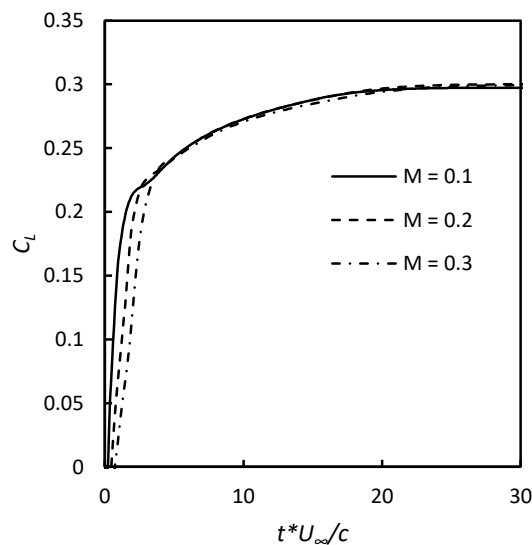


Figure 7.11: The step response for a  $C_L$  increment of 0.3 under different Mach number.  $M = 0.1$  ( $Re = 1.04 \times 10^6$ ),  $M = 0.2$  ( $Re = 2.07 \times 10^6$ ),  $M = 0.3$  ( $Re = 3.11 \times 10^6$ ), for the modified TE NACA0013.

jet.

The nozzle pressure determines the separation position of the jet stream. The jet stream separates early from the trailing edge when the nozzle pressure is lower. According to the previous step response study, the  $C_L$  rises very fast when the separation point is on the Coanda surface of the trailing edge. Whereas the jet stream attaches to the lower surface of the aerofoil

when the nozzle pressure is high, and the jet sheet has a large  $C_{\mu}$ . In this situation, the lift response is slower. To compare the lift response with various initial nozzle pressure, the  $C_L$  vs. nozzle pressure curve was interpolated and equally divided by  $\Delta C_L = 0.2$ , as shown in Figure 7.12. According to the interpolated curve, the initial pressure settings in the nozzle are 0kPa, 3.3kPa, 6kPa, and 8.6kPa, respectively, and these four cases were running for 1 physical second to converge. Then a  $C_L$  increment of 0.2 was used as a target output, and the nozzle pressure in each case increased to the corresponding value to 2kPa, 4.6kPa, 7.4kPa, 10.1kPa respectively to achieve the  $\Delta C_L = 0.2$  increment.

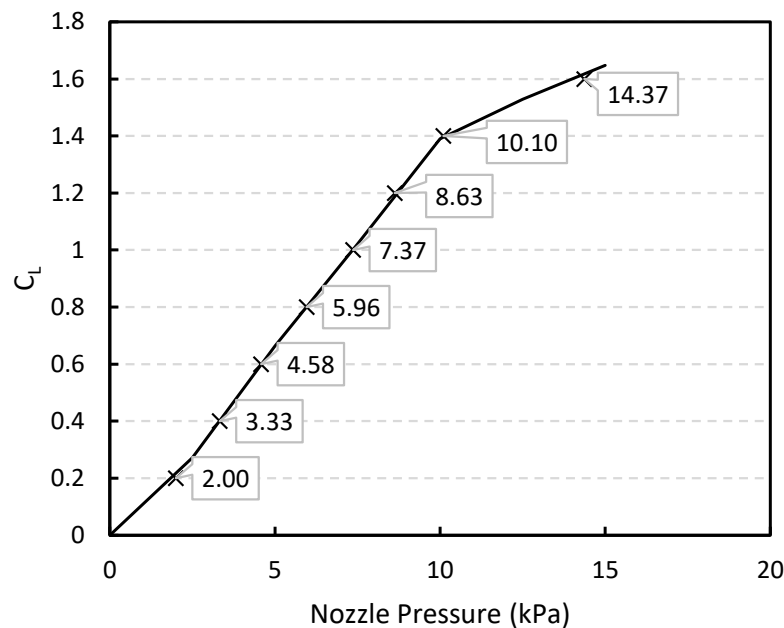


Figure 7.12: The  $C_L$  versus nozzle pressure at  $M = 0.1$ ,  $AoA=0^\circ$ , for the modified TE NACA0013, the data labels show exact values on the x-axis.

Figure 7.13 presents the step response with different initial pressure ( $P_{tJ}$ ), the lift is normalised between the initial value  $C_{L0}$  and the final steady state value  $C_{Lss}$  when the flow field is stabilised. The 0kPa and 3.3kPa cases are both at stage (a), according to Figure 7.4 on page 210. The 6.0kPa case is at stage (b), and the 8.6kPa case is at stage (c). Apparently, the step response at stage (a) shows a steep rise from the beginning, while the 8.6kPa case in stage (c) is slower, and the lift drops at  $T=0.1s$ , which is similar to the previous step response when the jet attaches to the bottom. However, there is no difference in the final settling time of the four cases.

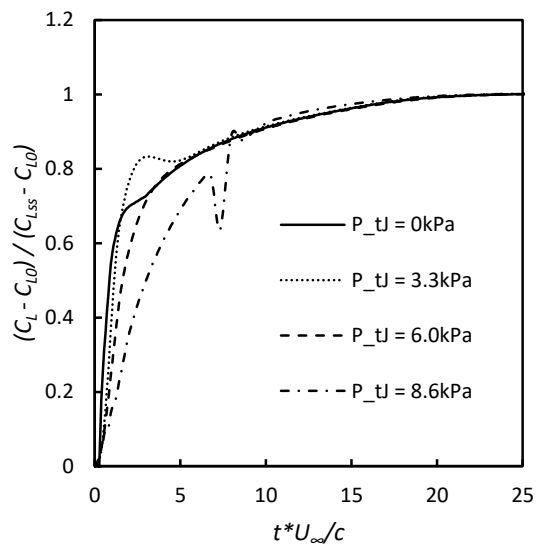


Figure 7.13: Step response of the  $C_L$  in different  $P_{tJ}$ , for the modified TE NACA0013 at  $M = 0.1$ ,  $AoA = 0^\circ$ .

### 7.3.4 Trailing Edge Shape

There is evidence to show that the trailing edge configuration of the CC aerofoil influences the performance of the lift augmentation. (Golden & Marshall 2010). This section demonstrates how the trailing edge shape affects the dynamic response and illustrates the flow field with various configurations at different stages.

The flow field of different configurations are compared in Figure 7.14 , 7.15 on page 222, 7.16 on page 223, 7.17 on page 224, 7.18 on page 225. When applying the same step input signal from 0Pa to 10kPa, the rate of  $C_L$  increase for the different configurations is different. The configurations that achieve a better  $C_L$  enhancement (the  $h/r=0.005$ ,  $r/c=0.02$  and the  $h/r=0.1$ ,  $r/c=0.01$ ) also produce a faster increasing rate of lift. Another interesting finding is that the configurations with a larger  $h/r$  ratio are not stable in the step response, as shown in Figure 7.19 on page 226, the time history  $C_L$  curves of the  $h/r=0.1$ ,  $r/c=0.01$  and the  $h/r=0.1$ ,  $r/c=0.005$  are not smooth at  $T=0.05s$ . These unstable  $C_L$  curves may be due to the unsteady movement of the separation point of the jet flow or the vortex shedding from the wake. As shown in Figure 7.17 on page 224 ( $T=0.05s$ ), the separation points are on the lower surface of the aerofoil where the jet flow penetrates to the free stream and contributes to the instability.

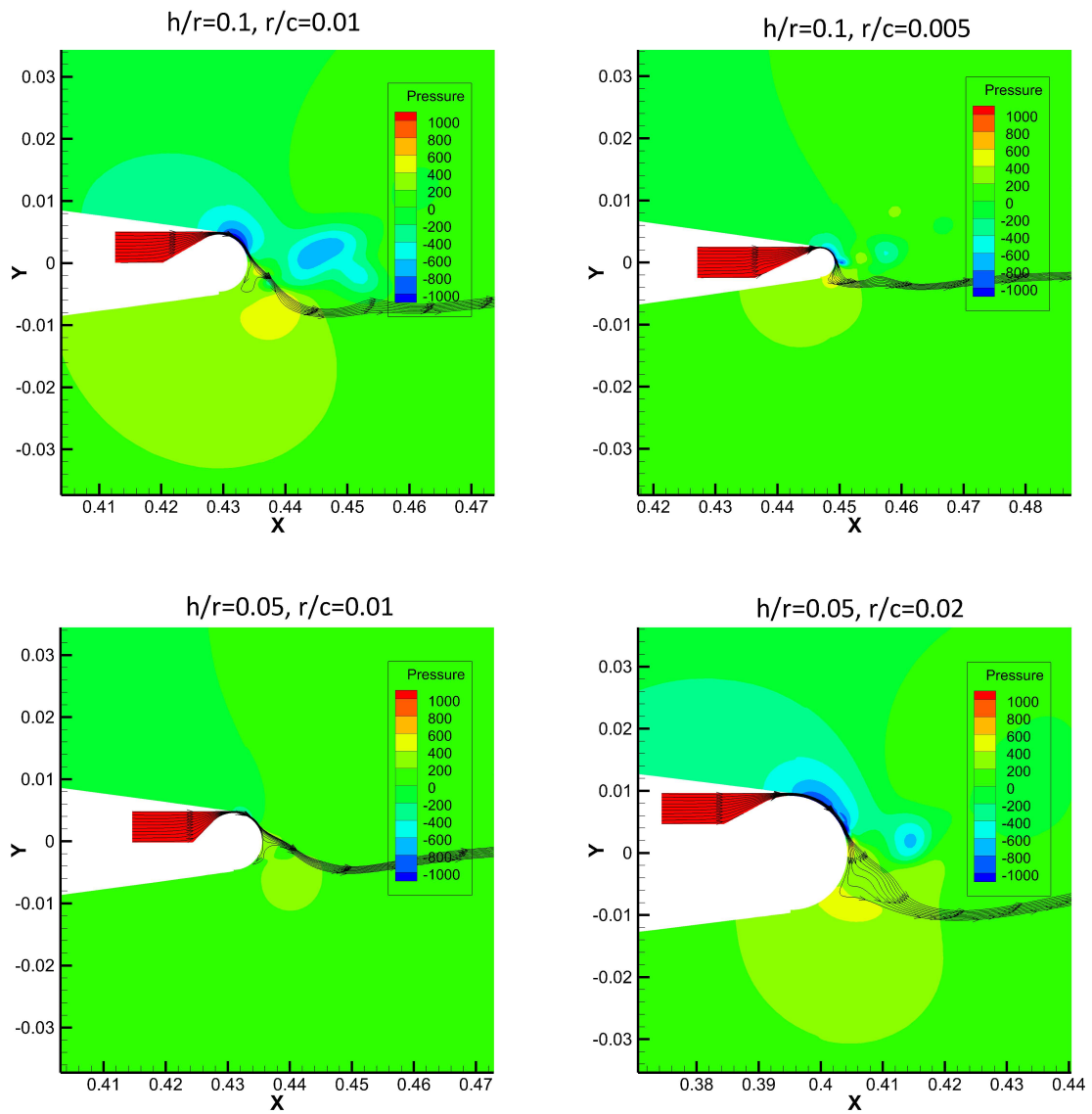


Figure 7.14: The flow field of different TE configurations at  $T=0.003s$ , when  $P_{t,J}$  rises from 0Pa to 10kPa, at  $T=0s$ ,  $M = 0.1$ ,  $AoA=0^\circ$ .

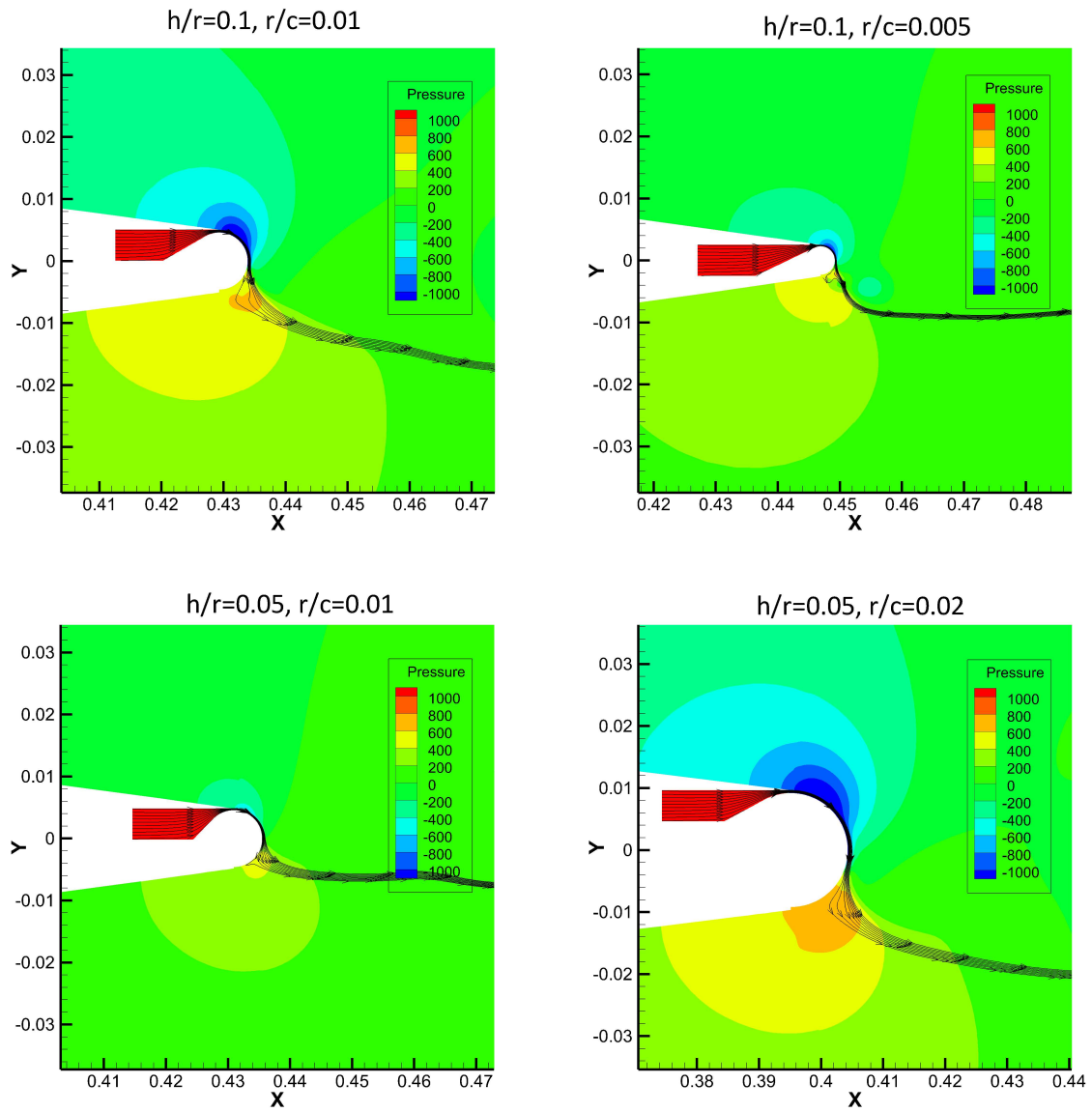


Figure 7.15: The flow field of different configurations at  $T=0.005s$ , when  $P_{t,J}$  rises from 0Pa to 10kPa, at  $T=0s$ ,  $M = 0.1$ ,  $AoA=0^\circ$ .

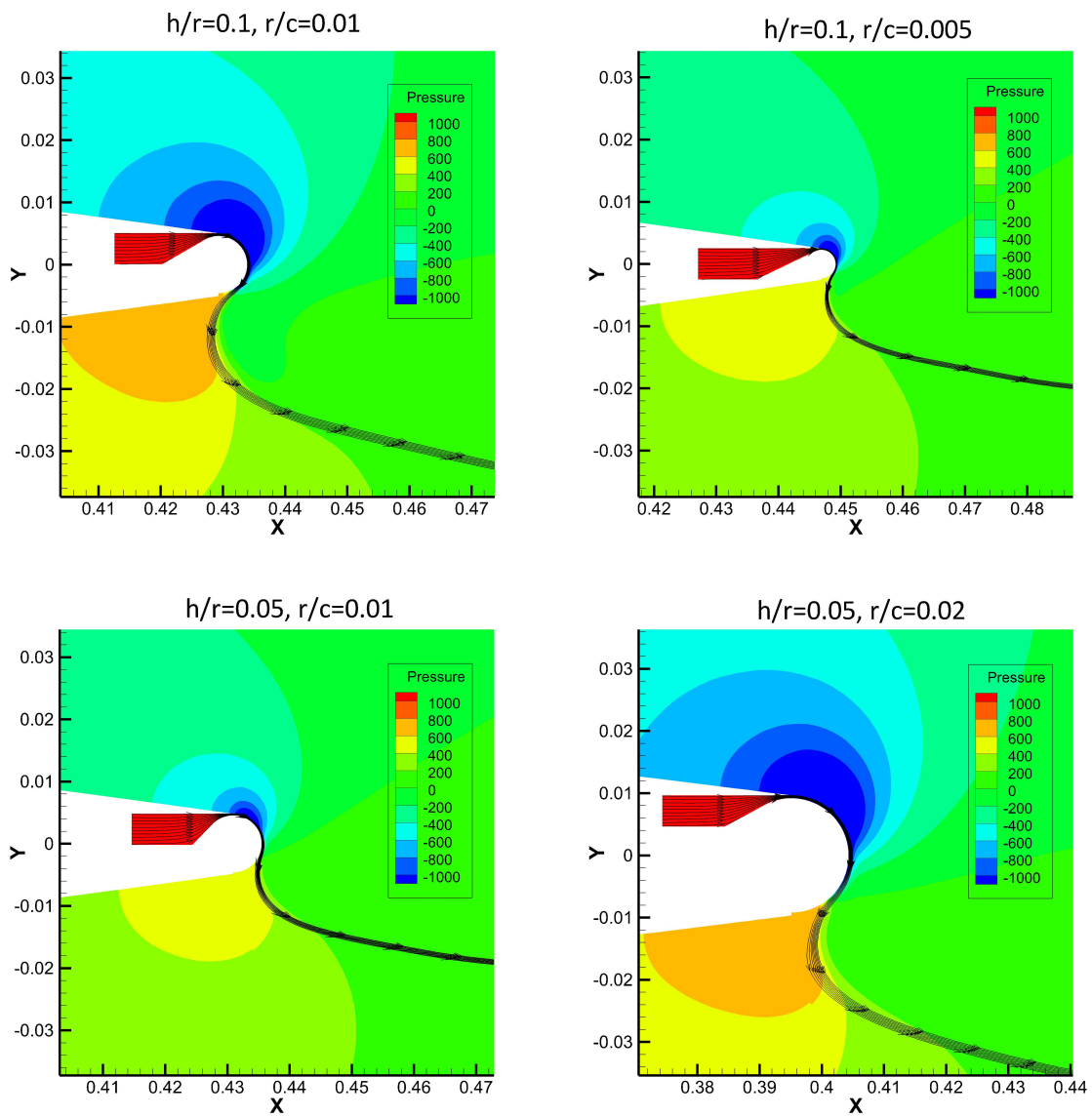


Figure 7.16: The flow field of different configurations at  $T=0.01s$ , when  $P_{t,J}$  rises from  $0Pa$  to  $10kPa$ , at  $T=0s$ ,  $M = 0.1$ ,  $AoA=0^\circ$ .

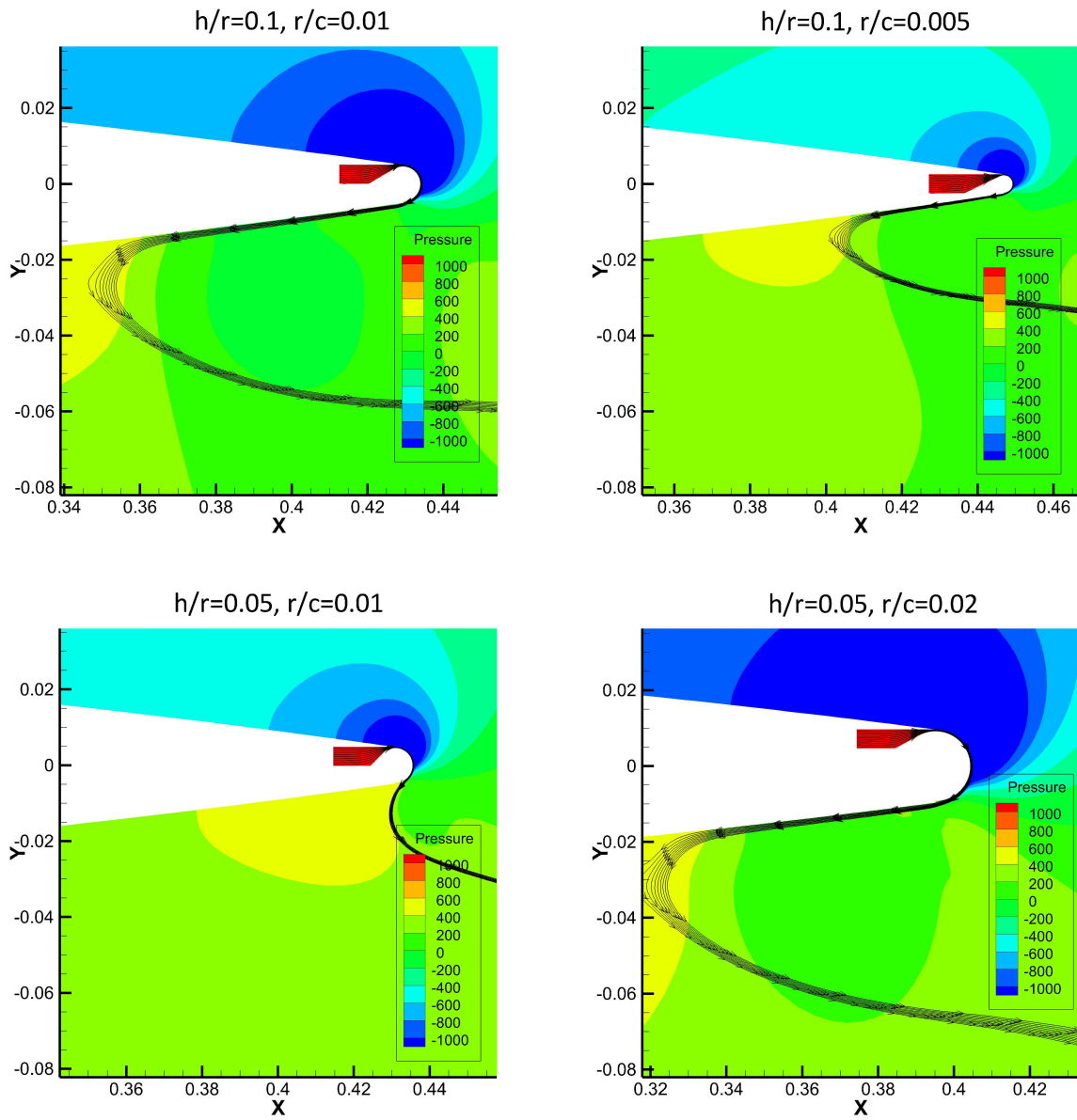


Figure 7.17: The flow field of different configurations at  $T=0.05s$ , when  $P_{tJ}$  rises from 0Pa to 10kPa, at  $T=0s$ ,  $M = 0.1$ ,  $AoA=0^\circ$ .

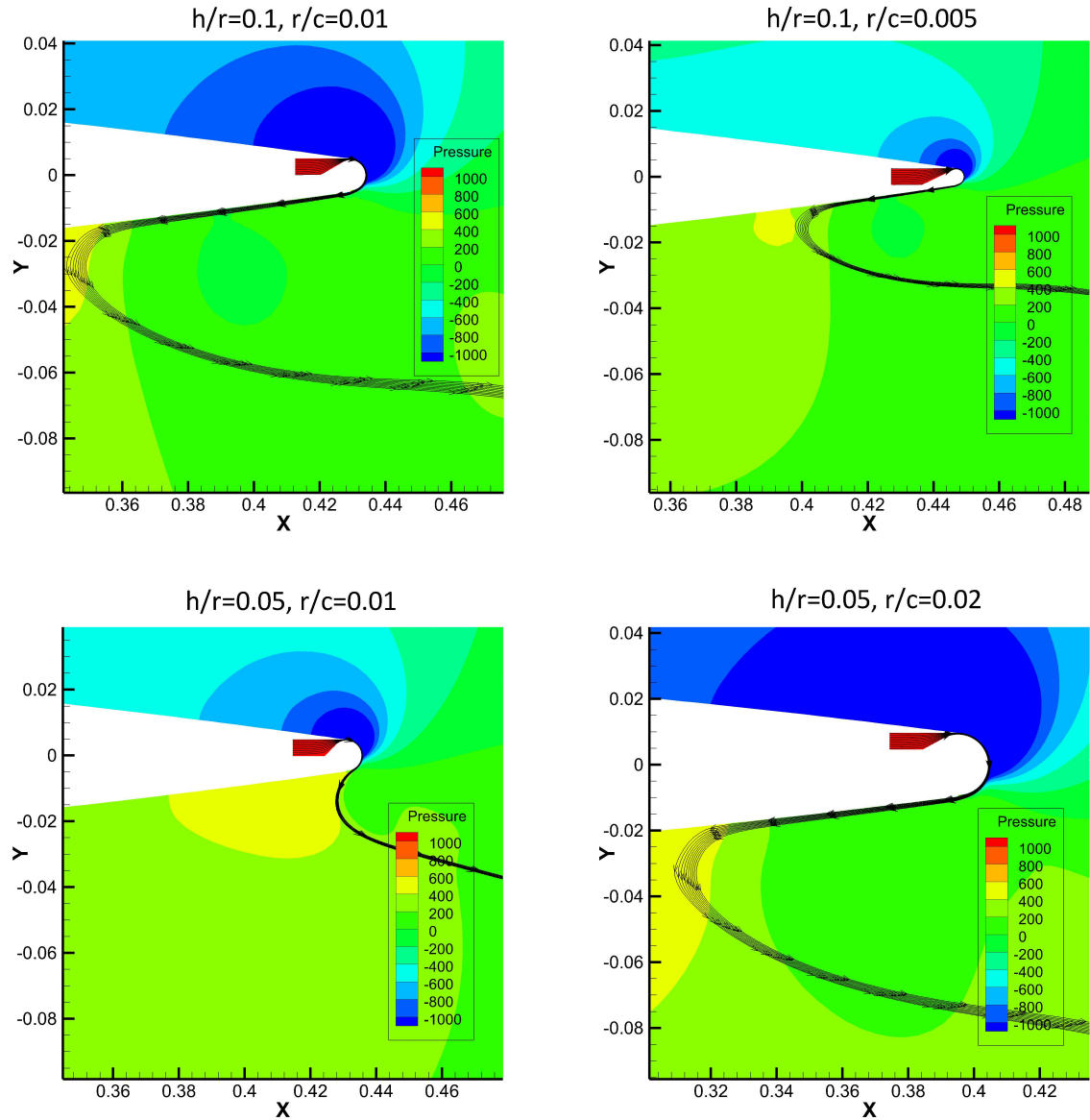


Figure 7.18: The flow field of different configurations at  $T=0.1s$ , when  $P_{t,J}$  rises from  $0Pa$  to  $10kPa$ , at  $T=0s$ ,  $M = 0.1$ ,  $AoA=0^\circ$ .

The step response of different aerofoils are compared, and the time history of the  $C_L$  is shown in Figure 7.19. A step input was applied to the plenum boundary at  $t=0$ . For comparison, the result conducted by Friedman (Friedman et al. 2016) is also presented. He used a different CC aerofoil, the NCCR 1510-7067N. The blowing jet is abruptly rising from  $C_\mu = 0.0218$  to  $C_\mu = 0.0568$ , resulting in a lift increment  $\Delta C_L \approx 1$ . The flow conditions for Friedman's result are comparable with the results in the current study. All simulations shown in Figure 7.19 have Reynolds number in the range between  $0.5 \times 10^6$  and  $1 \times 10^6$ , Mach number  $M \approx 0.1$ , and  $\Delta C_L \approx 1$ .

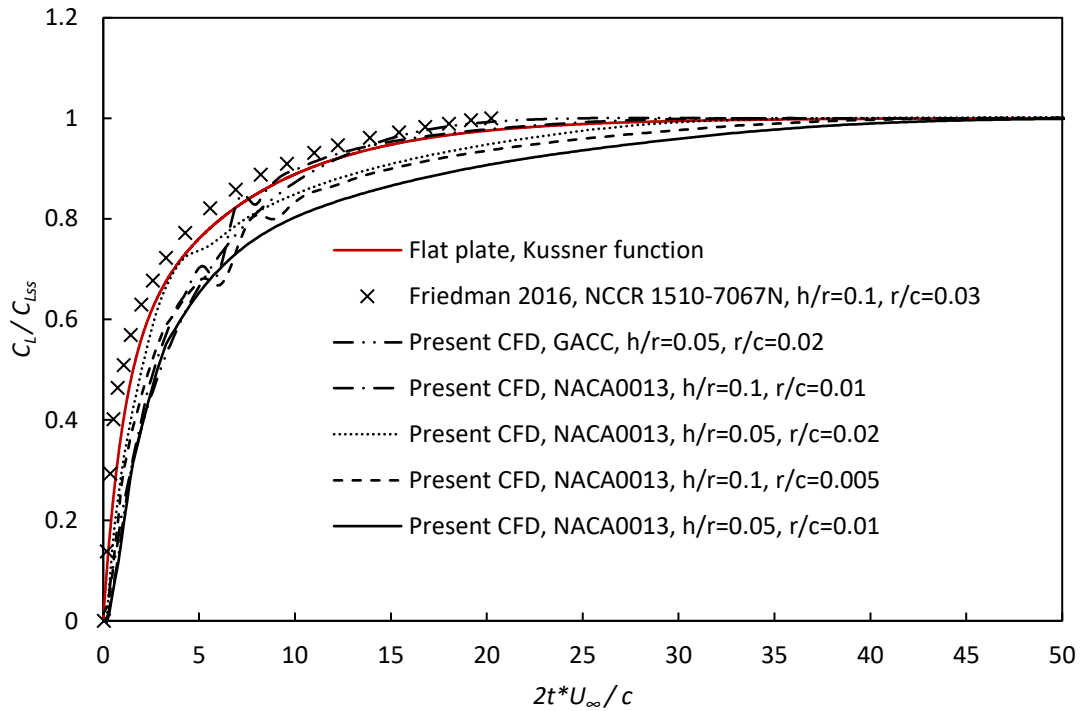


Figure 7.19: The time history  $C_L$  of different TE configurations, when  $P_{t,J}$  rises from 0Pa to 10kPa, at  $t=0$ ,  $M = 0.1$ ,  $\text{AoA}=0^\circ$ .

Although the six aerofoils have different geometry, their response curves have very similar profiles. The maximum rising slope occurs at  $2t * U_\infty / c=0$ , and then the slope gradually reduces until finally approaches the steady state. There is no overshoot which usually occurs when a mechanical flap performs a fast deflection (Phillips & Wygnanski 2013). The response profiles have no significant relation to the thickness and camber of the aerofoils. It seems that the aerofoil with a thicker trailing edge ( the ratio of TE radius and chord:  $r/c$  ) has a slightly faster response. The NCCR 1510-7067N aerofoil has the largest trailing edge  $r/c=0.03$ . Apparently, its response curve is ahead of the other cases. While the modified NACA0013 with  $r/c = 0.005$  or  $0.01$  are relatively slower. This trend can be quantified in Table 7.1 by the

stabilisation time in which the lift reaches 95%  $C_{L_{ss}}$ . For the same nozzle height, the aerofoil with a thicker trailing edge, in other words, a larger radius of Coanda surface, the stabilisation time is dramatically shorter. It is still unclear why a larger trailing edge results in a faster response.

Table 7.1: Comparison of stabilisation time of different aerofoils.

Aerofoil	Nozzle height (h/r)	TE radius (r/c)	Stabilisation time
Present CFD, NACA0013	0.1	0.005	22.9
Present CFD, NACA0013	0.1	0.01	14.5
Friedman 2016, NCCR 1510-7067N	0.1	0.03	13
Present CFD, NACA0013	0.05	0.01	27.9
Present CFD, NACA0013	0.05	0.02	20.4
Present CFD, GACC	0.05	0.02	14
Flat plate, Küssner function	-	-	15.4

As mentioned in Chapter 5, the lift build-up of a CC aerofoil is similar to a flat plate encountering a sharp-edge gust described by the Küssner function. This function is also plotted in Figure 7.19. It is very interesting that the six CC aerofoils: NCCR 1510-7067N, GACC, and the modified NACA0013, not only have a very similar profile but are also very close to the Küssner function. This comparison further proves the hypothesis mentioned in Chapter 5: the mechanism of the step response of CC is fundamentally the response of the surrounding fluid. It is not very sensitive to the geometry of the aerofoil boundary, providing the flow is incompressible. As displayed in Figure 7.11 on page 217, the step responses in the range between  $M=0.1$  and  $M=0.3$  have very little difference.

The Küssner function is derived in potential flow by assuming the wake remains plane and undistorted. If we only consider the circulatory effects, the gust front passing the aerofoil is equivalent to a sudden change in AoA, causing vorticity shedding in the wake, described by Wagner's theorem (Wagner 1924, Gülçat 2010). The contribution of the wake vorticities to the instantaneous lift can be calculated by superpositioning (von Karman & Sears 1938, Jones 1940, Andreu Angulo & Babinsky 2021). As a flat plate penetrates a gust field, the superposition of the vorticity in the wake ( Figure 7.20 top ) is probably mathematically similar to the additional circulation introduced by a jet from the trailing edge ( Figure 7.20 bottom ). Although Friedman and Arieli have demonstrated the similarity between CC and Wagner function (Friedman et al. 2016), the Küssner function was not compared in their study. The difference between the Wagner function and the Küssner function is that the latter has no ' added mass component ' due to the acceleration of surrounding fluid (Harding &

Bryden 2012). Similar to the Küssner problem, the aerofoil remains stationary, a CC jet creates circulation in the wake, and the wake affects the lift in the same way as the wake due to gust penetration. This is probably the reason that Küssner function is more consistent with the CC compared to Wagner's function. However, the analytical investigation of CC is not the focus of the present research and will leave to future work.

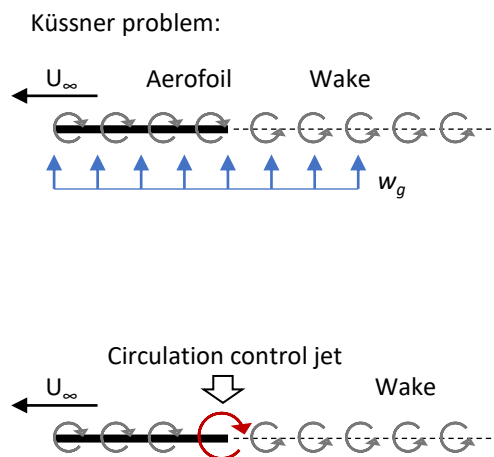


Figure 7.20: Comparison of the Küssner problem and the CC in potential flow.

The similarity between the gust encounter and the step response of CC is a very meaningful and promising result for applying gust alleviation. Based on the following assumption, a hypothesis is proposed:

- Incompressible flow without any separation.
- The aerofoil is thin, and the time delay due to flow valves or switches is negligible.
- The attachment of the Coanda jet happens in a short time and is negligible, as shown in Figure 7.5 on page 211.
- The CC has exactly the same response to the sharp edge gust encounter.
- The process that a gust front travels from the leading edge to the trailing edge ( $0 < 2t*U/c < 2$ ) is not considered.

When an aerofoil suddenly encounters the gust front, if the CC jet is actuated immediately, as soon as the gust front touches the aerofoil and creates a normal force opposite to the gust load, the indicial lift due to gust can be completely vanished by a CC since they have the same

response curve. The normal force created by CC can offset the force created by gust since, at any time, the two forces are equal in magnitude but in opposite directions. Moreover, the lift response to any arbitrary gust can be obtained through convolution of the Küssner function with Duhamel integral (von Karman & Sears 1938, Raveh 2007, Gülçat 2010, Harding & Bryden 2012, Sedky et al. 2022). Since from the frequency domain, a step response already contains information of various frequencies. On the other hand, any arbitrary profile of lift can be created by the CC, and this means the unsteady load due to any arbitrary gusts in any frequencies can be completely alleviated by CC.

In a realistic fluid, the performance of CC will inevitably be affected by viscosity and compressible effects such as vortex shedding and flow separation, and the instantaneous AoA due to aircraft motion. A more realistic simulation is performed in the next chapter to evaluate the gust alleviation effect for a 3D aircraft.

To the best of the author's knowledge, this is the first time that the lift responses of different CC aerofoil are compared with a flat plate entering a sharp edge gust.

## 7.4 Transfer Function Modelling of the CC for dynamic analysis

The previous step response study was mainly focused on the flow field and pressure distribution around the aerofoil. Following the flow analysis of the CC, it is necessary to study their dynamic characteristics on the control side. Therefore such models can be used for controller design.

Firstly the steady state  $C_L, C_D, C_M$  with various AoA and  $C_\mu$  is obtained by CFD, as shown in Figure 7.21.

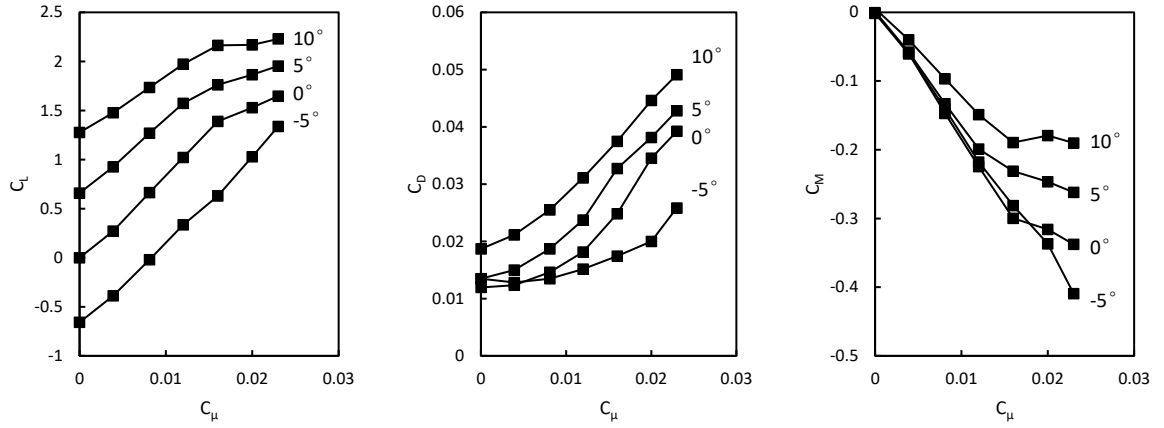


Figure 7.21: Steady state  $C_L, C_D, C_M$  on various AoA for the modified TE NACA0013, at  $M = 0.1$ .

In order to compare the response in different conditions, the  $C_{L/D/M}$  is normalised to  $C_{L/D/M}^*$  given by

$$C_L^* = \frac{C_L}{C_{Lss}} \quad (7.1)$$

$$C_D^* = \frac{C_D}{C_{Dss}} \quad (7.2)$$

$$C_M^* = \frac{C_M}{C_{Mss}} \quad (7.3)$$

The  $C_{Lss}, C_{Dss}, C_{Mss}$  is the equilibrium coefficient under the same boundary condition. Therefore the final value of  $C_{L/D/M}^*$  as  $t \rightarrow \infty$  is 1. Then the step response curve under different AoA was normalised and shown in Figure 7.22 .

In Chapter 5, the following equation of the Küssner problem has been presented (Sears 1941):

$$\Psi(s) = 1 - 0.5e^{-0.13s} - 0.5e^{-s} \quad (7.4)$$

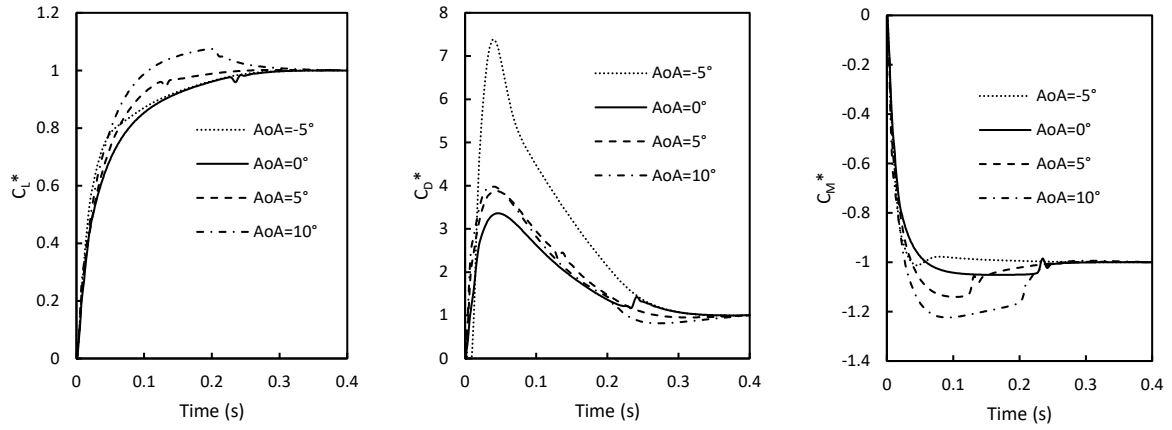


Figure 7.22: The step response under various AoA, for the modified TE NACA0013, at  $M = 0.1$ .

This equation is a simplified time-domain algebraic approximation based on the Bessel function (von Karman & Sears 1938) for the Küssner problem, but it can also be written in the following form through Laplace transformation (Bisplinghoff et al. 2013, Andreu Angulo & Babinsky 2021). This form is equivalent to a general second-order system with the unit step input, assuming the fluid is a Linear Time Invariant system (Zaide & Raveh 2006). Hence the widely used transfer function models can be used instead of Equation 7.4 for the convenience of developing control algorithms.

$$H(s) = \frac{b_2 s^2 + b_1 s + b_0}{a_2 s^2 + a_1 s + a_0} \quad (7.5)$$

According to the CFD results shown in Figure 7.19 on page 226, CC has a similar profile to the Küssner function, thus the step response curves can also be identified in the form of Equation 7.5. The input is the normalised boundary condition in the plenum chamber  $P_{tJ}$  and the output is  $C_L^*$ .

Figure 7.23 presents the  $C_L^*$  output of both the CFD result and the identified model. The transfer function is shown in Table 7.2. In order to compare the performance of CC on different AoA, the bandwidth was also calculated according to the transfer function.

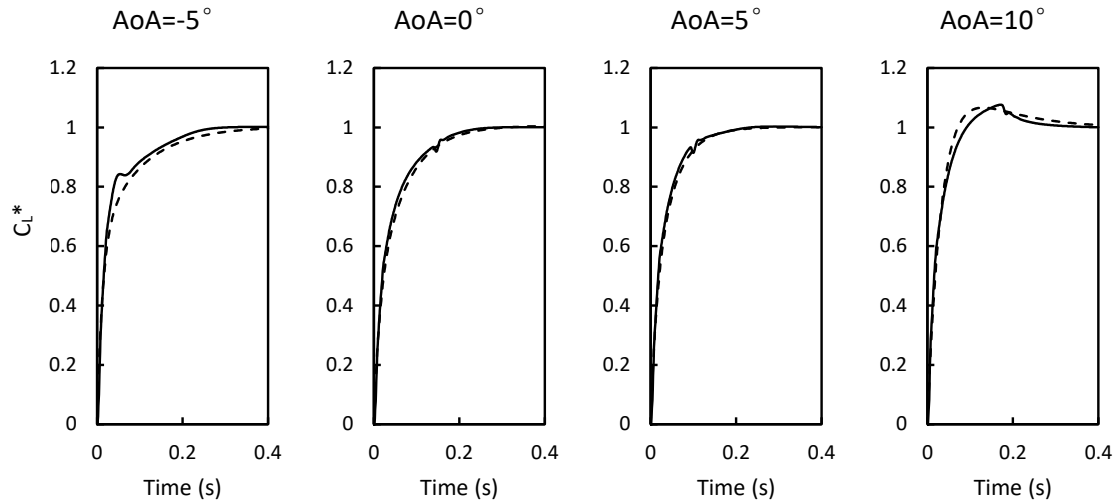


Figure 7.23: The step response identified by the second-order model (solid line: CFD results, dash line: second-order model).

Table 7.2: Identified model of different AoA

Condition	Transfer function	Bandwidth (rad/s, -3 dB)
$AoA = -5^\circ$	$\frac{52.26s+816.5}{s^2+89.19s+814.5}$	21.9
$AoA = 0^\circ$	$\frac{38.06s+1109}{s^2+89.63s+1102}$	19
$AoA = 5^\circ$	$\frac{39.99s+1658}{s^2+98.34s+1657}$	26.6
$AoA = 10^\circ$	$\frac{35.59s+248.1}{s^2+38s+248.7}$	40.4

Figure 7.24 shows the bode diagram, where the magnitude response is similar with different AoA. At low frequencies, the phase response of AoA=10° is slightly slower. The AoA has a weak influence on the dynamic characteristics. In the magnitude diagram, there is no resonance peak, indicating it is well-damped. The magnitude drops around 20 dB/decade, and the high-frequency limit is around 90 degrees. This is similar to a stable first-order system with weak non-linearity. However, higher-order transfer functions are used to make precise identification of the system.

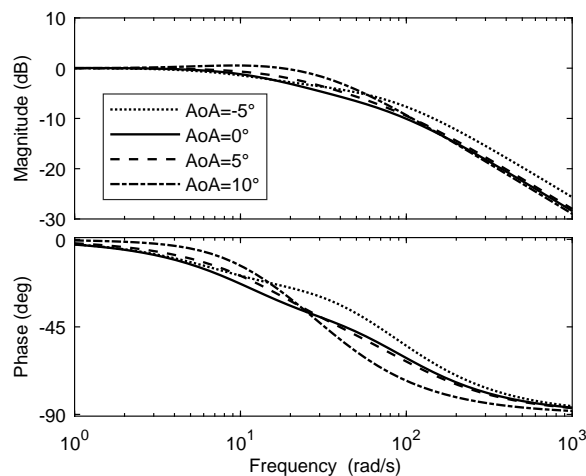


Figure 7.24: The bode diagram under various AoA identified by the second-order model for the modified TE NACA0013 aerofoil.

## 7.5 Summary

This chapter investigated the dynamic response of a NACA0013 aerofoil with a CC trailing edge. The time history flow field of CC was analysed by capturing different frames of the flow after deploying the blowing jet. The acquired streamlines and pressure distributions show that the jet sheet attached to the Coanda surface instantly at the beginning, then it gradually affected the pressure distribution around the aerofoil which takes a longer period of time (120ms). Finally, the jet sheet was attached to the lower surface and the lift reached the equilibrium value. The change of flow field when switching off the blowing was also investigated.

The factors that affect the dynamic characteristics of CC are compared. These factors include the mesh density, Reynolds number, nozzle pressure and the trailing edge shape. The mesh density and Mach number have limited influence on the response curve.

A very interesting result is obtained by comparing the step response of different CC aerofoil,

with the gust encounter problem. The lift response to a step input of CC is identical to the response of a thin aerofoil (flat plate) to a sharp edge gust, and the response is not sensitive to the shape of the aerofoil. Since any arbitrary profile can be obtained through the convolution of step responses, theoretically, an arbitrary load due to gust can be completely offset by a CC. It appears to be the first time that such a comparison has been conducted, and the mechanism that CC has a very high bandwidth has been explained.

Finally, the dynamic model of CC for different AoA was identified, which will be used in the next chapter for the controller design.

# Chapter 8:

## Application of the CC on Gust Alleviation

This chapter provides a state-space model of the aircraft according to the aerodynamic data from previous chapters. The direct lift control method is used to reduce gust loading during steady and level cruise flights. A controller is designed using the LQR approach and simulated with a continuous vertical gust disturbance. The gust alleviation performance of CC is compared with a conventional elevator.

### 8.1 LQR Controller Design

According to the information provided by previous chapters, the control loop can be closed. The aircraft model for controller design will take advantage of the CFD results, a state space model is used to represent the rigid aircraft with multiple states, and linearised transfer function models are used to represent the actuators.

The following diagram shows the full control loop.

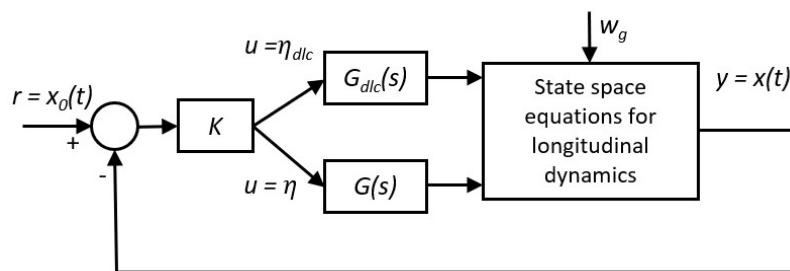


Figure 8.1: The control architecture for the gust alleviation system based on a CC actuator.

where the state space function is given in Equation 2.58 on page 41 and relevant aerodynamic derivatives are given in Chapter 6, Table 6.6 on page 196.  $G_{dlc}(s)$  is the transfer function of the CC actuator given in Chapter 7, Table 7.2 on page 232,  $G(s)$  is the transfer function of a conventional mechanical control surface, given in Chapter 5, Section 5.2.2 on page 142.  $w_g$  is the gust profile which will be discussed later. Since all the information is available, here we only need to design the feedback gain  $K$ .

The CC can adjust lift on the wing according to the wind gust. In fact, this control method is the same as the Direct Lift Control which usually uses a symmetric aileron or spoiler to

dynamically adjust the lift. As the CC also affects the pitch moment, the elevator is simultaneously adjusted to trim the aircraft. Thus there are two inputs to be controlled.

According to the aircraft model from Equation 2.58 on page 41 and 2.56 on page 38, written as follows

$$\dot{\mathbf{x}} = \mathbf{A}\mathbf{x} + \mathbf{B}\mathbf{u} \quad (8.1)$$

$$\mathbf{y} = \mathbf{C}\mathbf{x} + \mathbf{D}\mathbf{u} \quad (8.2)$$

$$\mathbf{x} = [u \ w \ q \ \theta \ h]^T \quad (8.3)$$

$$\mathbf{u} = [\eta_{dlc} \ \eta]^T \quad (8.4)$$

$$\mathbf{y} = [u \ w \ q \ \theta \ h \ a_z]^T \quad (8.5)$$

A feedback control law could be designed to demonstrate a gust alleviation control. As there are multiple states to be controlled and two input channels ( CC nozzle and elevator ), a gain matrix  $\mathbf{K}$  needs to be designed to satisfy the performance standard. The matrix of feedback gains is given by

$$\mathbf{u} = -\mathbf{K}\mathbf{x} \quad (8.6)$$

The LQR with full state feedback is used to find the desired feedback gain matrix. This is achieved by establishing a cost function and minimising the cost.

$$J = \frac{1}{2} \int_0^{\infty} (\mathbf{x}^T \mathbf{Q} \mathbf{x} + \mathbf{u}^T \mathbf{R} \mathbf{u}) dt \quad (8.7)$$

where  $\mathbf{Q}$  and  $\mathbf{R}$  are positive-semidefinite and positive-finite weighting matrices respectively. The weighting matrix  $\mathbf{Q}$  defines the weight of each element of the state according to the desired flight performance.

As mentioned in Page 41, the matrix  $\mathbf{Q}$  specifies the level of importance for each variable. A higher value means that this state has a higher cost, it is preferred to regulate this state to the desired value more quickly, compared with a lower-weight state. For example, if the penalise term corresponding to  $w$  has a larger value, in a disturbance, state  $w$  will return to 0 faster.

On the other hand, matrix  $\mathbf{R}$  penalises the control vector, a higher value means that this control variable is expensive to use. For example, the control actuator consumes energy when being deployed, a higher value in  $\mathbf{R}$  indicates that this actuator consumes more energy so the system should use a smaller control input. Stevens et al. (2015)

The vertical velocity  $w$  and height  $h$  are the main variables to evaluate the gust alleviation performance. Both states are weighted to ensure that a random vertical gust  $w_g$  has the least influence on the aircraft. If the controller can minimise the disturbed  $w$  and  $h$  due to gust, the gust loading in the vertical axis, including the induced wing root bending moment, will be sufficiently suppressed. Therefore the deviation of  $w$  and  $h$  is considered as a criterion, and the diagonal terms of  $\mathbf{Q}$  are manually adjusted until  $w$  and  $h$  have the minimal deviation in a gust. The following weighting matrix  $\mathbf{Q}$  is obtained by trial-and-errors.

$$\mathbf{Q} = \begin{bmatrix} 1 & 0 & 0 & 0 & 0 \\ 0 & 100 & 0 & 0 & 0 \\ 0 & 0 & 10 & 0 & 0 \\ 0 & 0 & 0 & 1 & 0 \\ 0 & 0 & 0 & 0 & 100 \end{bmatrix} \quad (8.8)$$

The weighting matrix of input  $\mathbf{R}$  regulates the CC and elevator. In this case, the CC has more control authority and actuates faster than the conventional elevator so the elevator has a larger penalise factor. The weighting matrix  $\mathbf{R}$  is chosen by

$$\mathbf{R} = \begin{bmatrix} 0.1 & 0 \\ 0 & 10 \end{bmatrix} \quad (8.9)$$

To find an optimal  $\mathbf{K}$  that minimises the cost function 8.7, the following algorithm is used, the detailed derivation process is provided in reference (Stevens et al. 2015) - Page 472.

By substituting Equation 8.6 to the state space functions, the state equation can be written as

$$\dot{\mathbf{x}} = (\mathbf{A} - \mathbf{BK})\mathbf{x} = \mathbf{A}_c\mathbf{x} \quad (8.10)$$

By substituting Equation 8.6 to the cost function 8.7, it can be written as

$$J = \frac{1}{2} \int_0^{\infty} \mathbf{x}^T (\mathbf{Q} + \mathbf{K}^T \mathbf{R} \mathbf{K}) \mathbf{x} dt \quad (8.11)$$

Assuming there is a constant matrix  $\mathbf{P}$ , so that,

$$\frac{d}{dt} (\mathbf{x}^T \mathbf{P} \mathbf{x}) = -\mathbf{x}^T (\mathbf{Q} + \mathbf{K}^T \mathbf{R} \mathbf{K}) \mathbf{x} \quad (8.12)$$

It can be expressed as the following form by using Equation 8.10

$$-\mathbf{x}^T (\mathbf{Q} + \mathbf{K}^T \mathbf{R} \mathbf{K}) \mathbf{x} = \mathbf{x}^T (\mathbf{A}_c^T \mathbf{P} + \mathbf{P} \mathbf{A}_c) \mathbf{x} \quad (8.13)$$

This equation should be valid for all states  $\mathbf{x}(t)$  so that the following part should equal 0.

$$0 = \mathbf{A}_c^T \mathbf{P} + \mathbf{P} \mathbf{A}_c + \mathbf{Q} + \mathbf{K}^T \mathbf{R} \mathbf{K} \quad (8.14)$$

The optimal feedback gain is defined as

$$\mathbf{K} = \mathbf{R}^{-1} \mathbf{B}^T \mathbf{P} \quad (8.15)$$

By combing Equation 8.10, Equation 8.14 and Equation 8.15. The following Algebraic Riccati equation is obtained

$$0 = \mathbf{A}^T \mathbf{P} + \mathbf{P} \mathbf{A} + \mathbf{Q} - \mathbf{P} \mathbf{B} \mathbf{R}^{-1} \mathbf{B}^T \mathbf{P} \quad (8.16)$$

Only  $\mathbf{P}$  is unknown in this equation so it can be solved directly. Consequently, the feedback gain matrix  $\mathbf{K}$  can be solved which is

$$\mathbf{K} = \begin{bmatrix} -0.451 & -3.098 & -0.064 & -1.651 & 0.156 \\ -0.277 & 1.547 & -9.789 & -150.054 & -31.584 \end{bmatrix} \quad (8.17)$$

## 8.2 Statistical Modelling of the Wind Gust

Continuous wind turbulence was used in the study to demonstrate the effectiveness of the controller. Continuous turbulence is the random disturbance in various scales, frequencies and directions. At lower altitudes, the disturbance occurs when the wind is affected by terrain, trees or buildings. Such disturbance deteriorates the flight quality and affects the flight path. It is particularly dangerous when the aircraft is tracking the landing path or making low level flying. The continuous turbulence also occurs at high level flight but the intensity is lighter.

The aircraft flying through turbulence could encounter perturbation from every direction including axial, lateral and normal. Additionally, turbulence also affects rotation axes including roll, pitch and yaw. In the process of mathematical modelling, the random gust is considered a 'frozen field', the gust components are distributed in this field and are stationary in time and space. When the aircraft encounters the field, the temporal frequency  $\omega$  is relevant to the flight velocity  $V_0$  and the spatial frequency  $\Omega$ , given by  $\omega = \Omega V_0$ . The most widely used mathematical models to describe continuous turbulence are the von Kármán model and the

Dryden model which were described in the standard MIL-F-8785C (Moorhouse & Woodcock 1980). Both models defined a series of filters that filter the white noise signal and output a spectrum distribution of gust components.

The von Kármán model gives power spectra of the gust components in the axial, lateral and normal directions ( $ug, vg, wg$ ). The power spectra density functions are given by

$$\Phi_{ug}(\Omega) = \sigma_{ug}^2 \frac{2L_u}{\pi} \frac{1}{\left(1 + (1.339L_u\Omega)^2\right)^{\frac{5}{6}}} \quad (8.18)$$

$$\Phi_{vg}(\Omega) = \sigma_{vg}^2 \frac{L_v}{\pi} \frac{\left(1 + \frac{8}{3}(1.339L_v\Omega)^2\right)}{\left(1 + (1.339L_v\Omega)^2\right)^{\frac{11}{6}}} \quad (8.19)$$

$$\Phi_{wg}(\Omega) = \sigma_{wg}^2 \frac{L_w}{\pi} \frac{\left(1 + \frac{8}{3}(1.339L_w\Omega)^2\right)}{\left(1 + (1.339L_w\Omega)^2\right)^{\frac{11}{6}}} \quad (8.20)$$

where  $L$  is the scale length,  $\sigma$  is the turbulence intensity.

In practice, the von Kármán model contains some fractional exponents which are relatively difficult to compute. The Dryden model has simpler exponents and is very similar in shape compared to the von Kármán model. As an alternative to the von Kármán model, it is widely used in industry in the past, due to the lower computational cost. Although for modern computers, the computational cost is negligible. The power spectra density functions for the Dryden model are given by

$$\Phi_{ug}(\Omega) = \sigma_{ug}^2 \frac{2L_u}{\pi} \frac{1}{\left(1 + (L_u\Omega)^2\right)} \quad (8.21)$$

$$\Phi_{vg}(\Omega) = \sigma_{vg}^2 \frac{L_v}{\pi} \frac{\left(1 + 3(L_v\Omega)^2\right)}{\left(1 + (L_v\Omega)^2\right)^2} \quad (8.22)$$

$$\Phi_{wg}(\Omega) = \sigma_{wg}^2 \frac{L_w}{\pi} \frac{\left(1 + 3(L_w\Omega)^2\right)}{\left(1 + (L_w\Omega)^2\right)^2} \quad (8.23)$$

It can be seen that both models have similar forms but only the exponent terms are different. They are essentially different fitting curves of the frequency distribution in natural atmosphere turbulence. The Dryden model is used in the following simulation since it is well understood in engineering and academic research.

In this study, only the vertical wind turbulence is considered so the normal transfer function is used, as shown in Equation 8.24 and 8.25, they are provided by the MIL-F-8785C, derived

from Equation 8.23. The turbulence  $w_g(s)$  is obtained by filtering the white noise  $N(s)$ . The profile of the vertical gust is shown in Figure 8.2 ( $\sigma_w = 5m/s, L_w = 533m, V = 34m/s$ )

$$H_w(s) = \sigma_w \sqrt{\frac{L_w}{\pi V}} \cdot \frac{1 + \frac{\sqrt{3}L_w s}{V}}{(1 + \frac{L_w s}{V})^2} \quad (8.24)$$

$$u_g(s) = N(s)H_w(s) \quad (8.25)$$

where  $L_w$  is the appropriate scale lengths.

### 8.3 Gust Alleviation Results using Closed-loop LQR Control

The simulation was performed with an LQR controller to compare the gust reduction performance with and without CC. Assuming the aircraft is in level cruise flight and encounters continuous turbulence in the normal direction defined by Equation 8.25. All the states are used as feedback signals and regulated by the  $\mathbf{K}$  matrix ( Equation 8.17 on page 238 ).

Two types of controller are compared in this study, the conventional feedback control using elevator only ( blue lines in Figure 8.2 and Figure 8.3 ), and the direct lift control using both CC and elevator ( black lines in Figure 8.2 and Figure 8.3 ).

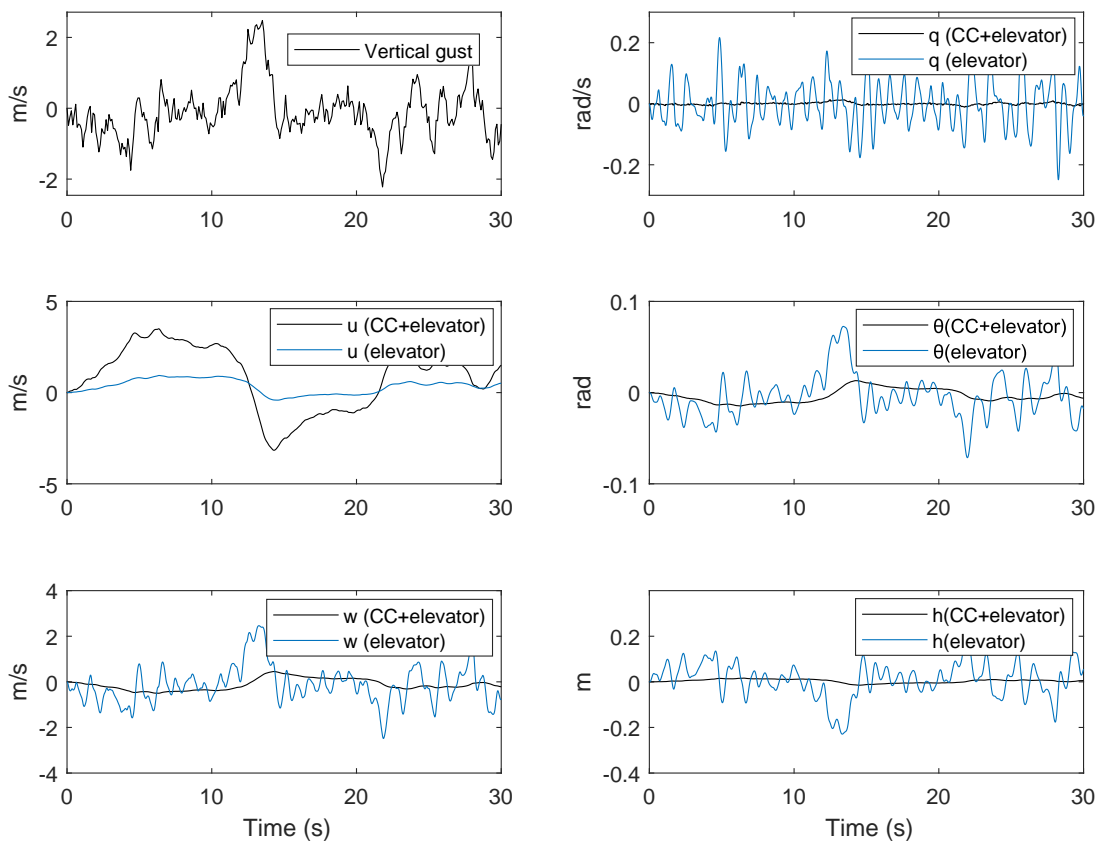


Figure 8.2: The aircraft response to continuous vertical turbulence.

Currently, there are few studies that have considered controlling aircraft motion encountering atmosphere gusts using CC. Most of them are only for the stationary aerofoil, for example, the simulation conducted by Li et al. (Li & Qin 2020), introduced in Section 3.7 on page 85. The studies that include aircraft motion, however, are mainly using conventional ailerons and elevators (Fonte 2018). The 'elevator' plot in Figure 8.2 can be considered as a baseline performance and represents a normal approach to deal with gusts using conventional elevators.

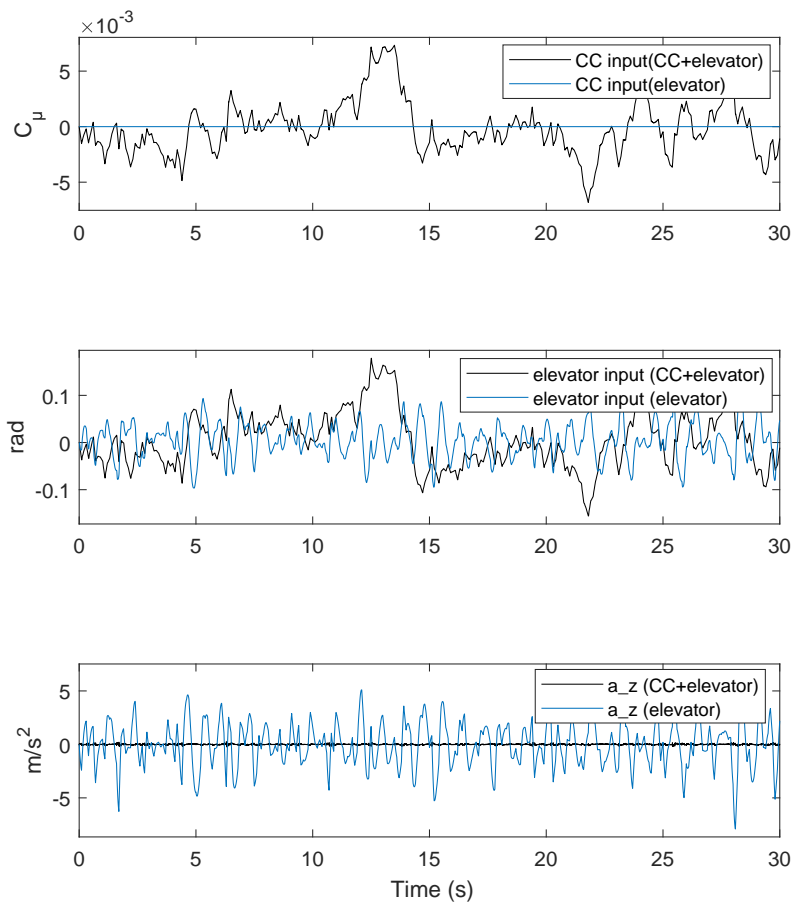


Figure 8.3: The controller input and the normal acceleration of the aircraft.

The results in Figure 8.2 clearly show that the direct lift control (CC + elevator) reduces gust loading to a minimum level. The pitch rate and angle, vertical speed and height are relatively stable compared to pure elevator control. The vertical acceleration is also reduced dramatically, as shown in Figure 8.3. The maximum deviation of height ( $h$ ) with a conventional elevator was 0.23m, whilst the CC DLC was only 0.016m. The maximum vertical acceleration ( $a_z$ ) of the former was  $6.34m/s^2$ , whilst the latter was only  $0.25m/s^2$ . This is equivalent to a 96% gust loading reduction.

However, the DLC has a greater influence on the axial velocity, due to the higher drag coefficient from the CC. Comparing the 'Vertical gust' and the ' $u$  (CC + elevator)' plots in Figure 8.2, it is apparent that there are fewer high-frequency components in  $u$ , since they are attenuated by the aircraft dynamics. The axial velocity  $u$  can be stabilised easily by adding the throttle terms to the matrix **A** and **B**. The dynamic model of the throttle is not included in this research and it will depend on the type of engine. For example, electric motors usually have a much faster dynamic response and shorter delay than gas turbine engines. On the other hand, spoilers can be used to stabilise the  $u$ , as they have a faster response than the throttle.

Nevertheless, the dynamics of the throttle have little influence on the vertical acceleration which is the main consideration of the gust alleviation system, since it is related to the wing root bending moment and trajectory following.

In this research, the baseline aircraft has a take-off weight of 13.2kg. The largest gust in Figure 8.2 is 2.3 m/s, it requires a blowing of  $C_\mu = 0.007$  to alleviate, corresponding to a mass flow rate  $\dot{m} = 0.036$  kg/s, nozzle pressure  $P_{t,J} = 5$  kPa. Assuming the Jetcat P130-RX turbojet engine is used ( it can also be used as a turboprop with an additional gearbox ), it has 130N thrust, maximum mass flow rate 0.3kg/s. The air bleeding consumes 12% of the total mass flow rate. According to the research conducted by Gill et al. (Gill et al. 2007), this results in approximately 12.5% lower thrust. The influence on the engine due to flow control would seem acceptable but needs further analysis.

## 8.4 Summary

Based on the aerodynamic data from previous CFD results, the steady and dynamic derivatives of the aircraft were obtained. A state-space model was established. In order to study the feasibility of using CC as a means of gust alleviation actuator, a control algorithm was designed to reduce the unsteady loading by a vertical wind gust. Simulation results show that the approach can effectively reduce gust loading and maintain steady and level flight.

To the best of the author's knowledge, at the time of writing, this is the first time that a CC-based, close-loop gust alleviation system is developed, together with a simulation of the longitudinal dynamics and a controller. The overall system shows significant improvement over conventional gust alleviation systems with mechanical surfaces. The simulation covers some essential aspects of engineering integration such as modelling the dynamics of CC and the influence of aircraft dynamics. This research suggests the following features for engineering:

- The system provides a much higher control authority (Sectional  $\Delta C_L > 3$ ), without sacrificing dynamic response. Both static and dynamic performance is significantly better than conventional mechanical actuators.
- The CC has a much faster dynamic response, as mentioned in Chapter 5. It creates transient loading to the structure and may affect the structural design of a wing.
- It is essential that the valves and pipelines can withstand a fast-changing pressure, during the process of gust alleviation.
- The complexity of a CC system should be less than a conventional system since there are

no mechanical gears and levers, and it should be possible to implement within existing wings. However the trailing edge shape would need to be modified and have increased thickness.

- It requires a high-pressure air supply from the engine or dedicated compressor. This means additional energy consumption, components, and maintenance cost.

# Chapter 9:

## Conclusions and Future Work

UAVs are more susceptible to vertical wind gusts than manned transport aircraft due to their smaller weight and inertia, and since they typically fly at lower altitudes where turbulence is greater. The aim of this research was to seek designs that could improve the gust resilience of a UAV to improve stability and expand its mission profile. The bandwidth and authority of conventional mechanical control surfaces is the main limiting factor for the performance of gust alleviation systems. In comparison, the actuation of circulation control (CC) is almost instantaneous, and the dynamic response mainly depends on the reaction speed of the fluid. The dynamics of this fluidic response were studied in the present research using CFD, and subsequently using this information to design a suitable control method. Note that the challenge of installing and operating CC in a UAV, with a limited internal wing volume, has not been considered in this research and is acknowledged as a necessary future study. However, the DEMON UAV (Buonanno 2009) has successfully demonstrated that this is achievable.

To achieve the aim, a preliminary CFD study of the fluidic response of CC with steady blowing was compared with published experimental data, described in Chapter 5. This validated the CFD methodology for steady conditions, with CFD results closely matching the wind tunnel measurements of lift. Subsequently an unsteady validation was conducted using published analytical and numerical response data for a sharp edge vertical gust profile, also reported in Chapter 5. Using this validated approach the time domain and frequency domain lift responses of CC were predicted using sinusoidal blowing in various frequencies, and the frequency response was compared with published data for mechanical control surfaces to quantify potential improvements in the fluidic reaction. The results showed that the frequency response and phase delay of CC were significantly superior to mechanical actuators.

The next stage in the research was to assess the feasibility of using CC to suppress wind gusts by designing a control algorithm based on the dynamic response of CC. The gust alleviation process requires active control of the blowing (i.e. the plenum pressure) according to the gust loading, where a closed-loop control system is needed. In this research, a novel simulation method was adopted that coupled CFD with a feedback control algorithm as a user defined function. The successful demonstration of a controlled aerofoil encountering a dis-

crete gust was reported in Chapter 5, with results showing that CC could eliminate the gust loading very rapidly to maintain a constant lift.

The superior dynamic response of CC and the effectiveness of closed-loop control indicated that CC was feasible as a means of UAV gust alleviation. The analysis was subsequently extended to 3D with a 13kg, 2.65m span datum aircraft, similar in size to a commercial UAV, used to investigate the CC performance. Chapter 6 provided steady state simulation results of the datum aircraft and aerodynamic derivatives were obtained. When conducting the 3D simulation, a unique trailing vortex pattern was identified that forms at the trailing edge of the wing when CC is used and reduces the effectiveness of CC compared with 2D. The mechanism of this vortex was studied, and it was found that a thicker trailing edge could eliminate the vortex and improve the jet sheet performance. Finally, the aerodynamic derivatives obtained in Chapter 6 were used to build a model for simulating the aircraft flight dynamics.

Since Chapter 6 provides static aerodynamic derivatives, further work reported in Chapter 7 was for the unsteady analysis and modelling of the 2D CC aerofoil for the datum aircraft, considering a wider range of flow conditions including blowing coefficients and angles of attack, to better understand the dynamic performance resulting from step changes in the plenum pressure.

Using steady-state aerodynamic data for the CC wing (Chapter 6) and the dynamic data for the CC aerofoil (Chapter 7), a linear model of the aircraft was established, as reported in Chapter 8. The aircraft flying in an unsteady wind environment was simulated incorporating a full state feedback LQR controller to maintain the attitude and reduce gust loading on the aircraft. Results showed that the aircraft fitted with a CC wing, and using a control strategy such as that developed in this research, could significantly suppress gust loading.

The main novel contributions of this research are concluded in the following sections.

## 9.1 The Dynamic Performance of CC

There is very little published data available for the dynamic performance of CC i.e. considering both the actuation speed and fluidic response. Data generated in this research for the time and frequency domain characteristics of the CC lift response to step and sinusoidal changes in nozzle pressure, will allow improved controller design for flight manoeuvre and longitudinal stability using CC. Compared to the results reported by Friedman and Arieli (Friedman et al. 2016) (discussed in Section 3.7 on page 85 ), the present research considers multiple aerofoils and flow conditions in both the time domain and frequency domain.

It was found that the step response of a circulation controlled aerofoil was insensitive to

geometry and velocity ( Figure 7.19 on page 226 ). For different thicknesses, camber, nozzle heights, trailing edge radius, and free stream velocities, the response curves had a similar shape. In addition, the step response of CC is identical to the response of a thin aerofoil ( flat plate ) encountering a sharp edge gust. To the best of the author's knowledge, it is the first time that this similarity has been observed between the Küssner's function and response profiles of various CC aerofoils.

## 9.2 Assessment of the bandwidth for gust alleviation relative to conventional actuators

Actuation rates were also compared with published data for conventional mechanical actuators (discussed in Section 5.2.2 on page 142). In the time domain, at a freestream velocity  $U = 34\text{m/s}$ , the settling time of a high speed mechanical flap was equivalent to the non-dimensional time range  $t * U/c = 17 - 85$ . This compared to a settling time of around  $t * U/c = 7 - 9$  for the GACC aerofoil, which improved further at a higher velocity, and achieved this without any mechanical limitations or hinge loading effects. In the frequency domain, the dynamic performance of the GACC aerofoil was also significantly better than mechanical flaps. When the magnitude of the lift response was reduced to -3dB, the mechanical flap response was in the range of 4-20 rad/s, compared to a much wider 60-101 rad/s for the GACC. In terms of the phase lag, the mechanical flap reaches -45 deg in the range of 53-77 rad/s, compared with the GACC at 90-97 rad/s. In other words, GACC can perform an effective actuation at a frequency as high as  $10^2$  rad/s.

## 9.3 Coupled Simulation of CFD and Closed-Loop Control

A novel coupled system has been designed and implemented by integrating a closed-loop feedback controller within a high-fidelity unsteady CFD simulation to maintain steady lift when a vertical gust is encountered. After each time step, the lift value (system output) was fed to the script. Then the control algorithm could compute an appropriate nozzle pressure value (system input) to adjust the velocity of the jet to maintain a constant lift.

The main advantage of this technique was that the results were very close to real physical experiments, compared to the conventional control design method based on linearised low order models. As the CC involves non-linear complex behaviours such as boundary-layer separation, near wall jet flows and entrainment, conventional modelling methods such as transfer functions are not appropriate, but the coupled CFD simulation and control algorithm was ca-

pable of simulating these non-linearities within a high-fidelity flow field.

Notger and Rudibert presented a similar method in 2010 (Heinz, King, Höll, Wassen & Thiele 2010) to control the flow separation on a mechanical flap in a steady-state flow condition. Their approach used a reduced order mathematical model to represent the flow control device in the system. While in this research the simulation was potentially more accurate and solved the full URANS equations for the control loop so that the transient flow field during the disturbance could be obtained. This approach will contribute to a better understanding of unsteady aerodynamics, particularly involving non-linear control problems.

## 9.4 The Applications of CC on Gust Alleviation

Chapter 5 described a closed-loop PID control algorithm using CC to maintain constant lift when encountering a discrete wind gust. A more realistic simulation was performed in Chapter 8 where an aircraft dynamic model was developed and used including its longitudinal dynamics i.e. response to vertical movements and pitching. In addition, a controller was designed to automatically compensate for the gust loading. Both simulations in Chapters 5 and 8 showed that CC could effectively reduce gust loading. Figure 8.2 on page 241, showed the maximum vertical movement of the aircraft with a conventional elevator was predicted to be 0.23m, whilst the maximum movement of CC DLC was only 0.016m. The maximum vertical acceleration of the former was  $6.34\text{m/s}^2$ , whilst the latter was only  $0.25\text{m/s}^2$  (Reduced 96% gust loading).

Most existing research concerning CC, particularly with closed-loop control, does not consider the aircraft dynamics. In this research, an approach to utilise CC during flight was explored, where the coupling effect between CC and flight dynamics was addressed. There are great challenges associated with this application, as the actuation of CC not only increases lift, but also changes the pitching moment and typically creates additional drag. These factors were all considered when modelling the CC and designing the controller. The state space model with CC flap and the LQR controller described in this research provided a valuable contribution to the engineering applications of CC, and a new direction of the flow control.

Previous work, such as the CFD simulations conducted by Li et al. (Li & Qin 2020) (discussed in Section 3.7 on page 85), only considered a stationary aerofoil in a pre-defined gust profile without any feedback controller. At the time of writing, the present research seems to be the first time that a close-loop gust alleviation system based on CC has been developed, together with a simulation of the longitudinal dynamics and a controller.

## 9.5 Future Work

There are still some issues that need to be addressed in the engineering integration of the CC-based gust alleviation system. Such as the routing and positing of the plumbing system, pneumatic valves and pressure chambers; The high flow rate air supply; The redundancy and fail-safe design. It is recommended that future work will focus on developing lightweight, low-cost and low-maintenance actuation systems for CC.

This research only focused on the low speed flight ( $M < 0.3$ ) for application to small UAVs flying at low altitudes and low velocities. Future work should be focused on the dynamics of CC at higher Mach numbers, exploring the possibility of expanding the application to large transport aircraft or high-speed UAVs.

Future research should also seek to expand the application of joint-simulation approaches which combine CFD and a control algorithm. This approach can be used in many other flow control problems such as feedback separation control. Finally, as the actuation speed of CC is fast, it could potentially be used in the flutter control of the wing, which is an additional direction for future work.

The content described in Sections 9.1 and 9.2 have been published in the AIAA Journal of Aircraft entitled "The dynamic response of circulation control for step and sinusoidal inputs". Whilst the novel contribution highlighted in Sections 9.3 and 9.4, which include Chapters 6 - 8, will be published in the future.

# Bibliography

- Allen, J. M. (2013), Thunderstorms - advisory circular 00-24c, Federal Aviation Administration, ASAE CENTER, 1575 I St NW, Washington, DC 20005, United States, p. 6.
- Anderson, J. D. & Bowden, M. L. (2005), Introduction to flight, McGraw-Hill Higher Education New York, 1325 Avenue of the Americas, New York, NY 10019, pp. 288–435.
- Anderson Jr, J. D. (2016), Part 4 viscous flow, in 'Fundamentals of aerodynamics', Tata McGraw-Hill Education, pp. 923–1062.
- Andreu Angulo, I. & Babinsky, H. (2021), Unsteady modelling of pitching wings for gust mitigation, in 'AIAA Scitech 2021 Forum', p. 1999.
- Ansys (2018), Turbulence, in 'ANSYS fluent theory guide, release 19.1', ANSYS Inc, Canonsburg, Southpointe. 2600 Ansys Drive. Canonsburg PA 15317. USA., pp. 39–133.
- ANSYS, I. P. (2010), Lecture 5 solver settings, in 'Introduction to ANSYS FLUENT', Release 13.0, Canonsburg, Southpointe. 2600 Ansys Drive. Canonsburg PA 15317. USA, p. 4.
- Arampatzis, G., Assimacopoulos, D. & Mitsoulis, E. (1994), 'Treatment of numerical diffusion in strong convective flows', *International journal for numerical methods in fluids* **18**(3), 313–331.
- Atkin, C. & Courtenay, W. (2002), Predicting the cruise performance of a retrofit hybrid laminar flow control system, in 'CEAS Aerospace Aerodynamics Research Conference (June 2002)'.
- Babinsky, H. (2003), 'How do wings work?', *Physics Education* **38**(6), 497.
- Babister, A. W. (2013), Part ii: Longitudinal dynamic stability and response, in 'Aircraft Dynamic Stability and Response: Pergamon International Library of Science, Technology, Engineering and Social Studies', Elsevier, pp. 65–115.
- Baker, W. & Paterson, E. (2006), Rans cfd simulation of a circulation-control foil: Validation of performance, flow feild, and wall jet, in '3rd AIAA Flow Control Conference', p. 3010.

- Bardina, J., Ferziger, J. & Reynolds, W. (1980), Improved subgrid-scale models for large-eddy simulation, in 'Fluid Dynamics and Co-located Conferences: 13th fluid and plasmadynamics conference', Snowmass,CO,U.S.A., p. 1357.
- BARFIELD, A. & DAZZO, J. (1983), Multivariable control laws for the afti/f-16, in '22nd Aerospace Sciences Meeting', Reno,NV,U.S.A., p. 237.
- Barnard, R. H. & Philpott, D. R. (2010), Chapter 1 lift, in 'Aircraft flight: a description of the physical principles of aircraft flight', Pearson education, Edinburgh gate, Harlow, Essex, England, pp. 1–65.
- Bartels, R. E. (2012), *Development, Verification and Use of Gust Modeling in the NASA Computational Fluid Dynamics Code FUN3D*, National Aeronautics and Space Administration, Langley Research Center.
- Becker, R., King, R., Petz, R. & Nitsche, W. (2007), 'Adaptive closed-loop separation control on a high-lift configuration using extremum seeking', *AIAA journal* **45**(6), 1382–1392.
- Bisplinghoff, R. L., Ashley, H. & Halfman, R. L. (2013), Chapter 5 aerodynamic tools, in 'Aeroelasticity', Dover Publications, Inc., Mineola, New York, pp. 237–293.
- Blazek, J. (2005a), Chapter 1 - introduction, in J. Blazek, ed., 'Computational Fluid Dynamics: Principles and Applications (Second Edition)', second edition edn, Elsevier Science, Oxford, pp. 1 – 4.  
**URL:** <http://www.sciencedirect.com/science/article/pii/B9780080445069500035>
- Blazek, J. (2005b), Chapter 5 - turbulence modelling, in J. Blazek, ed., 'Computational Fluid Dynamics: Principles and Applications (Second Edition)', second edition edn, Elsevier Science, Oxford, pp. 225 – 256.  
**URL:** <http://www.sciencedirect.com/science/article/pii/B9780080445069500035>
- Blottner, F. (1970), 'Finite difference methods of solution of the boundary-layer equations', *AIAA journal* **8**(2), 193–205.
- Boysan, H. F., Choudhury, D. & Engelman, M. S. (2009), Commercial cfd in the service of industry: The first 25 years, in E. H. Hirschel & E. Krause, eds, '100 Volumes of 'Notes on Numerical Fluid Mechanics': 40 Years of Numerical Fluid Mechanics and Aerodynamics in Retrospect', Springer Berlin Heidelberg, Berlin, Heidelberg, pp. 451–461.  
**URL:** [https://doi.org/10.1007/978-3-540-70805-6\\_35](https://doi.org/10.1007/978-3-540-70805-6_35)

- Bryan, G. H. (1911), *Stability in aviation: an introduction to dynamical stability as applied to the motions of aeroplanes*, MacMillan, London.
- Buonanno, A. (2009), Aerodynamic circulation control for flapless flight control of an unmanned air vehicle, PhD thesis, Cranfield University.
- Buonanno, A. & Cook, M. (2006), Flight dynamic simulation of a flapless flight control uav, in '25th International Congress of the Aeronautical Sciences', September 2006, Hamburg, Germany.
- Cagle, C. (2002), A wind tunnel model to explore unsteady circulation control for general aviation applications, in '22nd AIAA Aerodynamic Measurement Technology and Ground Testing Conference', p. 3240.
- Cai, Z., Angland, D., Zhang, X. & Chen, P. (2015), 'Iterative learning control for trailing-edge flap lift enhancement with pulsed blowing', *AIAA Journal* **53**(7), 1969–1979.
- Carpenter, P. & Green, P. (1997), 'The aeroacoustics and aerodynamics of high-speed coanda devices, part 1: Conventional arrangement of exit nozzle and surface', *Journal of Sound and Vibration* **208**(5), 777–801.
- Casey, M., Wintergerste, T. & Innotec, S. (2000), 'Ercoftac special interest group on quality and trust in industrial cfd', *Best Practices Guidelines* .
- Cates, M. C., Paranto, J. N. & Larsen, T. A. (2013), 'Multifunction aircraft lidar'. US Patent 8,508,721.
- Cattafesta III, L. N. & Sheplak, M. (2011), 'Actuators for active flow control', *Annual Review of Fluid Mechanics* **43**, 247–272.
- Caverly, R., Forbes, J. R., Danowsky, B. P. & Suh, P. M. (2017), Gust-load alleviation of a flexible aircraft using a disturbance observer, in 'AIAA Guidance, Navigation, and Control Conference', p. 1718.
- Chambers, E. (1955), 'Clear air turbulence and civil jet operations', *The Aeronautical Journal* **59**(537), 613–628.
- Chanetz, B., Déleroy, J., Gilliéron, P., Gnemmi, P., Gowree, E. R. & Perrier, P. (n.d.), Chapter 1 the experimental approach in aerodynamic design, in 'Experimental Aerodynamics', Springer, 42nd St Fl 15 New York, NY 10036 United States, pp. 1–24.

- Chang, P., Slomski, J., Marino, T. & Ebert, M. (2005), Numerical simulation of two and three dimensional circulation control problems, *in* '43rd AIAA Aerospace Sciences Meeting and Exhibit', p. 80.
- Choi, J. J., Annaswamy, A. M., Lou, H. & Alvi, F. S. (2006), 'Active control of supersonic impingement tones using steady and pulsed microjets', *Experiments in fluids* **41**(6), 841–855.
- Ciobaca, V., Kühn, T., Rudnik, R., Bauer, M., Gölling, B. & Breitenstein, W. (2013), 'Active flow-separation control on a high-lift wing-body configuration', *Journal of aircraft* **50**(1), 56–72.
- Ciobaca, V. & Wild, J. (2013), 'An overview of recent dlr contributions on active flow-separation control studies for high-lift configurations', *AerospaceLab* (6), p–1.
- Cobleigh, B. (1994), High-angle-of-attack yawing moment asymmetry of the x-31 aircraft from flight test, *in* '12th Applied Aerodynamics Conference', p. 1803.
- Cook, M. V. (2012), Chapter 14 flight in a non-steady atmosphere, *in* 'Flight dynamics principles: a linear systems approach to aircraft stability and control', Butterworth-Heinemann, The Boulevard, Langford Lane, Kidlington, Oxford, OX5 1GB, UK, pp. 441–485.
- CRAeS, P. J. H. (2014), 'Fw lanchester and the great divide', *Journal of Aeronautical History Paper No* p. 02.
- Crittenden, T., Glezer, A., Funk, R. & Parekh, D. (2001), 'Combustion-driven jet actuators for flow control', *AIAA paper* **2768**, 2001.
- Crowther, W. J., Wilde, P., Gill, K. & Michie, S. (2009), 'Towards integrated design of fluidic flight controls for a flapless aircraft', *The Aeronautical Journal* **113**(1149), 699–713.
- De Breuker, R., Abdalla, M. & Marzocca, P. (2007), Aeroelastic control and load alleviation using optimally distributed synthetic jet actuators, *in* '48th AIAA/ASME/ASCE/AHS/ASC Structures, Structural Dynamics, and Materials Conference', p. 2134.
- Dearing, S., Lambert, S. & Morrison, J. (2007), 'Flow control with active dimples', *Aeronautical Journal* **111**(1125), 705–714.
- DEFENSE, D. O. (1997), Flying qualities of piloted aircraft, Interface Standard MIL-STD-1797A, DEPARTMENT OF DEFENSE, Washington, DC.
- DeSalvo, M., Heathcote, D., Smith, M. J. & Glezer, A. (2019), Direct lift control using distributed aerodynamic bleed, *in* 'AIAA Scitech 2019 Forum', p. 0591.

- Dotz, T. (2011), 'Introducing the 787 - effect on major investigations and interesting tidbits', <https://isasi.org/Documents/library/technical-papers/2011/Introducing-787.pdf>.
- Doormaal, J. P. V. & Raithby, G. D. (1984), 'Enhancements of the simple method for predicting incompressible fluid flows', *Numerical Heat Transfer* **7**(2), 147–163.  
**URL:** <https://doi.org/10.1080/01495728408961817>
- Dovey, J. (2003), 'Lift curve of wings with high-lift devices deployed at low speeds', *The Royal Aeronautical Society ESDU* **96003**, 13–14.
- Dunaevich, L. & Greenblatt, D. (2020), 'Stability and transition on a coandă cylinder', *Physics of Fluids* **32**(8), 084106.  
**URL:** <https://doi.org/10.1063/5.0013534>
- Economon, T. D., Milholen II, W. E. & Branch, C. A. (2008), 'Parametric investigation of a 2-d circulation control geometry', *Configuration Aerodynamics Branch Research and Technology Directorate Submitted: August 7*.
- Englar, R. J. (1975a), Experimental investigation of the high velocity coanda wall jet applied to bluff trailing edge circulation control airfoils, Technical report, DAVID W TAYLOR NAVAL SHIP RESEARCH AND DEVELOPMENT CENTER BETHESDA MD . . . .
- Englar, R. J. (1979), Development of the a-6/circulation control wing flight demonstrator configuration, Technical report, DTIC Document.
- Englar, R. J. (2000a), Circulation control pneumatic aerodynamics: blown force and moment augmentation and modification- past, present and future, in 'Fluids 2000 Conference and Exhibit, Denver, CO'.
- Englar, R. J. (2000b), Development of pneumatic aerodynamic devices to improve the performance, economics, and safety of heavy vehicles, Technical report, Georgia Tech Research Institute, Atlanta, GA (US).
- Englar, R. J. (2005), Overview of circulation control pneumatic aerodynamics: Blown force and moment augmentation and modification as applied primarily to fixed wing aircraft, in 'Proceedings of the 2004 NASA/ONR Circulation Control Workshop, NASA CP-2005-213509', pp. 23–66.
- Englar, R. J., Hemmerly, R. A., Taylor, D. W., Moore, W. H., Seredinsky, V., Valckenaere, W. & Jackson, J. A. (1981), 'Design of the circulation control wing stol demonstrator aircraft', *Journal of Aircraft* **18**(1), 51–58.

- Englar, R. J. & Williams, R. M. (1971), Design of a circulation control stern plane for submarine applications, Technical report, DAVID W TAYLOR NAVAL SHIP RESEARCH AND DEVELOPMENT CENTER BETHESDA MD AVIATION AND SURFACE EFFECTS DEPT.
- ENGLAR, R., JONES, G., Allan, B. & Lin, J. (2009), 2-d circulation control airfoil benchmark experiments intended for cfd code validation, *in* '47th AIAA Aerospace sciences meeting including the new horizons forum and aerospace exposition', p. 902.
- Englar, R. L. L. (1975*b*), 'Circulation control for high lift and drag generation on stol aircraft', *Journal of Aircraft* **12**(5), 457–463.
- Eppel, J., Shovlin, M., Jaynes, D., Englar, R. & Nichols Jr, J. (1982), 'Static investigation of the circulation control wing/upper surface blowing concept applied to the quiet short haul research aircraft'.
- ESDU (1956-05), 'Esdu controls w.01.01.03. rate of change of lift coefficient with control deflection in incompressible two-dimensional flow', *IHS ESDU* .
- F. Moukalled, L. Mangani, M. D. (2016), Chapter 3 mathematical description of physical phenomena, *in* 'The Finite Volume Method in Computational Fluid Dynamics', Springer International Publishing, 11 W 42nd St Fl 15 New York, US, pp. 43–86.
- FAA (November 25, 1988), Ac 00-54 - pilot windshear guide, Advisory Circulars 00-54, Federal Aviation Administration, Washington, DC.
- Fay, J. A. & Riddell, F. R. (1958), 'Theory of stagnation point heat transfer in dissociated air', *Journal of the Aerospace Sciences* **25**(2), 73–85.
- Ferrell, J. & Colgren, R. (2003), Development of flight control systems for jet airliners, *in* 'AIAA Guidance, Navigation, and Control Conference and Exhibit', p. 5764.
- Fezans, N., Joos, H.-D. & Deiler, C. (2019), 'Gust load alleviation for a long-range aircraft with and without anticipation', *CEAS Aeronautical Journal* **10**(4), 1033–1057.
- Fielding, J. & Smith, H. (2006), Flaviir an innovative university/industry research program for collaborative research and demonstration of uav technologies, *in* 'Proceedings of the 25th International Congress of the Aeronautical Sciences, ICAS'.
- Fluent, A. (2011*a*), '14.0 user's manual', ANSYS Inc., Canonsburg, PA .
- Fluent, A. (2011*b*), 'Fluent 14.0 user's guide', Ansys Fluent Inc .

- Fonte, F. (2018), 'Design and validation of active gust load alleviation systems for aircraft'.
- Forster, M., Biava, M. & Steijl, R. (2016), Multipoint optimisation of coanda surfaces for transonic circulation control using the adjoint method, in '8th AIAA Flow Control Conference', p. 3773.
- Förster, M. & Breitsamter, C. (2015), 'Aeroelastic prediction of discrete gust loads using non-linear and time-linearized cfd-methods', *Journal of Aeroelasticity and Structural Dynamics* 3(3).
- Friedman, C., Arieli, R. & Levy, Y. (2007), Numerical investigation of unsteady circulation control, in '25th AIAA Applied Aerodynamics Conference'.  
**URL:** <https://arc.aiaa.org/doi/abs/10.2514/6.2007-3918>
- Friedman, C., Arieli, R. & Levy, Y. (2016), 'Lift build-up on circulation control airfoils', *Journal of Aircraft* 53(1), 231–242.
- Gerrits, M. (1994), 'Direct lift control for the cessna citation ii', *Mémoire de maîtrise du Eindhoven University of Technology, Eindhoven, Netherlands* .
- Ghee, T. A. & Leishman, J. (1992), 'Unsteady circulation control aerodynamics of a circular cylinder with periodic jet blowing', *AIAA journal* 30(2), 289–299.
- Ghoreyshi, M., Greisz, I., Jirasek, A. & Satchell, M. (2018), 'Simulation and modeling of rigid aircraft aerodynamic responses to arbitrary gust distributions', *Aerospace* 5(2), 43.
- Gill, K., Wilde, P., Gueroult, R. & Crowther, W. (2007), Development of an integrated propulsion and pneumatic power supply system for flapless uavs, in 'AIAA Aviation Technology, Integration and Operations Conference, Belfast, UK, Sept', pp. 18–20.
- Glezer, A. & Amitay, M. (2002), 'Synthetic jets', *Annual Review of Fluid Mechanics* 34(1), 503–529.
- Golden, R. & Marshall, D. (2010), Design and performance of circulation control flap systems, in '48th AIAA Aerospace Sciences Meeting Including the New Horizons Forum and Aerospace Exposition', p. 1053.
- Goldhammer, M. (2009), The next decade in commercial aircraft aerodynamics: a boeing perspective, in 'Proc. KATnet II Conf. of Key Aerodynamic Technologies, Bremen'.
- Gross, A. & Fasel, H. (2008), Cfd for investigating active flow control, in '4th Flow Control Conference', p. 4310.

- Grossman, K., Cybyk, B., VanWie, D. et al. (2003), 'Sparkjet actuators for flow control', *AIAA paper* **57**, 2003.
- Gudmundsson, S. (2013), Chapter 10 the anatomy of lift enhancement, in 'General aviation aircraft design: Applied Methods and Procedures', Butterworth-Heinemann, pp. 402–443.
- Gülçat, Ü. (2010), Chapter 3 incompressible flow about an airfoil, in 'Fundamentals of modern unsteady aerodynamics', Springer, pp. 59–94.
- Hahn, K.-U. & König, R. (1992), Attas flight test and simulation results of the advanced gust management system lars, in 'Guidance, Navigation and Control Conference', p. 4343.
- Hamada, Y., Kikuchi, R. & Inokuchi, H. (2020), 'Lidar-based gust alleviation control system: Obtained results and flight demonstration plan', *IFAC-PapersOnLine* **53**(2), 14839–14844.
- Harding, S. F. & Bryden, I. G. (2012), Development of fixed hydrodynamic lifting surfaces to stabilise anchoring structures in energetic tidal flows, in 'International Conference on Offshore Mechanics and Arctic Engineering', Vol. 44885, American Society of Mechanical Engineers, pp. 343–351.
- Harley, C. D. (2011), Aerodynamic Performance of Low Form Factor Spoilers, PhD thesis, School of Mechanical, Aerospace and Civil Engineering, The University of Manchester, Manchester, UK.
- Heinz, N., King, R. & Gölling, B. (2010), Robust closed-loop lift control on an industry-relevant civil aircraft half model, in 'Active flow control II', Springer, pp. 125–139.
- Heinz, N., King, R., Höll, T., Wassen, E. & Thiele, F. (2010), Numerical investigation of robust closed-loop flow control of a high-lift configuration, in '5th Flow Control Conference', p. 4967.
- Henning, L., Pastoor, M., King, R., Noack, B. R. & Tadmor, G. (2007), Feedback control applied to the bluff body wake, in 'Active flow control', Springer, pp. 369–390.
- Hoholis, G., Steijl, R. & Badcock, K. (2016), 'Circulation control as a roll effector for unmanned combat aerial vehicles', *Journal of Aircraft* **53**(6), 1875–1889.  
**URL:** <https://doi.org/10.2514/1.C033642>
- Honeywell (2021), *HG1125/HG1126 Inertial Measurement Unit*, Honeywell Aerospace.  
**URL:** <https://aerospace.honeywell.com/us/en/learn/products/sensors/inertial-measurement-units>

- Huff, D. L. (2013), 'Nasa glenn's contributions to aircraft engine noise research', *Journal of Aerospace Engineering* **26**(2), 218–250.
- Itsariyapinyo, P. & Sharma, R. N. (2018), 'Large eddy simulation of a naca0015 circulation control airfoil using synthetic jets', *Aerospace Science and Technology* **82**, 545–556.
- Jabbal, M., Liddle, S. & Crowther, W. (2010), 'Active flow control systems architectures for civil transport aircraft', *Journal of Aircraft* **47**(6), 1966–1981.
- Jasak, H. (1996), 'Error analysis and estimation for the finite volume method with applications to fluid flows.'
- Jategaonkar, R. (1993), 'Identification of actuation system and aerodynamic effects of direct-lift-control flaps', *Journal of Aircraft* **30**(5), 636–643.
- John D. Anderson, J. (1995), Chapter 2 the governing equations of fluid dynamics, in 'Computational fluid dynamics: the basics with applications', McGraw-Hill, 1221 Avenue of the Americas New York, NY 10020, US, pp. 37–93.
- Johnston, J. P. & Nishi, M. (1990), 'Vortex generator jets-means for flow separation control', *AIAA journal* **28**(6), 989–994.
- Jones, G. S. & Joslin, R. D. (2005), 'Proceedings of the 2004 nasa/onr circulation control workshop, part 1'.
- Jones, G. S. & Joslin, R. D. (2006), Experiments and applications: Aerospace, in 'Applications of circulation control technology', Vol. 214, American Institute of Aeronautics and Astronautics, pp. 191–442.
- Jones, G. S., Lin, J. C., Allan, B. G., Milholen, W. E., Rumsey, C. L. & Swanson, R. (2008), 'Overview of cfd validation experiments for circulation control applications at nasa', *2008 International Powered Lift Conference; London; 22-24 Jul. 2008; United Kingdom* .
- Jones, G. S., Milholen, W. E., Chan, D. T., Allan, B., Goodliff, S. L., Melton, L., Anders, S. G., Carter, M. & Capone, F. (2013), Development of the circulation control flow scheme used in the ntf semi-span fast-mac model, in 'The 31st AIAA applied aerodynamics conference', pp. 1–20.
- Jones, G. S., Viken, S. A., Washburn, A. E., Jenkins, L. N. & Cagle, C. M. (2002), 'An active flow circulation controlled flap concept for general aviation aircraft applications', *AIAA paper* **3157**(1).

- Jones, J. (1980), 'Modelling of gusts and wind shear for aircraft assessment and certification', *Proceedings of the Indian Academy of Sciences Section C: Engineering Sciences* **3**(1), 1–30.
- Jones, R. T. (1940), The unsteady lift of a wing of finite aspect ratio, Technical report.
- Jones, W. & Launder, B. E. (1972), 'The prediction of laminarization with a two-equation model of turbulence', *International journal of heat and mass transfer* **15**(2), 301–314.
- Joslin, R. D. & Miller, D. N. (2009), Chapter 5. dynamic and closed-loop control, in 'Fundamentals and applications of modern flow control', American Institute of Aeronautics and Astronautics, pp. 115–142.
- Kaimal, J. C. & Finnigan, J. J. (1994), Chapter 4 flow over changing terrain, in 'Atmospheric boundary layer flows: their structure and measurement', Oxford university press, Great Clarendon Street Oxford OX2 6DP, UK, pp. 109–154.
- Kalman, R. E. (1960), 'A new approach to linear filtering and prediction problems'.
- Kalman, R. E. (1963), 'Mathematical description of linear dynamical systems', *Journal of the Society for Industrial and Applied Mathematics, Series A: Control* **1**(2), 152–192.
- Kalman, R. E. et al. (1960), 'Contributions to the theory of optimal control', *Bol. soc. mat. mexicana* **5**(2), 102–119.
- KARAKAŞ, M. (2020), 'Gust alleviation techniques and design methods of active aeroelastic wing'.
- Keesman, K. J. (2011), Part i data-based identification, in 'System identification: an introduction', Springer Science & Business Media, pp. 17–57.
- Keller, D. & Rudnik, R. (2015), 'Numerical investigation of engine effects on a transport aircraft with circulation control', *Journal of aircraft* **52**(2), 421–438.
- Kelm, R. & Grabietz, M. (2000), 'Method of reducing wind gust loads acting on an aircraft'. US Patent 6,161,801.
- Kerstens, W., Pfeiffer, J., Williams, D., King, R. & Colonius, T. (2011), 'Closed-loop control of lift for longitudinal gust suppression at low reynolds numbers', *AIAA journal* **49**(8), 1721–1728.
- Khalil, A. & Fezans, N. (2021), 'Gust load alleviation for flexible aircraft using discrete-time preview control', *The Aeronautical Journal* **125**(1284), 341–364.

- King, R. (2010), Part vi: Optimal flow control, in 'Active Flow Control II 2010', Springer, Berlin, Germany, pp. 391–405.
- King, R., Heinz, N., Bauer, M., Grund, T. & Nitsche, W. (2013), 'Flight and wind-tunnel tests of closed-loop active flow control', *Journal of Aircraft* **50**(5), 1605–1614.
- Kohlman, D. L. & Brainerd, C. H. (1974), 'Evaluation of spoilers for light aircraft flight path control', *Journal of Aircraft* **11**(8), 449–456.
- Kopal, Z. (1947), Tables of supersonic flow around cones, in 'technical report 1, 1947', Massachusetts Institute of Technology.
- Kundu, A. K. (2010), Chapter 3 - aerodynamic considerations, in 'Aircraft design', Cambridge aerospace series ; 27, Cambridge University Press, Cambridge, pp. 43–97.
- Küssner, H. G. (1936), 'Zusammenfassender bericht über den instationären auftrieb von flügeln', *Luftfahrtforschung* **13**(12), 410–424.
- Laney, C. B. (1998), *Computational Gasdynamics*, Cambridge University Press.  
**URL:** <https://app.knovel.com/hotlink/toc/id:kpCG000004/computational-gasdynamics/computational-gasdynamics>
- Lee-Rausch, E., Vatsa, V. & Rumsey, C. (2006), Computational analysis of dual radius circulation control airfoils, in '3rd AIAA flow control conference', p. 3012.
- Leishman, J. G. (1994), 'Unsteady lift of a flapped airfoil by indicial concepts', *Journal of Aircraft* **31**(2), 288–297.
- Leonard, B. (1979), 'A stable and accurate convective modelling procedure based on quadratic upstream interpolation', *Computer Methods in Applied Mechanics and Engineering* **19**(1), 59–98.  
**URL:** <https://www.sciencedirect.com/science/article/pii/0045782579900343>
- Li, Y. & Qin, N. (2020), 'Airfoil gust load alleviation by circulation control', *Aerospace Science and Technology* **98**, 105622.
- Lichtwardt, J. & Marshall, D. (2011), Investigation of the unsteady behavior of a circulation control wing using computational fluid dynamics, in '49th AIAA Aerospace Sciences Meeting including the New Horizons Forum and Aerospace Exposition', p. 1041.

- Liu, Y., Sankar, L., Englar, R., Ahuja, K. & Gaeta, R. (2004), Computational evaluation of the steady and pulsed jet effects on the performance of a circulation control wing section, *in* '42nd AIAA Aerospace sciences meeting and exhibit', p. 56.
- Ljung, L. (2022), 'System identification toolbox', *The Matlab user's guide* .
- Lui, Y. et al. (n.d.), Computational evaluation of the steady and pulsed jet effects on the performance of a circulation control wing section. 2004 nasa/onr circulation control workshop, march 16-17, 2004, Technical report, NASA/CP-2005-213509.
- Lungu, M. (2020), 'Backstepping and dynamic inversion combined controller for auto-landing of fixed wing uavs', *Aerospace Science and Technology* **96**, 105526.
- LYKKEN, O. & SHAH, N. M. (1972), 'Direct lift control for improved automatic landing and performance of transport aircraft lowell', *Journal of Aircraft* **9**(5), 325–332.
- Machunze, W., Gessler, A., Fabel, T., Horst, P., Rädcl, M., Wolf, K., Ulbricht, A., Münter, S. & Hufenbach, W. (2016), 'Active flow control system integration into a cfrp flap', *CEAS Aeronautical Journal* **7**(1), 69–81.  
**URL:** <http://dx.doi.org/10.1007/s13272-015-0171-2>
- Margalit, S., Greenblatt, D., Seifert, A. & Wygnanski, I. J. (2002), 'Active flow control of a delta wing at high incidence using segmented piezoelectric actuators', *1st Flow Control Conference 2002* .
- Matsuzaki, Y., Ueda, T., Miyazawa, Y. & Matsushita, H. (1989), 'Gust load alleviation of a transport-type wing-test and analysis', *Journal of aircraft* **26**(4), 322–327.
- McDaniel, D., Cummings, R., Bergeron, K., Morton, S. & Dean, J. (2007), Comparisons of cfd solutions of static and maneuvering fighter aircraft with flight test data, Technical report, AIR FORCE ACADEMY COLORADO SPRINGS CO.
- McGhee, R. J. (1980), *NASA TN D-7428, Low-speed aerodynamic characteristics of a 17-percent-thick medium speed airfoil designed for general aviation applications*, National Aeronautics and Space Administration.
- McGowan, G. & Gopalarathnam, A. (2005), Cfd analysis of circulation control airfoils using fluent, *in* 'Proceedings of the 2004 NASA/ONR Circulation Control Workshop, Part 2'.
- McGowan, G., Gopalarathnam, A. & Jones, G. (2004), Analytical and computational study of adaptive circulation control airfoils, *in* '22nd Applied Aerodynamics Conference and Exhibit', p. 4721.

- McLean, J., Crouch, J., Stoner, R., Sakurai, S., Seidel, G., Feifel, W. & Rush, H. (1999), *Study of the application of separation control by unsteady excitation to civil transport aircraft*, Boeing Commercial Airplane Co., Seattle, WA United States.
- McManus, K. & Magill, J. (1996), 'Separation control in incompressible and compressible flows using pulsed jets', *AIAA paper* **1948**, 1996.
- Medina, A., Ol, M. V., Mancini, P. & Jones, A. (2017), 'Revisiting conventional flaps at high deflection rate', *AIAA Journal* **55**(8), 2676–2685.
- Menter, F. R. (1994), 'Two-equation eddy-viscosity turbulence models for engineering applications', *AIAA journal* **32**(8), 1598–1605.
- Menter, F. & Rumsey, C. (1994), Assessment of two-equation turbulence models for transonic flows, in 'Fluid Dynamics Conference', p. 2343.
- Milholen, W., Jones, G. & Cagle, M. (2010), Nasa high-reynolds number circulation control research-overview of cfd and planned experiments, in '48th AIAA Aerospace Sciences Meeting Including the New Horizons Forum and Aerospace Exposition', p. 344.
- Minzner, R., Pond, H. & Champion, K. S. (1959), *The ARDC model atmosphere, 1959*, Vol. 59, Geophysics Research Directorate, Air Force Cambridge Research Center.
- Moorhouse, D. & Woodcock, R. (1980), 'Us military specification mil-f-8785c', *US Department of Defense: Washington DC, USA* .
- Morrison, J. F., Dearing, S. S., Arthur, G. G., McKeon, B. J. & Cui, Z. (2006), 'Fluid flow control using boundary layer control'.
- Nelson, R. C. et al. (1998), Chapter 6 aircraft response to control or atmospheric inputs, in 'Flight stability and automatic control', Vol. 2, WCB/McGraw Hill New York, pp. 212–234.
- Nelson, T. (2005), '787 systems and performance', *The Boeing Company* .
- Neuendorf, R. & Wygnanski, I. (1999), 'On a turbulent wall jet flowing over a circular cylinder', *Journal of Fluid Mechanics* **381**, 1–25.
- Nield, B. (1995), 'An overview of the boeing 777 high lift aerodynamic design', *The Aeronautical Journal* **99**(989), 361–371.
- Nishino, T., Hahn, S. & Shariff, K. (2010), 'Large-eddy simulations of a turbulent coanda jet on a circulation control airfoil', *Physics of fluids* **22**(12), 125105.

- NOVAK, C., CORNELIUS, K. & ROADS, R. (1987), Experimental investigations of the circular wall jet on a circulation control airfoil, *in* '25th AIAA Aerospace Sciences Meeting', p. 155.
- NTSB (AUGUST 2,1985), Aircraft accident report - delta air lines, lockheed l-101 l-385-1, n726da dallas/fort worth international airport, texas, AIRCRAFT ACCIDENT REPORT NTSB AAR-86/05, NATIONAL TRANSPORTATION SAFETY BOARD, Washington, DC.
- Ol, M., Zeune, C., White, T. & Kudla, T. (2013), Wind tunnel evaluation of powered static aerodynamics of an aerobatic uav, *in* '51st AIAA Aerospace Sciences Meeting including the New Horizons Forum and Aerospace Exposition', p. 241.
- Paschal, K., Neuhart, D., Beeler, G. & Allan, B. (2012), Circulation control model experimental database for cfd validation, *in* '50th AIAA Aerospace Sciences Meeting including the New Horizons Forum and Aerospace Exposition', p. 705.
- Patankar, S. V. (1980), Chapter 2 mathematical description of physical phenomena, *in* 'Numerical heat transfer and fluid flow', McGraw-Hill, 1221 Avenue of the Americas New York, NY 10020, US, pp. 11–22.
- Patel, M. P., Sowle, Z. H., Corke, T. C. & He, C. (2007), 'Autonomous sensing and control of wing stall using a smart plasma slat', *Journal of aircraft* **44**(2), 516–527.
- Patel, M., Prince, T., Carver, R., DiCocco, J., Lisy, F. & Ng, T. (2002), Control of aircraft stall via embedded pressure sensors and deployable flow effectors, *in* 'AIAA 2002-3170, 1st Flow Control Conference, St. Louis, Missouri'.
- Paterson, E. & Baker, W. (2004), Simulation of steady circulation control for marine-vehicle control surfaces, *in* '42nd AIAA Aerospace Sciences Meeting and Exhibit', p. 748.
- Pegasus (2017), 'Ct-17-1000 celeroton turbo compressor datasheet'.  
**URL:** [https://www.celeroton.com/fileadmin/user\\_upload/produkte/kompressor/datasheets/Datasheet-CT-17-1000.pdf](https://www.celeroton.com/fileadmin/user_upload/produkte/kompressor/datasheets/Datasheet-CT-17-1000.pdf)
- Pfingsten, K. C. & Radespiel, R. (2009), Experimental and numerical investigation of a circulation control airfoil, *in* '47th AIAA Aerospace Sciences Meeting Including The New Horizons Forum and Aerospace Exposition', p. 533.
- Phillips, E. & Wagnanski, I. (2013), 'Use of sweeping jets during transient deployment of a control surface', *AIAA journal* **51**(4), 819–828.

- Pinsker, W. (1970a), The control characteristics of aircraft employing direct-lift control, in 'Reports and Memoranda No. 3629', Aerodynamics Dept., RIA.E., Bedford, HM Stationery Office.
- Pinsker, W. (1970b), 'Direct lift control', *The Aeronautical Journal* **74**(718), 817–825.
- Pironneau, O. & Pironneau, O. (1989), Chapter 5 the navier-stokes equations, in 'Finite element methods for fluids', Wiley Chichester.
- Pointwise (n.d.), 'T-rex hybrid meshing in pointwise'. User Manual.  
**URL:** <https://www.pointwise.com/theconnector/2011-July/T-Rex-Hybrid-Meshing-Pointwise.html>
- Rainey, A. G. (1971), Advanced active controls technology, in 'Vehicle Technology for Civil Aviation: the Seventies and Beyond: Proceedings of a Conference Held at Langley Research Center, Hampton, Virginia, November 2-4, 1971', Vol. 292, Scientific and Technical Information Office, National Aeronautics and Space . . . , p. 245.
- Raman, G., Khanafseh, S., Cain, A. & Kerschen, E. (2004), 'Development of high bandwidth powered resonance tube actuators with feedback control', *Journal of Sound and Vibration* **269**(3), 1031–1062.
- Raveh, D. E. (2007), 'Cfd-based models of aerodynamic gust response', *Journal of Aircraft* **44**(3), 888–897.
- Reader, K. R. & Wilkerson, J. B. (1977), Circulation control applied to a high speed helicopter rotor, Technical report, DAVID W TAYLOR NAVAL SHIP RESEARCH AND DEVELOPMENT CENTER.
- Reba, I. (1966), 'Applications of the coanda effect', *Scientific American* **214**(6), 84–93.
- Reckzeh, D. (2003), 'Aerodynamic design of the high-lift-wing for a megaliner aircraft', *Aerospace Science and Technology* **7**(2), 107–119.
- Regan, C. D. & Jutte, C. V. (2012), 'Survey of applications of active control technology for gust alleviation and new challenges for lighter-weight aircraft'.
- Richardson, B. L. F. (1922), 'Weather prediction by numerical process', *Quarterly Journal of the Royal Meteorological Society* **48**(203), 282–284.  
**URL:** <https://rmets.onlinelibrary.wiley.com/doi/abs/10.1002/qj.49704820311>

- Richardson, L. F. & Glazebrook, R. T. (1910), 'On the approximate arithmetical solution by finite differences of physical problems involving differential equations, with an application to the stresses in a masonry dam', *Proceedings of the Royal Society of London. Series A, Containing Papers of a Mathematical and Physical Character* **83**(563), 335–336.  
**URL:** <https://royalsocietypublishing.org/doi/abs/10.1098/rspa.1910.0020>
- Robertson-Welsh, B. (2017), On the Influence of Nozzle Geometries on Supersonic Curved Wall Jets, PhD thesis, The University of Manchester (United Kingdom).
- Rogers, E. & Donnelly, M. (2004), Characteristics of a dual-slotted circulation control wing of low aspect ratio intended for naval hydrodynamic applications, in '42nd AIAA Aerospace Sciences Meeting and Exhibit', p. 1244.
- Rosén, C., Kanistras, K., Saka, P. C., Valavanis, K. P. & Rutherford, M. J. (2018), 'System identification and controller implementation of a centrifugal compressor for circulation control applications', *Journal of Intelligent & Robotic Systems* **91**(3), 629–650.
- Rosen, C., Kanistras, K., Saka, P., Valavanis, K. & Rutherford, M. (2017), Design and development of a control scheme for the uc2av: Unmanned circulation control aerial vehicle, in '55th AIAA Aerospace Sciences Meeting', p. 1528.
- Rudolph, P. K. (1996), 'High-lift systems on commercial subsonic airliners', *NASA Contractor report No. NASA-CR-4746*.
- Rumsey, C. L. & Nishino, T. (2011), 'Numerical study comparing rans and les approaches on a circulation control airfoil', *International Journal of Heat and Fluid Flow* **32**(5), 847–864.
- Salem Said, A.-H. & Ragab, S. (2008), Rans simulation of circulation control on a circular planform wing, in '4th Flow Control Conference', p. 4326.
- Saric, W. S. et al. (1994), 'Gortler vortices', *Annual Review of Fluid Mechanics* **26**(1), 379–409.
- Savvaris, A., Buonanno, A., Jamil, R. & Tsourdos, A. (2013), Design and development of the demon uav fluidic flight control system, in 'AIAA Infotech@ Aerospace (I@ A) Conference', p. 4820.
- Schaeffler, N. W., Hepner, T. E., Jones, G. S. & Kegerise, M. A. (2002), 'Overview of active flow control actuator development at nasa langley research center'.
- Schlecht, R. & Anders, S. (2007), Parametric evaluation of thin, transonic circulation-control airfoils, in '45th AIAA Aerospace Sciences Meeting and Exhibit', p. 272.

- Schlichting, H. & Gersten, K. (2003), Fundamentals of boundary-layer theory, in 'Boundary-layer theory', Springer Science & Business Media, pp. 29–49.
- Sears, W. R. (1941), 'On the reaction of an elastic wing to vertical gusts', *Journal of the Aeronautical Sciences* **8**(2), 64–67.
- Sedky, G., Gementzopoulos, A., Andreu-Angulo, I., Lagor, F. D. & Jones, A. R. (2022), 'Physics of gust response mitigation in open-loop pitching manoeuvres', *Journal of Fluid Mechanics* **944**.
- Seifert, A., Eliahu, S., Greenblatt, D. & Wygnanski, I. (1998), 'Use of piezoelectric actuators for airfoil separation control', *AIAA journal* **36**(8), 1535–1537.
- Seifert, A. & Pack, L. (1999), 'Oscillatory control of separation at high reynolds numbers', *AIAA journal* **37**(9), 1062–1071.
- Sellars, N., Wood, N. & Kennaugh, A. (2002), Delta wing circulation control using the coanda effect, in '1st Flow Control Conference', p. 3269.
- Semaan, R., El Sayed, M. Y. & Radespiel, R. (2019), Sparse model of the lift gains of a circulation control wing with unsteady coanda blowing, in 'Active Flow and Combustion Control 2018', Springer, pp. 3–18.
- Shires, A. (2016), Chapter 1 introduction, in 'Aerodynamics & Aerospace Propulsion Lecture Notes - Volume 1: Aerodynamics', University of Leeds, pp. 5–14.
- Shires, A. & Kourkoulis, V. (2013), 'Application of circulation controlled blades for vertical axis wind turbines', *Energies* **6**(8), 3744–3763.
- Skogestad, S. & Postlethwaite, I. (2007), Chapter 9 controller design, in 'Multivariable feedback control: analysis and design', Vol. 2, Citeseer, p. 368.
- Slomski, J., Chang, P. & Arunajatesan, S. (2006), Large eddy simulation of a circulation control airfoil, in '3rd AIAA Flow Control Conference', p. 3011.
- Slomski, J., Gorski, J., Miller, R. & Marino, T. (2002), Numerical simulation of circulation control airfoils as affected by different turbulence models, in '40th AIAA Aerospace Sciences Meeting & Exhibit', p. 851.
- Slomski, J., Marino, T., Ebert, M. P. & Abramson, J. (2006), 'Full reynolds-stress modeling of circulation control airfoils', *Applications of Circulation Control Technology, Progress in Astronautics and Aeronautics* pp. 445–468.

- SMC (n.d.), *SX10 High-speed 2 Port Valve*, SMC Pneumatics LTD.
- Smith, D. R. & Warsop, C. (2019), Nato avt-239 task group: 'innovative control effectors for manoeuvring of air vehicles'—introduction and overview, in 'AIAA Scitech 2019 Forum', p. 0041.
- Smith, J., Liu, C. & Chen, W.-H. (2016), Disturbance observer based control for gust alleviation of a small fixed-wing uas, in '2016 International Conference on Unmanned Aircraft Systems (ICUAS)', pp. 97–106.
- Sommerwerk, K., Krukow, I., Haupt, M. C. & Dinkler, D. (2016), 'Investigation of aeroelastic effects of a circulation controlled wing', *Journal of Aircraft* **53**(6), 1746–1756.
- Spalart, P. & Allmaras, S. (1992), A one-equation turbulence model for aerodynamic flows, in '30th aerospace sciences meeting and exhibit', p. 439.
- Stanewsky, E. (2001), 'Adaptive wing and flow control technology', *Progress in Aerospace Sciences* **37**(7), 583–667.
- Stevens, B. L., Lewis, F. L. & Johnson, E. N. (2015), Chapter 5 modern design techniques, in 'Aircraft control and simulation: dynamics, controls design, and autonomous systems', John Wiley & Sons, 111 River St, Hoboken, New Jersey, US, pp. 377–500.
- Strüber, H. (2014), The aerodynamic design of the a350 xwb-900 high lift system, in '29th International Congress of the Aeronautical Science', pp. 913–921.
- Subhash, M. & Dumas, A. (2013), 'Computational study of coanda adhesion over curved surface', *SAE International Journal of Aerospace* **6**(2013-01-2302), 260–272.
- Swanson, R. C., Rumsey, C. L. & Anders, S. G. (2005a), Aspects of numerical simulation of circulation control airfoils, in 'Proceedings of the 2004 NASA/ONR Circulation Control Workshop, Part 1'.
- Swanson, R. & Rumsey, C. (2006), Numerical issues for circulation control calculations, in '3rd AIAA Flow Control Conference', p. 3008.
- Swanson, R. & Rumsey, C. (2009), 'Computation of circulation control airfoil flows', *Computers & Fluids* **38**(10), 1925–1942.
- Swanson, R., Rumsey, C. & Anders, S. (2005b), Progress towards computational method for circulation control airfoils, in '43rd AIAA Aerospace Sciences Meeting and Exhibit', p. 89.
- Taha, H. E. & Rezaei, A. S. (2019), On the dynamics of unsteady lift and circulation and the circulatory-non-circulatory classification, in 'AIAA Scitech 2019 Forum', p. 1853.

- Theodorsen, T. & Mutchler, W. (1935), 'General theory of aerodynamic instability and the mechanism of flutter'.
- Trancossi, M. (2011), An overview of scientific and technical literature on coanda effect applied to nozzles, Technical report, SAE Technical Paper.
- UTC (2017), *Angle of Attack (AOA) Systems*, UTC aerospace systems.  
**URL:** <https://www.collinsaerospace.com/-/media/project/collinsaerospace/collinsaerospace-website/product-assets/files/commercial/flight-deck/surveillance/air-data-systems/angle-of-attack-aoa-systems.pdf?rev=5334a65820844e7ebc8b8b89d7bf4422>
- Vartio, E., Shimko, A., Tilmann, C. & Flick, P. (2005), Structural modal control and gust load alleviation for a sensorcraft concept, in '46th AIAA/ASME/ASCE/AHS/ASC Structures, Structural Dynamics and Materials Conference', p. 1946.
- Versteeg, H. K. & Malalasekera, W. (2007), Turbulence and its modelling, in 'An introduction to computational fluid dynamics: the finite volume method', Pearson education, pp. 40–113.
- von Karman, T. H. & Sears, W. R. (1938), 'Airfoil theory for non-uniform motion', *Journal of the Aeronautical Sciences* 5(10), 379–390.
- Wagner, H. (1924), 'Über die entstehung des dynamischen auftriebes von tragflügeln'.
- Wagner, M. & Norris, G. (2009), *Boeing 787 dreamliner*, Zenith Press.
- Walton, V. M., Borland, C. J., Siu, T. L., Najmabadi, K., Coleman, E. E., Marquis, D. P., McMullin, D. L. & Milligan, K. H. (2014), 'Vertical gust suppression system for transport aircraft'. US Patent 8,774,987.
- Wendt, J. F. (2008), Chapter 11 introduction to finite volume methods in computational fluid dynamics, in 'Computational fluid dynamics: an introduction', Springer Science & Business Media, p. 275.
- Whalen, E. A., Lacy, D. S., Lin, J. C., Andino, M. Y., Washburn, A. E., Graff, E. C. & Wygnanski, I. J. (2015), Performance enhancement of a full-scale vertical tail model equipped with active flow control, in '53rd AIAA Aerospace Sciences Meeting', pp. 1–11.
- Wilcox, D. C. et al. (1998), Chapter 4 one-equation and two-equation models, in 'Turbulence modelling for CFD', Vol. 2, DCW industries La Canada, CA, 5354 Palm Drive, La Canada, California 91011, pp. 107–230.

- Wilde, P., Buonanno, A., Crowther, W. & Savvaris, A. (2008), Aircraft control using fluidic maneuver effectors, in '26th AIAA applied aerodynamics conference', p. 6406.
- Wille, R. & Fernholz, H. (1965), 'Report on the first european mechanics colloquium, on the coanda effect', *Journal of Fluid Mechanics* **23**(4), 801–819.
- Williams, D., Kerstens, W., Pfeiffer, J., King, R. & Colonius, T. (2010), Unsteady lift suppression with a robust closed loop controller, in 'Active Flow Control II', Springer, pp. 19–30.
- Williams, D. R. & Seidel, J. (2016), Crossed-actuation afc for lateral-directional control of an ice-101/sacon ucav, in '8th AIAA Flow Control Conference', p. 3167.
- Wood, N. & Nielsen, J. (1985), Circulation control airfoils-past, present, future, in '23rd Aerospace Sciences Meeting', p. 204.
- Wright, J. R. & Cooper, J. E. (2008), Chapter 14 gust and turbulence encounters, in 'Introduction to aircraft aeroelasticity and loads', Vol. 20, John Wiley & Sons, pp. 299–335.
- Xiaoping, X., Xiaoping, Z., Zhou, Z. & Ruijun, F. (2011), 'Application of active flow control technique for gust load alleviation', *Chinese Journal of Aeronautics* **24**(4), 410–416.
- Yang, X., Mejias Alvarez, L. & Molloy, T. (2012), A gust-attenuation controller for fixed-wing uavs during collision avoidance course, in 'Proceedings of the 2012 International Conference on Unmanned Aircraft Systems (ICUAS'12)', International Conference on Unmanned Aircraft Systems Association, Inc., pp. 1–11.
- Yang, Z., Igarashi, H., Martin, M. & Hu, H. (2008), An experimental investigation on aerodynamic hysteresis of a low-reynolds number airfoil, in '46th AIAA aerospace sciences meeting and exhibit', p. 315.
- Yeo, D. W., Rehm, N., Bradley, J. M. & Chopra, I. (2019), Flow-aware computational wings for improved gust mitigation on fixed-wing unmanned aerial systems, in 'AIAA SciTech 2019 Forum', p. 1689.
- Zaide, A. & Raveh, D. (2006), 'Numerical simulation and reduced-order modeling of airfoil gust response', *AIAA journal* **44**(8), 1826–1834.
- Zhang, P. (2010), Chapter 4 transducers and valves, in 'Advanced industrial control technology', William Andrew, pp. 117–152.

Zhou, Q., Chen, G., Da Ronch, A. & Li, Y. (2017), 'Reduced order unsteady aerodynamic model of a rigid aerofoil in gust encounters', *Aerospace Science and Technology* **63**, 203–213.

**URL:** <https://www.sciencedirect.com/science/article/pii/S1270963816313943>

Zienkiewicz, O. C., Taylor, R. L., Nithiarasu, P. & Zhu, J. (1977), Chapter 1 the standard discrete system and origins of the finite element method, in 'The finite element method', Vol. 3, McGraw-hill London, 1221 Avenue of the Americas, New York, NY 10020, US, pp. 1–13.

Zivko (2003), 'Zivko aeronautics inc. edge 540 specifications'.

**URL:** <http://www.zivko.com>

Åström, K. & Hägglund, T. (2001), 'The future of pid control', *Control Engineering Practice* **9**(11), 1163–1175.

**URL:** <https://www.sciencedirect.com/science/article/pii/S0967066101000624>